Geochemical and fluid inclusion study of hydrothermal mineralization in the Busang Southeast Zone, Kalimantan, Indonesia: Unique insight into the Bre-X Scandal

EVAN SLATER

Co-Supervisors: Marcos Zentilli (DAL) and Jacob Hanley (SMU)

2013-04-26

Thesis submitted as partial fulfilment for the degree of BSc (Honours)

Department of Earth Sciences, Dalhousie University,

Halifax, Nova Scotia, B3H-4R2, Canada

DALHOUSIE UNIVERSITY
Inspiring Minds

Department of Earth Sciences
Halifax, Nova Scotia
Canada B3H 4R2
(902) 494-2358
FAX (902) 494-6889

DATE: April 4th, 2013

AUTHOR: Evan. T. Slater

TITLE: Geochemical and fluid inclusion study of hydrothermal mineralization in the Busang Southeast Zone, Kalimantan, Indonesia: Unique insight into the Bre-X Scandal

Degree: B.Sc. Hons. Convocation: May Year: 2013

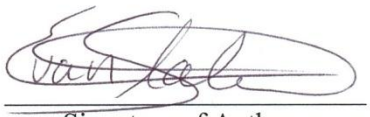

Signature of Author

Table of contents

List of figures

List of tables

List of equations

Abstract

Geochemical and fluid inclusion study of hydrothermal mineralization in the Busang Southeast Zone, Kalimantan, Indonesia: Unique insight into the Bre-X Scandal

From 1992 to 1997 Bre-X Minerals Ltd. alleged to have found one of the richest gold deposits on earth in central Kalimantan, Indonesia. In 1997 Dalhousie professor Dr. G.C. Milligan was invited to visit Busang and collect samples from the highest grade zones. Initial study of these samples in Halifax failed to detect any gold. In 1997 independent evaluations determined that Busang samples had been systematically salted, unearthing one of the worst mining hoaxes in history.

The suite collected by Dr. Milligan includes 12 samples of drillcore from the Busang Southeast Zone. Here they have been re-studied petrographically, analyzed for major and trace elements, and microthermometry of quartz-hosted fluid inclusions has been carried out on mineralized veinlets.

The samples are volcanic and subvolcanic basaltic andesite-andesite. Their geochemistry suggests calc-alkaline magmas generated in an island arc typical of the host rocks in the Kalimantan Gold Belt. Alteration consists of silicification, calcitization, sericitization, and chloritization. In quartz-calcite (±gypsum/anhydrite) veinlets, ore-microscopy recognizes pyrite, sphalerite, galena, bournonite-seligmannite, lesser chalcopyrite, and minor tetrahedrite-tennantite, but no discrete Au or Ag minerals. Pyrite is ubiquitous throughout the altered rocks as dendritic veinlets and clots. Fluid inclusions in veinlet-hosted quartz are small (<20 μm), rare, and irregular with dominantly two-phases (aqueous liquid + vapour), and high temperatures of homogenization (198-330^{o}C). Most are unclassified however some likely represent primary assemblages as they occur along primary growth zones in quartz.

In conclusion, the suite represents a moderately mineralized system with base metals, generated by hydrothermal fluids of predominantly meteoric origin, which were likely heated by an intrusion. As such, it is compatible with location at the fringe of a low-sulfidation epithermal precious metal system. However, the absence of a significant gold anomaly (8-139 ppb Au), the lack of promising textures, and the relatively high temperatures of the hydrothermal fluids are incompatible with the suite representing a rich ore deposit. It is likely that these samples came from deep in an epithermal system, and that any associated precious metal mineralization has been removed by erosion.

Acknowledgements

I would like to thank my supervisors Marcos Zentilli (Dalhousie University) and Jacob Hanley (Saint Mary's University). Their dedication to students and their breadth of knowledge is truly an inspiration. I hope to one day provide the next generation of geoscientists with the same mentorship which they have bestowed upon me. I also thank Martin Gibling for going above and beyond the call of duty in his role as coordinator of the honour class providing guidance through every stage of the project. I thank Dr. George Clinton Milligan for his willingness to let me destroy his samples in the name of science and for his words of encouragement. I thank Yana Fedortchouk for entrusting me with her excellent microscope, and Dan Macdonald for providing assistance with microprobe analysis while taking extra care to ensure that my data was of excellent quality. The perfect polished-thin sections prepared by Gordon Brown were essential to the success of this study.

Research was financed through the SEG Canada Foundation, Shell Experiential Learning Fund (SELF) (c/o Department of Earth Sciences, Dalhousie) and contributions from MZ Geoscience and Jacob's research funds. Without this financial support I would not have been able to study these samples with the vigor that they deserved. My family has helped to support me through my undergraduate degree and I am grateful to have had their unconditional support and guidance through this rewarding experience.

Additional information about the geological environment of Busang was sent by Dr. Phillip Hellman of HS Consultants of Australia a few days before the closing deadline for this thesis. This information was not incorporated into the thesis; however, it will be of great importance in any future work or publications on these samples.

I finally thank Marcos for providing me with this unique and challenging project. The Bre-X affair is a tragedy of immeasurable magnitude resulting in great financial and personal losses. It will forever be a part of Dalhousie's legacy and I am honoured to have made a contribution to shed some modest light into an event of such great significance.

Chapter 1: Introduction

1.1 General statement

Epithermal precious metal deposits are significant mineral deposits for their potential to be very large and for their global abundance. These are hydrothermal deposits that typically occur in convergent-plate settings where subducted oceanic lithosphere produces magmatism in volcanic-arc settings. Intrusions into these magmatic arcs are thought to provide heat which drives the convection of hydrothermal fluid. These hydrothermal fluids are metal-bearing and principally waters derived from magmas, meteoric waters or a mixture of both. The ratio of magmatic to meteoric waters has notable effects on features associated with these deposits. These fluids are channelled in shallow crustal levels (the epizone), and when coupled with a mechanism for precipitating the dissolved metals, such as boiling or mixing, ore is deposited. The Southwest Pacific Rim has been the target for hydrothermal precious metal deposit exploration due to its favourable geological setting; the many subduction zones and volcanic terrains have resulted in significant precious metal occurrences (Leach & Corbett, 1997).

In 1996-1997, Bre-X Minerals Ltd. advertised their Busang gold deposit as being the largest gold deposit ever discovered, having 200 million ounces of gold (Francis, 1997). The Busang property is remotely located in the Indonesian portion of the rainforest-covered island of Borneo (Fig. 1.1-1). Their deposit was classified as an epithermal gold deposit and was noted as being similar to other epithermal deposits in the Pacific Rim. In 1996, Dalhousie graduate John Felderhof received the “Mining Man

of the Year" award from the *Northern Miner* for his role in the discovery. In February 1997, Dalhousie Professor Dr. George Clint Milligan was invited by his former student Mr. Felderhof to visit Busang, and to collect samples from the highest grade zone for the Earth Sciences Department. These samples are the principal subject of the study. In March of 1997 Freeport-McMoRan Copper & Gold Inc., Bre-X's partner in Busang, was conducting "due diligence" and drilling its own holes to confirm Bre-X's results. Freeport was unable to replicate assay results, finding gold in only trace amounts. An independent investigation later concluded that the samples from Bre-X had been "salted" with extraneous gold before being sent for assay (Francis, 1997). The scandal exploded, unearthing one of the most damaging mine hoaxes in history. Since then, virtually all aspects of the mining industry have been affected by the lessons learned from Bre-X. Mining regulations have been increased in order to prevent a future fraud from occurring, and to ensure the accountability of the professionals involved (Francis, 1997), (Andrew, 2005).

During the exploration of Busang, numerous geologists and consultants studied and reviewed the work of Bre-X. During these reviews there were few notable concerns regarding their work or the authenticity of the deposit. The assay results appeared to be consistent with the genetic model for epithermal gold deposits in this region, except that they were anomalously high. There must have been some reason why these professionals were so easily convinced of the legitimacy of Bre-X's findings. It is likely that the geology of Busang closely resembled that of an epithermal gold deposit, specifically a low-sulfidation epithermal gold deposit.

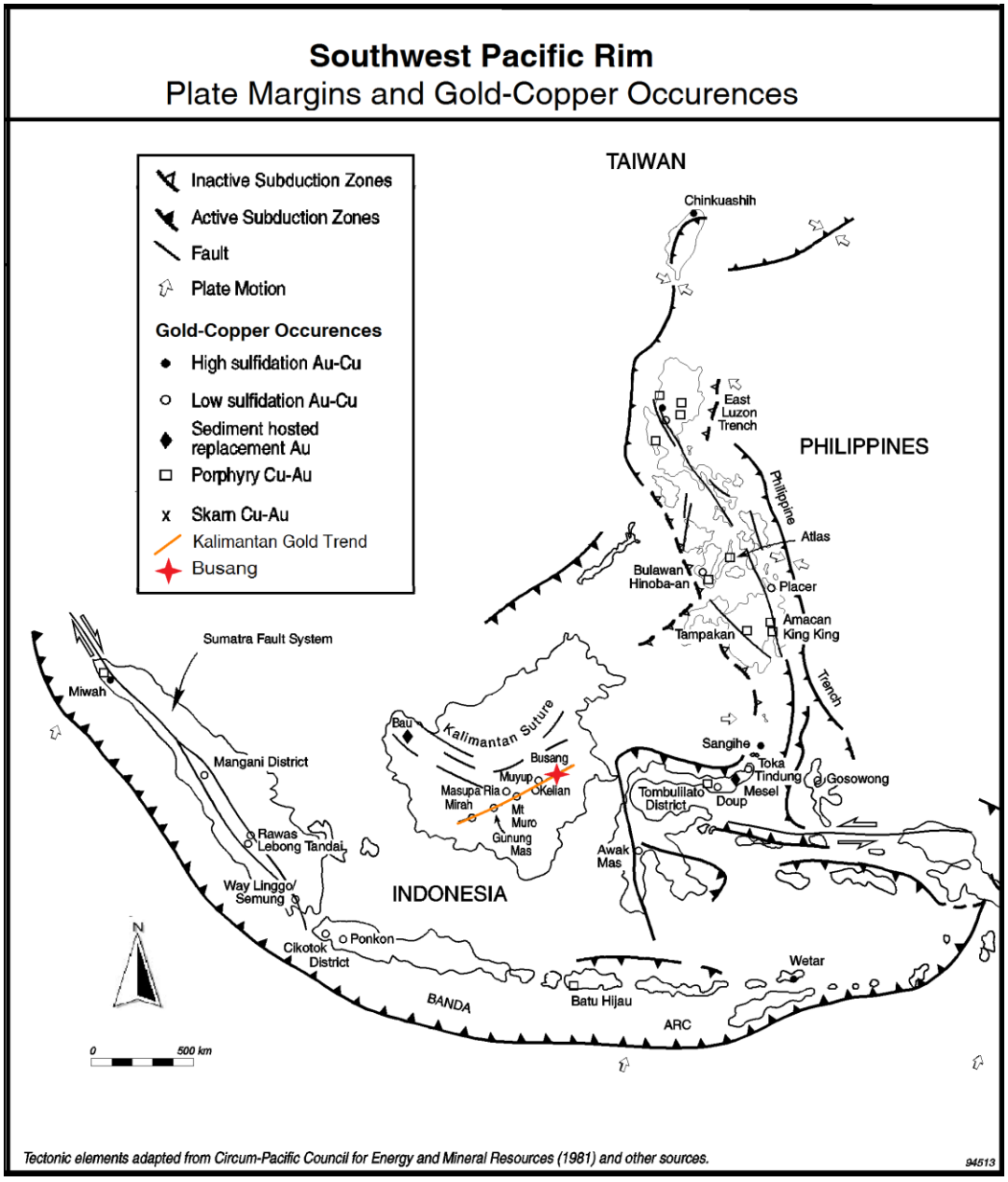

Figure 1.1-1: Southwest Pacific Rim gold and copper deposits and tectonic setting. The location of Busang and the Kalimantan Gold Trend (Belt) is indicated. (Modified from Leach & Corbett, 1997)

1.2 The Bre-X saga

The following is a summary of the events involved in the mining scandal perpetrated by Bre-X Minerals Ltd. between 1992 and 1997. The details, and facts regarding this event were obtained principally from the book “Bre-X the Inside Story” by

Diane Francis (1997) unless otherwise stated. Similar accounts have been used to educate professional engineers and geoscientists about ethics (Andrew, 2005).

The island of Borneo (1336 km by 996 km) is covered by mountainous rainforest and is located in the Southwest Pacific Rim. On the island is the property known as Busang I (later referred to as the Central Zone) which was owned by an Australian company. It was explored with funds raised from the Australian Stock market and between 1988 and 1989 $3 million was spent on trenches and the drilling of 19 holes. In these holes they found some gold mineralization and the trenches yielded even more promising results. The positive results became less frequent as exploration continued and rough economic times put a halt to work on the property.

Bresea Resources Inc. run by promoter David Walsh was listed on the Vancouver stock exchange in 1984. The company was small and had not yet found its niche, taking on projects ranging from petroleum to mineral exploration. Bre-X Minerals Ltd., a subsidiary of Bresea and also run by David Walsh, in 1991 held market securities of merely $15,000. In 1992 Bre-X's stock hovered around 27 cents a share as it switched its focus to exploring for diamonds on their properties in the Northwest Territories. This created a short interest in their stock due to claims near successful diamond fields, but these properties were eventually sold.

David Walsh had been communicating with geologist John Felderhof about properties in the Pacific Rim. Based on Felderhof's claims that there were potential resources in Busang Indonesia, David Walsh decided to buy the property and recruited

Felderhof to the Bre-X team. On February 26th, 1993 a stock option agreement between Bre-X and Bresea was reached. Bresea bought 500 000 Bre-X shares at 11.25 cents each; the fate of these two companies was connected from this point onwards. Drilling commenced and promising results were reached on the third hole. This attracted the attention of mining giant Barrick Gold. In the fall of 1994, Bre-X had no proven reserves but made claims about having a potential 2 million ounces of gold. They agreed to let a Barrick team inspect the Busang property and discuss geological theories with Bre-X geologists. Word of Barrick's potential involvement caused the stock to jump to $1.50 a share. By September 20th, 1994, 31 holes had been drilled of which 22 hit "significant mineralization". Bre-X management estimated that there were 3-6 million ounces on the property. Later that year Bre-X and Bresea stock hit a record high of $2.85 and $1.40, respectively.

In February 1995, Bre-X made an announcement that the Central Zone may have one million ounces of gold reserves minable by open pit. On May 15th, 1995 the stock had closed at $4.05 following the results of the first three holes in the Southeast Zone which were promising, and by July 10, 1995 the stock hit a record high, closing at $8 a share. Bre-X stepped out in the Southeast Zone in an attempt to define the boundaries of the ore body by drilling holes far apart. The results were positive, and on August 18th Bre-X management estimated that they had up to 13 million ounces in Busang. The stock climbed as analysts hyped the stock and made buying recommendations, and at the year's end Bre-X closed at $53 and Bresea at $5.62. By January 15th, 1996 the stock jumped to $74 a share when Felderhof announced that drill results indicated that a

resource of 30 million ounces could be obtained. It was announced later that Bre-X stock was going to be split 10 to 1 to make it more affordable for smaller investments. The stock sky-rocketed to the equivalent of $167 after the split.

Bre-X hired Kilborn Engineering, a well-respected company, to perform metallurgical studies and to assist with the pre-feasibility study, likely with the hope that Kilborn's reputation would add credibility to the discovery. The results showed that a high recovery was possible as much of the gold was easily liberated. During April of 1996 the stock climbed from $148 to the equivalent of $200. Bre-X had made it big and on April 23, it was listed on the Toronto Stock Exchange and immediately the stock went even higher, reaching the equivalent of $261 per share pre-split.

With this great publicity came great obstacles. Information was leaked that Bre-X did not have adequate permits to do drilling on the property; they merely had the right to explore with man-power. Some believed that the permit issue was very serious and that it constituted a material fact which should have been disclosed to the public. Along with this, several high-ranking Indonesians wanted a piece of the action (Francis, 1997). These issues sparked the first real fears in Bre-X investors and stocks dipped for some time. In a positive note, on December 30th (1996) the *Northern Miner* named Felderhof and Walsh as "mining men of the year" for their role in the Busang discovery.

Bre-X was about to take a big hit which would challenge the integrity of its management and their promotion practices. The Indonesian government had intervened and forced Bre-X into a deal with mining giant Freeport-McMoRan Copper & Gold Inc. or

simply “Freeport”, the terms of which were ruthless. February 17, 1997 a deal was announced between Bre-X and Freeport; Bre-X would retain a mere 45%, Freeport would obtain 15% and would put up $1.6 billion for development, and the Indonesians would obtain 40%. Bre-X management tried to do damage control saying that they never expected to retain their 90% ownership of the deposit. However, this was considered by many to be an expropriation by the government and did not sit well with investors. Possibly in an effort to prevent losses, Felderhof made a statement that Busang could have as much as 200 million ounces. This claim was merely speculative and was not supported by material evidence. Some took offence to this claim, for shortly after Bre-X lost half its share of the deposit, it made speculations that its deposit was twice as big as previously thought.

Bre-X’s problems were far from over. On March 10th, Jim Moffet of Freeport received a phone call which would challenge not only the integrity of the management, but the integrity of the deposit itself. Freeport had begun its “due diligence” and was drilling its own holes to confirm Bre-X’s results. Moffet was told over the phone that no gold had been found in Freeport’s first 3 holes. Bre-X management was shocked and believed a mistake had been made. They agreed to send their chief geologist Michael de Guzman to clear up the inconsistency of assay results.

On March 19th de Guzman got in a chartered helicopter to take him from the town of Samarinda to Busang. En route to the site, the pilot noticed that the cabin had filled with rushing air. He looked back and De Guzman was gone. The Indonesian

authorities concluded that De Guzman had committed suicide by jumping out of the helicopter. The nature of De Guzman's death is highly debated and some skeptics believe he faked his own death or was murdered.

Bre-X hired Strathcona led by Graham Farquharson to conduct an independent investigation into the credibility of the work done by Bre-X and Freeport. Bre-X feared Freeport was trying to drive down the stock prices, making for a cheap takeover. Once the news became public that Bre-X might be a bust, Bre-X issued a halt on trading until they could clear up the matter. Walsh tried to prolong the halt as long as possible but barring any new information, trading reopened, and within the first 30 minutes of trading, the stock collapsed representing one of the largest losses by a single company in one day in all of history. The net worth of Bre-X shares went from $6 billion to $600 million. On March 29th, Strathcona began drilling as the world waited for word of their findings. The core was methodically logged and assayed in a manner which made tampering impossible. Strathcona prepared a thorough report and presented it to Bre-X management. It stated that "there is virtually no possibility of an economic gold deposit in the Southeast Zone I of the Busang property". It also recommended that an investigation into the cause of the fraud be launched. As a result of the investigation, the stock was delisted and on May 8th, 1997 Bre-X filed for bankruptcy (e.g. Goold & Willis, 1997).

1.3 Dr. G.C. Milligan's samples

There are 12 samples of drill core belonging to Dr. G.C. Milligan and seven thin sections. Each sample has a drill hole name beginning with BSSE (Busang Southeast) and

the drill hole number. The depth range from which the samples came was also indicated on the sample bag. Each sample has been given a simplified name as shown in Table 1.2-1.

Table 1.2-1: Bre-X sample names

Original Name	Simplified Name
BSSE-1: 192.50-193.50m	Bre-X1
BSSE-1: 309.50-310.50m	Bre-X2
BSSE-2: 42.00-43.00m	Bre-X3
BSSE-2: 301.00-302.00m	Bre-X4
BSSE-2: 329.00-330.00m	Bre-X5
BSSE-295: 235.75-235.85m	Bre-X6
BSSE-295: 368.00-369.00m	Bre-X7
BSSE-333: 154.00-155.00m	Bre-X8
BSSE-333: 272.00-273.00m	Bre-X9
BSSE-333: 286.00-287.00m	Bre-X10
BSSE-333: 308.00-309.00m	Bre-X11
BSSE-333: 396.00-397.00m	Bre-X12

1.4 Purpose and scope

The purpose of this thesis is to determine whether an unbiased study of the suite of samples belonging to Dr. G.C. Milligan could lead a geologist to suspect they come from an epithermal gold system or deposit. Here we are given a unique perspective into the Bre-X scandal as this particular set of samples has never been studied in this much detail.

The focus of this study is the samples themselves and not the politics or economics of Bre-X's mining scandal. Previous work during the investigation into the fraud was used for reference, however an effort was made to study these samples

without bias. The samples were studied to independently determine exactly what they are if they do not belong to an epithermal gold deposit. Tools employed by exploration geologists were used to determine the potential of these samples to belong to or be associated with an epithermal gold system. The samples are limited, making it difficult to extract meaningful quantitative results. However, with purposeful study and attention to detail, a large amount of data was collected from this small sample set which gives insight into the geological setting from which they came.

1.5 Methodology

For this study a suite of 12 core samples belonging to Dr. G.C. Milligan were available along with seven accompanying thin sections. From visual observations and analytical data the nature of these samples was determined. The samples were described in detail, photographed and slabbed for whole-rock geochemical analysis. Thin sections and polished thin sections were prepared and studied with reflected and transmitted light microscopy. Representative wall rocks and vein materials were sent for major and trace element analysis. Double-polished thin sections were also made for ore-fluid analysis and fluid inclusion microthermometry. A comparison was made with the genetic model for Pacific Rim epithermal deposits as described by experts in the field (e.g. Leach & Corbett, 1997).

The samples used in this study have historical significance; therefore precautions were taken to preserve them as much as possible. Before samples could be cut they were photographed for archival purposes. Thin sections were made or re-polished and scanned to assist in visual observations. Hand samples were described in detail to

preserve a record of their original condition. They were described in terms of the groundmass, phenocrysts, veins, and ore minerals. The morphology of the veins and sulfides was given special attention. Carbonates were tested for with dilute hydrochloric acid. Annotated photographs and sketches were used to assist in making observations.

Thin sections were cut at Dalhousie University for petrological, electron microprobe and fluid inclusion studies. Nine normal thin sections were cut from the samples. These thin sections were made to assist in refracted light microscopy which is difficult using polished thin sections alone; in most cases where a polished or double-polished thin section was made, a normal thin section was made to accompany it. Representative sections of the wall rocks were cut and made into thin sections for igneous petrological analysis. Three polished thin sections were made for reflected light ore microscopy and for electron microprobe analysis. The chemical zonations in feldspar phenocrsysts, variations in carbonates, and composition of sulfides were analyzed with these methods.

Selected samples were slabbed for whole-rock geochemical analysis. The cut surfaces were buffed to remove any surface contaminants. From the geochemical data the host rocks of the Busang Southeast Zone were classified and geochemical anomalies assessed, comparing mineralized and unmineralized samples. Comparisons were made between the most altered and least unaltered rocks to describe chemical alteration.

Five double-polished thin sections were cut from sections which likely contained fluid inclusions in the vein-hosted minerals (quartz). These were also used in reflected

light ore-microscopy. From these double-polished thin sections, fluid inclusion salinities and minimum temperatures and pressure of entrapment were determined. The fluid inclusions were combined with petrology to put the results into meaningful context.

Chapter 2: Regional Geology

The island of Borneo is situated in the Southwest Pacific Rim and hosts many precious metal occurrences due to its favorable geological setting. The basement of central and southern Borneo consists of Paleozoic, Mesozoic, and Paleogene sedimentary, metamorphic, granitic and volcanic rocks, but the pre-Cenozoic history of the island is not well known (Moss & Finch, 1997). This basement acted as a craton throughout the Mesozoic (Hamilton, 1979). The region from northern to central Borneo contains three distinct tectonic zones from northeast to southwest: the Miri, Sibu-Ranjang, and Kuching zones (Soeria-Atmadja et al., 1999). Central Kalimantan contains a NE-SW Tertiary magmatic belt which is related to two periods of subduction-induced magmatism with the younger superimposed upon the older; the first in the Eocene-Oligocene and the second in the Late Oligocence-Miocence (Neogene). Magmatism in the region was the result of subduction of oceanic lithosphere under the island of Borneo which slowed as the Luconia continental block collided and sutured with the craton-like Borneo. The first subduction occurred along the Lupar Line (Kalimantan Suture), and the second along the Palawan Trench (Soeria-Atmadja et al., 1999). Understanding the magmatism and regional structures in Borneo is important as they comprise the sources of metals, host rocks, and conduits which form mineral occurrences in the region.

2.1 Tectonic zones

As described by Soeria-Atmadja et al, (1990) the Miri Zone is part of the Luconia continental block and is bound to the northwest by the Palawan Trench which is the trace of the Miocence subduction. This zone consists of sedimentary rocks varying from stable-shelf limestones to fluvial and deltaic sediments. The Sibu-Rajang zone consists of highly folded and weakly metamorphosed sediments of the Rajang Group. These have been interpreted as turbidite deposits that have been compressed into an accretionary prism from Oligocence continental collision. The prism is overlain by less deformed sediments deposited in an outer-arc basin (Hamilton, 1979). The Lupar Line is a suture and forms the boundary between the Sibu-Rajang Zone and the Kuching Zone (Fig. 2.2-1). Here basement ophiolites of the Rajang Group are exposed representing the trace of the Late Cretaceous-Oligocene subduction. The Kuching Zone consists of Paleozoic crystalline schists overlain by carbonates and siliciclastic sediments of Paleogene and Mesozoic ages. Paleogene volcanics and Neogene intrusions are the igneous rocks in the region (Soeria-Atmadja et al., 1999).

2.2 Cenozoic tectonics and magmatism

The tectonic framework of Borneo is the result of NW-SE convergence in the Cenozoic. The rock chemistry and K-Ar ages of volcanic rocks suggest that magmatism was related to Oligocence-Early Miocence SE-dipping subduction of the oceanic lithosphere off the northern shore of Borneo (Soeria-Atmadja et al., 1999). Figures 2.2-3,4,5 illustrate the subduction geometry and magmatism produced by the NW-SE convergence during the Cenozoic. Table 2.2-1 summarizes magmatism in the region. The

earliest known subduction-related magmatism occurred in the Eocene to Early Oligocence with the emplacement of silica-rich calc-alkaline pyroclastics. This was followed by a period of continental collision and reduced magmatism. Subduction-related magmatism continued from the Late Oligocence to the Pleistocene at which time the magmas evolved from calc-alkaline to potassic-alkaline. Magmatism ended with basaltic flows in the Pliocence-Pleistocene (Soeria-Atmadja et al., 1999).

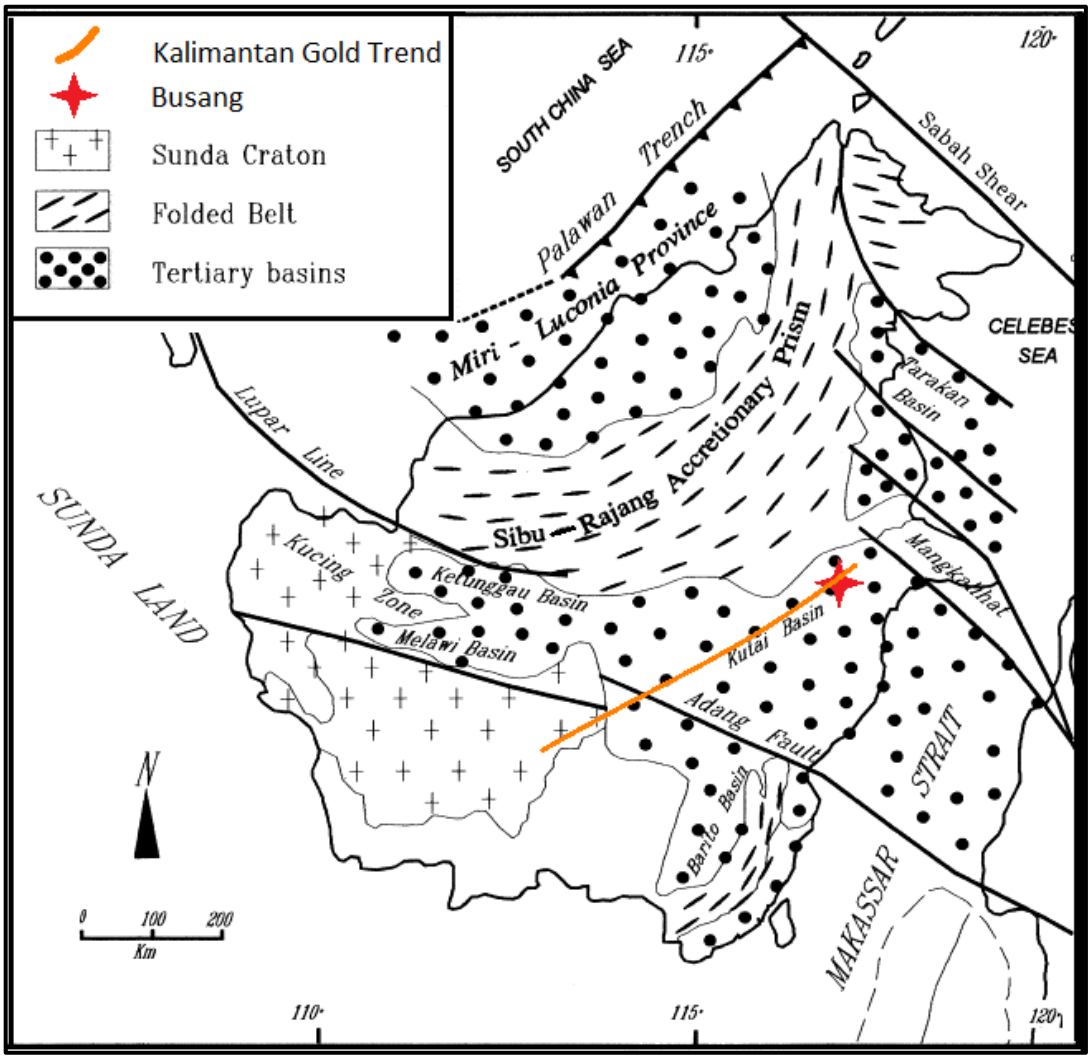

Figure 2.2-1: Tectonics of the island of Borneo. The Kalimantan Gold Trend is highlighted to show its tectonic setting (modified from Soeria-Atmadja et al., 1999)

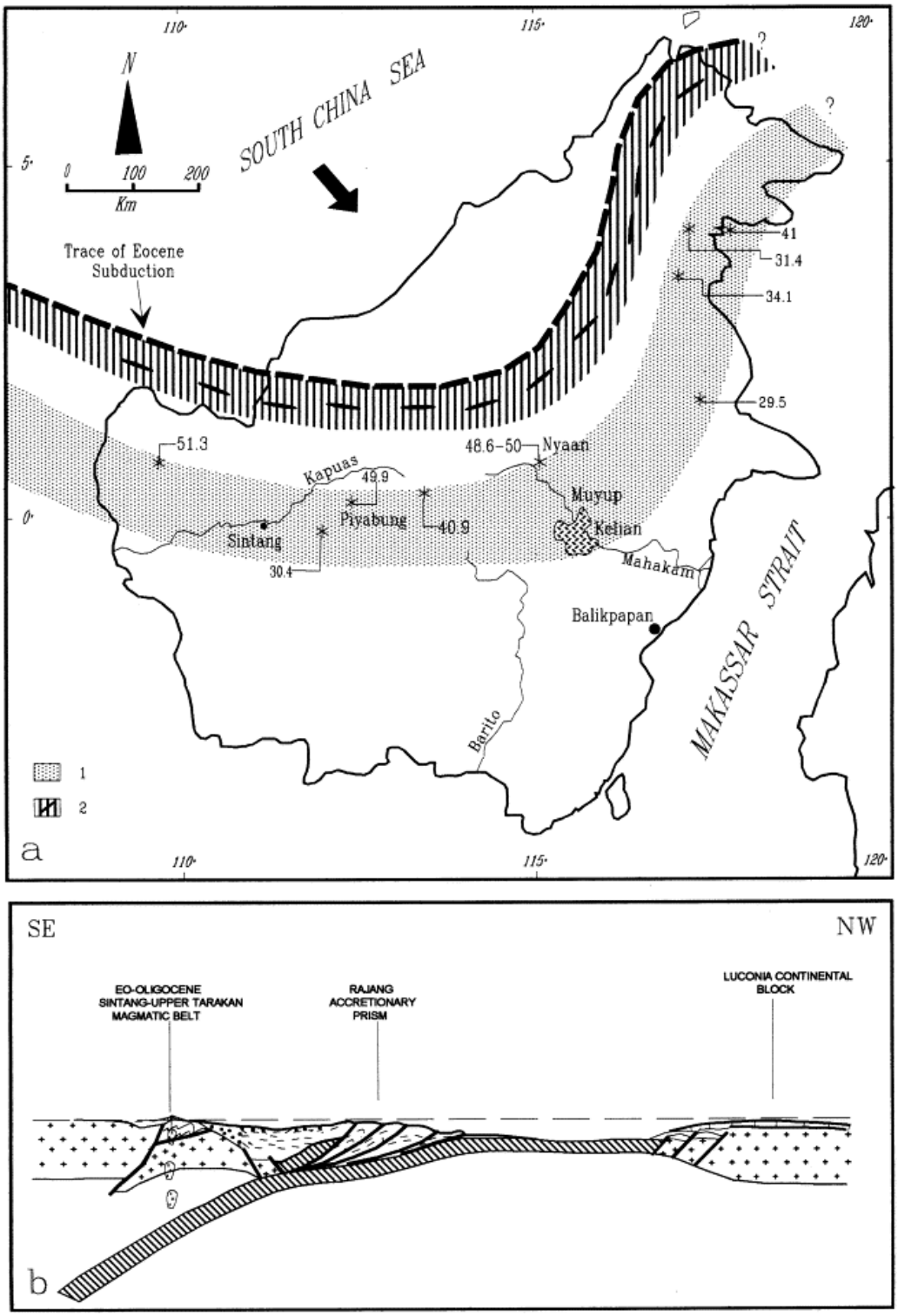

Figure 2.2-2: Tectonic geometry and magmatism during Eocene-Oligocene time. (a); Schematic map showing the trace of subduction (dashed line), the magmatic belt (1), and the Rajang accretionary prism (2). The K-Ar ages of volcanic rocks during this period are shown. (b); Schematic cross-section (from Soeria-Atmadja et al., 1999).

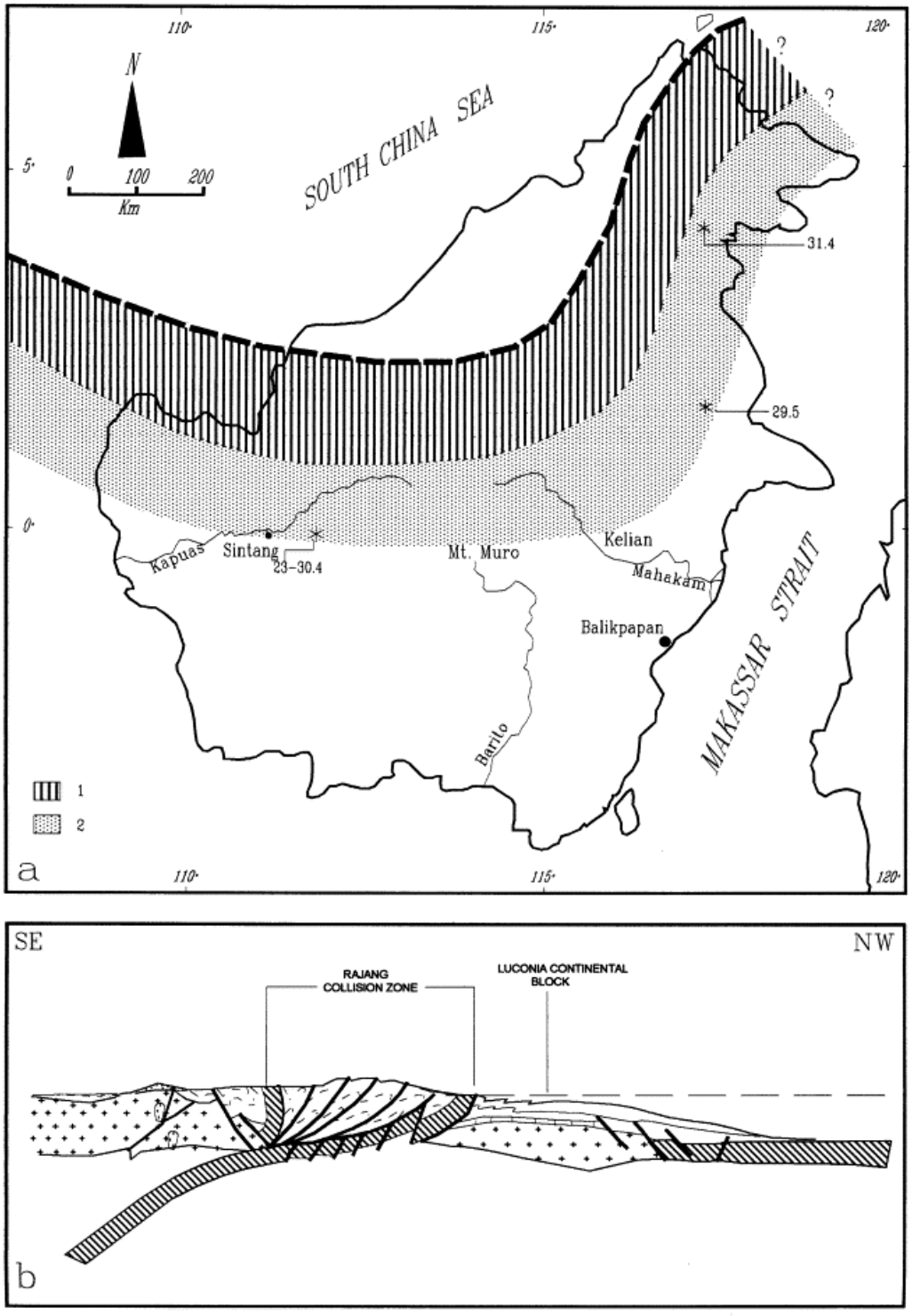

Figure 2.2-3: Tectonic geometry and magmatism during Middle Oligocene time. (a); Schematic map showing the trace of subduction (dashed line), deformation zone (1), and the magmatic belt (2). The K-Ar ages of volcanic rocks during this period are shown. (b); Schematic cross-section (From Soeria-Atmadja, et al., 1999).

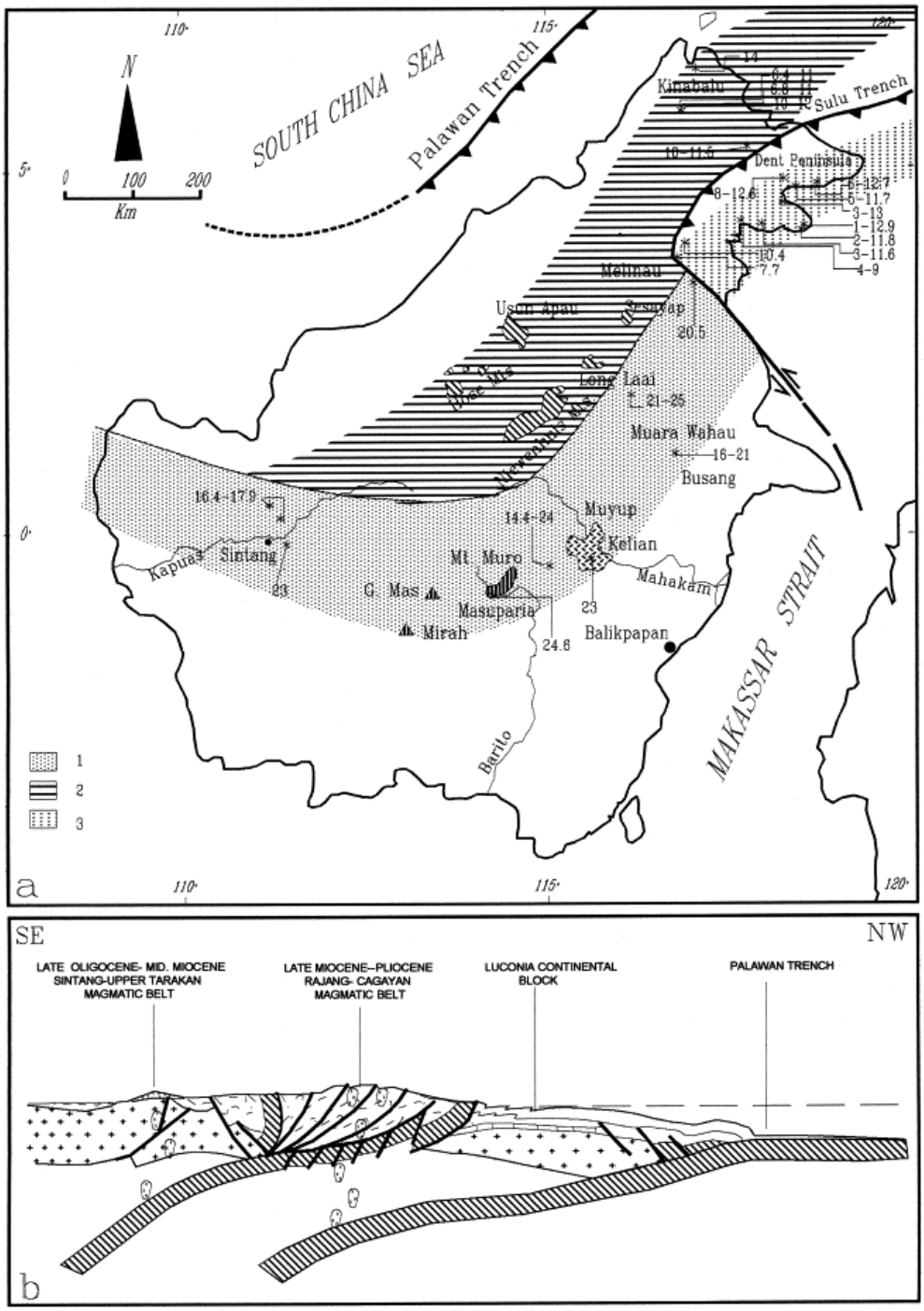

Figure 2.2-4: Tectonic geometry and magmatism during the Late Oligocene-Middle Miocene and Late Miocene-Pleistocene times. (a) Schematic map showing the trace of subduction (Palawan Trench), Late Oligocene-Middle Miocene magmatic belt related to Eocene subducted slab (1), Late Miocene-Pleistocene magmatic belt related to active subdction (2), and Late Miocene-Pleistocene magmatic belt related to subduction along the Sulu Trench (3). The K-Ar ages of volcanic rocks during this period are shown; (b) Schematic cross-section (from Soeria-Atmadja et al., 1999).

During the Eocene-Oligocene, oceanic lithosphere of the South China Sea was subducting under Borneo along the Lupar Line. This subduction produced the Rajang accretionary prism in the forearc, and a magmatic belt behind the subduction zone (Fig. 2.2-2). In the Middle Oligocene the Luconia continental block, a microcontinental fragment from Asia, collided with the overriding crust of Borneo, and the two crustal blocks were sutured together along the Lupar Line (Moss & Finch, 1997). This convergence without subduction resulted in the deformation and folding of the Sibu-Rajang accretionary prism and minor magmatism (Fig. 2.2-3). The oceanic crust to the northwest of the Luconia continental block began subducting under Luconia at the Palawan Trench. As convergence continued in the Late Oligocene-Middle Miocene, magmatism resumed which overprinted the earlier Eocene-Oligocene magmatic belt (Fig. 2.2-4). This was followed by Late Miocene-Pleistocene magmatism in the Sibu-Rajang folded accretionary prism. Plate convergence was also caused by subduction along the Sulu Trench in the northwest corner of Borneo producing the youngest volcanics in the region (Soeria-Atmadja et al., 1999).

Table 2.2-1: Summary of Cenozoic magmatism in Kalimantan

Period:	Plio-Pleistocene	Late Miocene-Pleistocene	Middle Miocene-Pliocene	Late Oligocene-Middle Miocene	Eocene-Early Oligocene
Magmatism and related tectonic environment	**Intra-plate magmatism (tholeiitic)**	**Subduction-related magmatism (calc-alkaline; some high in Mg)**	**Subduction-related magmatism (high K calc-alkaline)**	**Subduction-related magmatism (calc-alkaline)**	**Subduction-related magmatism (calc-alkaline)**
Murara Wahau				Andesite flows and pyroclastic tuffs (dacite), dacite dykes	
Busang	Basalt plugs and dykes			Acidic tuffs (andesites, dacites, rhyolites)	
Kelian	Plateau basalts			Andesite stocks, dykes	Silicic pyroclastics (rhyolite)
Muyup				Andesite stocks, dykes	
Mt. Muro	Plateau basalts			Andesite and basaltic andesite flows breccia and tuffs	
Sintang	Basalt flows			Basalts, andesites, dacites, rhyolites	
Usun Apau	Basalt flows		Dacite and ignimbrite tuffs		
Linau-Balui	Basalts		Dacites, andesites and basalts		
Dent and Sempora Peninsula		Flows, tuffs, and basalts			
Upper Tarakan basin		Andesites, basalts and tuffs			
Sulu Ridge		Sequence of andesites, basaltic flows and pyroclastics			
Nieuwenhuis Mt			Andesites and basalts		
Kinabalu			Granitoid intrusions		
Hose Mt.			Dacite tuffs and lavas		
Cagayan ridge			Basalts and porphyritic andesites		
Singkawang					Dacites
Mandai					Dacites
Piyabung					Pyroclastic tuffs and breccias
Nyaan					Agglomerates, ignimbrites and dacites

*Modified from Soeria-Atmadja et al., 1999

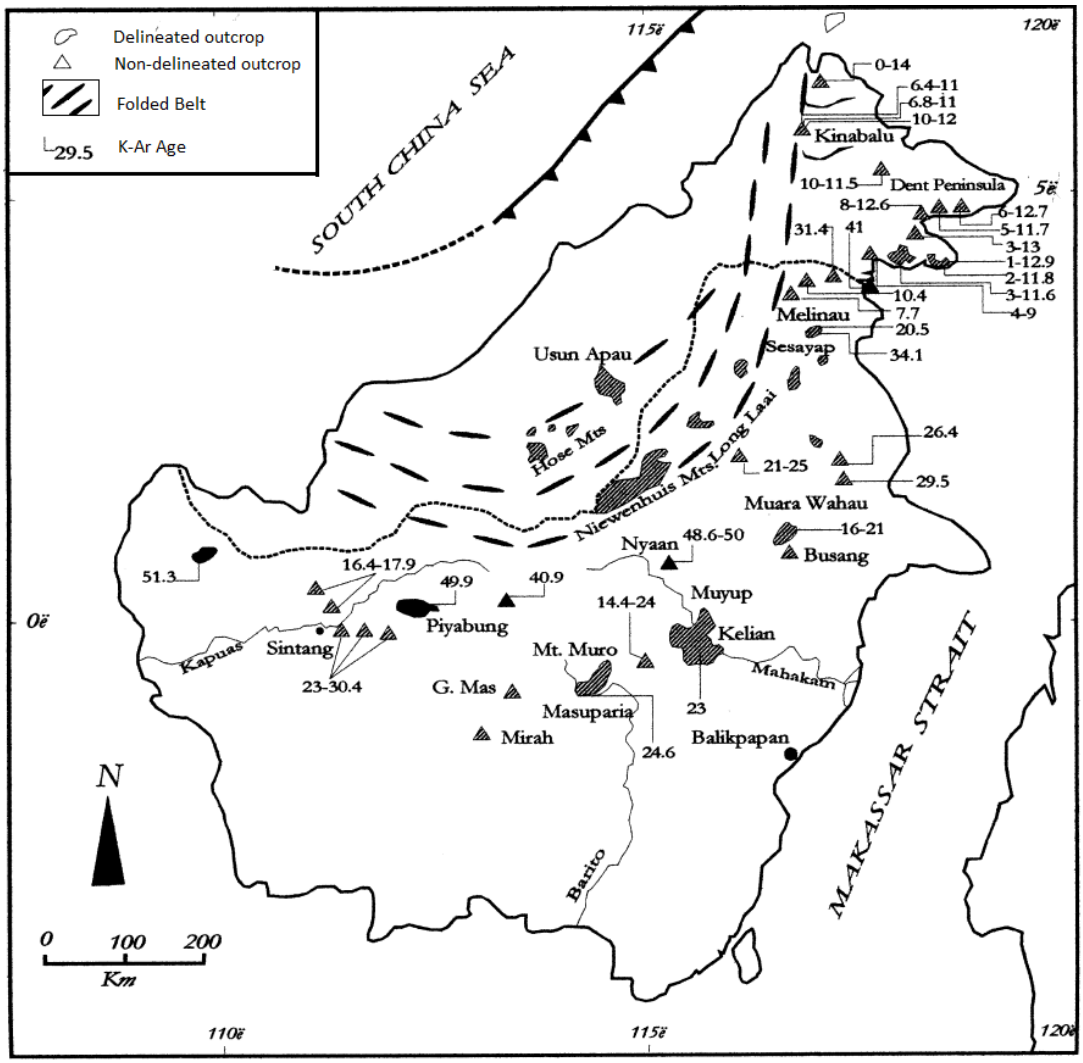

Figure 2.1-5: Distribution of volcanic outcrops and their K-Ar ages in Kalimantan (Modified from Soeria-Atmadja et al., 1999).

2.1.3 Kalimantan Gold Belt

Much of the geology of central Kalimantan is known from exploration for mineral deposits in the region. A trend of significant mineral occurrences, typically Au-rich LS epithermal deposits, occurs in central Kalimantan and is known as the Kalimantan Gold Belt (KGB) which includes Busang, Kelian, Muyup, Mt. Muro, Masuparia, Muara Wahau, and Sintang (Davies et al., 2008). The KGB follows this magmatic trend where Neogene

epithermal mineralization is found in central to proximal volcanic settings at shallow depths. The mineralization in this belt is hosted in Tertiary magmatic arcs, except for Kelian which is basement-hosted (Davie et al., 2008), which are effusive to pyroclastic rocks of intermediate calc-alkaline composition (Soeria-Atmadja et al., 1999).

Three magmatic episodes have been documented in the region. Eocene acidic volcanism followed by Late Oligocene-Miocene andesitic-rhyolitic volcanism; these are thought to have preceded epithermal mineralization. The latest volcanism took the form of Pliocene-Pleistocene basaltic volcanism producing basaltic flows and dykes. The magmatic belt forming the KGB is dominated by Late Oligocene-Miocene volcanics with limited exposure of the older Eocene-Oligocene volcanics (Soeria-Atmadja et al., 1999). Table 2.1-1 is a summary of the magmatism at various localities in Kalimantan and the volcanic rocks found there. The location and K-Ar ages of these rocks are shown in Figure 2.1-5.

Chapter 3: Gold deposits of Borneo: Epithermal gold

Epithermal gold deposits are a type of hydrothermal mineral deposit in which ore minerals, precious metals, and gangue minerals are deposited from hydrothermal fluids. They form in the "epizone" of the crust at shallow depths (<1 km) and low temperatures (<300^{o}) (Panteleyev, 1985). The formation of these hydrothermal deposits requires metal-bearing fluids to be focused with larger volumes of fluid flow and this must be accompanied by a mechanism to precipitate these metals. Hydrothermal fluids in these systems are principally waters, either magmatic, meteoric, or a mixture of both. They form in settings of plate convergence where subducting oceanic lithosphere produces magmas and volcanism. Young, thick volcanic terrains are ideal for hosting these deposits, including the Tertiary magmatic belts in Kalimantan. Permeability is enhanced by regional structures to allow for the widespread migration of hydrothermal fluids associated with alteration (e.g. Leach & Corbett, 1997). Epithermal systems are currently active today in the form of hot-springs, fumaroles, and geysers in proximity to active volcanic environments. Intrusions into the volcanic arcs are thought to provide the heat which drives the convection of these hydrothermal fluids (Leach & Corbett, 1997). Examples of comprehensive reviews on epithermal deposits are Simmons et al. (2005), and Hedenquist (2000).

Epithermal deposits are divided into two distinct end members: high-sulfidation (HS) epithermal deposits, and low-sulfidation (LS) epithermal deposits. HS epithermal deposits are formed proximal to intrusions and are dominated by magmatic fluids that are hot, acidic, and saline. LS epithermal deposits are typically formed distal to volcanic

centers and are dominated by meteoric waters that are relatively cool, near-neutral pH, and dilute. The two types of epithermal deposit are shown in Figure 3.1-1. The Busang "deposit" was referred to as a LS epithermal deposit, specifically a carbonate-base metal epithermal gold deposit (Leach & Corbett, 1997). It is important for the purposes of this thesis to independently classify the Busang hydrothermal system as being HS or LS.

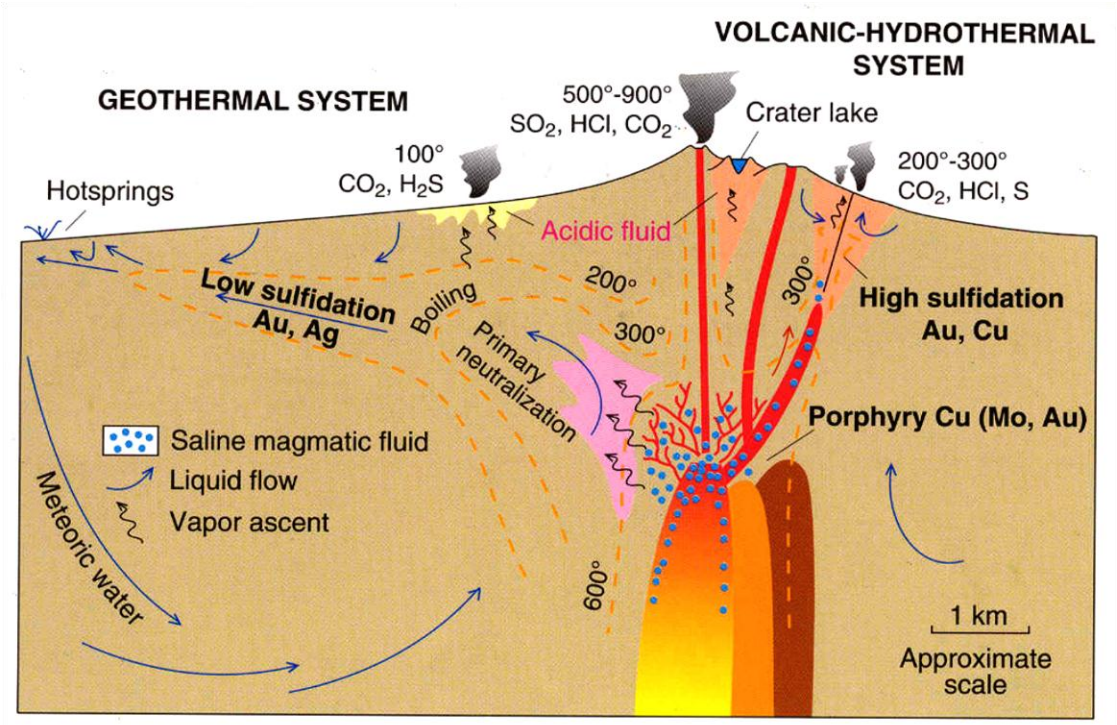

Figure 3.1-1: Schematic cross-section of the formation of epithermal mineral deposits and their association with intrusions (from Hedenquist et al., 1996).

3.1 Geological setting

The most common environment in which epithermal gold deposits are formed is in convergent-plate settings where subducting oceanic lithosphere produces magmas and volcanic arcs (Hedenquist & Lowenstern, 1994). The subduction of oceanic lithosphere introduces and concentrates metals and volatiles in the metasomatized lithospheric mantle wedge (Hedenquist & Lowenstern, 1994). Partial melting of the

lithospheric mantle wedge produces magmas which rise through the crust and are emplaced in volcanic arcs (Fig. 3.1-2).

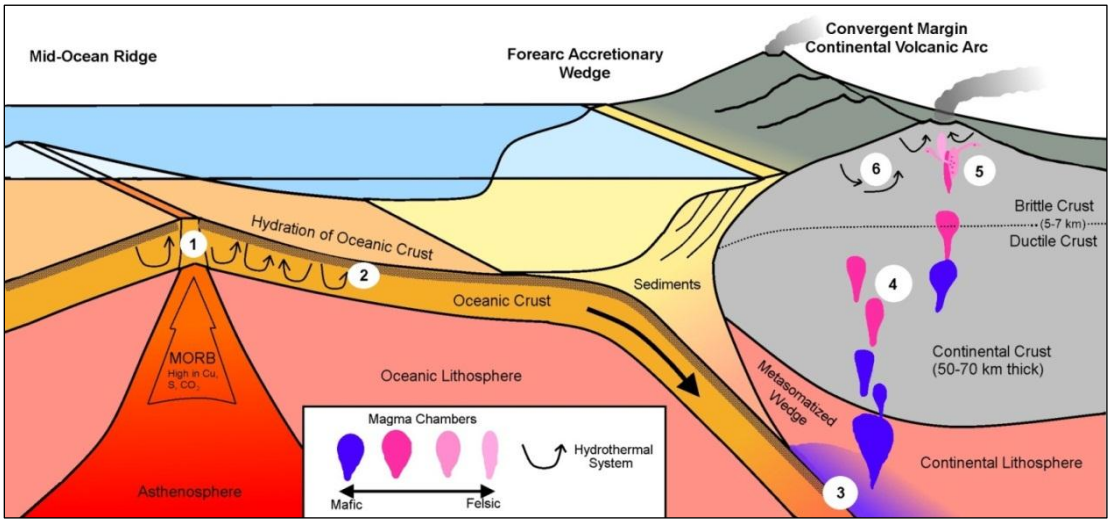

Figure 3.1-2: Schematic cross-section of the ideal setting for epithermal gold deposits. The figure suggests a mechanism by which magmatic intrusions acquire their metals and volatiles; (1) MORB, high in base metals and CO_2 forms oceanic crust; (2) oceanic crust becomes hydrated; (3) introduction of volatiles in the subcontinental lithosphere induces partial melting and the formation of magmas; (4) magmas rise through the ductile crust where they change compositions either by fractionation or by consuming continental crust; (5) multiple intrusions are emplaced into volcanic arcs which exsolve magmatic fluids; (6) heat from the intrusions drives the convection of meteoric waters (inspired by Hedenquist & Lowenstern, 1994).

The close geological association between intrusions and hydrothermal mineral deposits is well documented (Hedenquist & Lowenstern, 1994). Studies also note that there is a link between the composition of intrusions and the metals found in their associated hydrothermal deposits. Many hydrothermal systems derive their thermal energy from magmas in which multiple intrusive events can sustain a hydrothermal system for hundreds of thousands of years (Hedenquist & Lowenstern, 1994). However, there is debate as to what extent these magmas contribute water, metals, and ligands responsible for the solubility and transportation of precious metals. Although the magma-derived fluids are often subordinate, the episodic release of these fluids

containing dissolved gases and metals plays an important role in the formation of these deposits (Hedenquist & Lowenstern, 1994). The study of active epithermal systems suggests that the ore-forming fluids may only be active in relatively short pulses (White, 2011).

Magmas can obtain their metals from mantle melting and mass transfer from subducting oceanic lithosphere. The subduction of oceanic crust recycles metals and concentrates them beneath volcanic arcs. It is postulated that siderophile elements such as gold become entrained in basaltic magmas from the partial melting of the subcontinental lithospheric mantle (Hedenquist & Lowenstern, 1994). These magmas ascend into the crust along subduction zones and mid-ocean ridges. Isotopic evidence suggests that there may be a large amount of crustal assimilation into the rising magmas; this is a source for metals in some cases (Hedenquist & Lowenstern, 1994). Along with assimilation, crystal fractionation is one of the main controls on the concentration of ore components in magmas. Elements which have a high relative compatibility in magma will become trapped in mineral phases and therefore depleted in any fluids exsolved from the residual melt. An example of this process is the typically weak copper mineralization associated with felsic granitic intrusions; pyrrhotite is an early-formed mineral in these magmas and traps much of the copper and possibly gold before fluids can be exsolved. The residual melt is consequently depleted in these elements and so are exsolved fluids. Crystal fractionation alone cannot account for the concentration of metals to that of ore grades; other processes, such has hydrothermal deposition, must be involved (Hedenquist & Lowenstern, 1994).

3.2 Transport and deposition of gold

The principal economic commodity in epithermal deposits is gold. The solubility of gold in hydrothermal fluids is a function of several factors including pH, REDOX state, temperature, pressure, and salinity (Hedenquist & White, 1995). These factors can be affected by some combination of boiling, fluid mixing, reactions with host rocks, and changes in magmatic fluid input. The fluids forming LS epithermal deposits are typically low in salinity and are reduced. Here gold is typically transported in solution as a bisulfide complex (Hedenquist & White, 1995). The boiling of fluid releases H_2S into a vapour phase, reducing the solubility of gold in the liquid causing it to precipitate as shown in Equation 3.2-1 below.

Equation 3.2-1: $Au(HS)_2^- + 2H^+ + e^- \rightarrow Au^o + 2H_2S$ (White, 2011)

The fluids which form HS are oxidised, acidic, and saline. In this case gold is likely transported in the fluid as a chloride complex which has different controls on solubility than the former bisulfide complex (Hedenquist & White, 1995). The mechanisms which cause the precipitation of gold are very complex and variable from system to system.

3.3 Distinguishing features of HS and LS epithermal deposits

Although low- and high-sulfidation deposits have overlapping characteristics, they have unique and diagnostic features. To efficiently assess the mineralization potential of an epithermal gold deposit, one must determine which type of deposit is present (Hedenquist, 2000). Here, the features of these two types of epithermal deposits are compared in terms of geochemical signatures, ore and gangue mineralogy, texture, and alteration.

Both types are structurally controlled where fluid preferentially migrates though conduits depositing ore and gangue minerals. However, the effect of structures on the distribution of ore is more notable in LS than in HS deposits. Low-sulfidation epithermal deposits are dominated by open-space-filling veins. The pressure gradients in these systems are likely too low to deeply penetrate permeable rock. High-sulfidation epithermal deposits are dominated by disseminated ores with vein-type ores locally dominant but overall subordinate. The host rocks are leached and therefore often permeable. This allows the ore fluid to penetrate the host rocks and to deposit ore minerals, commonly through replacement of minerals with a basic affinity such as calcite (Hedenquist & White, 1995).

	Low-Sulfidation	High Sulfidation
Anomalously High	Au, Ag, As, Sb, Hg, **Zn**, Pb, **Se**, K, **Ag/Au**	Au, Ag, As, **Cu**, Sb, **Bi**, Hg, Te, Sn, Pb, **Mo**, Te/Se
Anomalously Low	Cu, Te/Se	K, Zn, Ag/Au

Table 3.3-1: Elements which are indicative of epithermal gold deposits. Those which are good discriminants between LS and HS systems are in bolded text (from Hedenquist & White, 1995).

3.3.1 Ore and Gangue Mineralogy

Mineral data compiled from many epithermal deposits shows a clear distinction between the two end-member types. The differences are mainly in the mineralogy of the sulfides which likely reflects the differences in the REDOX state of the ore fluids. Sphalerite and arsenopyrite are two such examples. Sphalerite is common in both types, but is much more abundant in the low-sulfidation type. Arsenopyrite is very rare in HS

	Low-Sulfidation	High Sulfidation
Pyrite	ubiquitous (a)	ubiquitous (a)
Sphalerite	common (V)	common (vm)
Galena	common (V)	common (m)
Chalcopyrite	common (V)	common (m)
Enargite -Luzonite	rare (vm)	ubiquitous (V)
Tennantite-Tetrahedrite	common (vm)	common (V)
Covellite	uncommon (vm)	common (m)
Stibnite	uncommon (vm)	rare (vm)
Orpiment	rare (vm)	rare (vm)
Realgar	rare (vm)	rare (vm)
Arsenopyrite	common (m)	rare (vm)
Cinnabar	uncommon (m)	rare (vm)
Electrum	uncommon (V)	common (m)
Native Gold	common (vm)	common (m)
Tellurides-Selenides	common (vm)	uncommon (V)

Table 3.3-2: Ore minerals in epithermal gold deposits; frequency of occurrence and abundance (a-abundant, V-variable, m-minor, vm-very minor). Minerals shaded dark grey are good discriminants between HS and LS environments (modified from White, 2011).

	Low-Sulfidation	High Sulfidation
Quartz	ubiquitous (a)	ubiquitous (a)
Chalcedony	common (V)	uncommon (m)
Calcite	common (V)	absent (except overprint)
Adularia	common (V)	absent
Illite	common (V)	uncommon (m)
Kaolinite	rare (except overprint)	common (m)
Pyrophyllite-Diaspore	absent (except overprint)	common (m)
Alunite	absent (except overprint)	common (m)
Barite	common (vm)	common (m)

Table 3.3-3: Gangue minerals in epithermal gold deposits; frequency of occurrence and abundance (a-abundant, V-variable, m-minor, vm- very minor). Minerals shaded dark grey are good discriminants between HS and LS environments; alunite is sometimes misleading if overprinting is present (modified from White, 2011).

deposits but common in LS deposits in small quantities. Sulfides with HS states such as tennantite-tetrahedrite can only exist in the more acidic system. HS deposits often contain copper minerals which are absent in LS deposits; the copper-bearing sulfosalts

enargite-luzonite are ubiquitous in the HS deposits. Abundance of sulfides is variable in both types of deposits and is not a good discriminant (Hedenquist & White, 1995).

Minerals preferentially form within certain pH ranges and within certain temperature and pressure ranges (Fig. 3.3-1). Quartz is ubiquitous in both types of epithermal deposits, being stable over a large pH range. Adularia (low-temperature polymorph of K-feldspar) and calcite are two hydrothermal minerals that are only stable in basic or near-neutral conditions, making them good indicators of LS deposits. Minerals that are stable in relatively acidic conditions will form in high-sulfidation environments. Here alunite, kaolinite, and minor phosphate-sulfate minerals are common. An acidic gangue can only be present in LS environments as the result of later overprinting of subsequent acidic assemblages (Hedenquist & White, 1995). Waning of the hydrothermal system or an increase in the flux of volatiles from the late stage cooling of magma may be responsible for this overprinting (Corbett & Leach 1997).

3.3.2 Textures

Texture is probably the best discriminant between these two types of epithermal deposit. LS deposits have spectacular textures which are much more diverse than those in HS deposits.

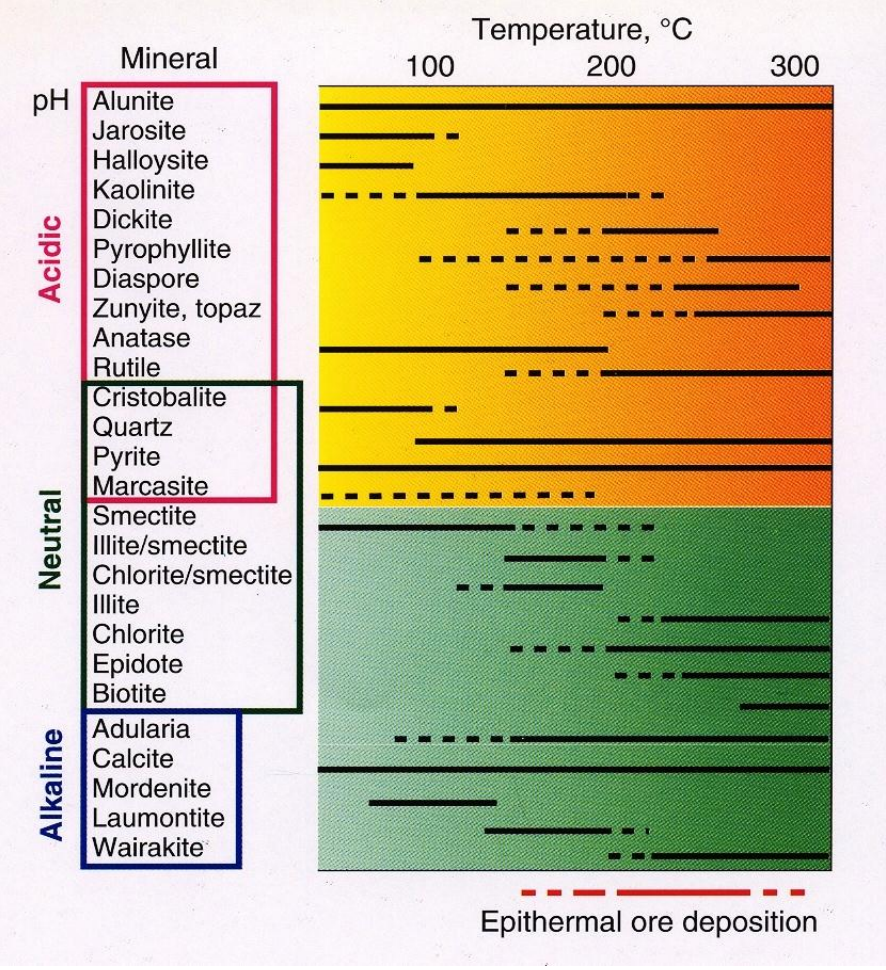

Figure 3.3-1: Mineral stability across pH and temperature ranges (from Hedenquist, Izawa, Arribas, & White, 1996).

Low-Sulfidation	High Sulfidation
Banded veins	Vuggy quartz
Crustified quartz veins	Massive quartz
Drusy cavities	Massive sulfide veins
Crustification	Crudely banded veins
Breccia veins	
Lattice texture	

Table 3.3-4: Characteristic textures of hydrothermal mineralization. Note that LS systems have more varied textures (from White, 2011).

In LS deposits the variable textures include banded and crustified quartz veins, drusy cavities, and multiple-episode breccias with crustification of clasts forming a cockade texture (White, 2011). The diverse textures are thought to be a reflection of a dynamic and ever-changing system where multiple stages of fluid flux, boiling, and hydraulic fracturing take place (Hedenquist & White, 1995). Often diatremes and hydrothermal eruptions at surface occur in these environments. Lattice-textured calcite is often deposited rapidly during the boiling process and may be replaced by quartz (White, 2011). Hot springs at surface may deposit silica-rich sinters. If the paleosurface has experienced little erosion, these sinters can be useful exploration targets (Hedenquist & White, 1995).

In HS deposits there is little variation in texture. Massive vuggy quartz is common, resulting from leaching of feldspars and carbonates by acidic magmatic hydrothermal fluids (pH <2). Fluids penetrate into the rock and deposit ore minerals and associated gangue, mainly quartz and pyrite, in a predominantly disseminated texture. Often the original quartz is dissolved and re-precipitated as massive quartz. The mineral deposition often occurs as a replacement of minerals such as calcite in the host rocks. Vein-type ore may be locally predominant over disseminated ore where structures are present, but disseminated ore is most abundant overall. The formation of sinters in this style of deposit is inhibited by the inability to precipitate quartz from acidic solutions (Hedenquist & White, 1995).

3.3.3 Alteration zones

Spatial zonation of hydrothermal alteration is another good discriminant between the two types of epithermal deposit. In LS epithermal deposits the alteration assemblages are associated with near-neutral pH hydrothermal fluid where the ore is deposited in the zone with the least acidic-alteration. HS epithermal deposits are associated with more acidic fluids and the ore is deposited in the zone with the most acidic alteration, although alteration can be misleading. Erosion and changes in environment can result in telescoping and overprinting of alteration assemblages. Therefore, the predominant alteration style may not be the alteration associated with the ore deposition. Also the outward extent of alteration is much larger than the actual ore zone, thus the presence of promising alteration zones does not mean one is near the most mineralized zone (Hedenquist, 2000).

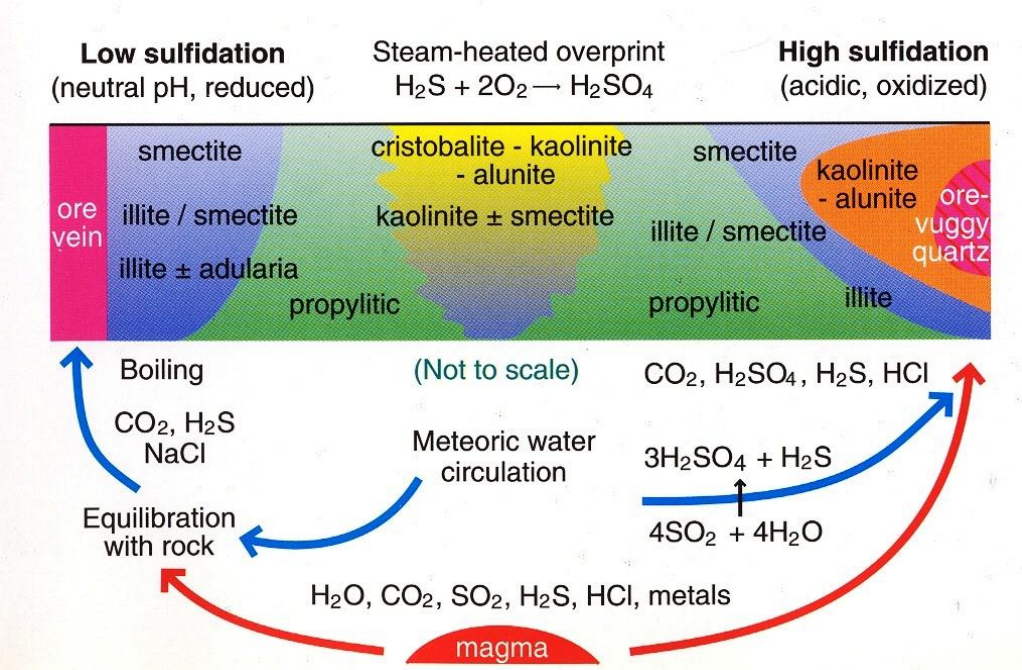

Figure 3.3-2: Distribution of hydrothermal alterations associated with HS and LS epithermal systems (from Hedenquist et al., 1996).

The distribution of hydrothermal alteration varies vertically and laterally in both types of hydrothermal system (Fig. 3.3-2). Quartz is stable and present in all zones of alteration. Propylitic alteration occurs where the water-to-rock ratio is low and therefore the width of the propylitic alteration halo decreases laterally with depth. The common minerals in this alteration assemblage are albite, calcite, epidote, chlorite, and pyrite. Steam-heated overprinting from hypogene fluids can occur in both types of epithermal deposit (Hedenquist & White, 1995). This alteration is most obvious in LS systems where the overprinting assemblage is very different from the alteration associated with the deposition of ore. The overprinting alteration also varies vertically in both types. At greatest depth the assemblage consists of illite, smectite, and pyrite. This grades upwards into kaolinite and smectite to near-surface kaolinite and alunite (Hedenquist & White, 1995).

LS epithermal deposits have alterations that are the result of near-neutral pH waters having decreasing temperature with decreasing depth and distance from the heat-source. The stability of alteration minerals is commonly directly temperature dependent. In LS epithermal deposits the majority of the ore minerals are deposited between 100 and 280^{o}C. If the alteration minerals suggest temperatures consistently higher than 280^{o}, it is likely that the best mineral potential sits above this zone. Clay minerals are the predominant alteration minerals and the best indicators of temperature. Smectite represents the lowest temperature alteration mineral. As temperature increases illite becomes the dominant alteration mineral (Hedenquist & White, 1995).

Minerals that are stable in acidic conditions form the alteration assemblage of HS epithermal deposits. These include kaolinite, dickite, pyrophyllite, diaspore, and alunite, many of which are temperature sensitive. Zunyite, topaz, and andalusite also indicate acidic conditions with temperatures over 260^{o}C. These form the advanced argillic alteration assemblage, a key indicator of HS systems. Advanced argillic alteration gives way to argillic alteration outwards from the fluid source. The fluids are neutralized as they permeate and react with host rocks allowing illite and smectite to become stable (Hedenquist & white, 1995).

3.3.4 Carbonate-base metal epithermal gold deposits

The LS epithermal gold deposits in Kalimantan are often described as carbonate-base metal epithermal gold deposits (Leach & Corbett, 1997). Corbett and Leach (1997) described a four-stage model for the formation of these deposits as set out below. The hydrothermal mineralization at Busang was noted as being similar to this model by Leach after the exposure of Bre-X's fraud (Leach T. M., 2001). The samples used in this study were compared to this four-stage model. Gold deposition usually occurs during Stage 3.

Stage 1: The initial emplacement of magmas at depth is concurrent with localized propylitic alteration. The intrusions produce diatremes and may finger outwards to form intrusive dyke-like bodies. This stage prepared the host rocks for the later migration of ore-fluid.

Stage 2: Early quartz is deposited from relatively hot (250-350^{o}C) but dilute (2-4 wt% NaCl) fluids. The alteration is predominantly quartz but may contain adularia or sericite/illite. The quartz takes the form of stockwork veins at depth and cockscomb to crustified banded quartz-adularia veins near the surface.

Stage 3: Carbonate-base metal sulfide veins often overgrow and crosscut earlier quartz veins. The base metal sulfides typically predate the carbonates. These begin with pyrite which is followed by sphalerite then galena. Copper minerals may over grow these minerals later. Minor base metal sulfides may continue to form into the beginning of the carbonate deposition. This stage is likely the result of an increase in the input of magmatic fluids.

Stage 4: Carbonates form as crustified banded veins with alternating bands of quartz and carbonate. This stage is likely indicative of fluid mixing producing low temperature dilute fluids.

Chapter 4: Sample descriptions

Bre-X samples were observed in hand-specimen and in thin section to characterize the lithologies, alteration, and mineralization. Normal thin sections were made for refracted light microscopy and polished thin sections were made for reflected light ore-microscopy. Observations are made on macroscopic and microscopic scales with the aid of annotated photographs and sketches. Refracted and reflected light microscopy are separated in this chapter. A summary of observations is in the section 4.3, Table 4.3-1.

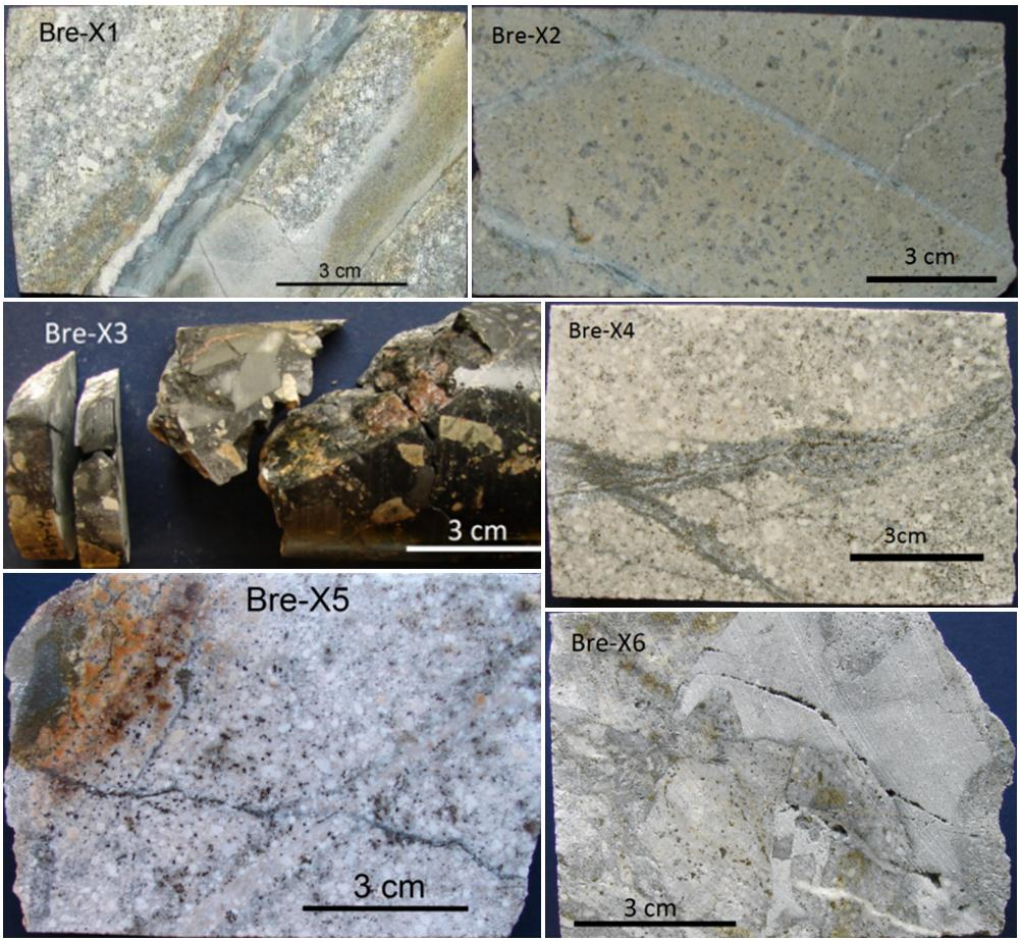

Figure 4-1: Photographs of samples Bre-X1-6.

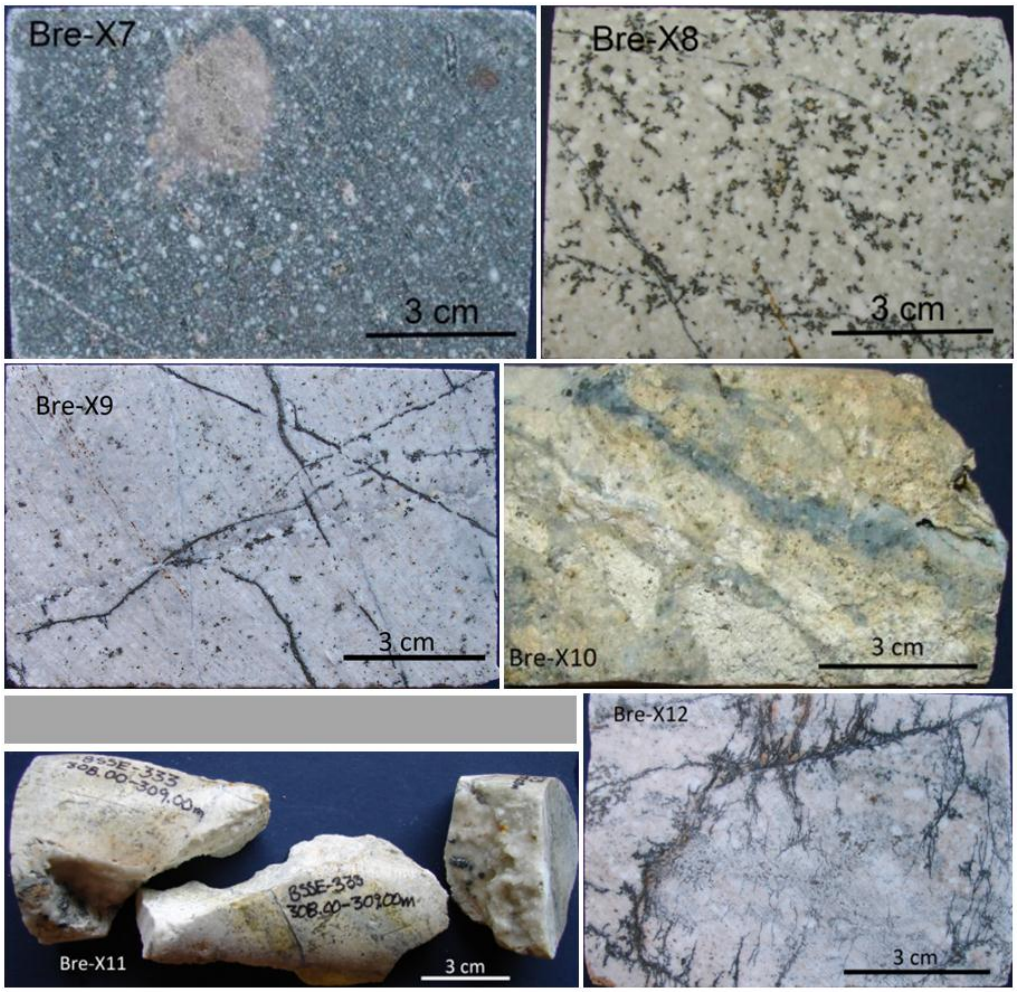

Figure 4-2: Photographs of samples Bre-X7-12.

From these observations the geochemical, and fluid inclusion data are put into context. This serves as the most detailed descriptive record of these samples to date and thus this thesis has an emphasis on observations. Samples were originally studied by A.K. Chaterjee in 1997 and his unpublished observations were used as a starting point for this thesis.

4.1 Refracted light microscopy

The samples were studied using refracted light microscopy to classify the rocks, and to look for features which might be associated with a hydrothermal style of

mineralization. The rocks were described in terms of protoliths, alteration, structures, and vein(let)s. For most samples normal thin section were made, however some samples had to be studied from polished/double-polished thin sections making optical identification of minerals difficult.

From visual inspection, the rocks include porphyritcic and non-porphyritic rhyodacites-andesites with varying degrees of alteration, veining, and mineralization. Sample Bre-X3 is particularity anomalous as it is a polymictic breccia with both sedimentary and igneous clasts. The samples with the most alteration and silicification tend to not have relict phenocrysts. It is possible that the alteration has obliterated the phenocrysts and mobilized their constituent elements or they may have been equigranular to begin with. Alteration and mineralization appears to vary in the samples; it is focused in vein(let)s and alteration halos or conversely it is widespread and ubiquitous throughout the sample.

4.1.1 Bre-X1: Porphyritic dacite

Relict plagioclase phenocrysts set in a groundmass of predominantly quartz, and lesser sericite and sulfides. Phenocrysts are strongly altered to sericite, lesser quartz, and rarely calcite or epidote. A vein cuts the sample which when viewed in thin section appears to consist of several parallel veinlets of quartz, calcite, sulfides, and minor gypsum/anhydrite (it is crudely banded). A homogenous domain of fine-grained quartz runs parallel to the vein except where it contacts the vein.

Mineral	Abundance	Predominant Size Range
Phenocrysts	**40**	**0.2-1.5 mm**
Sericite	20%	
Quartz	10%	
Sulfides	5%	<0.5 mm
Calcite	5%	
Epidote	3%	
Megacrysts	**5**	**0.5-1 mm**
Quartz	5%	
Groundmass	**45**	**<50 µm**
Quartz	35%	
Sericite	5%	
Sulfides	5%	<0.5 mm
Veinlets	**10**	
Quartz	7%	0.1-1 mm
Calcite	2%	0.1-0.5 mm
Sulfides	1	0.2-0.5 mm
Gypsum	<1%	0.1-0.5 mm

Phenocrysts are subhedral to euhedral and have the morphology of plagioclase. They are highly altered to bladed sericite and irregular quartz, sometimes resulting in fuzzy boundaries between phenocrysts and the matrix. Sulfides are frequently included in the phenocrysts but may extend past phenocryst-grain boundaries. A very fine-grained high-relief mineral, likely epidote, is rarely present in altered phenocrysts as a minor constituent.

The groundmass consists of equigranular quartz with irregular-fuzzy grain boundaries and lesser sericite. Sericite typically occurs interstitial to quartz in the matrix. Sulfides in the sample are typically subhedral isolated grains disseminated throughout.

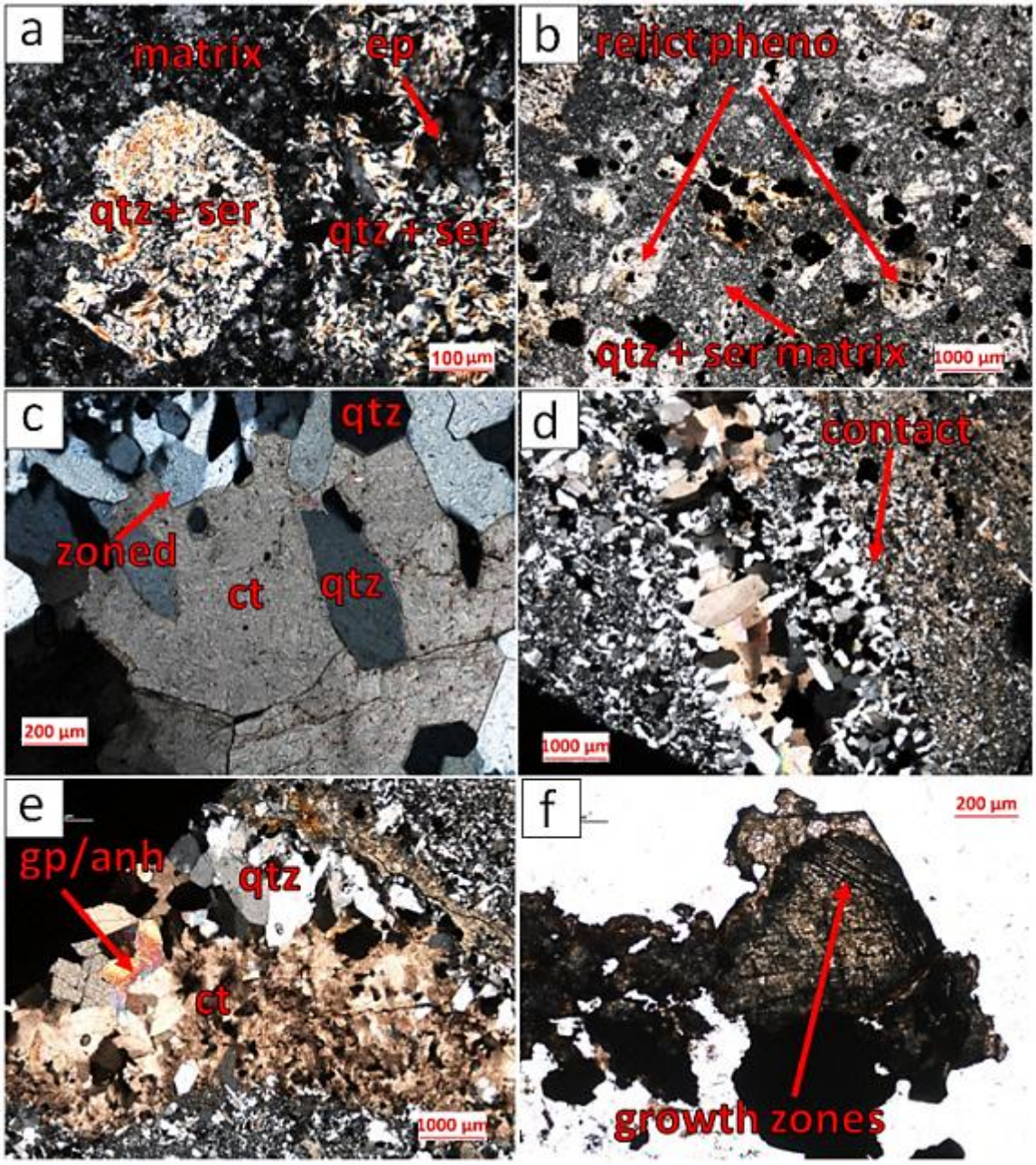

Figure 4.1-1: Bre-X1: (a) Close up view of relict phenocrysts highly altered to quartz, sericite, and locally epidote in cross-polarized light (XPL); (b) Relict phenocrysts in a fine grained matrix in XPL; (c) Close up of veinlet wall. Calcite and sulfides form interstitial to euhedral zone quartz in XPL; (d) Contact between vein (left) and host rock (right). Photograph shows a veinlet within the larger vein. The veinlet is bound on each side by coarse-grained euhedral quartz with a center of interstitial calcite and minor gypsum. XPL; (e) Veinlet within the vein containing quartz, irregular to euhedral calcite, and minor gypsum/anhydrite; (f) Translucent mineral determined to be sphalerite by ore-microscopy. Triangular zones interpreted to be growth zones are visible here in plane polarized light (PPL).

The sample is cut by a quartz-carbonate-sulfide vein which appears to consist of several parallel veinlets when viewed in thin section. The vein contains minor sulfides seams, and gypsum/anhydrite locally. The veinlet walls are typically crustified, that is stratified from the walls to the center in the following sequence: (1) irregular fine-grained quartz; (2) euhedral coarse-grained zoned quartz; (3) interstitial coarse- to fine-grained calcite and subhedral to irregular granular sulfides.

4.1.2 Bre-X2: Calcite-altered porphyritic dacite

Rare, highly altered plagioclase phenocrysts are set in a matrix dominated by quartz, and lesser sericite, calcite, and minor sulfides. Two planar veinlets cut the sample subparallel to each other. These veinlets contain quartz, carbonate, at least two sulfides, and minor sericite. The sequence of hydrothermal mineralization can be inferred from the stratigraphy and textural relationships in the veinlets. The sample has ubiquitous moderate calcite alteration.

Relict phenocrysts in the sample are rare. Those present are subhedral to euhedral and were likely originally plagioclase based on their morphology. They are highly altered to bladed sericite, patches of calcite, and irregular quartz, sometimes resulting in fuzzy boundaries between phenocrysts and the matrix. Sulfides are frequently included in the phenocrysts but may extend past phenocryst-grain boundaries.

Mineral	Abundance	Predominant Size Range
Phenocrysts	**20**	**0.2-1.5 mm**
Sericite	10%	<0.5 mm
Calcite	5%	
Sulfides	3%	
Quartz	2%	
Groundmass	**75**	**<50 µm**
Quartz	20%	
Sericite	20%	
Calcite	20%	
Sulfides	5%	<0.5 mm
Veinlets	**5**	
Calcite	3%	0.5-2 mm
Quartz	1%	0.1-.3 mm
Sulfides	1%	0.1-0.5 mm
Gypsum	<1%	<1 mm

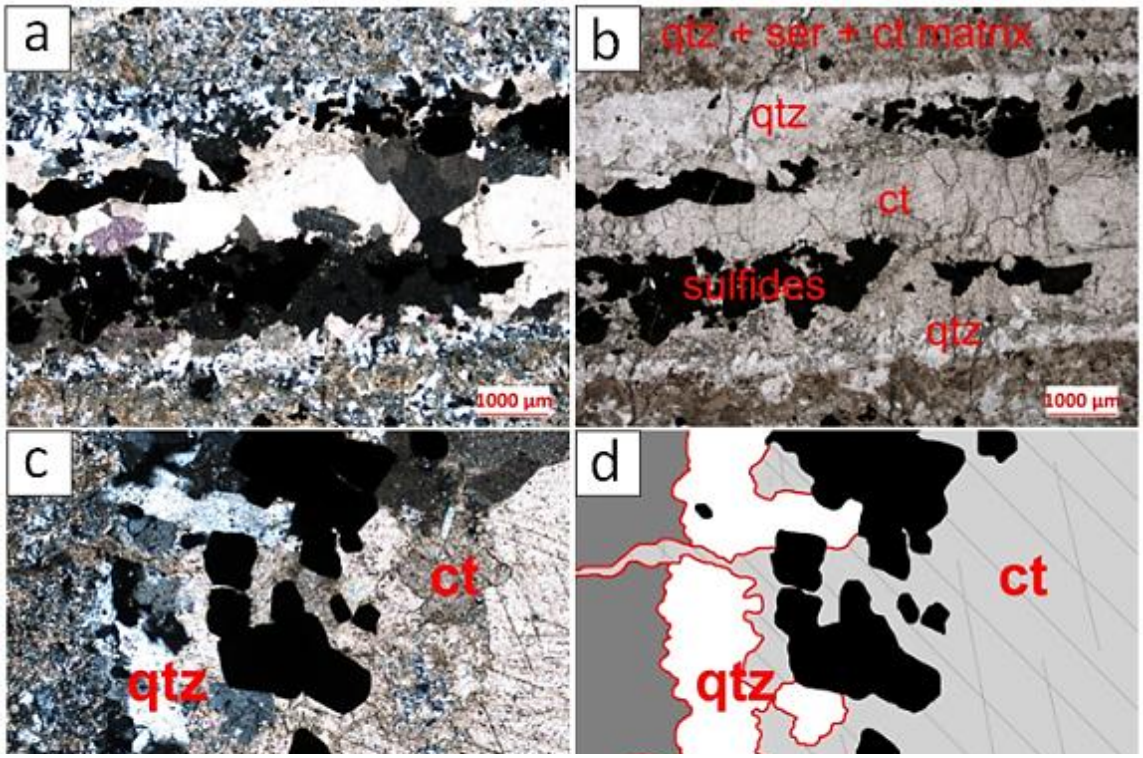

Figure 4.1-2: Bre-X2 (a) Quartz-carbonate-sulfide veinlet in XPL; (b) Quartz-carbonate-sulfide veinlet in PPL; (c) Close up view of the contact between quartz-carbonate-sulfide veinlet and the matrix in XPL. Stratification of hydrothermal minerals is shown from left (edge) to right (center) of the veinlet; matrix, quartz, calcite and sulfides, to calcite; (d) Schematic trace highlighting the features in "c".

Groundmass consists of equigranular quartz with irregular-fuzzy grain boundaries, sericite, and lesser calcite. Sericite typically occurs interstitial to quartz in the matrix and in patches; these patches may define the locations of obliterated phenocrysts. Sulfides in the matrix are typically irregular clots and interstitial to other alteration minerals.

4.1.3 Bre-X3: Polymictic breccia

This sample is a clast-supported breccia composed of both sedimentary and igneous clasts. From visual inspection, five types of clast are identified and described below. Rare fine calcite-quartz veinlets cut the sample. Sulfides are minor and evenly disseminated throughout.

At least five different types of clast can be seen in thin section. They are as follows: (1) a porphyritic felsic volcanic rock altered to clays and carbonate locally. The relict phenocrysts are elongated and up to 1 mm in length. A greenish-yellow mineral, possibly chlorite is present locally; (2) a clast composed of angular quartz (<200 μm) with a brown earthy matrix; (3) a rounded clast of felsic rock with a spherulitic texture, possibly a devitrified volcanic; (4) a clast of probable igneous origin. It contains an earthy matrix with light areas which may be quartz-rich clasts. The clast has been altered to clays, calcite, and a greenish-yellow mineral; and (5) dark-brown sedimentary rock which sometimes has colour banding inferred to be bedding (S_0).

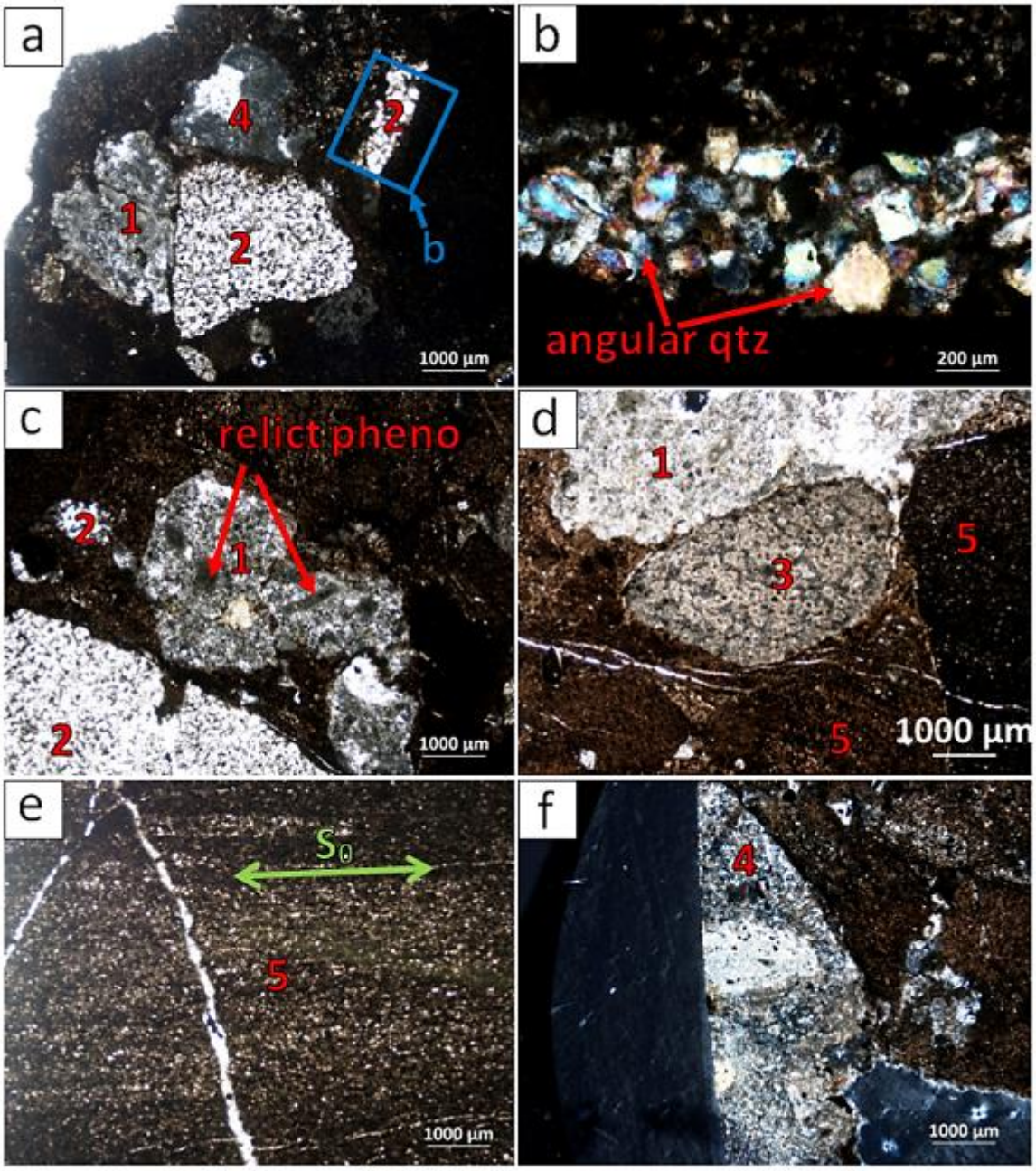

Figure 4.1-3: Bre-X3: Refracted-light photographs of polished thin section of Bre-X3. Different types of clasts are indicated by numbers 1-5 based on visual inspection as described in text above; (a) At least two types of clasts of probable igneous origin in a dark brown matrix viewed in PPL; (b) Close up view of clast from photograph a viewed in XPL. The bright-coloured angular crystals are inferred to be quartz; (c) Clast of an originally porphyritic volcanic rock viewed in PPL. The clast contains minor carbonate; (d) Rounded igneous clasts along with larger dark brown sedimentary clasts in minor dark brown matrix viewed in PPL. Here the rock is clast-supported with only a minor matrix component. The clast in the center of the slide appears to have a spherulitic texture and may be a devitrified volcanic rock; (e) Clast of dark brown sediment with bedding (S_0) shown in green; (f) Clast of volcanic rock with minor calcite.

Sulfides are minor in the sample and disseminated throughout. They occur as elongate fine blebs in the bedded sedimentary clasts and as isolated grains in the volcanic clasts. Rare calcite veinlets cut the sample and host minor sulfides.

4.1.4 Bre-X4: Porphyritic dacite

Altered plagioclase phenocrysts are present in a fine-grained matrix of quartz, sericite, calcite and sulfides. The sample is cut by fine veinlets of calcite, sulfides, and quartz. The veinlets are surrounded by a zone of strong alteration which extends about 0.5 cm outwards. Sulfides in the sample are concentrated in the alteration zone and veinlets, but isolated grains are also disseminated throughout.

Mineral	Abundance	Predominant Size Range
Phenocrysts	**30**	**0.2-1.5 mm**
Sericite	15%	
Plagioclase	5%	
Calcite	5%	
Sulfides	5%	
Groundmass	**69**	**<50 µm**
Quartz	40%	
Sericite	20%	
Sulfides	5%	<100 µm
Veinlets	**1**	
Calcite	0.4%	100-500 µm
Quartz	0.1%	0.1-.3 mm
Sulfides	0.5%	0.1-0.5 mm

Euhedral plagioclase phenocrysts are abundant in this sample and vary from weakly- to highly-altered. The alteration-pattern in the phenocrysts suggests that they were compositionally zoned. Frequently the outer rims of the phenocrysts are unaltered

plagioclase. Some growth zones within phenocrysts are highly altered while others are not. In the alteration zone surrounding the veinlets the phenocrysts have been completely altered and no plagioclase remains. Rare quartz megacrysts are present and are rounded.

The matrix is fine grained and consists of quartz, sericite and minor calcite. Here quartz often contains very fine-grained inclusions of a high-relief mineral, possibly apatite or tourmaline. Isolated grains of sulfide are disseminated throughout the matrix.

Fine carbonate-sulfide-quartz veinlets cut the sample. The veinlets are stratified from the walls to the center. Minor quartz lines the veinlet walls, then calcite, and then sulfides in the center. Quartz and calcite in the veinlets often share undulose extinction. Also, quartz in the veinlets commonly has inclusions of calcite. This relationship between quartz and calcite in the veinlets indicates that replacement has occurred between them.

The veinlets are surrounded by an alteration zone which extends outwards about 0.5 cm. Here the alteration of the host rocks is very strong. The matrix grain size is larger suggesting recrystallization (silicification). The phenocrysts in the alteration zone are completely altered to sericite. Extinction in the sericite locally shows a banding pattern which reflects relict zones in the original plagioclase. The abundance of sulfides is higher in the alteration zone. Sulfides are frequently included in the relict phenocrysts.

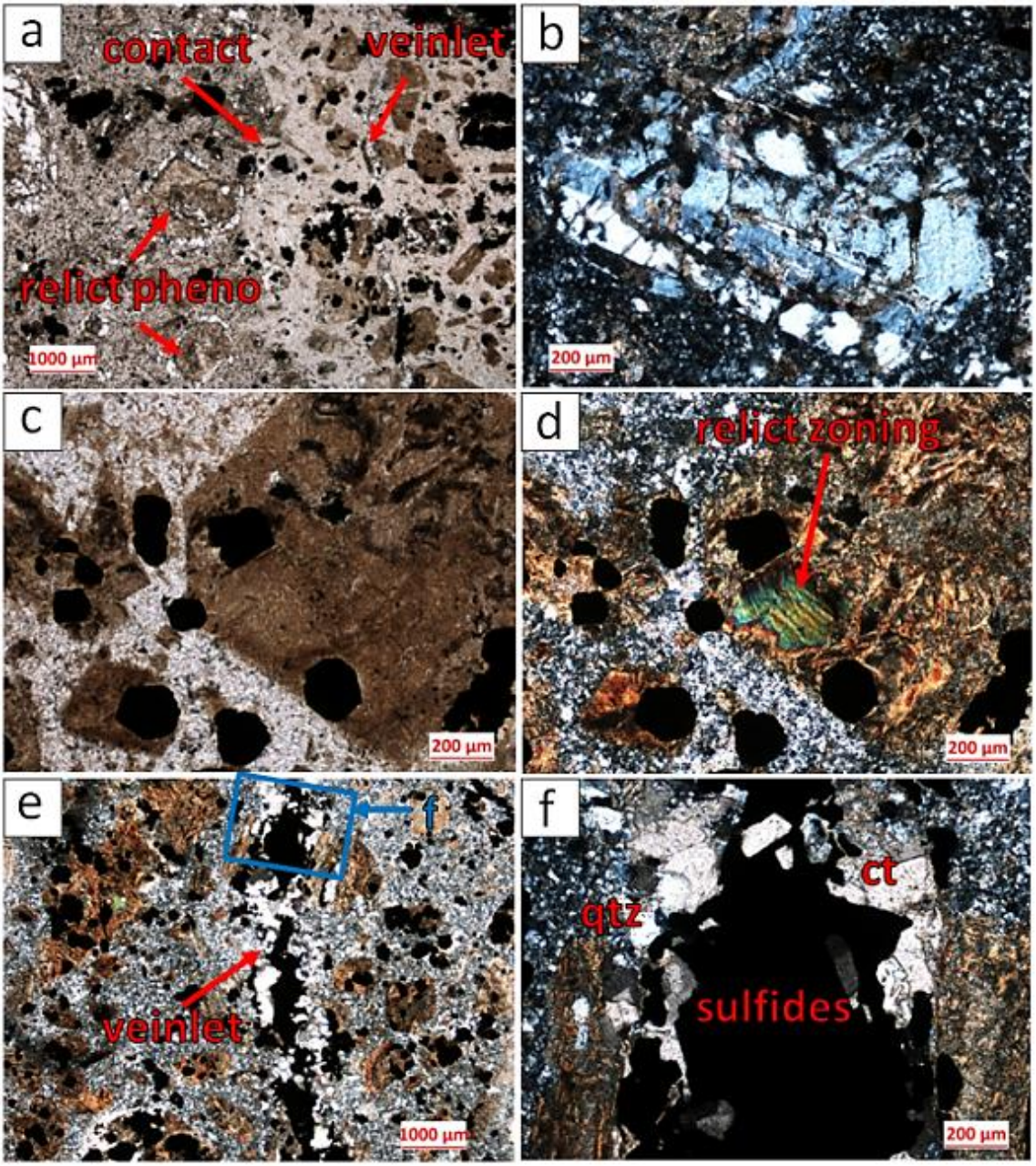

Figure 4.1-4: Bre-X4: (a) Representative section in PPL. The photograph shows the contact between the highly altered zone and the weakly altered wall rock. The weakly altered rock (left in photo) has a finer-grained matrix. The highly altered zone (right in photo) has more abundant sulfides and a coarser matrix; (b) Relatively unaltered plagioclase phenocryst in the weakly altered wall rock viewed in XPL. There is a highly altered zone in the middle of the grain. Alteration is also present in cracks and fractures; (c) Highly altered phenocryst in the alteration zone viewed in PPL. Photograph shows the euhedral habit and distinct grain boundaries of the relict phenocrysts; (d) Highly altered phenocryst in the alteration zone viewed in XPL. The extinction pattern in sericite may be a result of original compositional zoning; (e) Carbonate-sulfide-quartz veinlet viewed in XPL. The blue rectangle outlines the edges of photograph f; (f) Carbonate-sulfide-quartz veinlet viewed in XPL. The veinlet cross-cuts a relict phenocryst. The sulfides and calcite appear to be co-genetic or the sulfides formed after calcite.

4.1.5 Bre-X5: Porphyritic dacite

Hydrothermally altered porphyritic dacite with strongly to moderately altered relict phenocrysts. Fine irregular veinlets of calcite and lesser quartz cut the sample. Sulfides are isolated grains disseminated throughout the sample and present in some veinlets.

Mineral	Abundance	Predominant Size Range
Phenocrysts	**30**	**1-0.25 mm, and 0.01 mm**
Sericite	27%	
Calcite	5%	
Sulfides	2%	
Groundmass	**69**	**<50 µm**
Quartz	55%	
Sericite	10%	
Sulfides	4%	<100 µm
Veinlets	**1**	
Calcite	0.8%	0.2-0.3 mm
Quartz	0.15%	<0.1 mm
Sulfides	0.5%	

Phenocrysts in the sample appear to have a bimodal size-distribution (double porphyritic). They likely were originally plagioclase and are strongly to moderately altered to sericite and calcite. Near veinlets the phenocrysts are stained brown and have rare banding locally. Larger phenocrysts appear to be prismatic and zoned. Smaller phenocrysts are usually elongated laths.

The matrix is fine-grained equigranular quartz with minor sericite. Minor isolated sulfide grains are disseminated throughout. Fine calcite-quartz veinlets cut the sample. Here the calcite is irregular and separated by quartz. Some calcite veinlets have abundant sulfides.

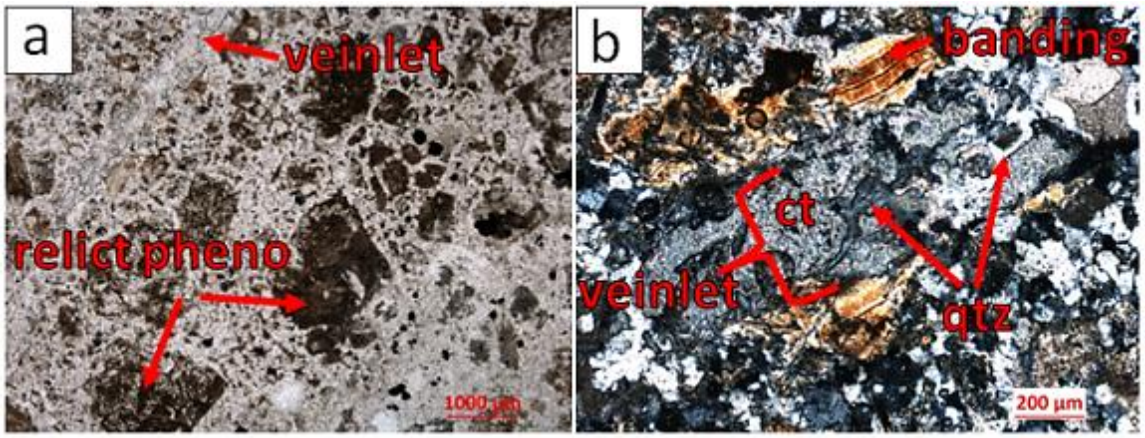

Figure 4.1-5: Bre-X5: (a) Representative section viewed in PPL. Relict highly altered phenocrysts of variable size in a fine grained siliceous matrix. A carbonate-quartz veinlet cuts the sample; (b) Carbonate-quartz veinlet viewed in XPL. The carbonate is irregular and separated by quartz. Where transected by the veinlet, the relict phenocryst shows local banding parallel to the veinlet.

4.1.6 Bre-X6: Altered porphyritic dacite, volcaniclastics, and homogenous silica

This sample comprises at least three rock types, two of which were recognized in thin section. The textural relationship between theses rock types is complex. It is interpreted to be a strongly altered dacite (1), which has been fractured and spaces filled by a fine grained volcanic (2). A third rock type which was not seen in thin section appears to be homogenous and siliceous (3). Vuggy calcite veinlets are locally abundant in the sample and cross-cut all rock types.

Mineral	Abundance	Predominant Size Range
Rock Type 1		
Phenocrysts	**50**	**1.5-0.2 mm**
Sericite	35%	
Quartz	12%	
Sulfides	3%	
Groundmass	**50**	**<50 µm**
Quartz	30%	
Sericite	15%	
Sulfides	5%	<200 µm
Rock Type 2		
Megacrysts/Clasts	**10**	**<200 µm**
Quartz	8%	
Calcite	2%	
Groundmass	**90**	**<50 µm**
Glass	88%	
Sulfides	2%	<100 µm

Rock-type 1 is a fine grained (sub)volcanic rock with angular fragments of quartz, patches of calcite, and rounded aggregates of fine-grained quartz set in a matrix of dark glass. The rounded aggregates are commonly elongated or tear-drop-shaped. Here sulfides are rare and occur as disseminated isolated grains.

Rock type 2 is a strongly altered porphyritic dacite, typical of the rocks in the suite. The relict phenocrysts have been completely altered to clays and lesser quartz. They are often elongate with indistinct grain boundaries. Here sulfides are more abundant and occur as coarser disseminated isolated grains.

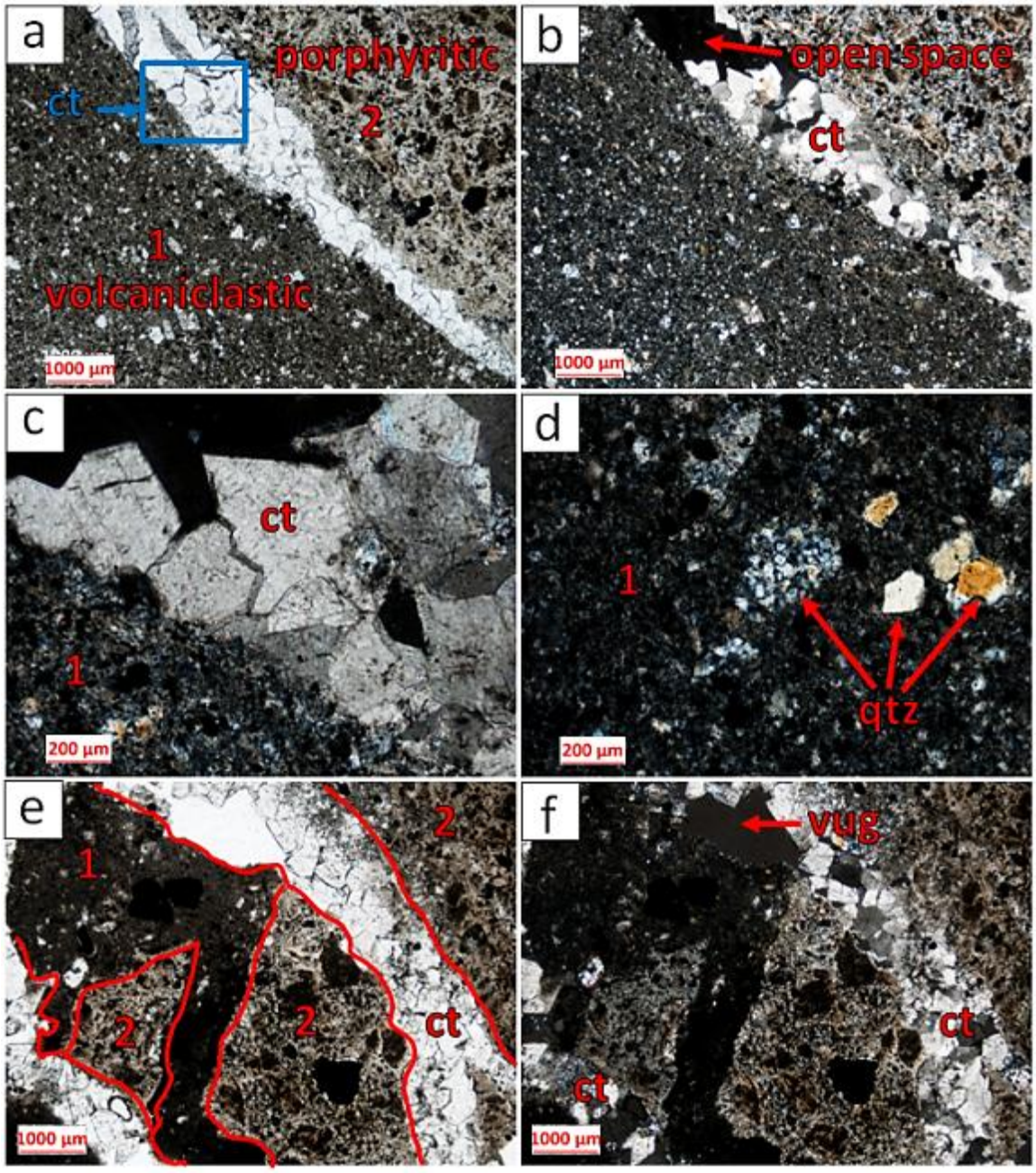

Figure 4.1-6: Bre-X6: Photographs of polished thin section Bre-X3. Two distinct rock types are observed and described above. (a) Calcite veinlet with vugs separating rock-types 1 and 2 viewed in PPL; (b) Same as "a" viewed in XPL; (c) Close up view of calcite from photographs "a,b". Here calcite is euhedral and has grown outwards into the open space; (d) Close up view of rock-type 1 viewed in XPL. Angular quartz fragments and rounded aggregates of fine-grained quartz are megacrysts and clasts in the rock; (e) Complex relationship between domains of the two rock- types viewed in PPL. Boundaries are traced in red. Two vuggy calcite veins cut both rock-types. Here rock-type 1 appears to have filled in spaces between clasts of type 2; (f) Same as "e" viewed in XPL.

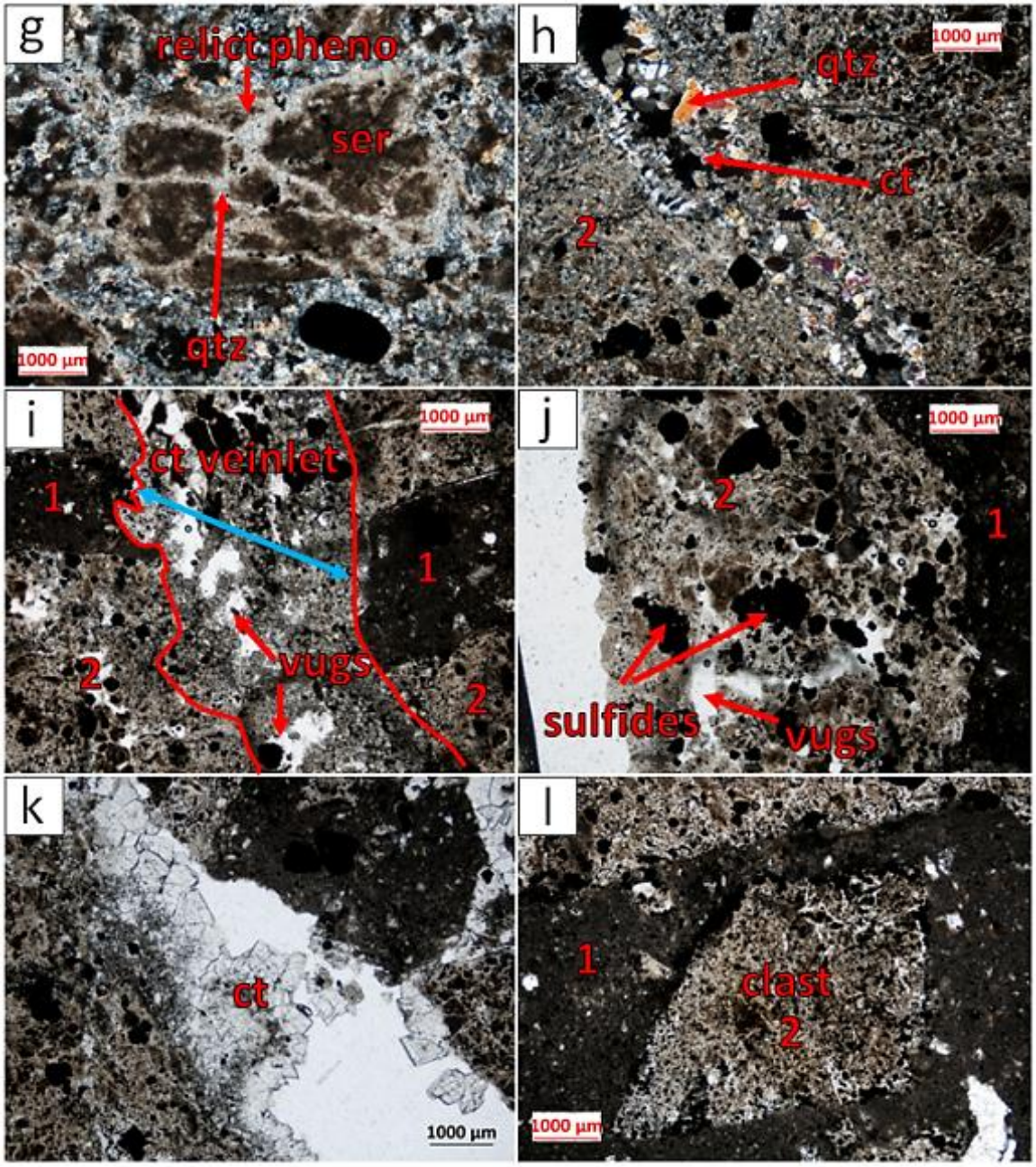

Figure 4.1-7: Bre-X6: Photographs of polished thin section Bre-X3. Two distinct rock types were observed and described above. (g) Relict phenocryst in rock type 2 which has been altered mostly to clays and lesser quartz viewed in XPL. Quartz-rich veinlets are marbled throughout the phenocryst; (h) Vuggy quartz-calcite veinlet in rock type 2 viewed in XPL. Quartz is subhedral and has grown from the veinlet walls. More fine-grained anhedral calcite has partially filled the open space after quartz; (i) Vuggy calcite veinlet appears to have cut and displaced a domain of rock type 1 viewed is PPL. Inferred displacement of the domain is indicated by a blue arrow; (j) Vuggy sulfide-rich domain of rock type 2 viewed in PPL; (k) Vuggy veinlet with euhedral calcite rhombs viewed in PPL; (k) apparent clast of rock type 2 surrounded by rock type 1 viewed in PPL.

Abundant vuggy calcite veinlets cut all three rock types. These typically contain euhedral rhombs of calcite and open spaces. Some veinlets are anomalous and contain subhedral quartz along the edges and anhedral finer-grained calcite in the middle.

It is interpreted that rock-type 2 was the original host rock. It was then fractured and in-filled by rock type 1. Rock-type 3 likely came after the first two; there may have been large open spaces which were silicified by hydrothermal fluids. Calcite veinlets cut all rock types and some minor component of strike-slip displacement has taken place along them.

4.1.7 Bre-X 7: Chloritized porphyritic andesite

Chloritized porphyritic andesite contains phenocrysts of plagioclase and strongly chloritized megacrysts which may be relict horblende or pyroxenes. These are set in a fine-grained matrix of quartz, chlorite, and plagioclase. The sample has local calcite alteration which appears to be spatially associated with sulfides. This is the most mafic rock in the suite of samples and the only sample which has visible chloritization.

The sample contains weakly altered plagioclase phenocrysts and strongly altered megacrysts. Plagioclase phenocrysts are euhedral to subhedral and vary in size. Smaller plagioclase grains typically have more subtle barcode-twinning and are zoned. Phenocrysts are weakly altered to calcite and lesser clays.

Strongly chloritized megacrysts (up to 1.5 mm across) vary from prismatic to rounded and may be relict hornblende or pyroxenes. They are altered to chlorite, lesser calcite, fine-grained earthy minerals, and opaques.

Mineral	Abundance	Predominant Size Range
Phenocrysts	**30**	**2-0.25mm**
Plagioclase	20%	
Calcite	5%	
Sericite	5%	
Sulfides	<1%	
Megacrsyts	**10**	**5-0.5mm**
Groundmass	**60**	**<50µm**
Plagioclase	20	50-100µm
Chlorite	15%	
Quartz	10%	50µm
Calcite	5%	

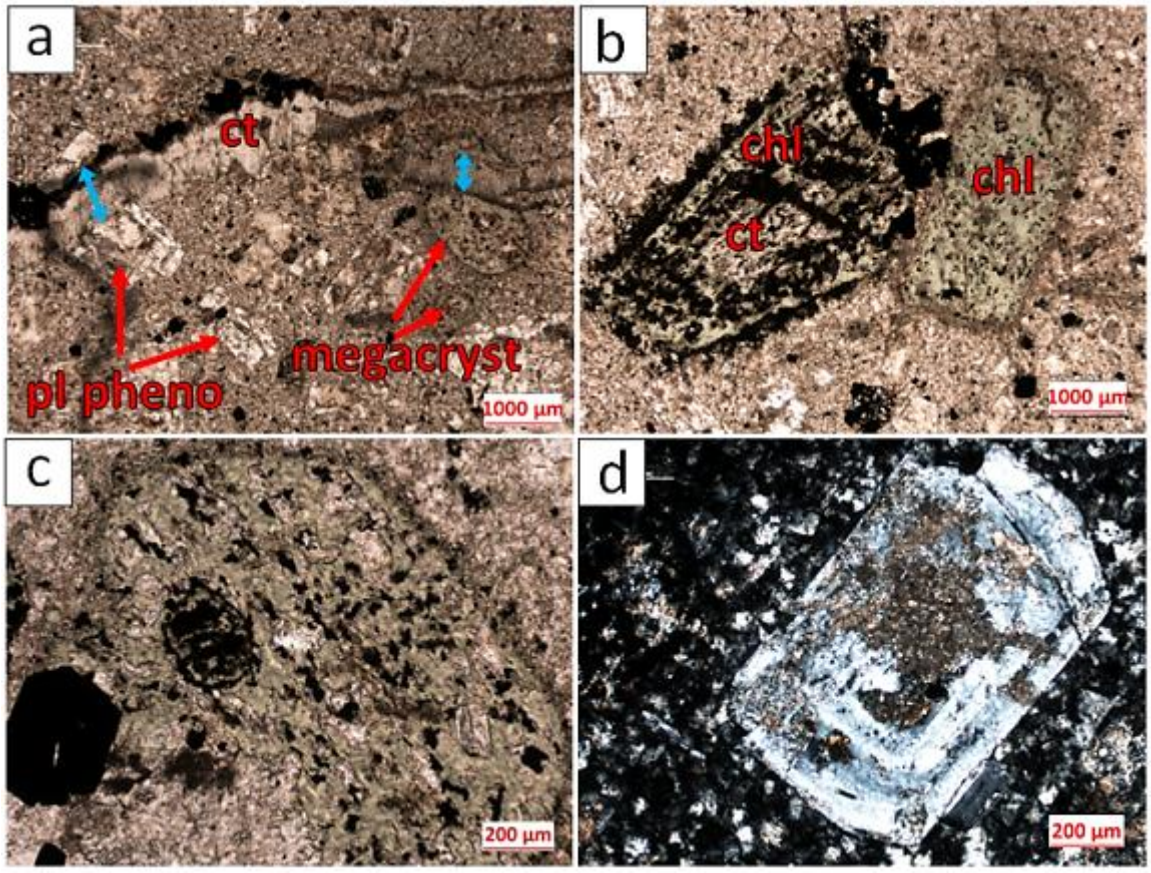

Figure 4.1-8: Bre-X7: (a) Representative section viewed in PPL. Plagioclase phenocrysts and chloritized megacrysts are shown. The sample is cut by an irregular carbonate veinlet with associated sulfides. The veinlet cross-cuts phenocrysts and megacrysts and displaces them. Blue arrows indicate this displacement; (b) Coarse megacrysts which have been highly altered to chlorite, calcite, opaques, and an earthy brown mineral viewed in PPL; (c) Megacryst which have been highly altered to chlorite, calcite, opaques, and an earthy brown mineral viewed in PPL; (d) Zoned euhedral plagioclase phenocryst which is weakly altered to calcite and minor clays viewed in XPL. The phenocryst sits in a matrix of quartz, chlorite, plagioclase, and minor clays.

The matrix in the sample consists of quartz, chlorite and plagioclase. The quartz is equigranular and more fine-grained than the plagioclase laths present in the matrix. The matrix contains clusters of a high-relief fine-grained earthy mineral, possibly epidote.

Irregular veinlets cuts the sample (<1 mm wide). They are filled with fibrous carbonate and lesser opaques. Opaques are concentrated along the veinlet edges. The veinlets cross-cut megacrysts and phenocrysts showing displacement, suggesting that the rock had been fractured and was opening as the carbonate formed.

4.1.8 Bre-X8: Carbonate-altered porphyritic dacite

Coarse relict phenocrysts are present in a fine-grained matrix of quartz, sericite, and carbonate. Relict phenocrysts are altered to sericite and carbonate. The sample contains a round highly altered domain rich in carbonate and sericite/muscovite. Muscovite porphyroblasts occur exclusively in this domain. Sulfide clots and stringers are abundant in the sample.

Mineral	Abundance	Predominant Size Range
Altered Host Rock		
Phenocrysts	**30**	**2-3 mm**
Sericite	25%	
Calcite	5%	
Groundmass	**70**	**<50 µm**
Quartz	40%	
Sericite	15%	
Sulfides	15%	<100 µm
Calcite-rich Domain		
Calcite	50%	50 µm
Sericite/muscovite	30%	<50 µm/<200 µm
Sulfides	20%	<100 µm

Coarse relict phenocrysts are strongly altered to sericite and carbonate. The phenocrysts were elongate and prismatic. They are too strongly altered to conclusively determine what they originally were, but their morphology resembles that of feldspars in other samples in the suite. The phenocrysts sit in a fine-grained matrix of quartz, sericite, and calcite.

The sample contains a round domain which is highly altered to calcite and muscovite/sericite. Here the relict phenocrysts are typically completely altered to sericite/muscovite (±calcite) obscuring their original morphology. Coarse muscovite grains are often inclusion-rich and are interpreted to be porphyroblasts. The domain locally contains open spaces.

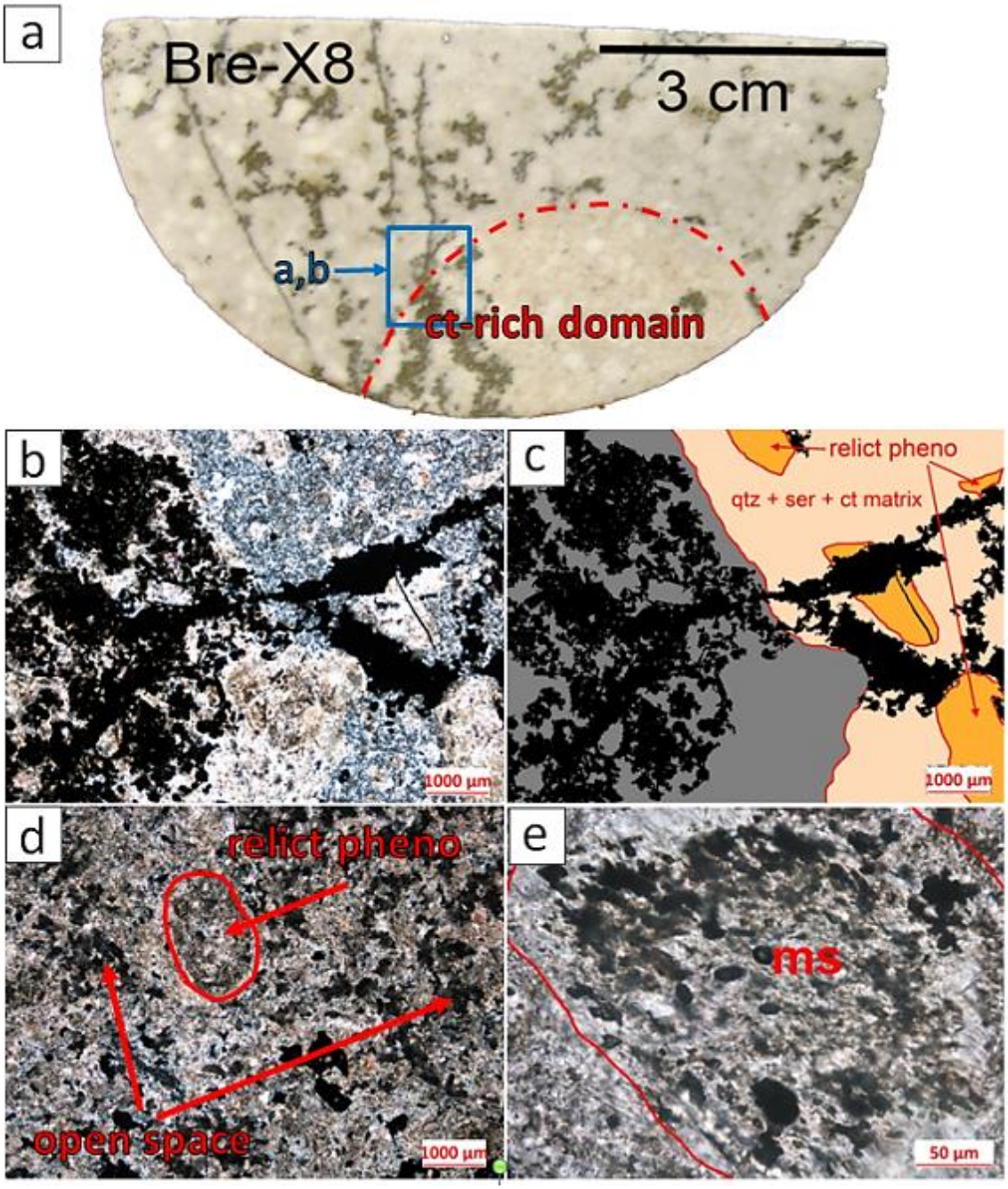

Figure 4.1-9: Bre-X8: (a) Orthogonal section of half-core sample Bre-X8. The calcite-rich round domain is outlined by the red dashed line. Blue square indicates a location similar to that of photograph "b" and schematic trace c; (c) Schematic trace of photograph "b" highlighting the sulfides (black), calcite-rich domain (grey), relict phenocrysts (orange) and matrix (tan). Note how the morphology and distribution changes across the contact between the calcite-rich domain and the typical host rock; (d) Calcite-rich domain with visible relict phenocrysts, open spaces, and abundant muscovite; (e) Close-up view of inclusion-rich muscovite in the calcite-rich domain.

Sulfides occur in the sample predominantly as dendritic clots and less often as veinlets. The clots rarely appear to be poly-metallic in hand-sample but this was not noted in the thin sections made for this study. The veinlets are discontinuous and cross-cut relict phenocrysts. In instances where a sulfide veinlet cross-cuts the strongly altered, carbonate-rich domain, its morphology and distribution changes; it thickens, becomes more dendritic, and sulfides are typically more concentrated. This is demonstrated in the schematic trace in Figure 4.1-9c. It is likely that the nature of this domain encouraged sulfide deposition, implying that it predates the sulfides in this sample.

4.1.9 Bre-X9: Porphyritic dacite with stockwork

This sample is a highly altered porphyritic dacite with silicification, sulfide veinlets, clay alteration in veins and in relict phenocyrsts, and calcite alteration in veins and in the wall rock. Dendritic sulfide veinlets are abundant in the sample and are associated with calcite-filled veinlets. Fine banded stringers or veinlets are present which have strong clay alteration both internally and as halos around them.

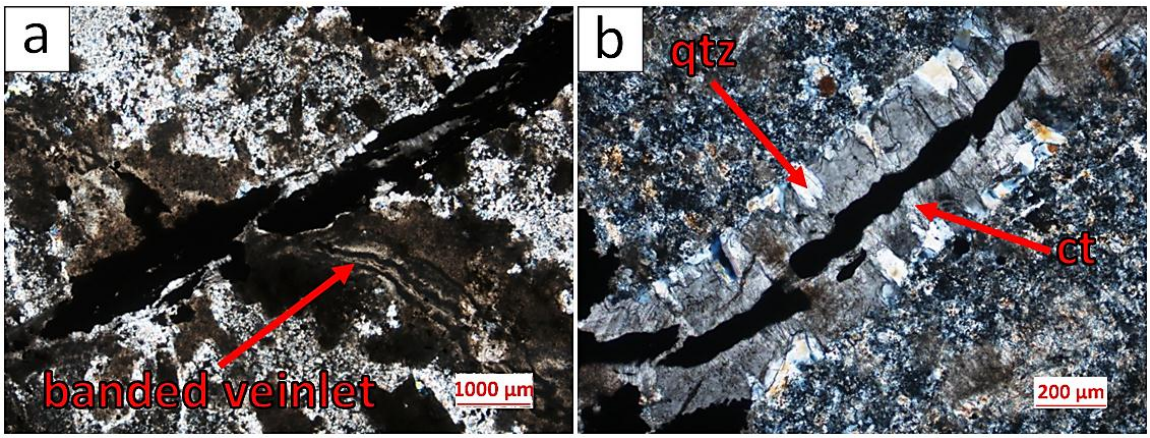

Figure 4.1-10: Bre-X9: (a) Sulfide stockwork veinlet and banded clay veinlet viewed in PPL; (b) Quartz, calcite, sulfide vein viewed in XPL. The veinlet appears to have been pulled apart during formation of quartz and calcite.

Mineral	Abundance	Predominant Size Range
Phenocrysts	**40**	**2-0.25 mm**
Sericite	45%	
Quartz	5%	
Groundmass	**50**	**<25 µm**
Quartz	35%	
Sericite	15%	

Relict phenocrysts are abundant and strongly altered to brown earthy clays, likely sericite, and lesser quartz. Their size is variable; typically the smaller relict phenocrysts are elongate. The matrix is composed of fine-grained equigranular quartz and lesser sericite.

Sulfide veinlets and stringers are abundant in the sample. They are dendritic and may contain two separate generations of sulfides. The veinlets are planar with no common orientation. Where veinlets intersect relict phenocrysts the sulfides are present in the phenocrysts as well. The veinlets are stratified from quartz to calcite to sulfides in the center which is likely not the order of formation.

4.1.10 Bre-X10: Silicified vuggy rhyodacite

This sample is a silicified and sericitized volcanic rock which may have been originally porphyritic, but phenocrysts have been completely obliterated by alteration. Quartz veinlets and stringers are abundant and often contain large drusy vugs with sulfides and oqaques. Euhedral isolated sulfide grains are disseminated throughout the sample.

Mineral	Abundance	Predominant Size Range
Groundmass	**50**	**<50 µm**
Quartz	35%	
Sericite	10%	
Sulfides	5%	<0.5 mm
Veinlets	**50**	
Quartz	45%	1-0.1 mm
Sulfides/opaques	5%	2-0.1 mm

The sample was likely originally a siliceous porphyritic volcanic rock similar to other rocks in the suite. Patches of clay minerals (sericite) may be the alteration products of obliterated feldspar phenocrysts. Evidence for this rock being porphyritic is much weaker than in most rocks in the suite. The matrix of the rock comprises equigranular quartz with interstitial sericite and clays.

The sample is strongly silicified locally with many quartz veins and stringers present. These silicified areas make up about half the sample. Quartz is coarser grained in the veinlets and stringers than the lesser silicifed wall rock. The sample is vuggy with large drusy cavities up to 2 cm long in in the quartz veinlets.

Euhedral isolated sulfide grains are disseminated throughout the sample. Other opaques and sulfides are concentrated in the silicified areas in veinlets and stringers. These are interstitial to quartz and host euhedral inclusions of quartz.

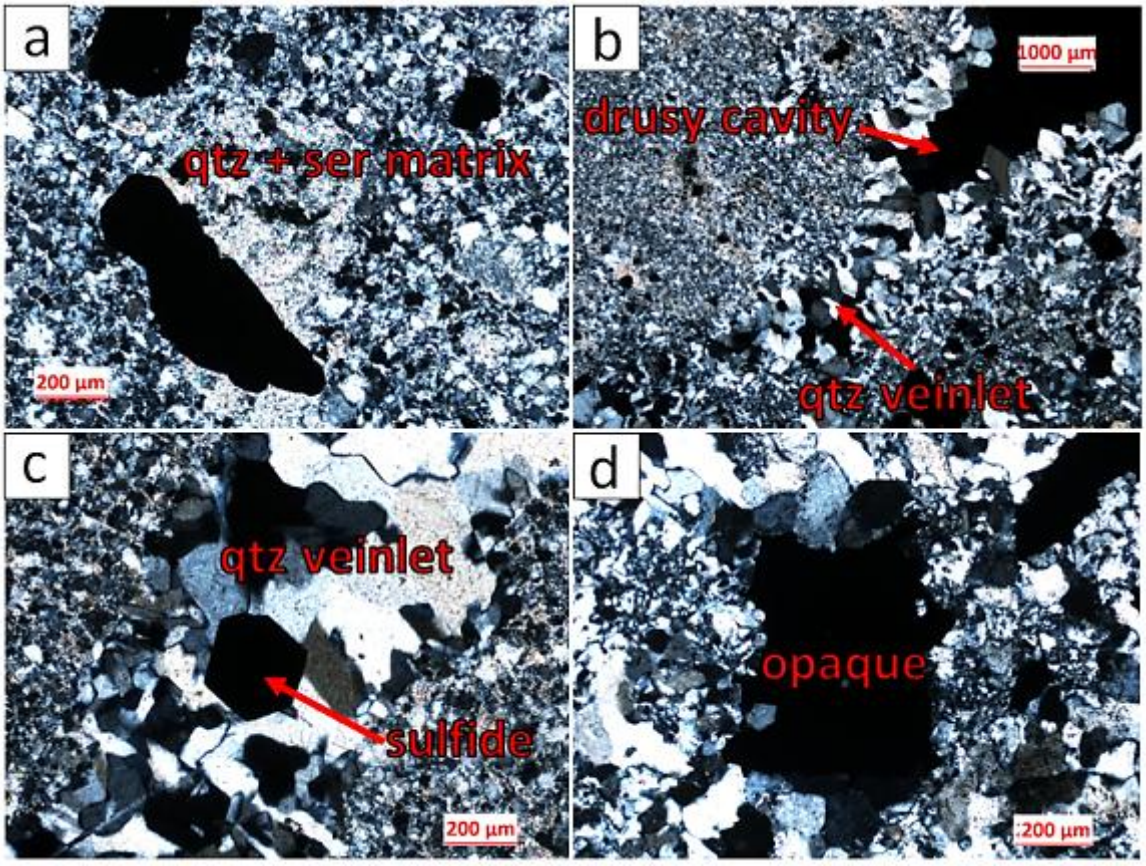

Figure 4.1-11: Bre-X10: (a) Close up view of matrix with a weakly silicified domain with equigranular quartz and interstitial sericite viewed in XPL; (b) Quartz veinlet with drusy cavity viewed in XPL. Coarse euhedral quartz lines the cavity; (c) Quartz veinlet with euhedral isolated sulfide grain. The sulfide likely formed before the quartz vein based on this textural relationship; (d) Cluster of opaque minerals which formed interstitial to quartz in a silicified domain. Quartz in this area is inequigranular.

4.1.11 Bre-X11: Dacite with drusy vein

This sample is a fine-grained siliceous volcanic rock with abundant sericite locally as patches. It was likely originally porphyritic but has been strongly altered. The drill core intersects the edge of a vuggy quartz vein lined with euhedral drusy quartz which grew into the open space. Poly-metallic clots are present in the quartz vein. Disseminated sulfides and minor fine sulfide veinlets are present in the volcanic rock.

Mineral	Abundance	Predominant Size Range
Groundmass	**95**	**<50 µm**
Quartz	50%	
Sericite	35%	
Sulfides	5%	<0.5 mm
Calcite	5%	
Vein	**5**	**Seriate**
Quartz	4.5%	2 mm-50 µm
Sericite	0.4%	<50 µm
Sulfides	0.1	<2 mm

The rock consists of fine-grained quartz and lesser sericite. There are patches of abundant sericite locally; these patches may be the alteration products of original feldspar phenocrysts. Sulfides are disseminated as isolated grains and clots throughout this volcanic rock. Fine sulfide veinlets are present locally.

The drill core intersects one side of a vuggy quartz vein which has minor sericite locally. Euhedral quartz has grown outwards into the open space in a drusy texture. The quartz in the vein has a seriate texture and often has undulose extinction. Sericite in the vein is present in patches similar to the wall-rock material. Polymetallic translucent clusters or clots are only present in the vein and are concentrated on the surface of the drusy surface. These clots have formed interstitial to quartz. The quartz in the vein has very fine-grained inclusions of a high relief elongate mineral with high birefringence (possibly tourmaline).

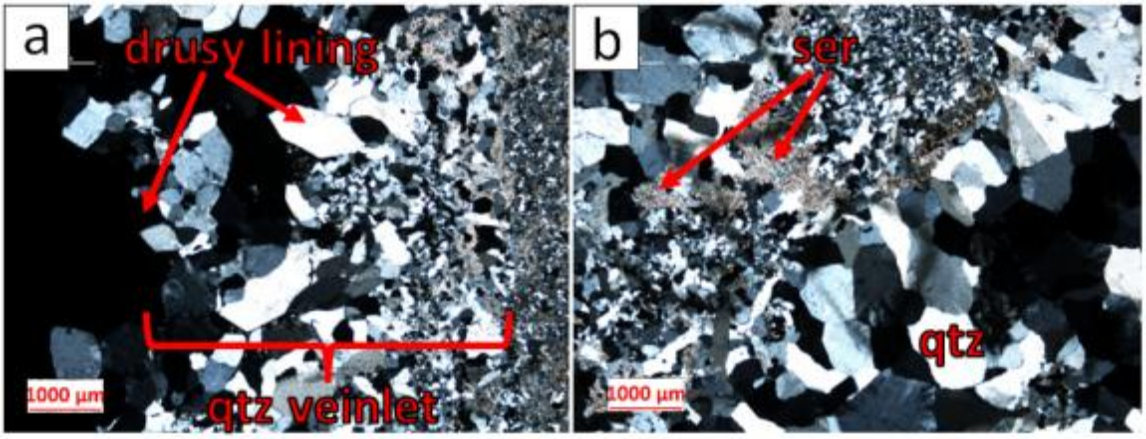

Figure 4.1-12: Bre-X11: (a) Thin section of the drusy quartz vein viewed in XPL. The contact between the vein and the wall-rock is on the right of the photograph; (b) Quartz vein with seriate quartz and patches of fine-grained quartz and sericite viewed in XPL. Undulose extinction can be seen in the quartz locally.

4.1.12 Bre-X12: Porphyritic dacite with sulfide stockwork

This sample is an altered porphyritic dacite-andesite with abundant dendritic sulfide veinlets and stringers cutting the sample. The relict phenocrysts were likely originally feldspars and have been completely altered to clays. The feldspars are set in a fine-grained matrix of equigranular quartz and sericite.

Mineral	Abundance	Predominant Size Range
Phenocrysts	**40**	**2-0.25 mm**
Sericite	45%	
Quartz	5%	
Groundmass	**50**	**<25 µm**
Quartz	35%	
Sericite	15%	

Relict phenocrysts are abundant and strongly altered to brown earthy clays, likely sericite, and lesser quartz. Their size is variable; typically the smaller relict phenocrysts are elongate. Alteration has resulted in fuzzy grain boundaries and often a

light quartz rich layer surrounds the phenocrysts. The matrix is composed of fine-grained equigranular quartz and lesser sericite.

Sulfide veinlets and stringers are abundant in the sample. They are dendritic and may contain two separate generations of sulfides. Coarse euhedral sulfide grains have overgrown the minerals in the host rock, entrapping matrix quartz grains and relict phenocrysts as inclusions. The veinlets are sub-parallel to two orientations which may be conjugate fracture sets. A second generation of sulfide veinlets/stringers branch off from these veinlets giving them the dendritic morphology.

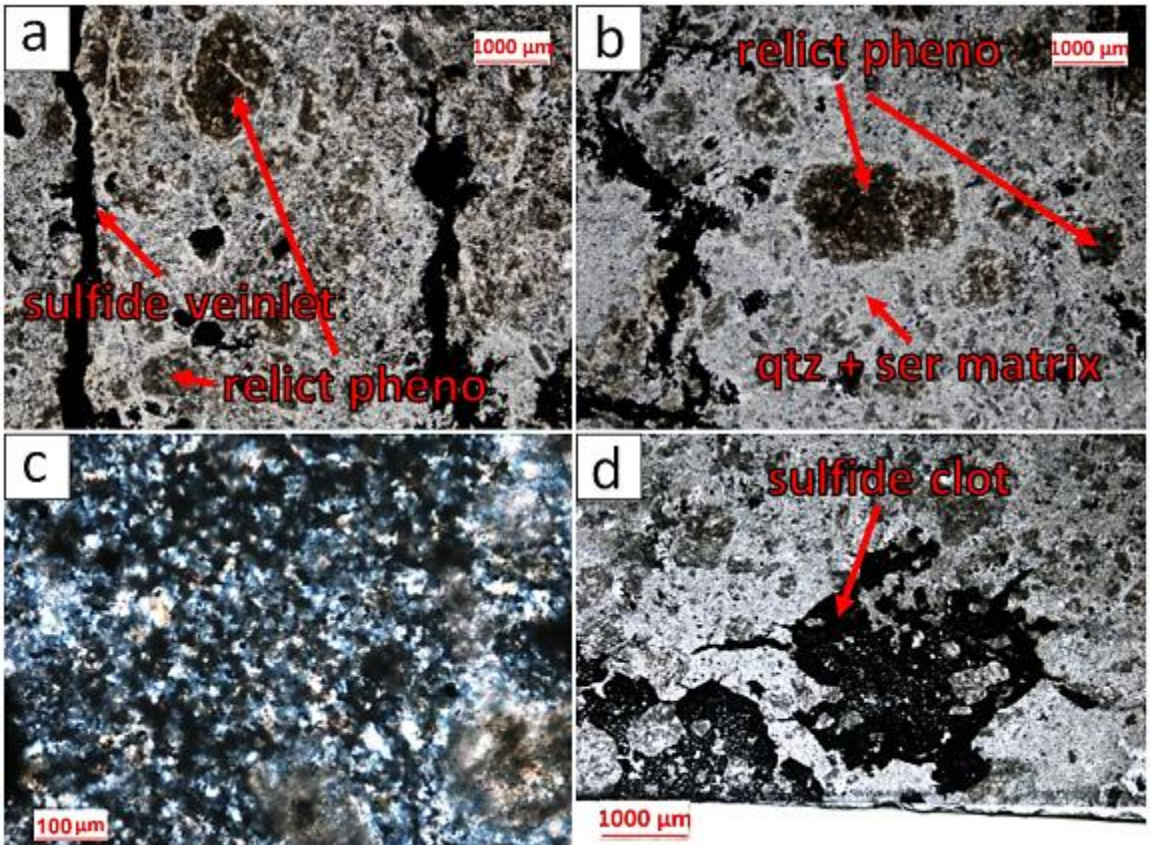

Figure 4.1-13: Bre-X12: (a) Representative section showing the relict phenocrysts, siliceous matrix, and sulfide veinlets viewed in PPL; (b) Similar to photograph "a" viewed in PPL. A quartz-rich layer surrounds the relict phenocrysts; (c) Close up view of the fine-grained matrix of equigranular quartz, and lesser sericite viewed in XPL; (d) Sulfide clot where euhedral sulfide grains have overgrown the matrix and relict phenocrysts.

4.2: Reflected light ore-microscopy:

4.2.1 Bre-X1

The sample contains a quartz-carbonate-sulfide vein and has disseminated sulfides and ore-minerals in the wall-rock. The vein contains a discontinuous seam of sulfides that include sphalerite, pyrite, galena, sulfosalts, and lesser chalcopyrite. Pyrite is more abundant in the host rock than in the vein. The host rocks contain clusters and isolated grains of pyrite as well as grain-shaped aggregates of a grey platy mineral with strong internal reflections which was determined to be rutile by qualitative electron analysis.

Sphalerite is the most abundant ore mineral in the vein. It has locally abundant fine inclusions of chalcopyrite. Chalcopyrite is abundant locally along the edges of the sphalerite and the contact between them is smooth. The pyrite in the veinlet is mostly inclusion-free and occurs as euhedral to subhedral isolated grains or as clusters of grains. Pyrite rarely contains rounded inclusions of light a grey mineral, likely galena. Galena is abundant and closely associated with sphalerite in the sample. It is often included in the sphalerite or in contact with sphalerite. Textural evidence suggests that sphalerite has partially replaced galena; triangular pits characteristic of galena sometimes extend into sphalerite. The sulfosalts and galena are spatially associated and have irregular contacts with each other, likely forming a reaction/replacement texture.

Chalcopyrite inclusions in the sphalerite are < 10 µm in maximum length and are rounded and often elongated. The inclusions follow linear trails which may represent growth zones or crystallographic features in the sphalerite. This texture is likely

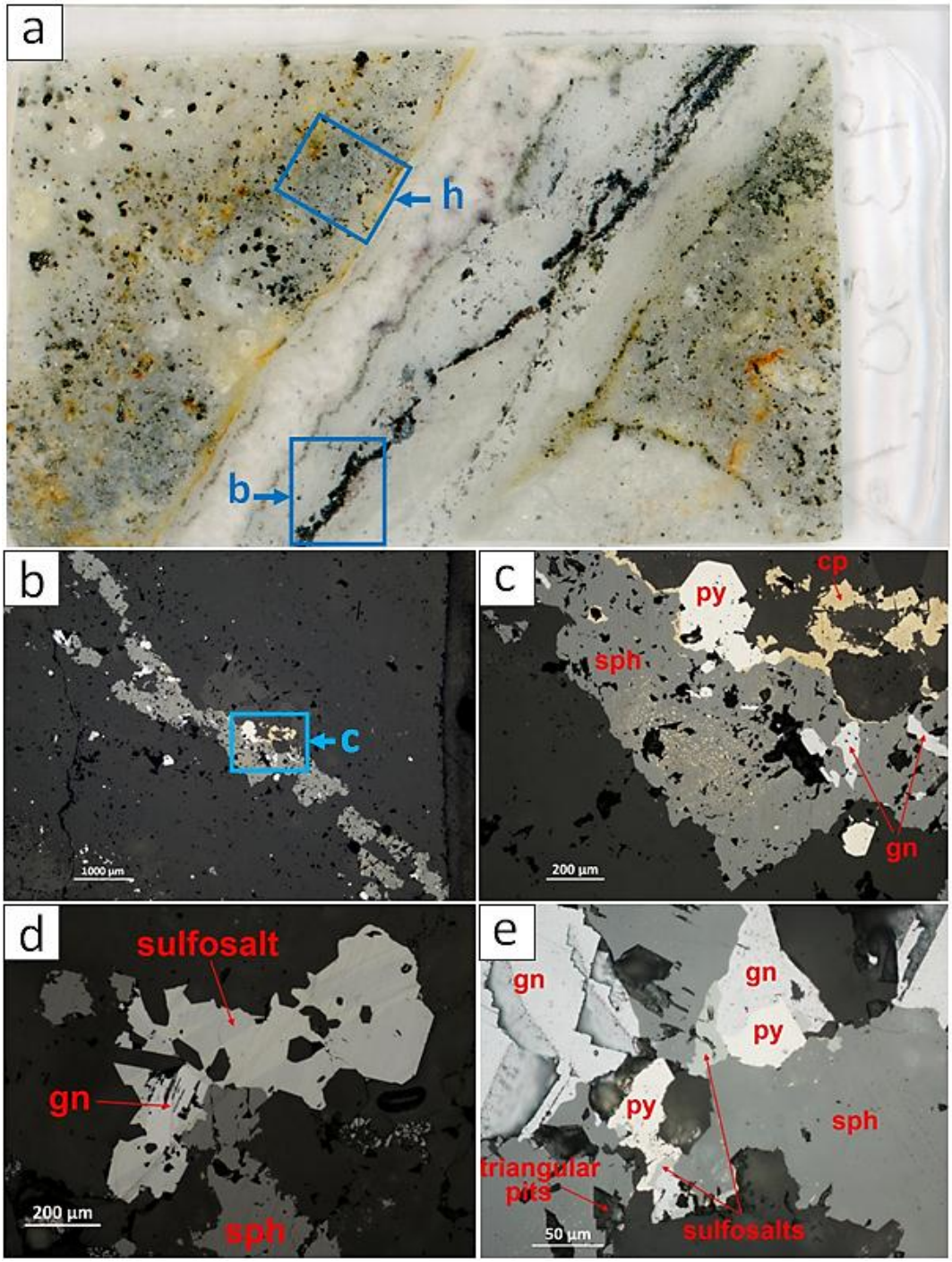

Figure 4.2-1: Bre-X1: (a) Scan of polished thin section with the location of photographs shown where appropriate (b) Sulfide seam as seen in polarized reflected light; (c) Close up of sulfide vein viewed in reflected light. Euhedral pyrite is overgrown by the other sulfides. Sphalerite, galena, and chalcopyrite are present; (d); Sphalerite, galena, and sulfosalt in the vein viewed in cross-polarized reflected light. The sulfosalt and galena have irregular rounded contacts. The sulfosalt has a distinct banded anisotropy; (e) Textural relationships between pyrite, sphalerite, galena, and sulfosalts. Pyrite shows complex intergrowth with sulfosalt, galena, and gangue. Triangular pits are present in the sphalerite which resemble those in which are characteristic of galena.

indicative of the co-precipitation of sphalerite and chalcopyrite or the growth of sphalerite which was partially replaced by the periodic pulses of Cu- and Fe-rich fluids (Nagase & Kojima, 1997).

In the wall rock pyrite occurs as irregular clusters or isolated grains <1mm across. Pyrite is euhedral to anhedral with few inclusions. A light grey platy mineral with strong orange internal reflections (rutile) typically occurs as grain shaped clusters <0.5 mm but also as fine platy grains.

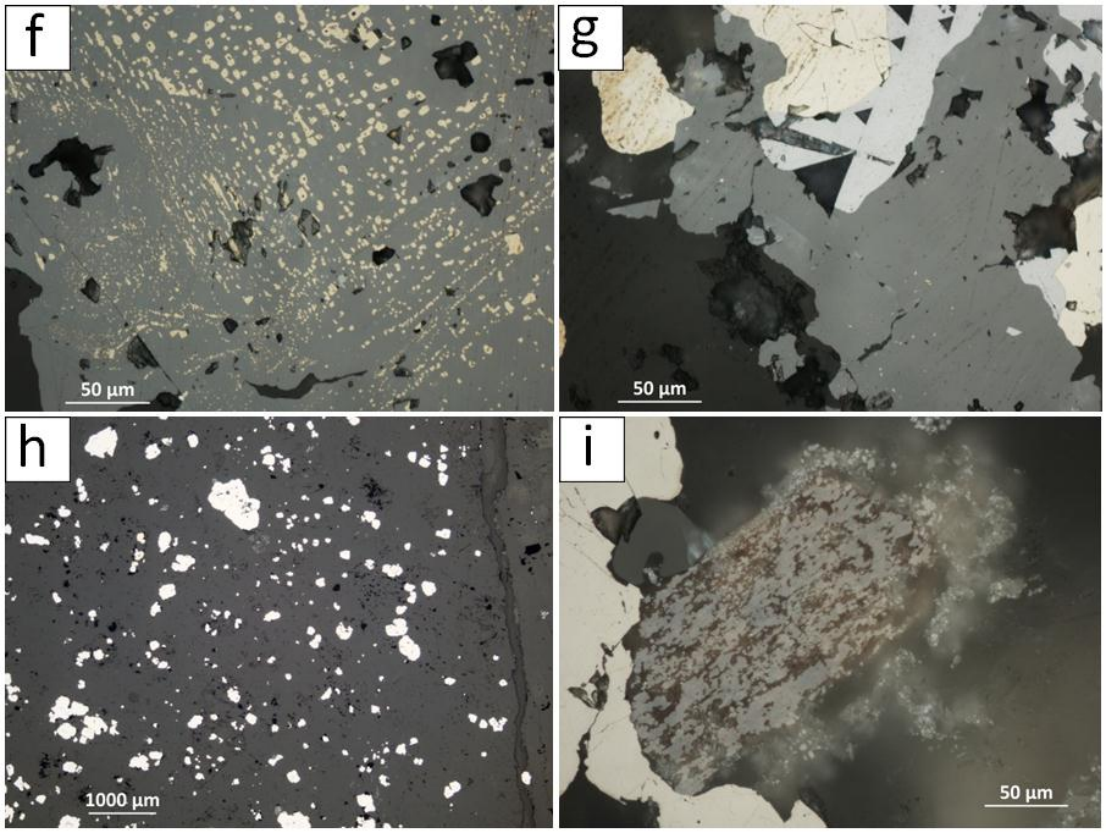

Figure 4.2-2: Bre-X1: (f) Sphalerite with chalcopyrite inclusions. The chalcopyrite inclusions appear to follow linear trails; (g) Triangular pit in galena crossing the galena-sphalerite contact. This suggests that sphalerite is replacing galena; (h) Disseminated pyrite in the host rocks adjacent to vein contact (right of photograph); (i) Cluster of platy light grey mineral pseudomorphing a prismatic grain. The mineral has strong orange internal reflections (rutile).

4.2.2 Bre-X2

The sample contains a quartz-calcite-sulfide veinlet, a smaller quartz-calcite-pyrite veinlet, and disseminated sulfide clots. The quartz-calcite-sulfide veinlet contains pyrite, sphalerite, galena, and lesser chalcopyrite. The host rocks contain disseminated pyrite clots and isolated pyrite grains.

The quartz-calcite-sulfide veinlet is approximately 3 mm wide (Fig. 4.2-3b,c). The sulfides occur as discontinuous seams hosted in the calcite. Pyrite and sphalerite are most abundant with lesser galena and minor chalcopyrite. The pyrite here is inclusion-free and locally fractured. It is commonly oxidized, showing colour variations (Fig. 4.2-3d). Fractures in the pyrite are locally filled with galena. Elongate galena inclusions are locally present in the pyrite (Fig. 4.2-3f) which suggests that galena filled fractures in the pyrite and then the pyrite continued to grow trapping galena inside. Rare dendritic pyrite is also present in the veinlet (Fig. 4.2-3g) and in only one clot (Fig. 4.2-3h). Sphalerite is exclusively in the veinlet and has abundant inclusions of chalcopyrite which are elongate to triangular in shape; this likely reflects the tetrahedral structure of sphalerite (Fig. 4.2-3e). The sphalerite is relatively opaque in this sample having few internal reflections.

The wall rock contains dendritic clots of pyrite with inclusions of a light grey mineral with strong internal reflections determined from qualitative SEM analysis to be rutile. One pyrite clot consists of a cluster of pyrite grains with a second generation of dendritic pyrite forming on the rims (Fig. 4.2-4h). There are also clusters of a light

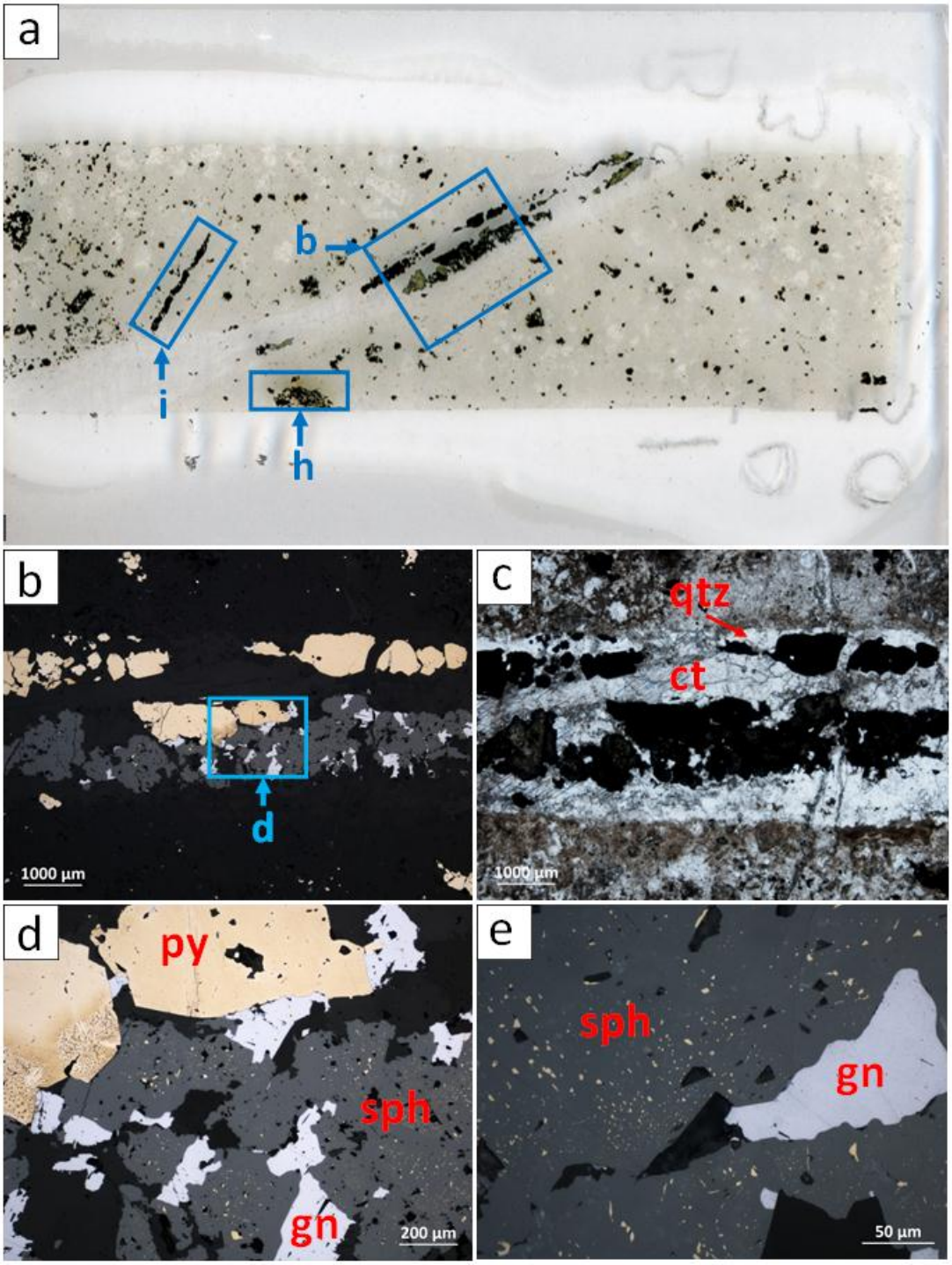

Figure 4.2-3: Bre-X2: (a) Scan of polished thin section Bre-X2 indicating the location of photographs where appropriate; (b) Quartz-carbonate-sulfide veinlet containing pyrite, sphalerite, galena, and minor chalcopyrite, viewed in reflected light; (c) Same as "photograph b" viewed in plane-polarized refracted light showing the sulfide's relationship with vein material; (d) Close up view of sulfides in the veinlet. Euhedral pyrite is overgrown by sphalerite and galena. Sphalerite has "chalcopyrite disease" as well as intergrowths and inclusions of galena; (e) Sphalerite with "chalcopyrite disease" and inclusion of galena. Sphalerite has triangular-shaped inclusions of gangue minerals reflecting the crystallographic structure of sphalerite.

grey platy mineral with strong internal reflections, having the shape of prismatic grains in the host rocks (rutile).

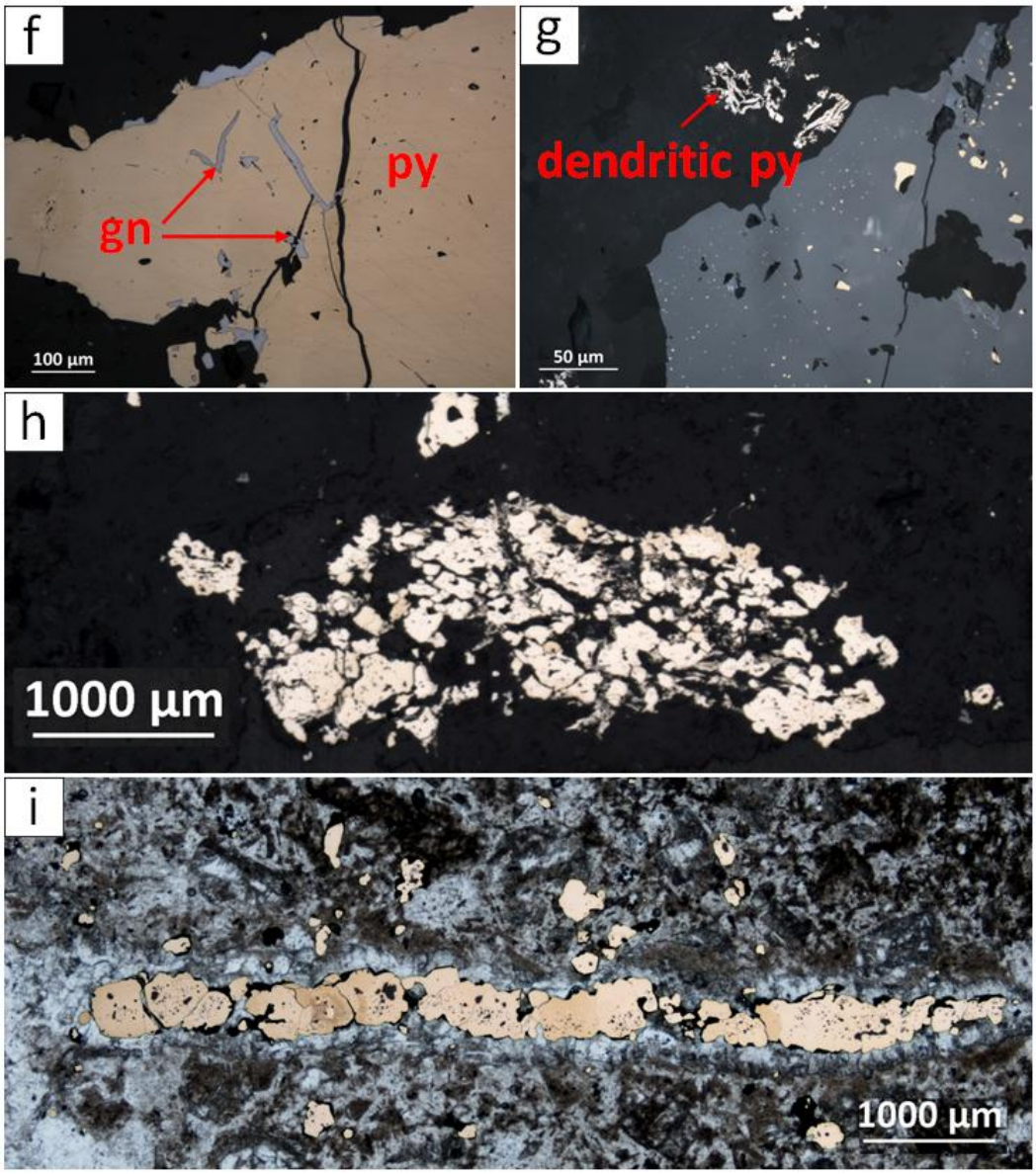

Figure 4.2-4: Bre-X2: (f) Fractured pyrite in veinlet with galena along the edges, filling fractures, and as elongate inclusions. The shape of the inclusions of galena suggests that pyrite has continued to form since galena deposition; (g) Sphalerite in veinlet with "chalcopyrite disease". Photograph shows dendritic pyrite which is rare in the sample; (h) Pyrite clot comprised of a cluster of pyrite grains with a second generation of dendritic pyrite forming on the rims. A light grey mineral occurs with the dendritic pyrite but it is not clearly seen in this photograph; (i) Fine quartz-carbonate-pyrite veinlet intersecting the larger polymetallic quartz-carbonate-sulfide veinlet in the sample. Here the pyrite from a reflected light photograph was superimposed upon onto the refracted light photograph to better show the relationship between the pyrite and the silicate/carbonate material in the sample. Pyrite grains are subrounded and contain many inclusions.

4.1.3 Bre-X3

This sample is a matrix-supported breccia with clasts of volcanic and sedimentary rocks. The mineralization here is minor overall. The clasts of sedimentary rock are most abundant and are dark brown in colour and layered. They contain elongated pyrite and rutile blebs which are parallel to bedding. The volcanic clasts are less abundant, smaller, and light in colour. They contain minor pyrite and grain-shaped clusters of a light grey mineral with strong internal reflections (rutile); The original mineral could have been titanomagnatite or titianite. Fine carbonate veinlets or stringers cut the sample and contain more abundant pyrite than the host rocks. Here pyrite blebs are present locally with few inclusions of vein material.

4.1.4 Bre-X4

The sample contains carbonate-pyrite veinlets and disseminated pyrite clots. The veinlets are surrounded by an alteration zone that extends about 1 cm outwards and has a sharp contact with the less-altered wall-rock. Pyrite is concentrated in the veinlets and in the alteration zone and is less abundant in the weakly altered wall-rock. Pyrite in the veinlet is discontinuous.

The veinlets intersect each other at an angle which suggests that they could have formed from conjugate fracture sets. The pyrite in the veinlets is anhedral with irregular grain boundaries (Fig. 4.1-6c), suggesting concurrent growth with the veinlet material. The alteration zone around the veinlets contains more pyrite than the rest of the sample. Figure 4.1-6d illustrates how pyrite abundance and morphology differs across the alteration zone boundary. In the entire sample pyrite is most abundant in the

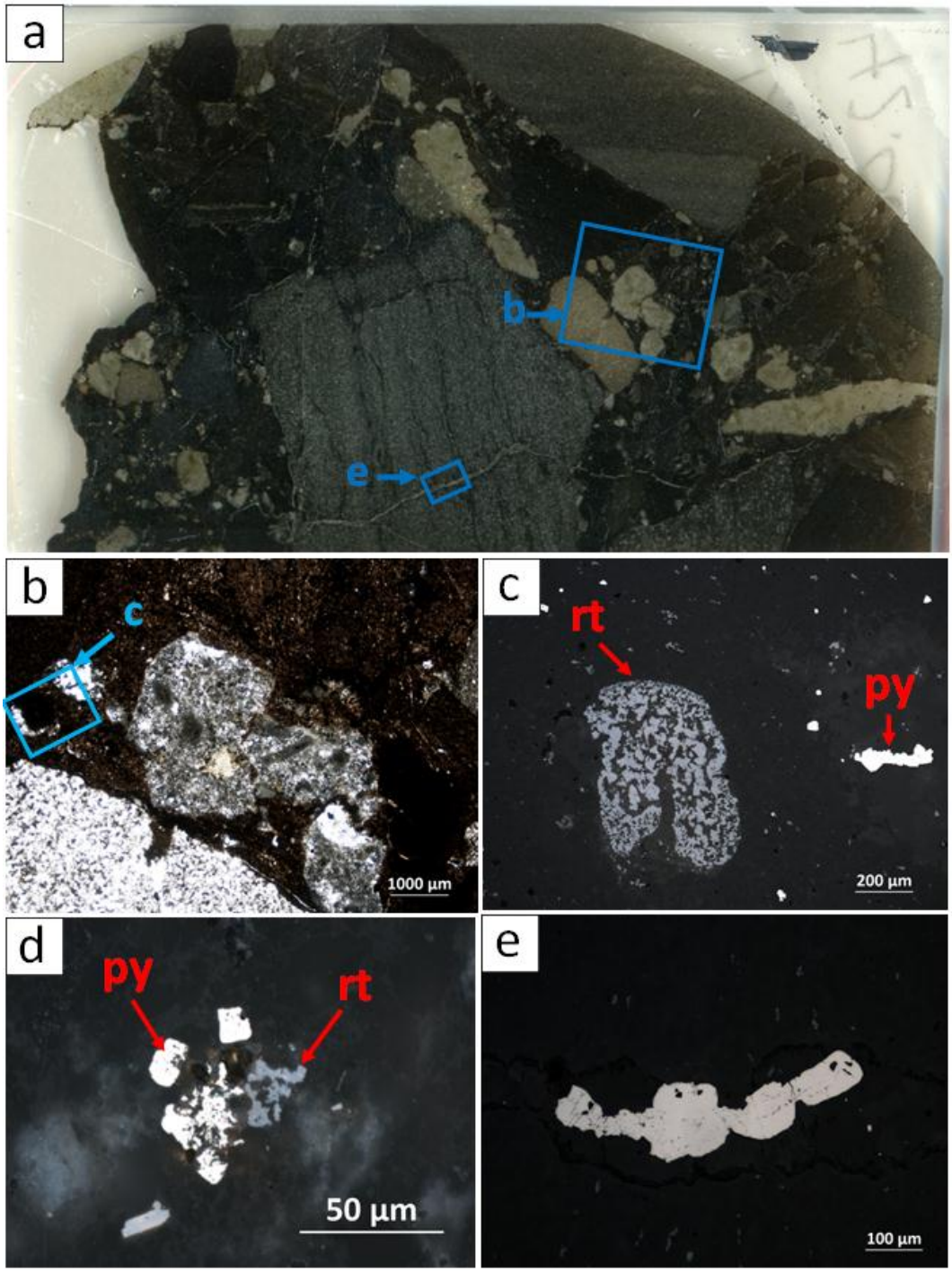

Figure 4.1-5: Bre-X3: (a) Scan of polished thin section Bre-X3 showing the location of photographs where appropriate; (b) Clasts of altered porphyritic rocks; (c) Grain-shaped cluster of rutile and pyrite clot in light coloured clasts; (d) Cluster of pyrite and rutile; (e) Pyrite cluster in fine carbonate veinlet.

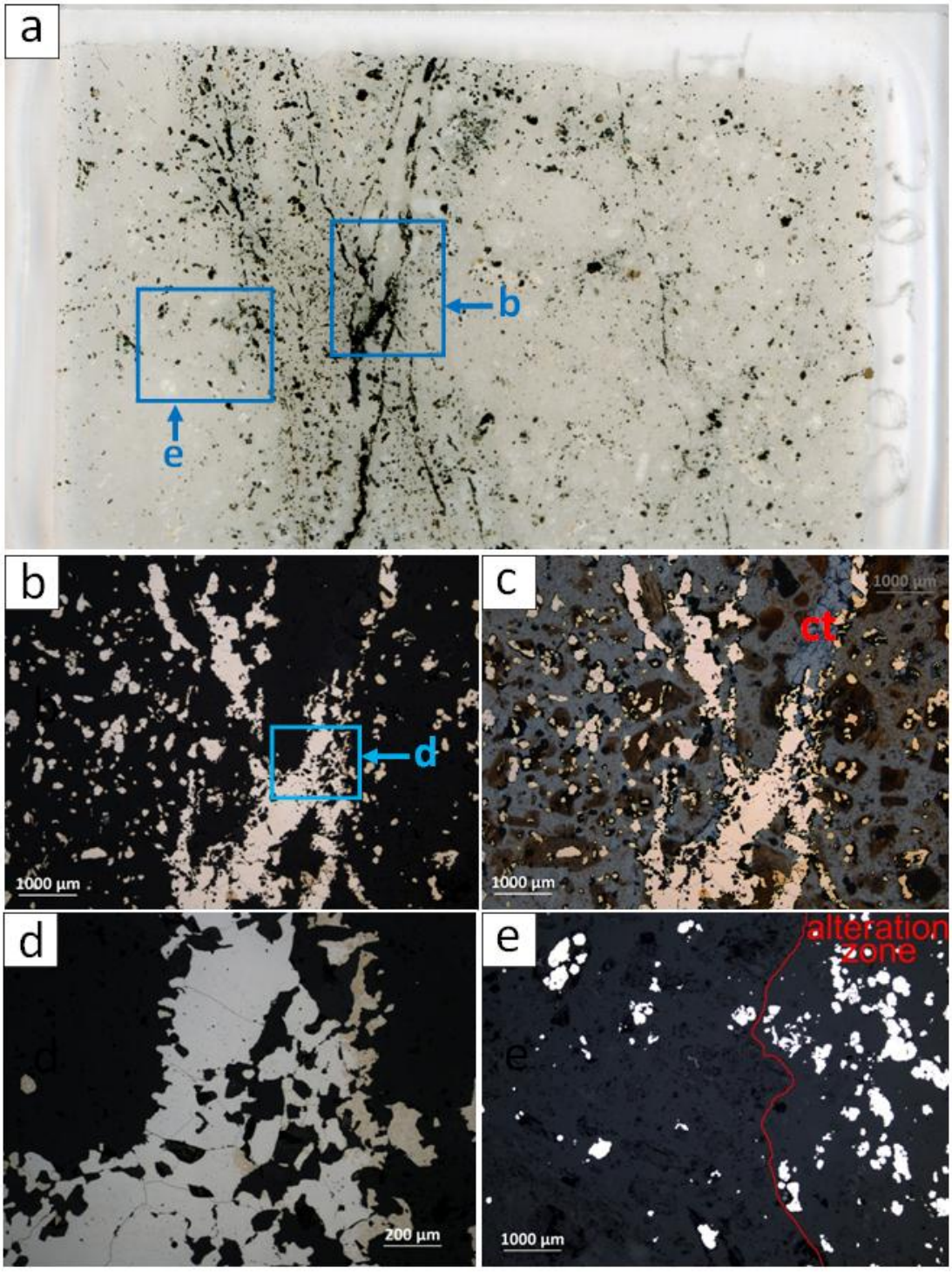

Figure 4.1-6: Bre-X4: (a) Scan of polished thin section showing the location of photographs where appropriate; (b) Pyrite in calcite veinlets with pyrite-rich alteration zone. The veinlets may be associated with conjugate fracture sets; (c) Overlay of reflected and refracted light images. Conjugate calcite veinlets in the porphyritic rocks. Pyrite is concentrated in the calcite veinlet and in the relict phenocrysts; (d) Close up view of photograph "b". pyrite is irregular and inclusion-rich; (e) Distribution of pyrite in the alteration zone and the less-altered host rock. Pyrite is significantly more abundant in the alteration zone.

relict phenocrysts. The chemical or physical nature of the altered phenocrysts may have encouraged the formation of pyrite.

The entire sample contains rare clusters of a platy grey mineral with strong internal reflections which make up the shape of prismatic grains (rutile). Figure 4.1-6e shows these clusters along with an isolated subhedral grain of pyrite inside a relict phenocryst.

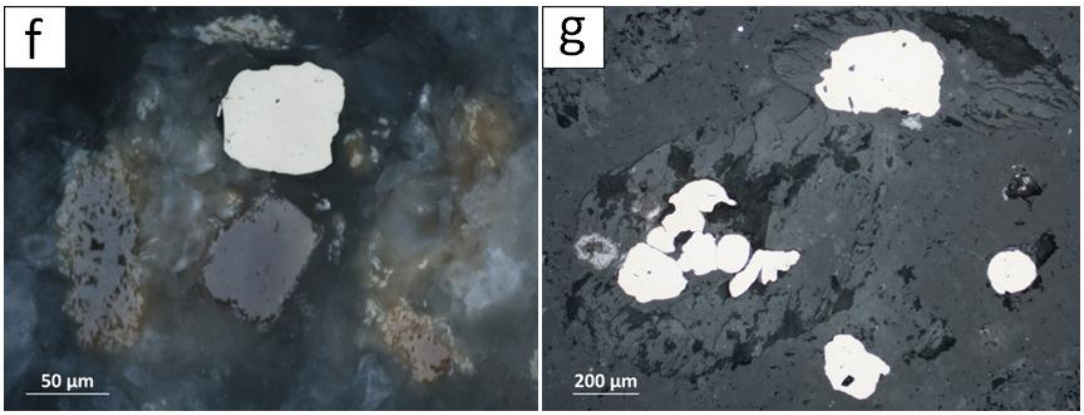

Figure 4.1-7: Bre-X4: (f) Isolated pyrite grain and grain-shaped clusters of grey mineral with strong internal reflections likely rutile; (g) pyrite concentrated in the relict phenocrysts.

4.1.5 Bre-X6

The sample has two principal domains; one is altered porphyritic rock with relict phenocrysts in a siliceous fine-grained matrix and the other is a dark fine-grained volcanic rock with clasts composed of fine-grained quartz. Carbonate veinlets with minor quartz cross-cut all domains and frequently have open spaces. Pyrite does not appear to be spatially associated with the carbonate veinlets in thin section-scale. The sample contains predominantly pyrite with very rare sphalerite. A light grey mineral

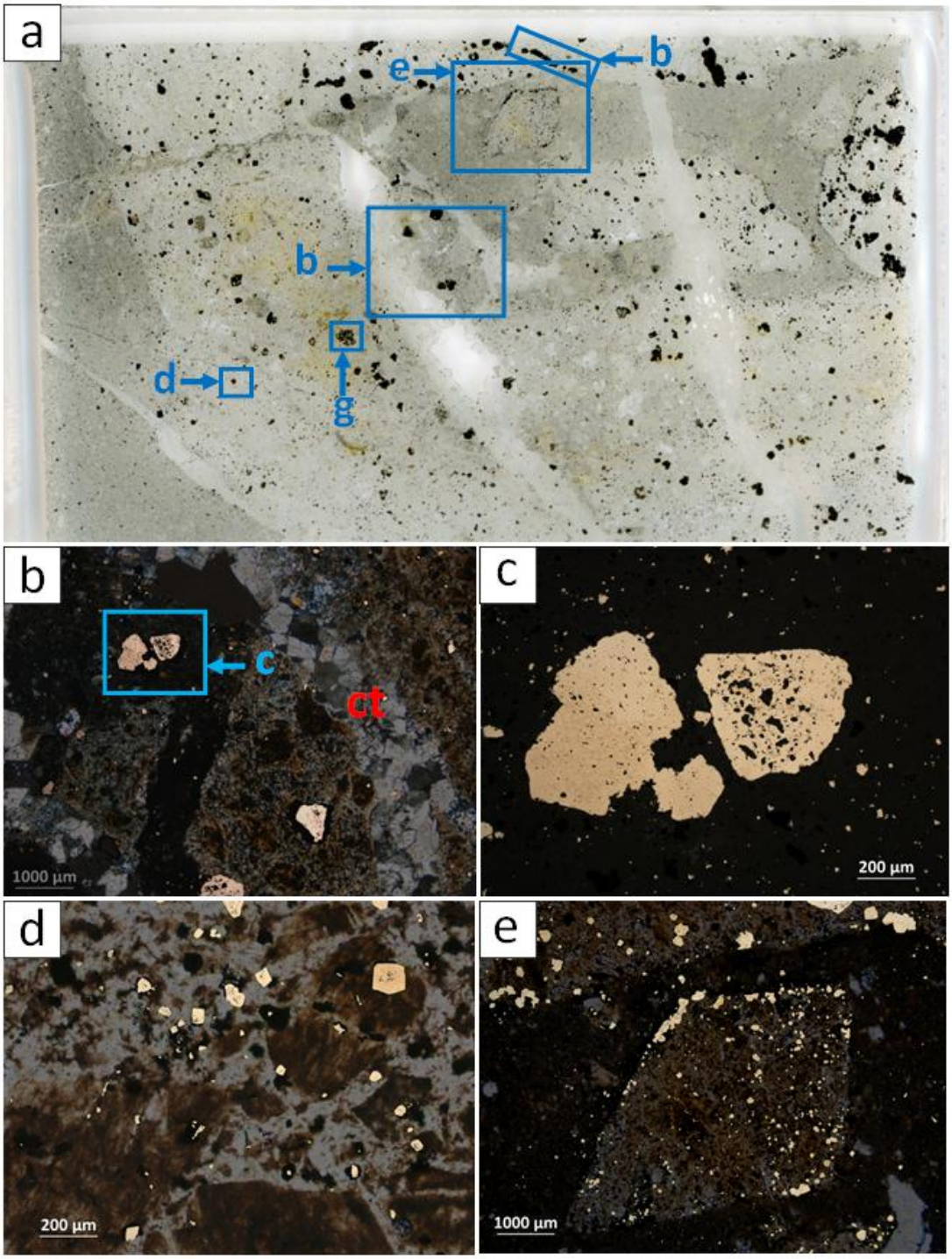

Figure 4.1-8: Bre-X6: Reflected and refracted light photographs are superimposed where appropriate to put the ore-minerals into context. (a) Scan of polished thin section. Location of photograph is indicated where appropriate; (b) Inclusion-rich grains of pyrite. Pyrite is present in both the lighter porphyritic domain and in the darker volcanic domain; (c) Close up view of pyrite grains in "b"; (d) Isolated disseminated pyrite grains in the porphyritic domain. Pyrite grains are both in the matrix and in the relict phenocrysts; (e) Clast of lighter porphyritic domain in the darker volcanic domain. Pyrite grains are concentrated along the inside edge of the clast.

with strong internal reflections is present in trace quantities throughout the sample (rutile).

Sulfides are present in both domains but are much more abundant in the porphyritic domain. Pyrite in the darker domain is typically finer-grained. In the porphyritic domain the pyrite is in both the matrix and the relict phenocrysts. Here pyrite is typically inclusion-rich and occurs predominantly as disseminated euhedral grains <100 µm on average but also occurs as elongated aggregates and clot-like

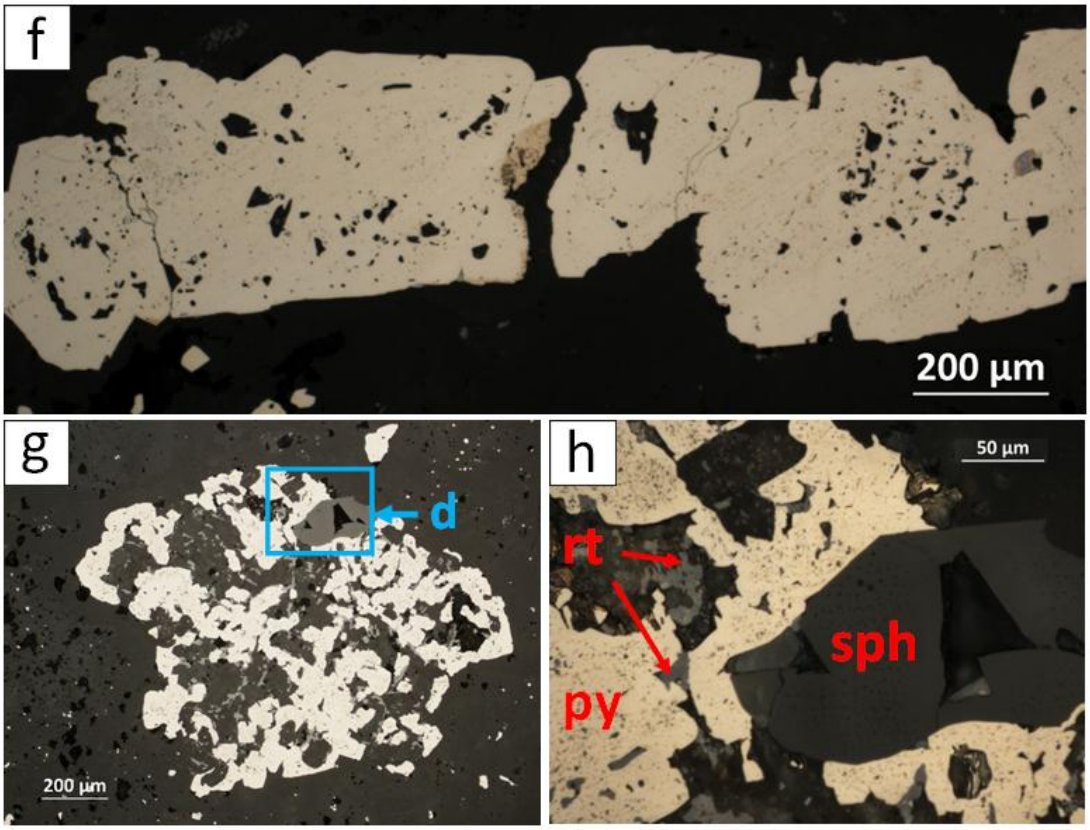

Figure 4.1-9: Bre-X6: (f) Pyrite veinlet with abundant inclusions in the interior of the grains; (g) Sulfide clot composed of a cluster of pyrite grains, lesser sphalerite and minor rutile; (h) Sphalerite, and inclusion-rich pyrite with inclusions of gangue minerals and rutile. Sphalerite is relatively opaque and has triangular pits.

clusters. The only sphalerite in the sample is in a clot consisting of a cluster of pyrite as seen in Figure 4.1-9g. Several large pyrite grains up to 500 µm across are present in the darker volcanic rocks (Fig. 4.9-8b).

A clast of the porphyritic domain is hosted in a matrix of the darker volcanic domain. Here the pyrite is concentrated along the inside edges of this clast as seen in Figure 4.1-9e. The edge of the clast may have acted as a permeable zone for fluids. It is also likely that the chemistry or physical properties of the porphyritic rock encouraged the formation of pyrite, which is less abundant in the darker volcanic rock.

4.1.6 Bre-X7

Sulfides in the sample occur as elongated clots along quartz-carbonate veinlets and as disseminated isolated grains. The ore minerals in this sample are predominantly pyrite with a minor light grey platy mineral with strong internal reflections (rutile). The relationship between pyrite and the veinlet material is ambiguous, however from the textural relationships it is clear that pyrite formed after quartz and probably after the carbonate.

Pyrite in the sample contains abundant inclusions but often has inclusion-free rims. Pyrite is more abundant in relict feldspar phenocrysts or in the highly chloritized megacrysts than in the matrix. Pyrite is concentrated along the edges of the veinlet which cuts the sample. Figure 4.2-10b shows that the pyrite occurs along the edge, but never in the quartz-carbonate veinlet.

A quartz-carbonate veinlet cuts the sample and is about 1 mm wide. The carbonate is fibrous and grows perpendicular to the orientation of the veinlet. Phenocrysts and megacrysts are cross-cut and displaced by the opening of the veinlet. However, the pyrite is not displaced and thus likely formed concurrent with or post-veinlet opening. The inclusions in the pyrite along the veinlet have the morphology of quartz. Therefore it is likely that the pyrite formed after the quartz and probably after the carbonate as well.

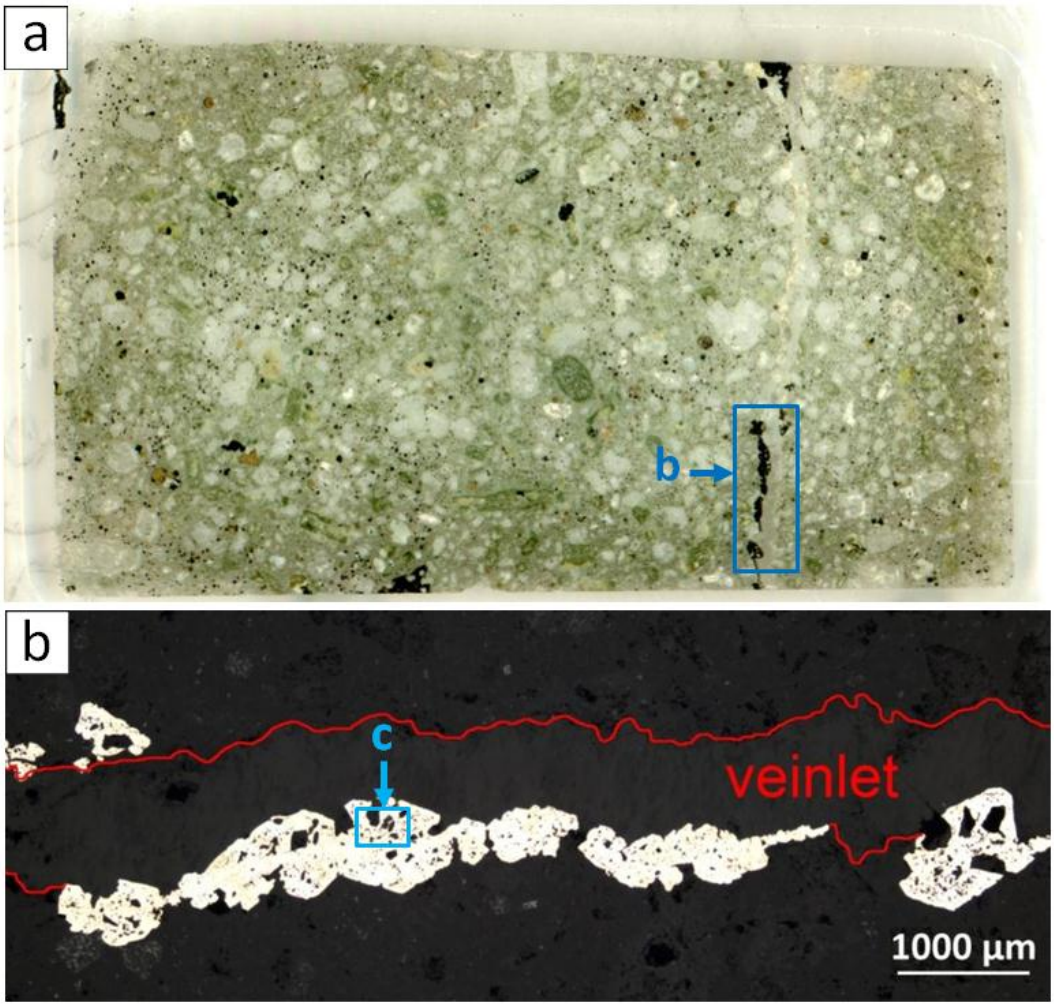

Figure 4.1-10: Bre-X7: (a) Scan of polished thin section Bre-X7 with locations of photographs shown where appropriate; (b) Quartz-carbonate veinlet with elongate bleb of inclusion-pyrite along its edge. The trace of the veinlet has been outlined in red.

Clusters of a platy light grey mineral with strong internal reflections have the shape of prismatic grains, and are probably rutile (Fig. 4.2-11e,f). These clusters frequently have inclusions of pyrite which often overgrow the light grey mineral filling in the spaces between grains. This same mineral is also present as inclusions in pyrite throughout the sample (Fig. 4.2-11d).

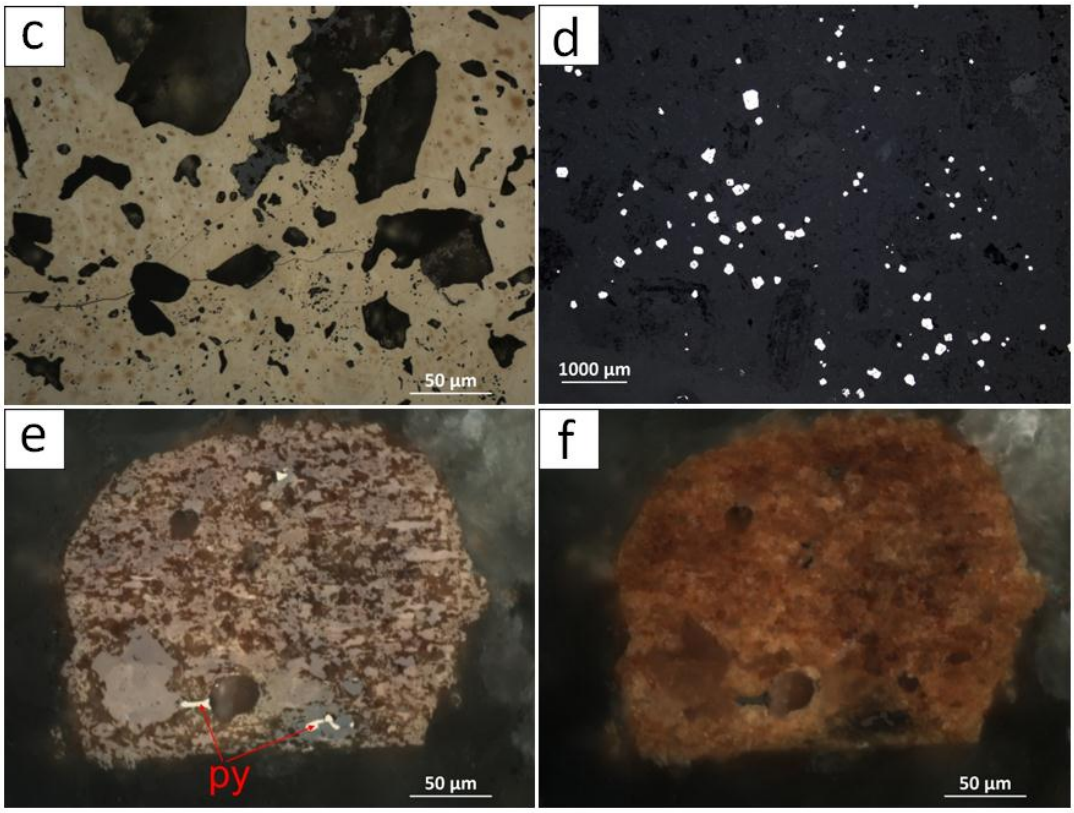

Figure 4.1-11: Bre-X7: (c) Close up view of pyrite along the edge of the veinlet. Inclusions of gangue, likely quartz, are abundant. In some of these inclusions there is a light grey platy mineral (likely rutile); (d) Disseminated isolated pyrite grains not spatially associated to the veinlet; (e) Grain-shaped cluster of light grey platy mineral with minor pyrite which likely formed after in normal reflected light; (f) Same as photograph "d" in cross-polarized reflected light. Strong red to yellow internal reflections are visible.

4.1.7 Bre-X8:

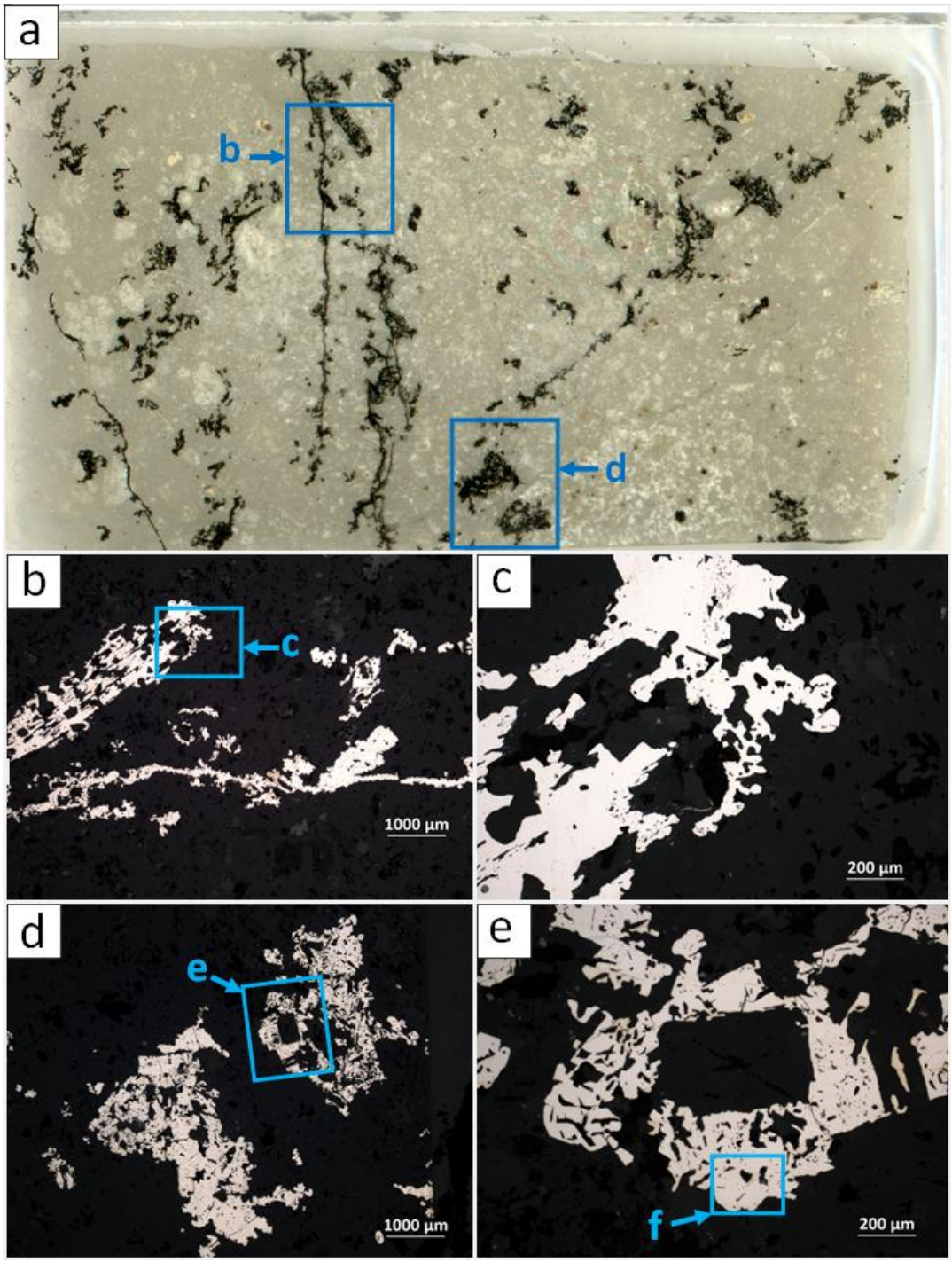

Figure 4.1-12: Bre-X8: (a) Scan of polished thin section Bre-X 8 showing the locations of photographs where appropriate; (b) Dendritic pyrite veinlet with pyrite replacement of an adjacent megacrysts; (c) Close up view of pyrite replacement of a megacryst. The pyrite has inclusion-free cores and inclusion-rich irregular rims; (d) Dendritic inclusion-rich pyrite clots; (e) Close up view of dendritic pyrite clot in photograph "d". Note the large rectangle-shaped inclusion.

The sample contains dendritic pyrite veinlets and clots that are more abundant than disseminated pyrite. The pyrite in the veinlets and clots is typically inclusion-rich with irregular wavy edges. The veinlets are discontinuous and irregular with no apparent preferred orientation. There may be two generations of pyrite in the sample. Some of the pyrite in the veinlets and clots has inclusion-free cores and inclusion-rich irregular edges.

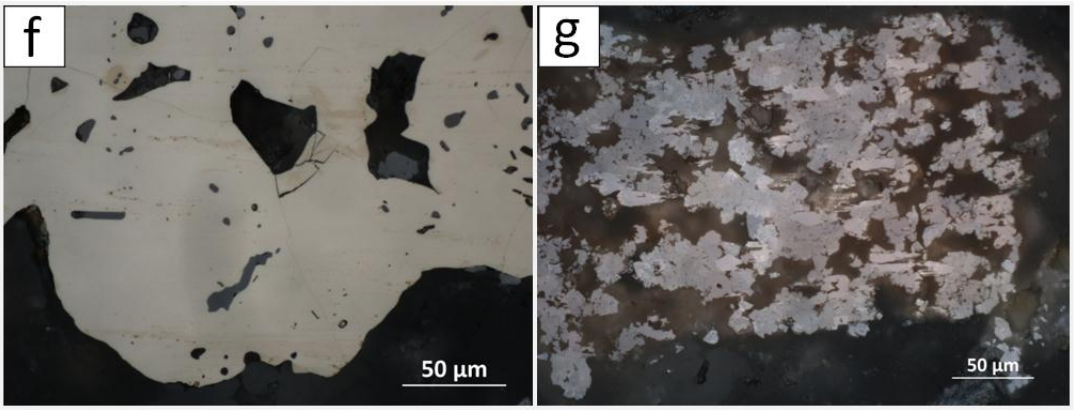

Figure 4.1-13: Bre-X8: (f) Close up view of pyrite clot in photographs d and e. The pyrite has many inclusions of gangue and a medium grey mineral; (g) Grain-shaped cluster of a light grey mineral with strong internal reflections (rutile or anatase).

The pyrite clots are especially inclusion-rich as shown in Figure 4.1-12e suggesting that they overgrew the gangue minerals. The pyrite in the veinlets is not highly fractured as is commonly seen in similar samples in this study. Inclusions of a medium grey mineral are present in some pyrite. Grain-shaped clusters of a light grey mineral with strong internal reflections (rutile) are present in the sample but minor overall.

The first generation of pyrite, which is subordinate in the sample, formed with few inclusions. It likely formed in open spaces or displaced minerals as it grew. The

second generation of pyrite likely formed around the pre-existing gangue minerals, trapping them as inclusions.

4.1.8 Bre-X9:

Sulfides occur in the sample as discontinuous dendritic veinlets <1 mm wide and as disseminated clots. The mineralization is predominantly pyrite with minor chalcopyrite. The sulfide veinlets are planar and discontinuous but branch outwards in a dendritic habit. There are two morphologically distinct generations of pyrite (pyrite-1,2). Chalcopyrite commonly has composite inclusions. Some of the second generation of pyrite has anisotropy and may have been altered to marcasite locally.

Two generations of pyrite are present in the sample. The first is typically euhedral with few inclusions and is highly fractured in the veinlets but not in the clots. The second generation is only in the veinlets and it has a distinct dendritic habit. It is inclusion-rich and has grown from the edges of the first generation of pyrite. This second generation locally shows anisotropy and might have been altered to marcasite (Fig. 4.1-14e). This pyrite has inclusions of a light grey mineral locally. The first generation of pyrite appears to have rare inclusions of chalcopyrite; however, this appearance may be an artifact of the two-dimensional thin section and the chalcopyrite may not be entirely within the pyrite. This is not conclusive textural evidence that chalcopyrite pre-dates the pyrite. Pyrite clots not connected with the veinlets are locally inclusion-rich but are locally euhedral and inclusion-free. Figure 4.1-15h shows a sulfide clot composed of a cluster of euhedral pyrite grains overgrown by chalcopyrite. A grey mineral occurs along the edges of the chalcopyrite locally.

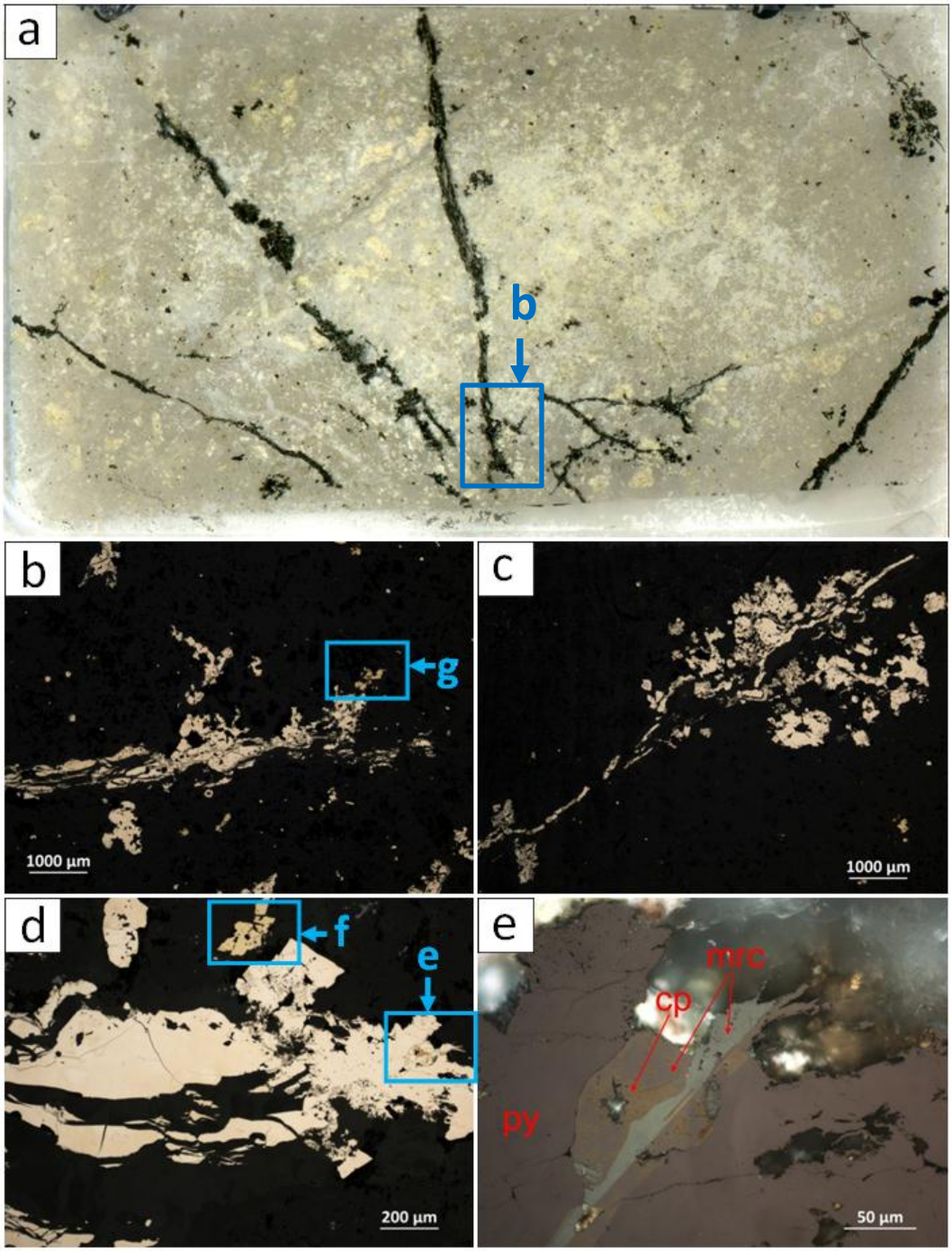

Figure 4.1-14: Bre-X9: (a) Scan of polished thin section Bre-X9 with the location of photographs indicated where appropriate; (b) Sulfide veinlet with two generations of pyrite and minor chalcopyrite; (c) Dendritic pyrite veinlet with two generations of pyrite. Dendritic pyrite clots extend from the veinlet; (d) Sulfide veinlet with two generations of pyrite and minor chalcopyrite; (e) Dendritic anisotropic mineral (marcasite) is hosted in chalcopyrite.

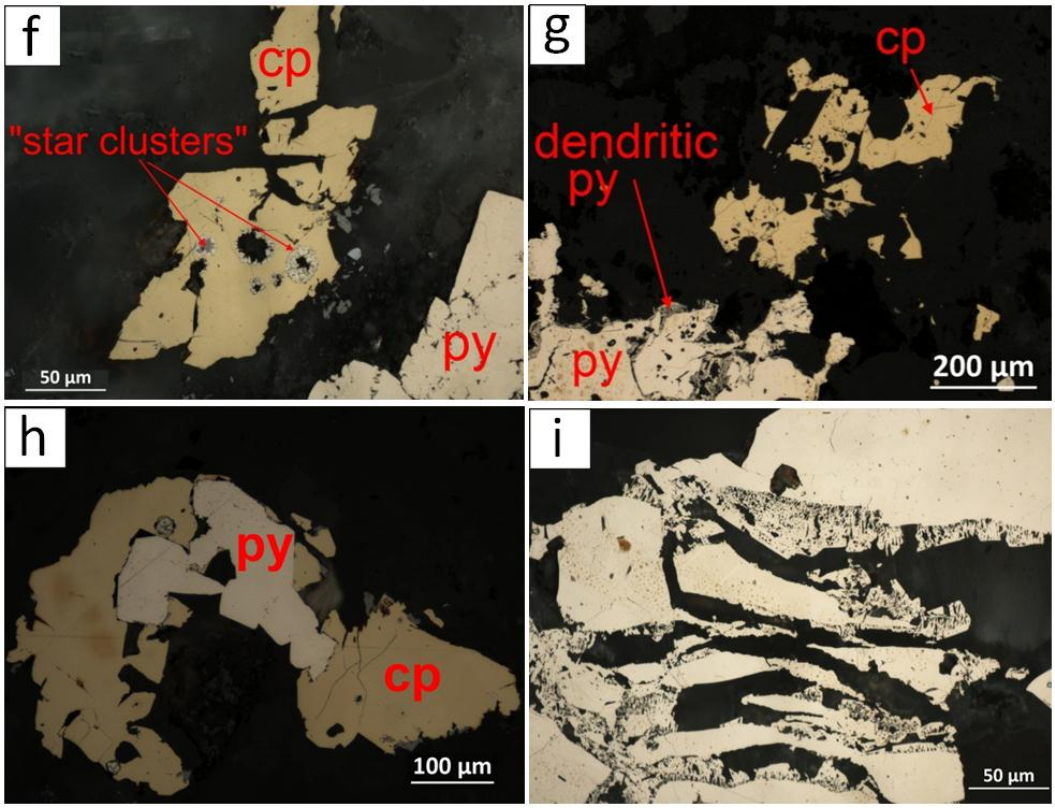

Figure 4.1-15: Bre-X9: (f) Chalcopyrite in veinlet with "star cluster" inclusions containing at least two ore minerals and sometimes gangue minerals; (g) Chalcopyrite and two generations of pyrite in sulfide veinlet; (h) Sulfide clot containing euhedral grains of pyrite overgrown by chalcopyrite. A minor grey mineral is also present around the edges of chalcopyrite; (i) Fractured first-generation pyrite with dendritic inclusion filled second-generation pyrite.

Chalcopyrite is locally present in the veinlets and clots. It is not fractured like the first generation of pyrite. Chalcopyrite often has composite "star cluster" inclusions. These are circular inclusions with a light yellowish mineral (likely pyrite or arsenopyrite) along the edges with a core of a light grey sulfosalt or gangue minerals (Fig. 4.1-15e).

4.1.9 Bre-X10

This sample is highly silicified and has many open-space cavities. Abundant sulfides are present in the form of clots and lesser disseminated isoated grains. The ore

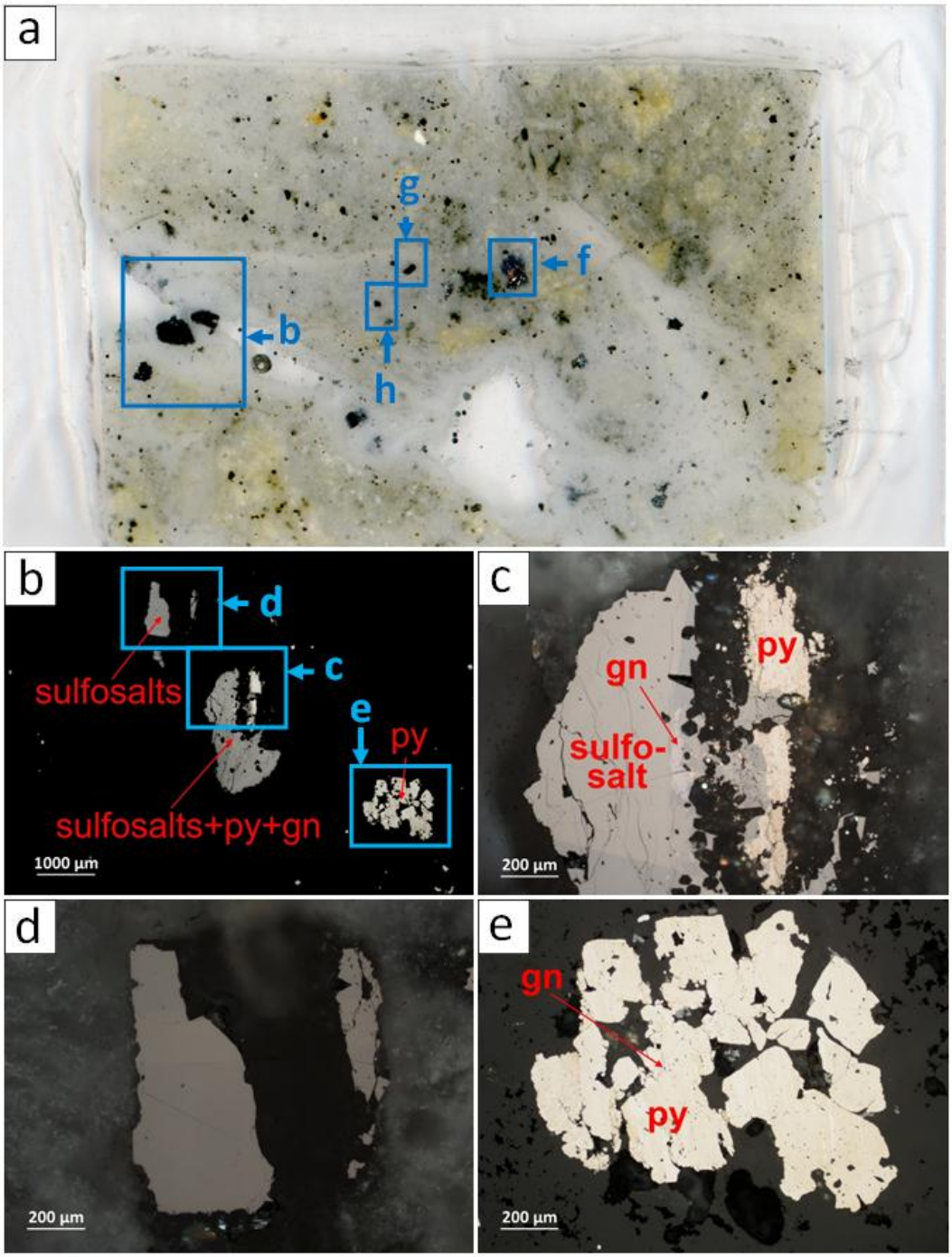

Figure 4.1-16: Bre-X10: (a) Scan of double-polished thin section Bre-X10B. Locations of reflected light photographs are indicated where appropriate; (b) Ore-minerals in vein material; (c) Pyrite, Sulfosalts, and minor galena in cross-polarized reflected light. Minor galena is included in the sulfosalt. Sulfosalt has distinct banded anisotropy with euhedral inclusions of quartz. Pyrite in this photo is an aggregate of smaller subrounded grains; (d) Sulfosalt with distinct anisotropy; (e) Cluster of pyrite grains with minor inclusions of galena. A grey mineral occurs locally along the edges of the pyrite. Some grains may be an aggregate of smaller subrounded pyrite. Pyrite contains many small inclusions of gangue.

minerals in this sample are pyrite, galena, and sulfosalts. The galena and sulfosalts appear to be spatially associated with the highly silicified areas whereas pyrite is ubiquitous throughout.

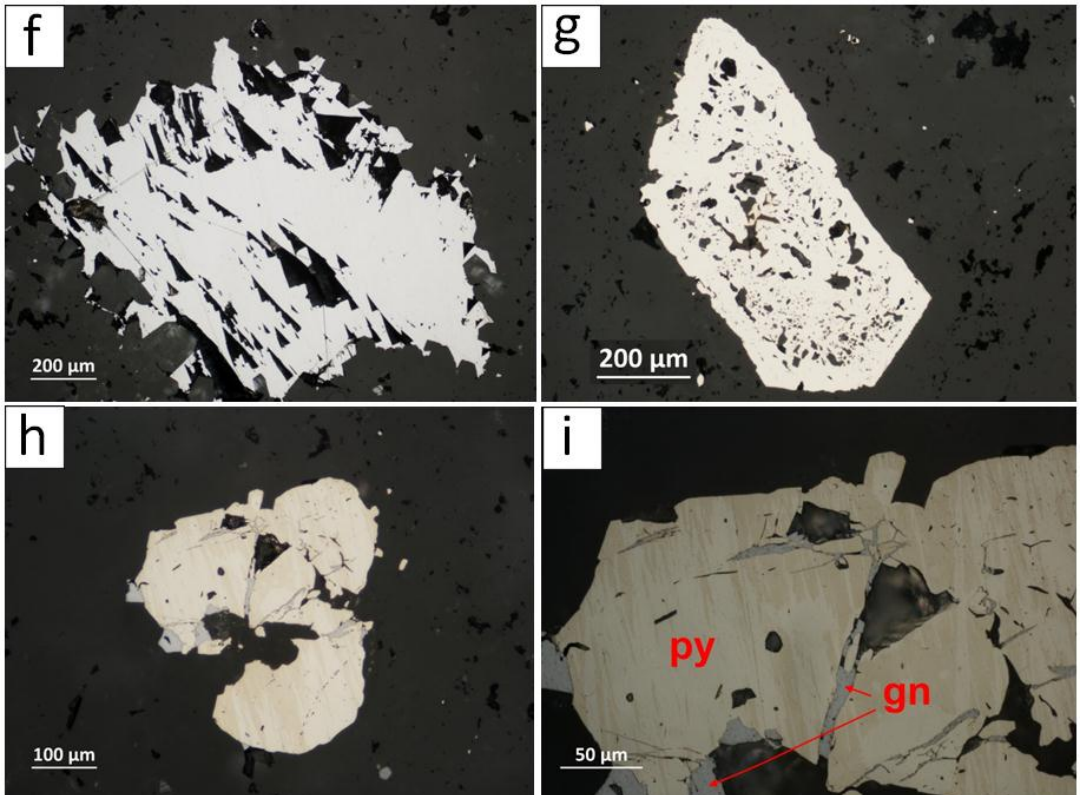

Figure 4.1-17: Bre-X10: (f) Coarse galena grain which has not been altered to a sulfosalt. (g) Inclusion-rich pyrite. Pyrite has an inclusions-free rim; (h,i) Pyrite with minor galena. Galena occurs along the edges of the pyrite, in fractures, and as elongated inclusions. Galena inclusions may indicate that pyrite continued to grow after galena deposition.

Pyrite in the sample tends to be euhedral and inclusion-rich. It occurs as isolated grains, clot-like clusters of grains, and as clusters in poly-metallic clots. Pyrite often has inclusions of galena as well as galena-filled fractures.

Galena is present adjacent to sulfosalts, as inclusions in pyrite, or as its own grains. The thin section contains one large galena grain shown in Figure 4.1-16f which has many triangular pits typical of galena.

The sulfosalts are present as distinct grains or in polymetallic clots with galena and pyrite. Sulfosalts have euhedral inclusions of gangue minerals and textures indicating that they formed interstitial to the gangue minerals, likely quartz. The sulfosalts have strong banded anisotropy.

4.1.10 Bre-X11

The sample is altered wall rock with a massive quartz vein containing polymetallic clots. These clots comprise sphalerite, pyrite, two sulfosalts, galena, and lesser chalcopyrite. The altered wall rock has abundant pyrite alteration as disseminated grains and clots as well as veinlets. Pyrite in the vein is euhedral and likely pre-dates the quartz vein or is coeval with it. Sphalerite either post-dates or is coeval with quartz and contains inclusions of chalcopyrite. Galena is likely coeval with sphalerite but predates the two sulfosalts.

Sphalerite is the most abundant ore mineral in the vein. It has an irregular contacts with the surrounding gangue minerals with no obvious textural clues as to which came first. It contains inclusions of euhedral pyrite which it likely overgrew. Inclusions of chalcopyrite in sphalerite are typically triangular reflecting the crystallographic structure of sphalerite suggesting co-precipitation. Galena is abundant in the vein and is interstitial to gangue minerals (quartz) but may be coeval with sphalerite. Two sulfosalts are present in the polymetallic clots and appear to be in reaction with galena (replacing galena). Sulfosalt 1 has a greenish tint and no anisotropy. Sulfosalt 2 has strong banded anisotropy and is likely bournonite-seligmannite (Fig. 4.1-18f).

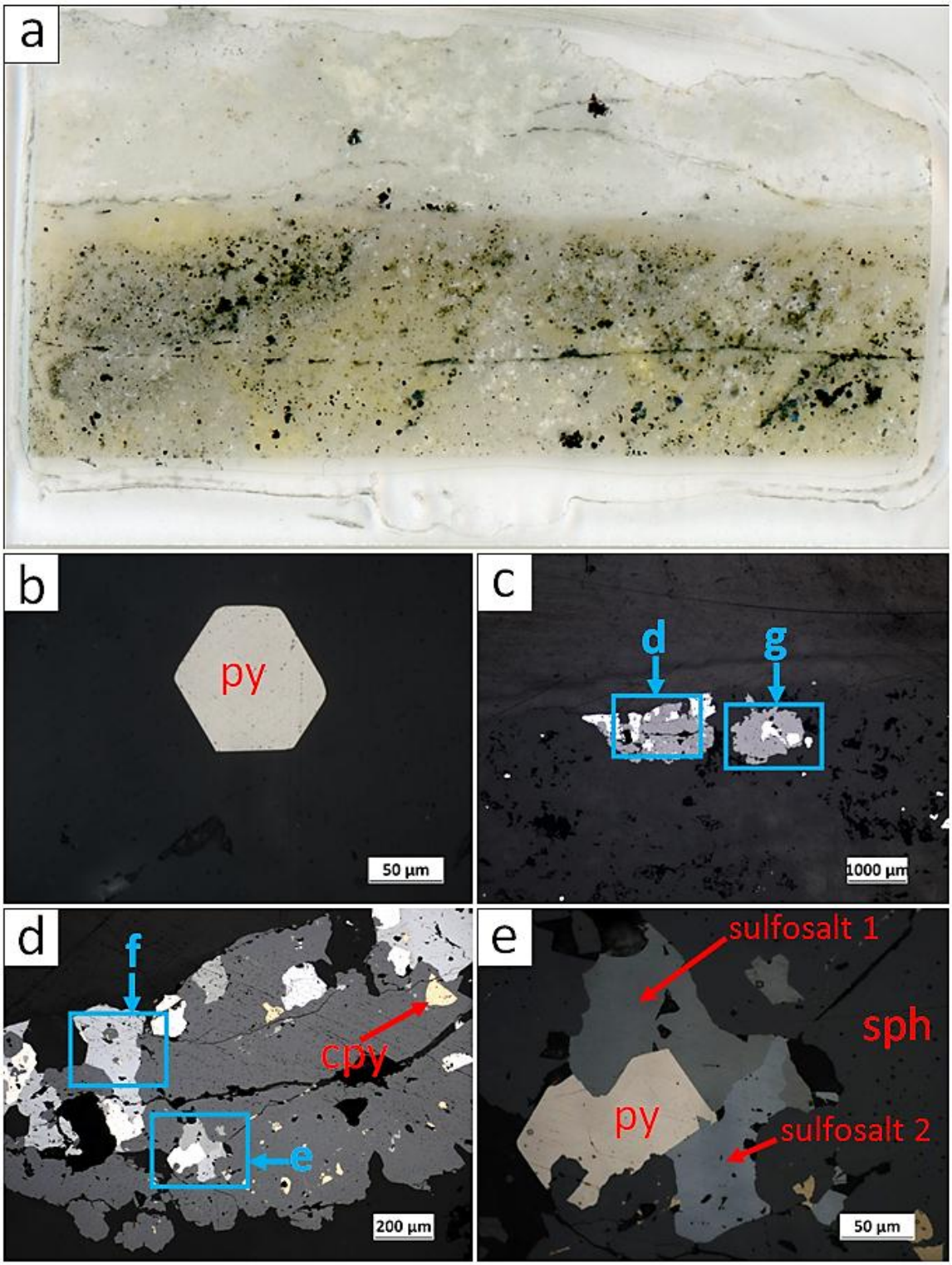

Figure 4.1-18: Bre-X11: (a) Scan of double-polished thin section Bre-X11B. Photographs were taken from thin section Bre-X11A which was destroyed to make chips for fluid inclusion analysis: (b) Euhedral pyrite which pre-dates quartz in vein; (c) Polymetallic clots in vein; (d) Close-up view of "c"; (e) Euhedral pyrite overgrown by sphalerite, and later by two sulfosalts. Chalcopyrite inclusions are also present in sphalerite.

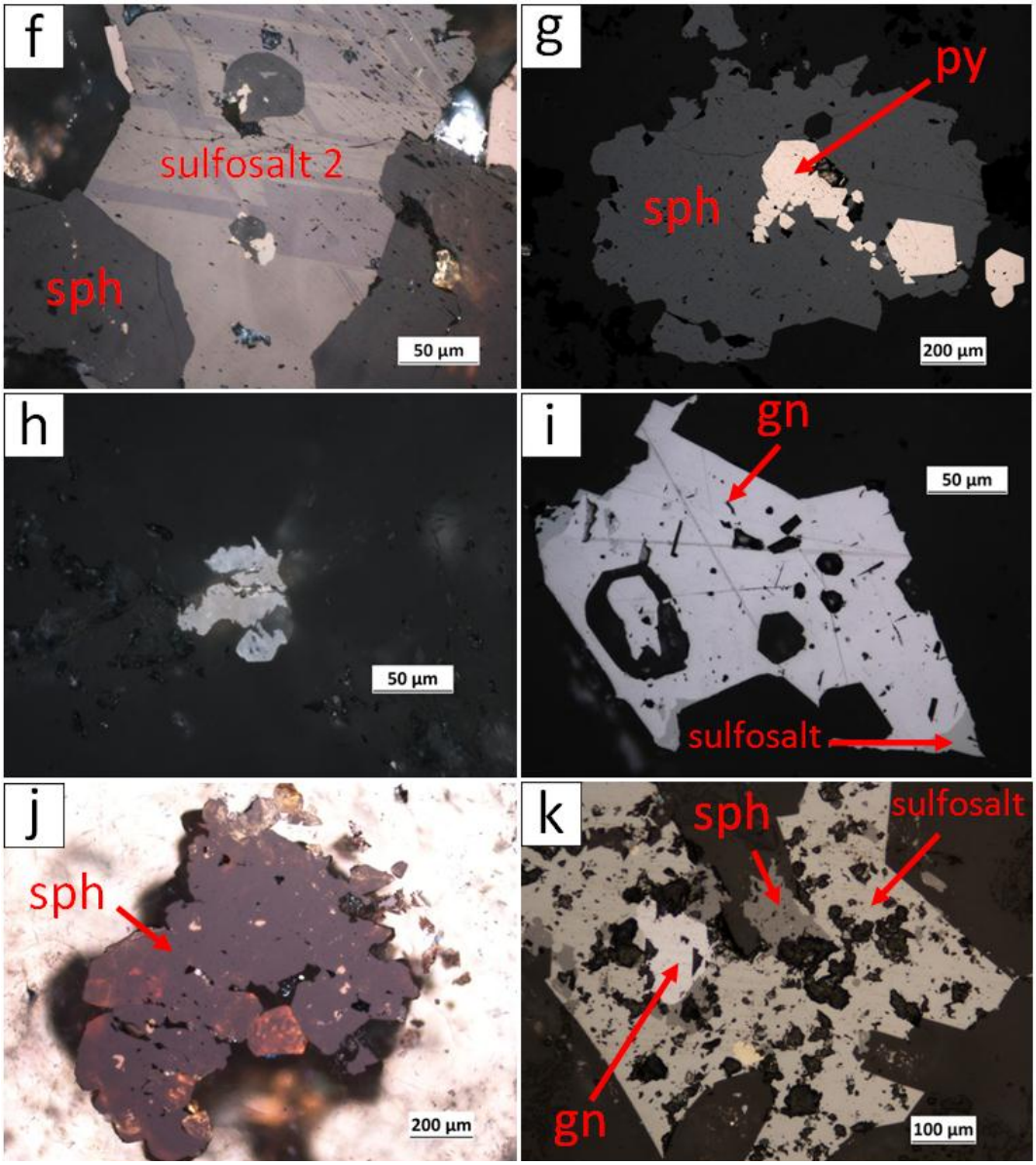

Figure 4.1-19: Bre-X11: (f) Sulfosalt (bournonite) with strong banded anisotropy; (g) Euhedral pyrite overgrown by sphalerite; (h) Light grey mineral with strong internal reflections; (i) Galena which has overgrown the gangue and is partially replaced by a sulfosalt; (j) Cluster of sphalerite grains with some internal reflections viewed in cross-polarized reflected light; (k) Sulfosalt interstitial to gangue overgrowing or replacing sphalerite, galena and chalcopyrite.

The altered wall rock has abundant pyrite as disseminated isolated grains and clots or as veinlets. This pyrite alteration does not occur in the vein and is typical of the wall rocks in the suite. This suggests that pyrite alteration occurred before the formation of the vein.

4.1.11 Bre-X12

The sample contains dendritic pyrite veinlets and lesser pyrite clots. The veinlets are commonly associated with inclusion-rich coarse pyrite grains. The veinlets approximately follow two orientations but are irregular and discontinuous. In places the veinlets appear to have formed along conjugate fracture sets having 60^{o} and 120^{o} angles of separation.

There appear to be at least two generations of pyrite in the sample. The first is in the center of the veinlets. It is inclusion-free and commonly fractured. The second forms its own veinlets or clots and also has formed along the edges of the first generation of pyrite. Many coarse inclusion-rich pyrite grains may represent the second generation of pyrite. These have inclusion-free rims.

Sulfides in the sample often shows strong anisotropy. It is probably that pyrite has altered to marcasite. Grain-shaped clusters of rutile are present in the sample which show strong orange internal reflections.

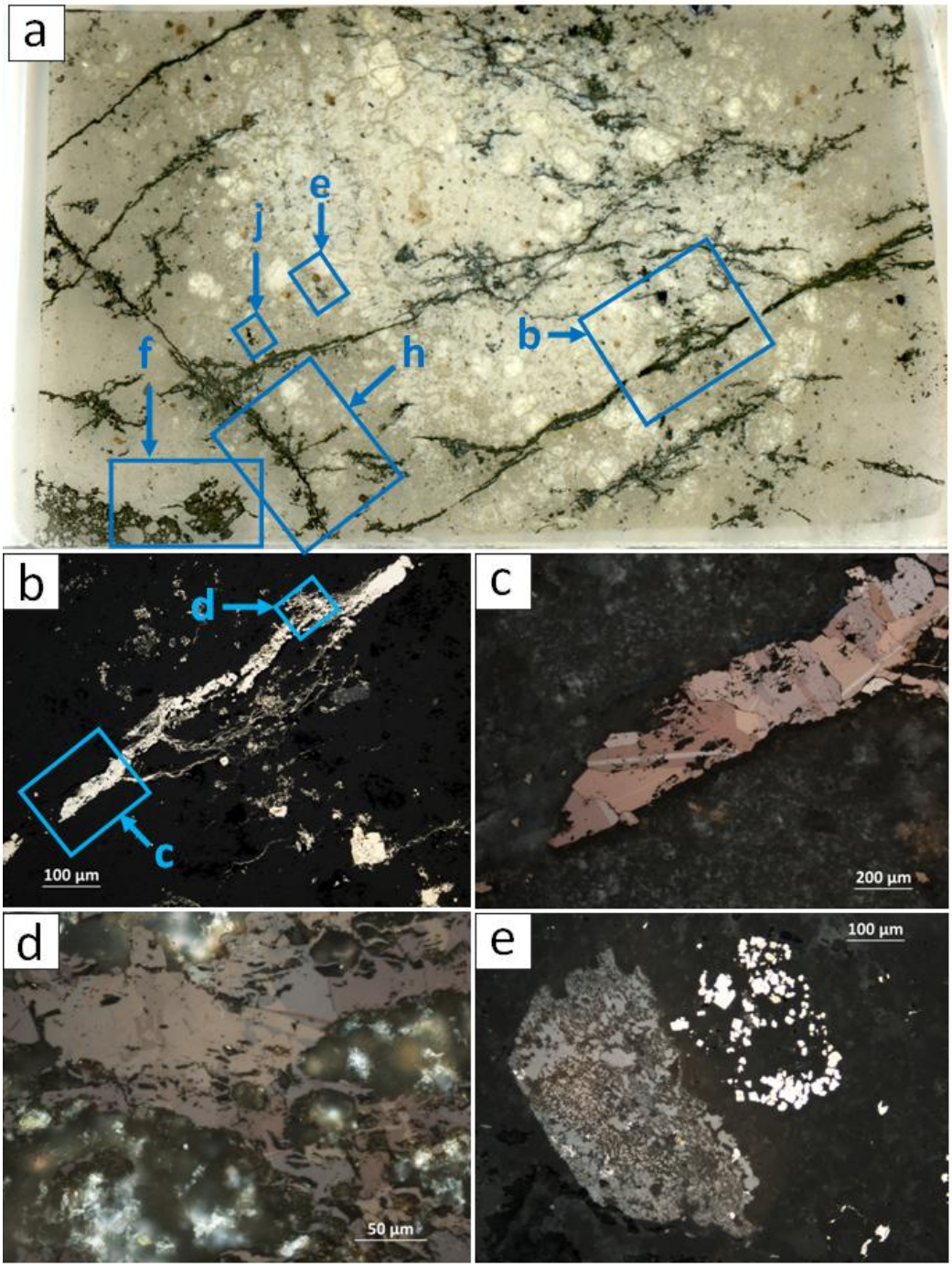

Figure 4.1-20: Bre-X12**:** (a) Scan of polished thin section Bre-X12 showing the location of photographs where appropriate. Dendritic sulfide veinlets are subparallel to two orientations; (b) Dendritic pyrite/marcasite veinlet with two generations of sulfides; (c) Close up view of photograph "b" in cross-polarized reflected light. Marcasite shows strong anisotropy; (d) Close-up of photograph "b" viewed in cross-polarized reflected light. Second generation of sulfides also shows anisotropy; (e) Grain shaped cluster of rutile with strong internal reflections next to a cluster of fine euhedral pyrite grains.

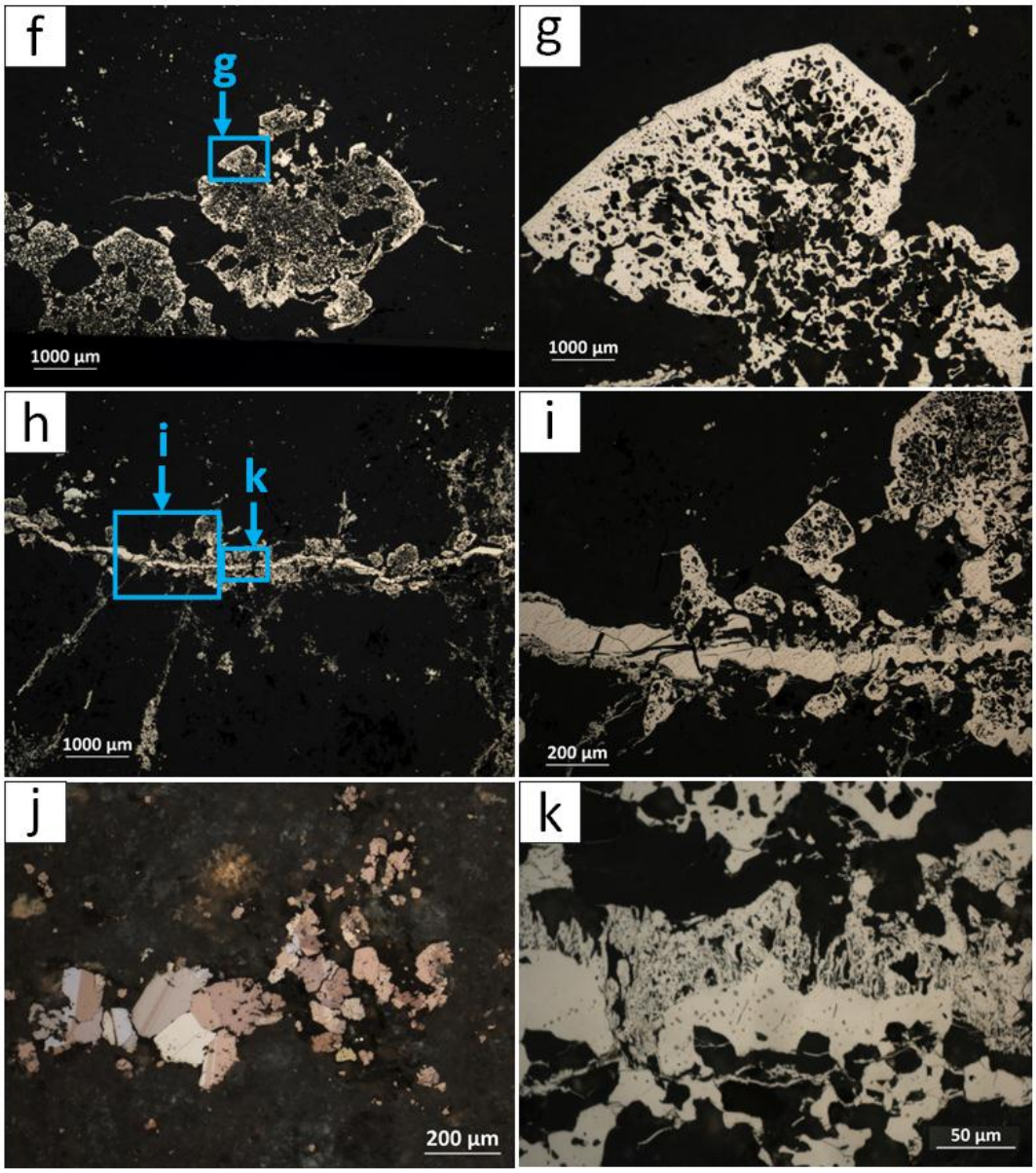

Figure 4.1-21: Bre-X12: (f) Inclusion-rich pyrite; (g) Close up of photograph "f". This clot has an inclusion-rich core and inclusion-free rims. (h) Pyrite veinlet with two generations of pyrite. The first generation is inclusion-free and fractured. The second generation of pyrite has formed on the rims of the first and is dendritic and inclusion-rich. This second generation of pyrite may have formed the inclusion-rich grains near the veinlet; (i) Close up view of photograph h; (j) Marcasite clot viewed in cross-polarized reflected light. Note the strong anisotropy; (k) Close up view of photograph "h". Note the dendritic pyrite which has formed from the rims of the original pyrite in the veinlet.

4.3 Summary of descriptions

Results from microscopy are summarized in table 4.3-1. Bre-X samples appear as altered porphyritic and non-porphyritic andesites to dacites. Geochemical classifications indicate they are actually basaltic andesites to andesites to; this is likely more accurate given the highly altered nature of the rocks.

Two mains styles of alteration are present: phyllic, and propylitic. Phyllic alteration is marked by quartz, sericite, and pyrite alteration in the wall rock. Propylitic alteration is marked by chlorite, epidote, and calcite alteration in the wall rock and in veins. Bre-X samples from deeper levels as indicated by drillcore depth are sub-volcanic whereas in upper levels (sample Bre-X3) there are polymictic breccias with igneous and sedimentary clasts. Leach (2001) refers to hydrothermal breccias being present at Busang and therefore sample Bre-X3 could be of hydrothermal origin; however, it must have been relatively impermeable to explain the lack of mineralization in this sample. Alteration appears to be regional and is not often associated with hand-specimen scale structures. From textural relationships it is not possible to constrain the relative timing of the phyllic and propyrlitic alterations.

It appears that some silicification occurs along fractures and in veins which texturally post-dates the original alteration. This silicicification was then followed by base metal deposition and minor carbonates. The stratification of veins was used to constrain this timing; good examples are Bre-X1 (Figure 4.1-1) and Bre-X2 (Figure 4.1-2).

Table 4.3-1: Summary of observations

DDH No.	Depth (m)	Sample	Protolith	Gangue Minerals		Ore Minerals		Textures
				Wall-rock Alteration	Veins	Disseminated	Veins/Stringers	
BSSE-1	192.5	Bre-X1	Porphyritic andesite	Quartz (a), sericite (a), calcite (m), epidote (vm)	Quartz (a), calcite (a), sericite (m), gyp/anh (vm)	Pyrite (a), rutile (vm)	Sphalerite (a), pyrite (m), galena(m), sulfosalts (m), chalcopyrite (m)	Crudely banded veins, massive quartz
BSSE-1	309.5	Bre-X2	Porphyritic andesite	Quartz (a), sericite (a), calcite (a)	Calcite (a), quartz (m), sericite (vm), gyp/anh (vm)	Pyrite (a), rutile (vm)	Sphalerite (a), pyrite (a), galena(m), calcopyrite (m)	Crudely Banded veins
BSSE-2	42	Bre-X3	Polymictic breccia	Sericite (m), quartz (m), carbonate (vm)	Calcite (a)	Pyrite (m), rutile (vm)	Pyrite (vm)	Brecciation (angular and rounded clasts)
BSSE-2	301	Bre-X4	Porphyritic andesite	Quartz (a), sericite (a), calcite (vm)	Calcite (a), quartz (vm)	Pyrite (a), rutile (vm)	Pyrite (a)	Alteration halos, massive veins
BSSE-2	329	Bre-X5	Porphyritic andesite	Quartz (a), sericite (a), calcite (vm)	calcite (a), quartz (m)	Pyrite (a)	N/A	Stringers, veinlets, alteration halos
BSSE-295	235.75	Bre-X6	Porphyritic andesite with volcanic infill	Quartz (a), sericite (a), calcite (vm)	Calcite (a), quartz (vm)	Pyrite (a), rutile (vm), sphalerite	N/A	Fractures, brecciation, drusy cavities/vugs, volcanic in-fill
BSSE-295	368	Bre-X7	Basaltic andesite	Chlorite (a), sericite (a), quartz (m), calcite (m)	Calcite/quartz (a)	Pyrite (a), rutile (vm)	Pyrite (a)	Expansion veinlets
BSSE-333	154	Bre-X8	Porphyritic andesite	Quartz (a), sericite/muscovite (a), calcite (m)	N/A	Pyrite (a), rutile (vm)	Pyrite (a)	Dendritic stringers and clots, discrete alteration domains
BSSE-333	272	Bre-X9	Porphyritic andesite	Quartz (a), sericite (a)	N/A	Pyrite (m), rutile (vm)	Pyrite-1 (a), pyrite-2 (m), chalcopyrite (m)	Dendritic stringers, stockwork veinlets
BSSE-333	286	Bre-X10	(±Porphyritic) andesite	Quartz (a), sericite (a)	Quartz (a)	Pyrite (a), rutile (vm)	Sulfosalts (m), galena (m), pyrite (vm)	Massive quartz, drusy cavities, silicified domains
BSSE-333	308	Bre-X11	(±Porphyritic) andesite	Quartz (a), sericite (a)	Quartz (a)	Pyrite (a), rutile (vm)	Shalerite (a), Sulfosalts (m), galena (m), pyrite (vm)	Massive/crudely banded quartz veins, veinlents, drusy cavities
BSSE-333	396	Bre-X12	Porphyritic andesite	Quartz (a), sericite (a)	N/A	Pyrite (m), marcasite(m), rutile (vm)	Pyrite-1 (a), marcasite (a), pyrite-2 (m)	Dendritic stringers, stockwork veinlets

Ore-microscopy identified ore minerals in quartz-carbonate-base metal veins and in stockwork veins. Quartz-carbonate-base metal veins contain pyrite sphalerite, sulfosalts, lesser galena, and minor chalcopyrite as clots or seams. Stockwork veins contain two generations of pyrite and lesser chalcopyrite. In stockworks chalcopyrite has fine composite inclusions comprising a yellow mineral and a rim of a grey mineral (Fig. 4.1-15f). No discrete Au or Ag minerals were identified in any of the sections.

Chapter 5: Geochemistry

Whole-rock geochemical analysis was performed on Bre-X samples to classify the host rocks, characterize alteration, distinguish between high- and low-sulfidation mineralization styles, and to qualitatively assess gold and silver abundance. Geochemistry of Bre-X samples was compared with that of typical volcanic rocks in Kalimantan. Raw geochemical data are given Table 5.2-1a,b.

Following whole-rock analyses, the scanning electron microprobe (SEM) was used to map element distributions and to determine which minerals are responsible for geochemical anomalies. Precious metals gold and silver were quantified using wave-dispersive spectroscopy (WDS) to better understand the mineralizing event(s).

5.1 Methods

Eight samples were sent for whole-rock geochemical analysis at Act-Labs in Ancaster, Ontario. Five samples represented altered wall rock and three samples were of vein material. Samples were analyzed for major elements and trace elements, including rare earth elements (REEs).

Wall rock samples were chosen to be representative of lithology and alteration styles. Slabs for analysis were cut containing as few vein(let)s as possible, and cleaned to avoid contamination from the diamond saw. Vein samples were chosen where vein material was abundant enough to get a sample without destroying the rest of the sample. Desire to preserve archival material from these small specimens restricts the representativeness of the whole-rock analyses. Methods used by Actlabs are shown in

table 5.1 and further explained below in sections 5.1.1-7. Procedures were acquired from the brochure in Actlab's website (see references).

Scanning electron microprobe (SEM) analysis was performed at Dalhousie University, Halifax, NS. The machine is a JEOL 8200 microprobe operated by technologist Dr. D. Macdonald. Element maps were made of select ore-minerals on several scales to confirm microscopy and search for precious metals. Subsequent Wave dispersive Spectroscopy (WDS) quantitative point analyses were carried out to assign a concentration to regions in the element maps. Energy-dispersive spectroscopy (EDS) was used on points to qualitatively confirm microscopy and determine the constituent elements in carbonates.

Abbreviation	Analytical Method Name
PPXRF	Pressed Pellet X-Ray Fluorescence
INAA	Instrument Neutron Activation Analysis
FUS-MS	Fusion Mass Spectrometry
FUS-ICP	Fusion Inductively Coupled Plasma
TD-ICP	Total Digestion Inductively Coupled Plasma
IR	Infrared
TITR	Titration
GRAV	Gravimetric

Table 5.1-1: Analytical methods used by Actlabs. (Actlabs 2013, refer to brochure)

5.1.1 Pressed pellet X-ray fluorescence:

This method is useful for major and trace elements and is particularly sensitive for Large Ion Lithophile Elements (LILE), transition metals and some High Field Strength Elements (HFSE) such as Nb, Zr, and Y. Here primary X-rays excite the sample and cause

the emission of characteristic secondary X-rays which are measured. The intensity of the emitted X-ray is proportional to the concentration of the element. The sample is prepared as a pressed pellet of powder from 6 g of sample. This method is favoured due to its low detection limit and its ability to compensate for some heterogeneity in samples.

5.1.2 Instrument neutron activation analysis

This method is versatile and able to measure a large number of elements simultaneously. It is sensitive for REEs, HFSE, and platinum group elements. For major elements 0.2 g of sample is fused to a graphite crucible and dissolved in acid. For base metals and trace elements 0.25 g of the sample is digested in acid and dried. The prepared samples are irradiated with a low thermal flux and allowed to decay for seven days. Radioactive isotopes emit gamma radiation which is measured. This method can measure many elements with low detection limits, but it does not account well for heterogeneity in samples using only a small subsample for measurements.

5.1.3 Fusion Inductively Coupled Plasma Mass Spectrometry

For major elements and selected trace elements 0.2 g of sample is fused to a graphite crucible and dissolved in acid. Here fused samples are diluted and analysed by mass spectrometry.

5.1.4 Total Dissolved Inductively Coupled Plasma Mass Spectrometry

For base metals and trace elements 0.25 g the sample is digested in four acids and dried. Sample is re-dissolved in acid and analysed by mass spectrometry. This

method is not used for silver which was above detection limits. Ti values may be suspect as phases such as sphene and rutile may not fully dissolve.

5.1.5 Infrared

This method is used to analyse volatiles sulfur and carbon. About 0.2 g of sample is combusted in pure oxygen. Sulfur and carbon are reduced and bind to oxygen. Sulfur and carbon oxides absorb specific infrared wavelengths which are measured.

5.1.6 Titration

This method determines FeO. The sample is digested in acid and the extent of dissolution is affected by Fe^{3+} content. It is then titrated using potassium dichromate.

5.1.7 Gravimetric

This method distinguished between moisture (H_20-) and interstitial water (H_2O+). Moisture is released at 110^oC and interstitial water at 1000^oC. H_2O at each temperature is measured by the infrared light it absorbs. 0.3 g of sample is used for this measurement.

5.1.8 Scanning electron microprobe

The WDS analyses were performed accounting for 14 elements: Au, Ag, As, Se, Fe, Pb, Sb, Cu, Bi, S, Zn, Hg, Cd, and Te. The SEM was run with a probe diameter of 1 μm and a probe current of 2.000e^{-8} A. Seven elements were mapped: Au, Ag, As, Pb, Cu, Sb, and S.

5.2 Rock Type Classification

Petrographic classification of the rock samples under the microscope is difficult because they are very fine-grained and altered. Figure 5.2-2 shows the analyses plotted in a classification diagram by Peccerillo and Taylor (1976), together with geochemical data for volcanic rocks from the Kalimantan volcanic belt compiled in Soeria-Atmadja et al. (1999) (Legend in Figure 5.2-1 is used in all further plots in this chapter). In terms of their silica content, the Bre-X rocks range in composition from andesite to rhyolite, but the spread in K_2O suggests that this is not their original igneous composition but that they have been altered, and the alkalis mobilized. The compositions shown for the Kalimantan volcanic belt samples cannot be igneous either, and they must have been extensively altered. Hence relatively immobile elements must be considered, and the samples are plotted in a Nb/Y vs. Zr/TiO_2 plot proposed by Winchester and Floyd (1997) (Fig. 2.2-2b).

Major elements normalized to be volatile-free are plotted below following Peccerillo and Taylor (1976). The host-rock samples plot as andesite-rhyolite in the tholeiitic, calc-alkaline, high-K calc-alkaline series. The vein samples plot as dacite-rhyolite of the calc-alkaline series. Sample Bre-X10 did not plot within the boundaries of the graph due to its very high silica content (~80%) in quartz veinlets.

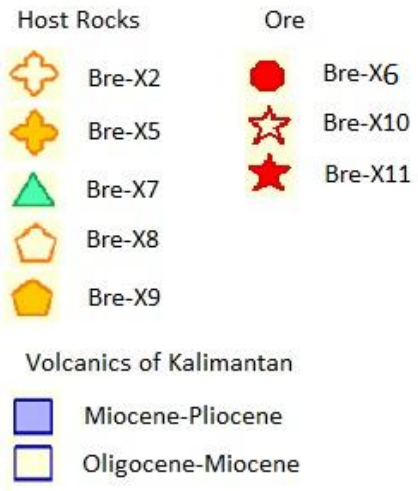

Figure 5.2-1: Legend of samples for geochemical analysis (used herein). "Ore" samples are principally vein material. Data for the volcanics of Kalimantan are from Soeria-Atmadja et al., (1999).

Immobile elements were plotted following Winchester and Floyd (1997). Here Bre-X samples plot as andesite to basaltic andesite and follow a trend consistent with the Oligocene-Miocene volcanic rocks of Kalimantan. The elements Nb, Y, and Zr are generally contained in refractory minerals like zircon which are not affected by alteration. Ti contained in sphene (titanite) is relatively immobile as it converts to rutile or anatase but stays in place.

5.2.1 Igneous Petrology

Harker plots were made to visualize the effects of alteration on the major elements (Fig. 5.3-3). Bre-X10 has silica content too high to display. The samples appear to be consistent with the volcanic rocks of Kalimantan, but it is likely the Kalimantan rocks have been altered in view of their erratic alkali contents. REE plots provide clues to the origin of the host rocks in the BSSE Zone.

Analyte Symbol	Unit Symbol	Detection Limit	Analysis Method	BREX-2	BREX-5	BREX-6	BREX-7	BREX-8	BREX-9	BREX-10	BREX-11
Ga	ppm	5	PPXRF	15	15	22	12	11	14	< 5	11
Pb	ppm	5	PPXRF	44	6	167	13	57	24	1300	263
Sn	ppm	5	PPXRF	< 5	< 5	< 5	< 5	6	5	< 5	< 5
Nb	ppm	1	PPXRF	2	2	2	1	2	2	< 1	2
Rb	ppm	2	PPXRF	51	62	52	54	137	13	43	111
C-Total	%	0.01	IR	1.83	0.29	1.5	1.1	1.27	0.55	0.27	0.2
Total S	%	0.01	IR	2.53	4.78	4.6	3.17	5.09	2.12	1.53	3.03
Cl	%	0.01	INAA	0.01	0.02	0.03	0.01	< 0.01	< 0.01	< 0.01	0.01
Mass	g		INAA	1.05	1.01	1.03	1.02	1.01	1.04	1.02	1.02
CO2	%	0.01	IR	6.52	0.96	5.37	3.95	4.49	1.94	0.97	0.71
FeO	%	0.1	TITR	2.7	3.5	4.5	3	2.9	4.1	0.4	3.5
H2O+	%	0.1	GRAV	4.9	4.5	1.2	3.5	2.1	2.5	1.3	2
H2O-	%	0.1	GRAV	1.4	0.8	0.4	1	0.6	0.7	0.5	0.6
SiO2	%	0.01	FUS-ICP	52.91	60.86	57.36	63.75	57.8	55.97	80.87	68.61
Al2O3	%	0.01	FUS-ICP	16.99	17.07	13.3	14.24	14.3	17.3	8.21	14.41
Fe2O3	%	0.01	FUS-ICP	1.12	2.72	1.98	1.28	3.67	2.31	2.1	0.9
MnO	%	0.001	FUS-ICP	0.133	0.054	0.193	0.111	0.291	0.377	0.393	0.163
MgO	%	0.01	FUS-ICP	1.02	0.44	3.4	0.63	2.33	3.04	0.52	0.86
CaO	%	0.01	FUS-ICP	7.4	1.38	3.92	4.77	3.42	6.27	0.84	0.68
Na2O	%	0.01	FUS-ICP	0.31	0.13	0.34	0.42	0.13	2.49	0.11	0.17
K2O	%	0.01	FUS-ICP	1.57	2.02	1.99	1.39	3.93	0.42	2.15	3.86
TiO2	%	0.001	FUS-ICP	0.622	0.603	0.46	0.318	0.484	0.625	0.185	0.343
P2O5	%	0.01	FUS-ICP	0.13	0.14	0.08	0.1	0.11	0.12	0.04	0.09
LOI	%		FUS-ICP	13.93	9.35	10.68	10.27	9.44	6.23	3.71	5.47
LOI2	%		FUS-ICP	13.63	8.96	10.17	9.93	9.11	5.77	3.67	5.08
Total 2	%	0.01	FUS-ICP	98.83	98.28	98.19	100.3	98.8	99.26	99.54	99.05
Total	%	0.01	FUS-ICP	99.14	98.67	98.7	100.6	99.12	99.71	99.58	99.45
Au	ppb	1	INAA	14	8	74	139	20	14	32	47
Ag	ppm	0.5	MULT INAA / TD-ICP	< 0.5	< 0.5	2.4	0.9	< 0.5	< 0.5	1.6	6.8
As	ppm	1	INAA	16	24	185	75	33	24	70	77
Ba	ppm	1	FUS-ICP	100	160	228	145	380	182	185	467
Be	ppm	1	FUS-ICP	1	< 1	2	< 1	< 1	< 1	< 1	< 1
Bi	ppm	0.1	FUS-MS	0.1	0.4	2.1	< 0.1	0.4	0.1	0.5	1.6
Br	ppm	0.5	INAA	< 0.5	1.6	< 0.5	1.4	1.1	< 0.5	1.1	< 0.5
Cd	ppm	0.5	TD-ICP	< 0.5	< 0.5	< 0.5	0.7	1.5	< 0.5	< 0.5	< 0.5
Co	ppm	0.1	INAA	12.3	18.1	15	9.3	16.2	14.8	5.7	8.3
Cr	ppm	0.5	INAA	11	16.2	28.4	19.2	10.7	9.9	12.6	28.9
Cs	ppm	0.1	FUS-MS	9.7	5.8	2.8	8.7	9.4	6.8	4.6	6.7
Cu	ppm	1	TD-ICP	25	13	17	1140	15	69	122	211
Ga	ppm	1	FUS-MS	16	15	25	13	13	15	7	14

Table 5.2-1(a): Analytical data from Actlabs. The unit symbol, detection limit, and analytical methods for each element are shown.

Analyte Symbol	Unit Symbol	Detection Limit	Analysis Method	BREX-2	BREX-5	BREX-6	BREX-7	BREX-8	BREX-9	BREX-10	BREX-11
Ge	ppm	0.5	FUS-MS	1.9	3.6	2.8	0.9	< 0.5	0.8	1.3	< 0.5
Hf	ppm	0.1	FUS-MS	2.2	3	1.8	2	2.2	2.4	1.5	2.1
Hg	ppm	1	INAA	< 1	2	< 1	< 1	< 1	< 1	< 1	< 1
In	ppm	0.1	FUS-MS	< 0.1	< 0.1	< 0.1	< 0.1	< 0.1	< 0.1	< 0.1	< 0.1
Ir	ppb	1	INAA	< 1	< 1	< 1	< 1	< 1	< 1	< 1	< 1
Mo	ppm	2	FUS-MS	< 2	< 2	2	19	2	< 2	6	< 2
Nb	ppm	0.2	FUS-MS	3.3	3.8	2.6	2.6	3.1	2.7	6.8	2.3
Ni	ppm	1	TD-ICP	8	9	11	10	4	6	13	8
Pb	ppm	5	TD-ICP	39	< 5	157	9	55	27	1420	285
Rb	ppm	1	FUS-MS	51	61	56	52	144	10	74	123
S	%	0.001	TD-ICP	2.67	5.21	4.93	3.38	5.13	2.05	1.66	3.37
Sb	ppm	0.1	INAA	4.1	2.9	9	1.3	6	4.2	117	81.5
Sc	ppm	0.01	INAA	14.7	13.3	12.6	7.9	11.7	14.1	3.57	11.6
Se	ppm	0.5	INAA	< 0.5	< 0.5	5.4	14.6	10.2	< 0.5	17.4	4.9
Sn	ppm	1	FUS-MS	3	3	2	1	2	< 1	< 1	3
Sr	ppm	2	FUS-ICP	94	37	63	101	51	262	24	30
Ta	ppm	0.01	FUS-MS	0.2	0.24	0.14	0.15	0.19	0.2	0.11	0.15
Th	ppm	0.05	FUS-MS	3.47	4.54	2.73	2.63	4.17	3.07	1.46	2.8
U	ppm	0.01	FUS-MS	0.85	1.07	1.04	0.65	0.94	0.73	0.41	0.74
V	ppm	5	FUS-ICP	160	123	124	67	119	145	32	96
W	ppm	1	INAA	< 1	3	< 1	< 1	< 1	< 1	< 1	< 1
Y	ppm	1	FUS-ICP	16	15	15	9	12	13	4	6
Zn	ppm	1	MULT INAA / TD-ICP	29	8	35	98	215	112	41	59
Zr	ppm	1	FUS-MS	87	114	65	80	85	83	65	84
La	ppm	0.05	FUS-MS	9.24	9.29	4.41	7.47	10.2	8.22	2.73	4.14
Ce	ppm	0.05	FUS-MS	19.9	19.5	10.4	14.7	20.1	18.1	4.77	8.41
Pr	ppm	0.01	FUS-MS	2.41	2.28	1.27	1.55	2.25	2.21	0.59	0.95
Nd	ppm	0.05	FUS-MS	10.3	8.91	5.44	5.93	8.68	9.36	2.3	3.56
Sm	ppm	0.01	FUS-MS	2.41	2.18	1.32	1.29	1.82	2.11	0.61	0.81
Eu	ppm	0.005	FUS-MS	0.685	0.704	0.261	0.55	0.588	0.725	0.193	0.208
Gd	ppm	0.01	FUS-MS	2.69	2.43	1.73	1.31	2.02	2.13	0.61	0.97
Tb	ppm	0.01	FUS-MS	0.44	0.44	0.35	0.22	0.33	0.38	0.11	0.17
Dy	ppm	0.01	FUS-MS	2.7	2.76	2.37	1.33	2.01	2.41	0.71	1.04
Ho	ppm	0.01	FUS-MS	0.57	0.59	0.53	0.28	0.42	0.5	0.15	0.22
Er	ppm	0.01	FUS-MS	1.78	1.77	1.62	0.84	1.26	1.54	0.5	0.68
Tl	ppm	0.05	FUS-MS	0.41	0.61	0.66	0.74	2.04	0.38	1.08	1.8
Tm	ppm	0.005	FUS-MS	0.272	0.266	0.239	0.125	0.187	0.231	0.076	0.11
Yb	ppm	0.01	FUS-MS	1.83	1.75	1.6	0.85	1.24	1.58	0.53	0.78
Lu	ppm	0.002	FUS-MS	0.3	0.29	0.258	0.141	0.207	0.284	0.089	0.138
Mass	g		INAA	1.007	1.011	1.008	1.038	1.016	1.062	1.024	1.021

Table 5.2-1(b): Analytical data from Actlabs. The unit symbol, detection limit, and analytical methods for each element are shown.

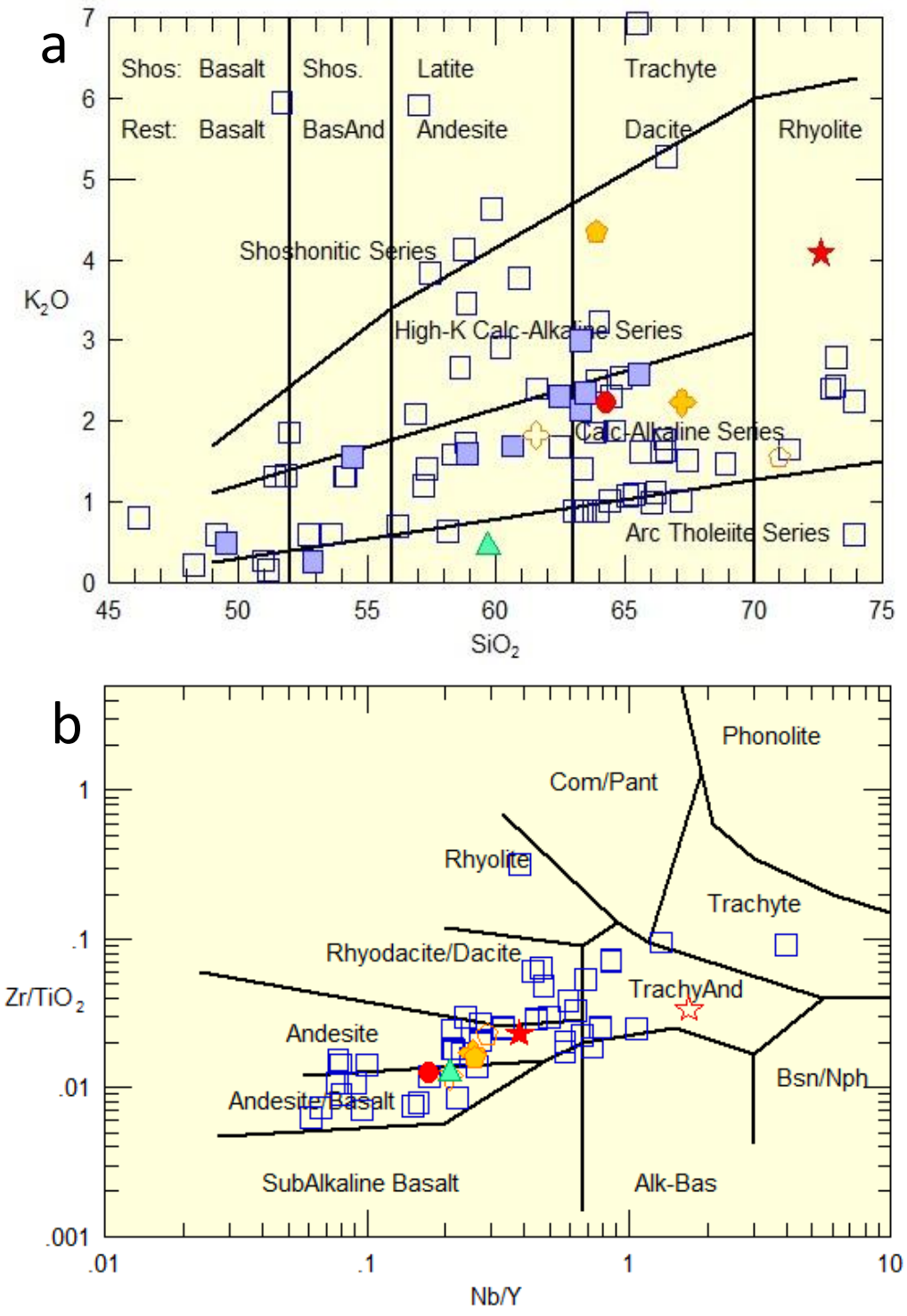

Figure 5.2-2: (a) Alkalis element plot following Peccerillo and Taylor (1976); (b) Immobile element plot following Winchester and Floyd (1997); Volcanic rocks from Kalimantan of and Oligocene-Miocene age are plotted based on data from Soeria-Atmadja et al. (1999) where it exists.

The REE abundances show a small enrichment in light REEs (LREE) and only a small fractionation of heavy REEs (HREE), typical of calc-alkaline rocks of island arc settings (Fig. 5.2-3). The relatively flat slope may be related to amphibole fractionation, but is notably flatter than in continental arcs such as the Andes. Only two samples show a minor Eu-depletion, reflecting feldspar fractionation. The REE contents are compatible with a formation by partial melting of spinel peridotite (e.g. Dostal et al., 1977). Two of the vein samples (red stars) have a relatively lower overall abundance of REE, but essentially the same slope. This behaviour is likely due to dilution by REE-free quartz present in veinlets in these samples (Zentilli, Marcos., per. comm., 2013).

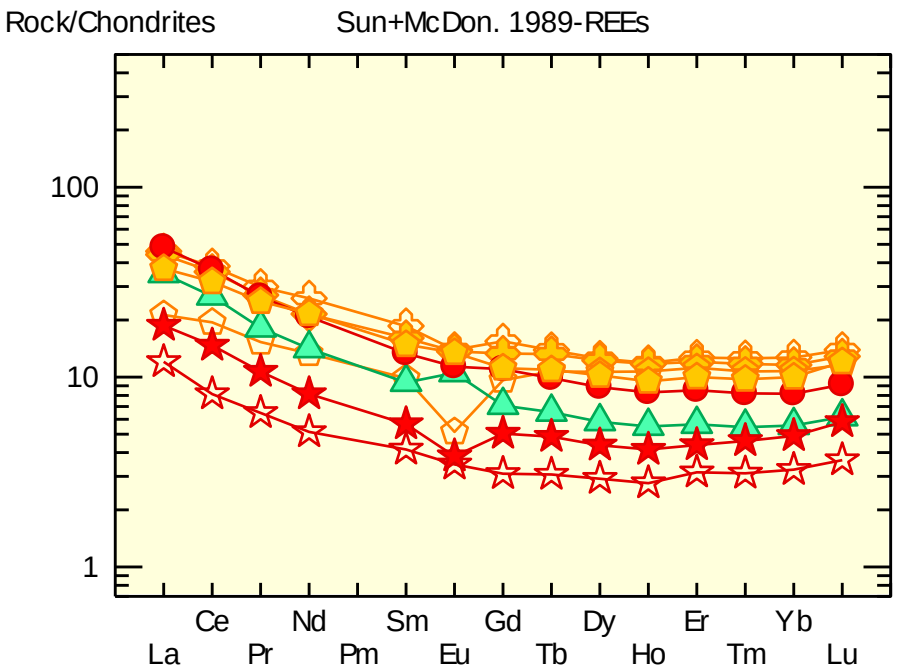

Figure 5.2-3: Spider diagram of REEs normalized to the Chondrite meteorite (from Sun & McDonough, 1998).

5.2.2 Alteration

Igneous rocks in their fresh state contain no more than 1 or 2 % volatiles, but the Bre-X rocks have an average of 8.3% LOI (Loss on Ignition) (range from 3.4 to 13%), which is a proxy for alteration, mostly hydration (H_2O+ and H_2O-) and carbonatization (CO_2). Here, there is no correlation between CO_2 and other elements and ratios. From petrography, Bre-X5 is the least altered sample but has almost 10% volatiles. Most striking is the Na depletion shown by most rocks except for Bre-X7. The analytical standards used by Actlabs show that the values are likely real and not a product of analytical error (see Appendix 1).

Iron, magnesium, titanium, manganese, and calcium all show negative trends with respect to silica content which is generally interpreted to be the result of fractionation. Bre-X samples are mildly enriched in iron relative to Kalimantan samples but not in calcium. This suggests that calcium was not added to the system; calcite likely formed form the destruction of Ca-bearing phases such as plagioclase.

Sodium and potassium show positive trends with respect to silica. Bre-X samples have potassium values consistent with the trends, but they are highly depleted in sodium except for Bre-X7. Sodium was likely mobilized and almost completely removed from the system during alteration.

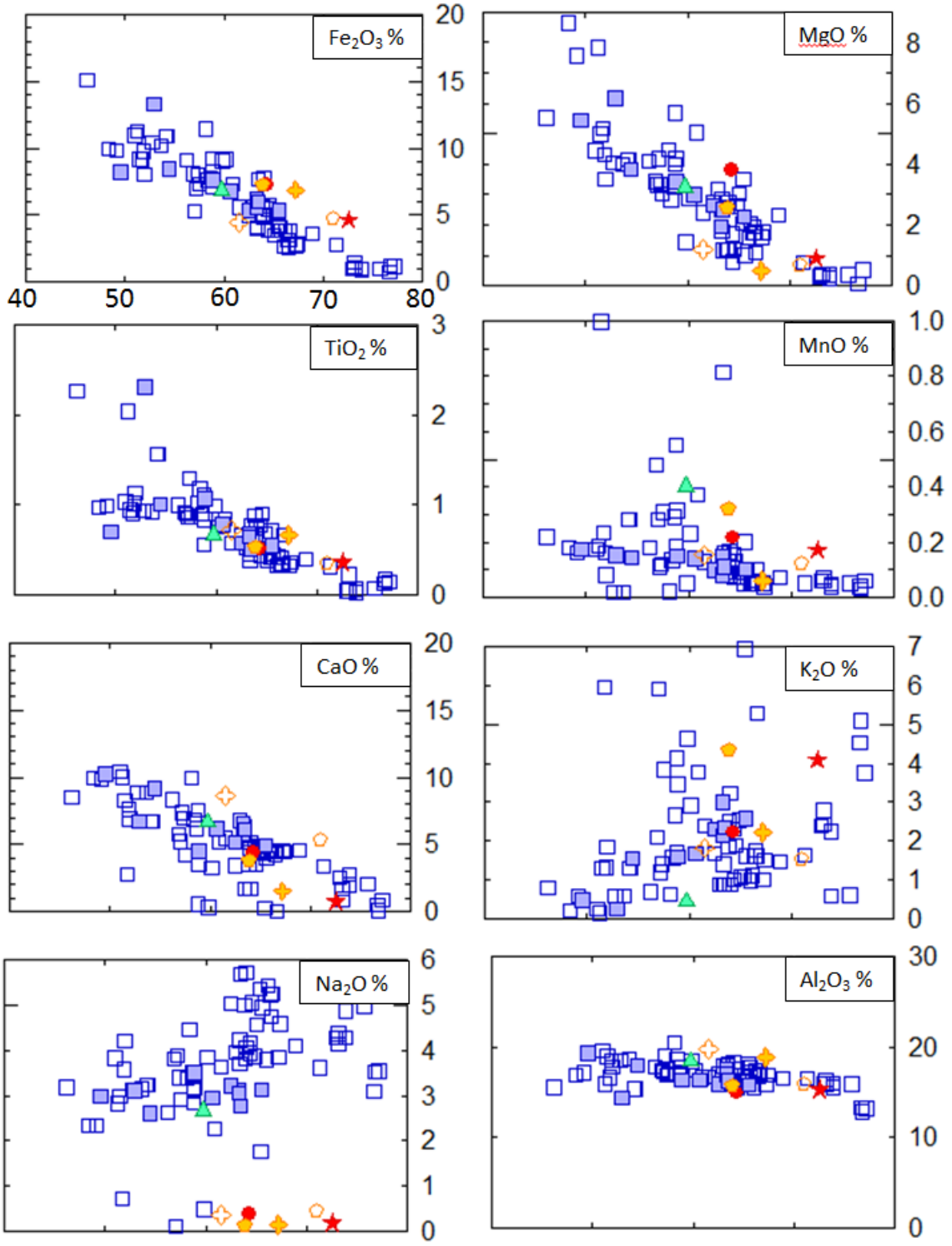

Figure 5.2-4: Harker plots comparing Bre-X samples to Kalimantan volcanic rocks. X-axis ranges from 40-80% SiO_2 with increments of 10%. Volcanic rocks from Kalimantan of Miocene-Pliocene and Oligocene-Miocene age are plotted based on data from Soeria-Atmadja et al., (1999).

5.3 Trace element geochemistry

Epithermal deposits have geochemical associations common to them. The associations can help distinguish between high- and low-sulfidation systems. Bre-X sample abundances are normalized to the average upper continental crust (UCC) from Rudnik and Gao (2003). Sample data was plotted for elements from Table 3.2-1 (Chapter 3) indicative of epithermal mineralization in Figure 5.3-1. Given small sample size, these values should be treated as qualitative depictions of rock chemistry with the understanding that elements may be misrepresented. Elements which were below detection limits were assigned the average UCC abundance where appropriate or half the detection limit.

Bre-X samples appear to be generally enriched in elements associated with epithermal environments, specifically a low-sulfidation environment. Vein samples tend to have higher contents of these elements. Silver, antimony, lead, and selenium are weakly to moderately enriched in these samples, suggesting epithermal mineralization. The highest gold anomaly is only around 100 times the average UCC abundance and this sample also has the highest copper and molybdenum anomalies, suggesting the potential for these elements to be related. There is no zinc anomaly although sphalerite is abundant in veins. Sphalerite grains were likely missed in the analysis. The silver to gold ratio is usually high in LS environments, but no enrichment is seen here.

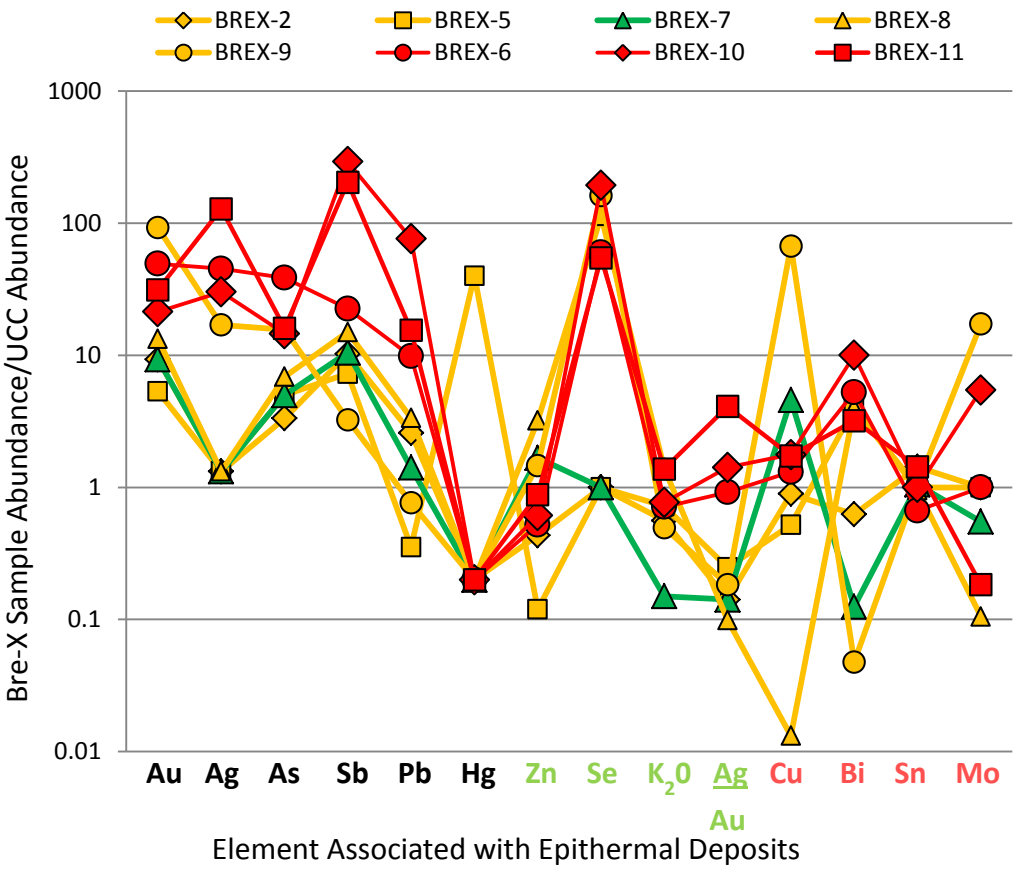

Figure 5.3-1: Relative abundance of elements associated with epithermal deposits. Bre-X samples abundance is divided by the average upper crustal abundance determined by Rudnik and Gao, (2003). Elements were chosen based on White and Hedenquist (1995). Elements in green text are indicators of LS and elements in red text are indicators of HS. Samples with yellow and green symbols are wall rock (or host rock) samples and samples with red symbols are vein material (or "ore").

X-Y plots show relationships between elements to determine which elements are associated with gold mineralization. Figures 5.3-2,3 compare the relationships between various elements and gold. Arsenic and copper are the only two which show a trend with respect to gold and are positively correlated.

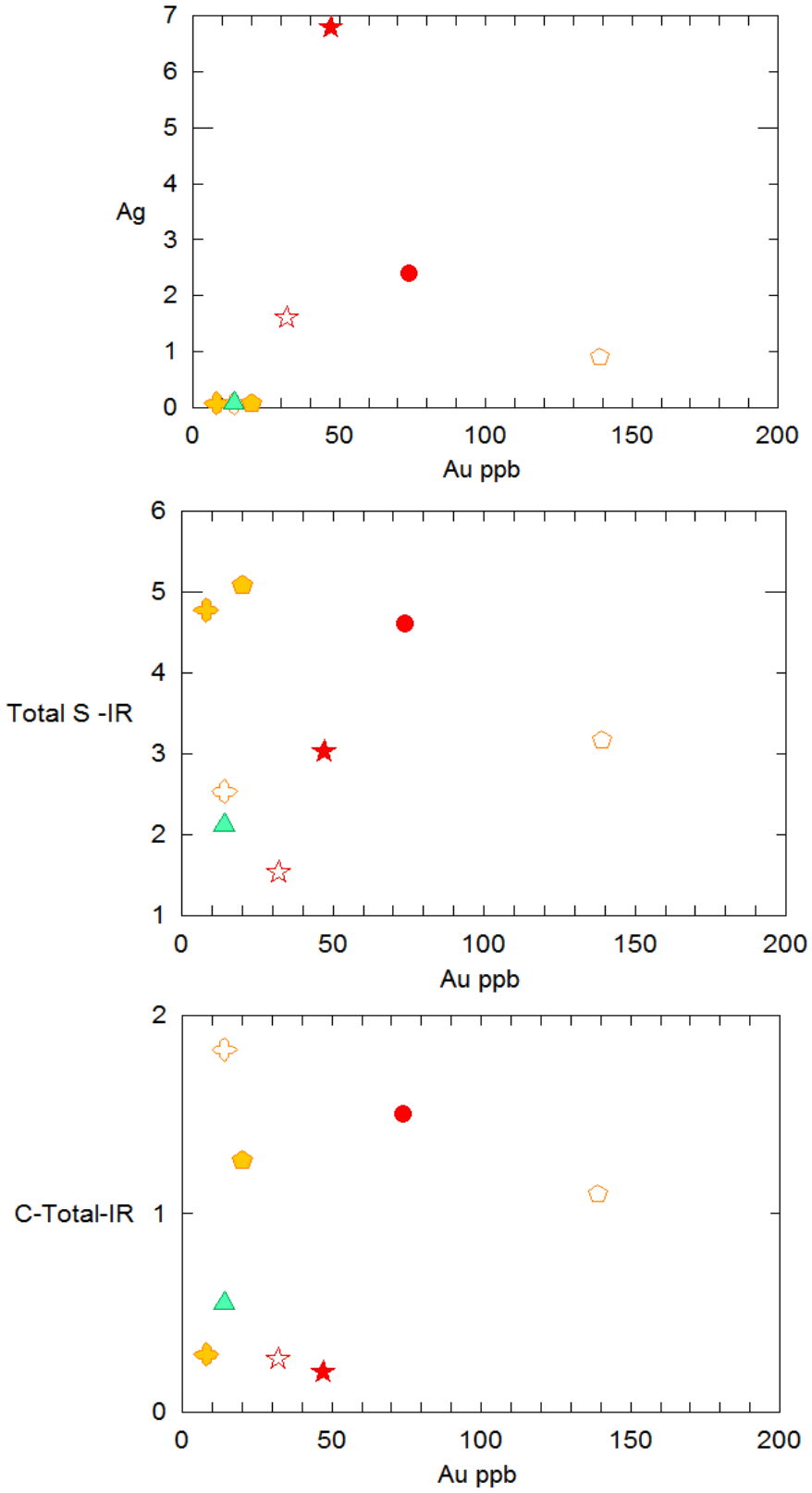

Figure 5.3-2: Plots of silver (ppm), total carbon (wt% oxide), and total sulfur (wt% oxide) vs. gold (ppb) from Bre-X samples.

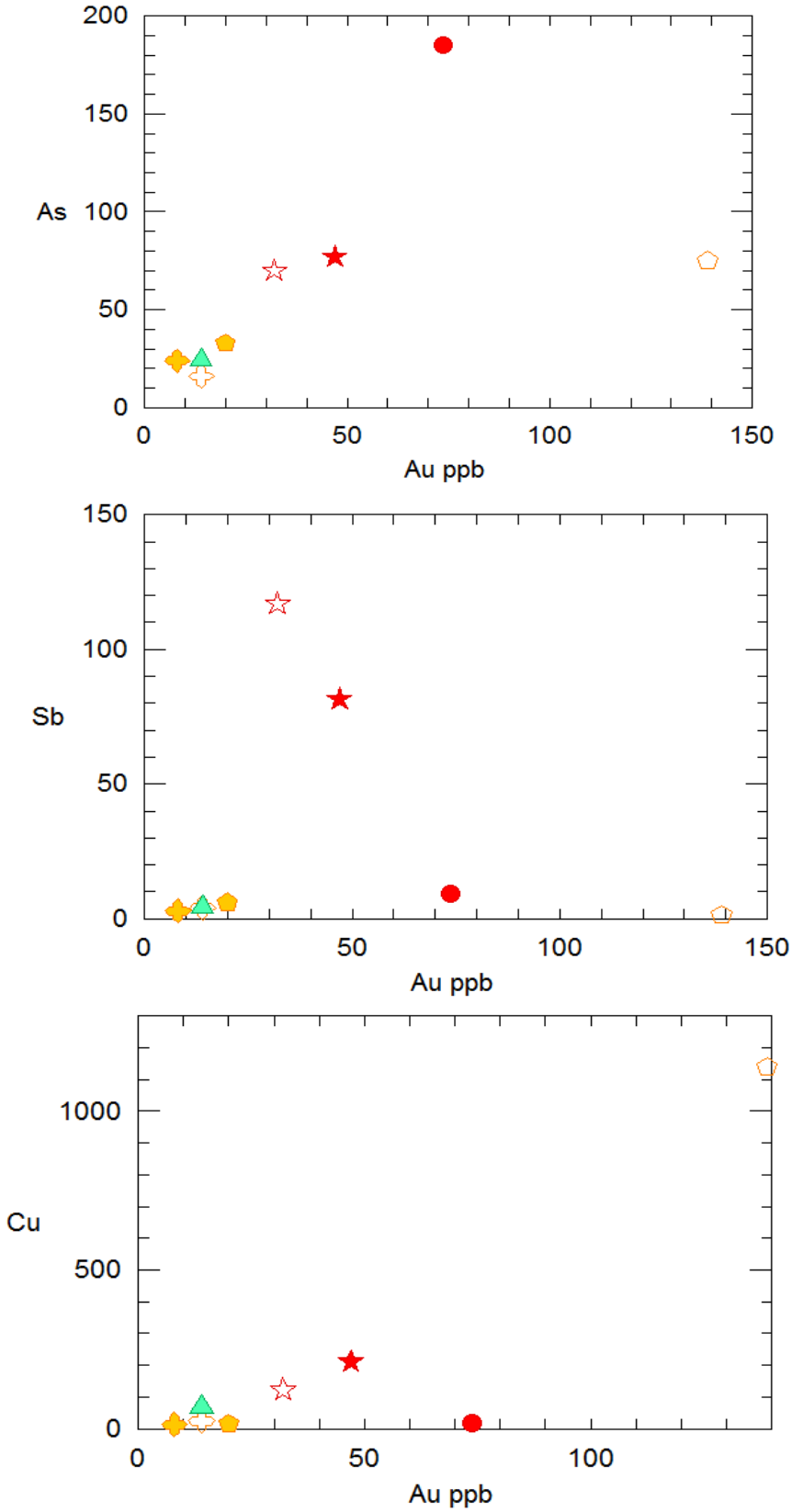

Figure 5.3-3: Plots of arsenic (ppm) antimony (ppm) and copper (ppm) vs. gold (ppb) from Bre-X samples.

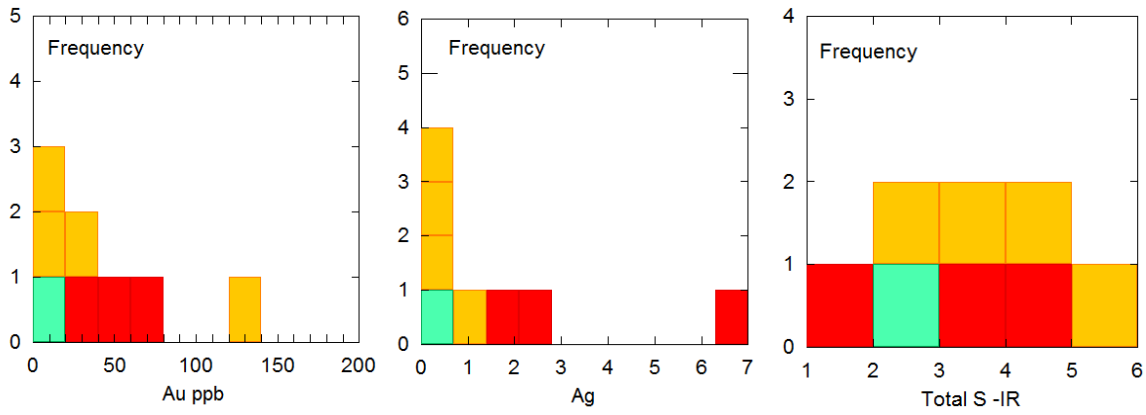

Figure 5.3-4: Histograms of gold, silver (ppm), and total sulfur (wt% oxide).

Histograms were produced for gold, silver, and sulfur (Fig. 5.3-4). Gold values ranged from 8-139 ppb. As expected, the vein samples have higher gold content than the host rock samples with the exception of sample Bre-X9. The silver content of the samples is also highest in the vein samples. This is a good indication that gold and silver are associated with veins, particularly those enriched in arsenic. Sulfur appears to be normally distributed amongst the samples and likely indicative of regional sulfur enrichment.

5.4 Scanning electron microscope analysis

5.4.1 Element maps

Semi-quantitative element maps show the relative distributions of desired elements displayed as raster images (Fig. 5.4-1,2a,b,3a,b). These maps confirm that the sulfosalts in the sample are bournonite-seligmannite and minor tennantite-tetrahedrite. Growth zones in the sulfosalts are defined by compositional banding, alternating between arsenic and antimony-rich bands. Bournonite-seligmannite has arsenic-rich

cores and more antimony-rich rims. It has a high lead content which may account for its textural association with galena.

Galena, pyrite, and chalcopyrite are chemically homogenous in terms of the mapped elements. Galena has consistently elevated silver concentrations over ore or gangue minerals but point analysis did not detect and precious metals. Tennantite-tetrahedrite has the highest elevated silver concentrations and is likely responsible for silver anomalies.

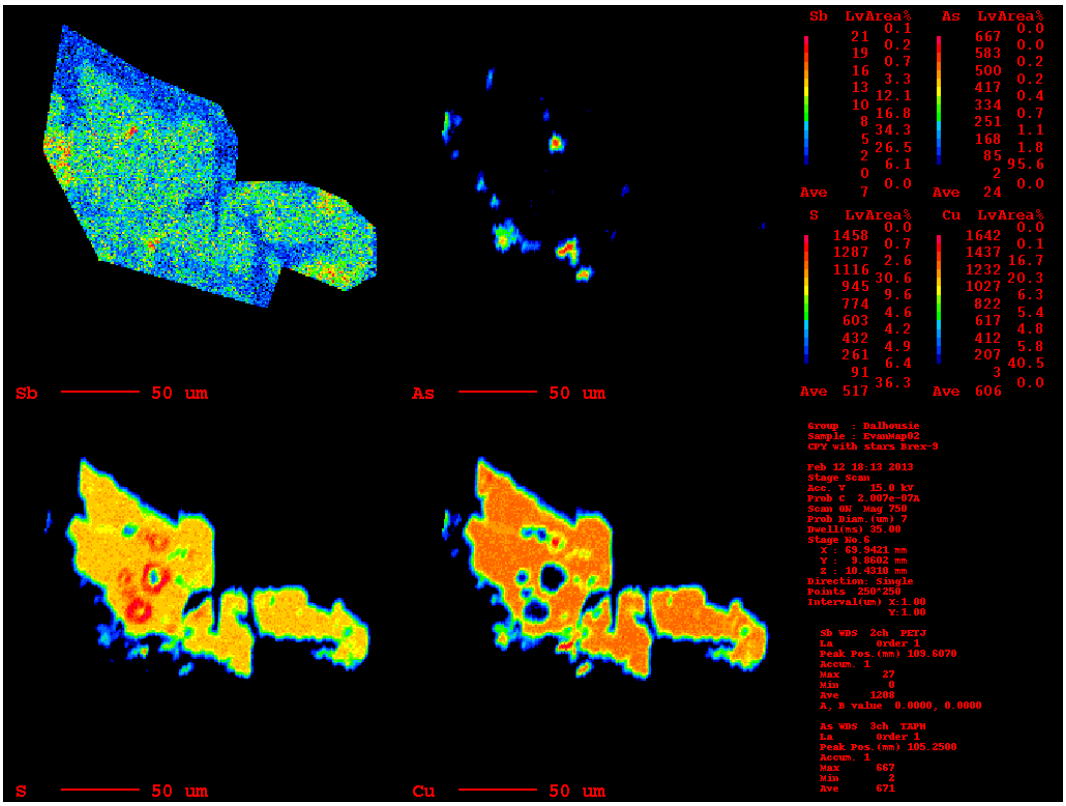

Figure 5.4-1: Element maps showing relative concentrations. Chalcopyrite in stockwork-veinlets from sample Bre-X9 with “star cluster” inclusions. Chalcopyrite or its inclusions do not host significant anomalies of gold or silver. Inclusions have sulfur, arsenic, or copper rich cores. These inclusions often have sulfur-rich and copper-poor rims.

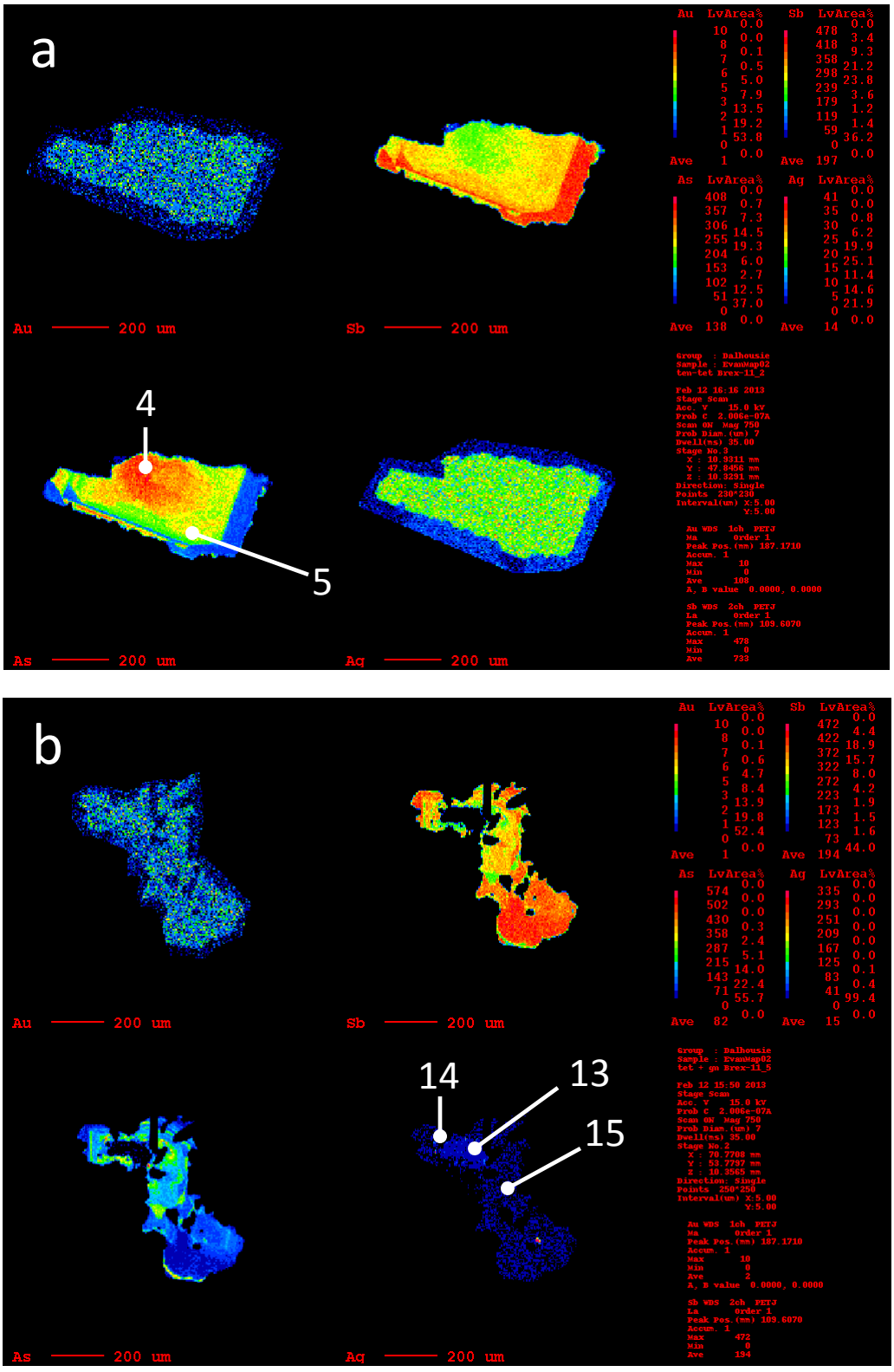

Figure 5.4-2: Element maps showing relative concentrations; (a) Bournonite-seligmannite in Bre-X10; (b) Bournonite-seligmannite in Bre-X1. Note chemical zonations alternating between arsenic- and antimony-rich growth layers. Silver and gold are enriched in this grain over the background, silver more than gold. Silver is enriched in galena more so than in the sulfosalts.

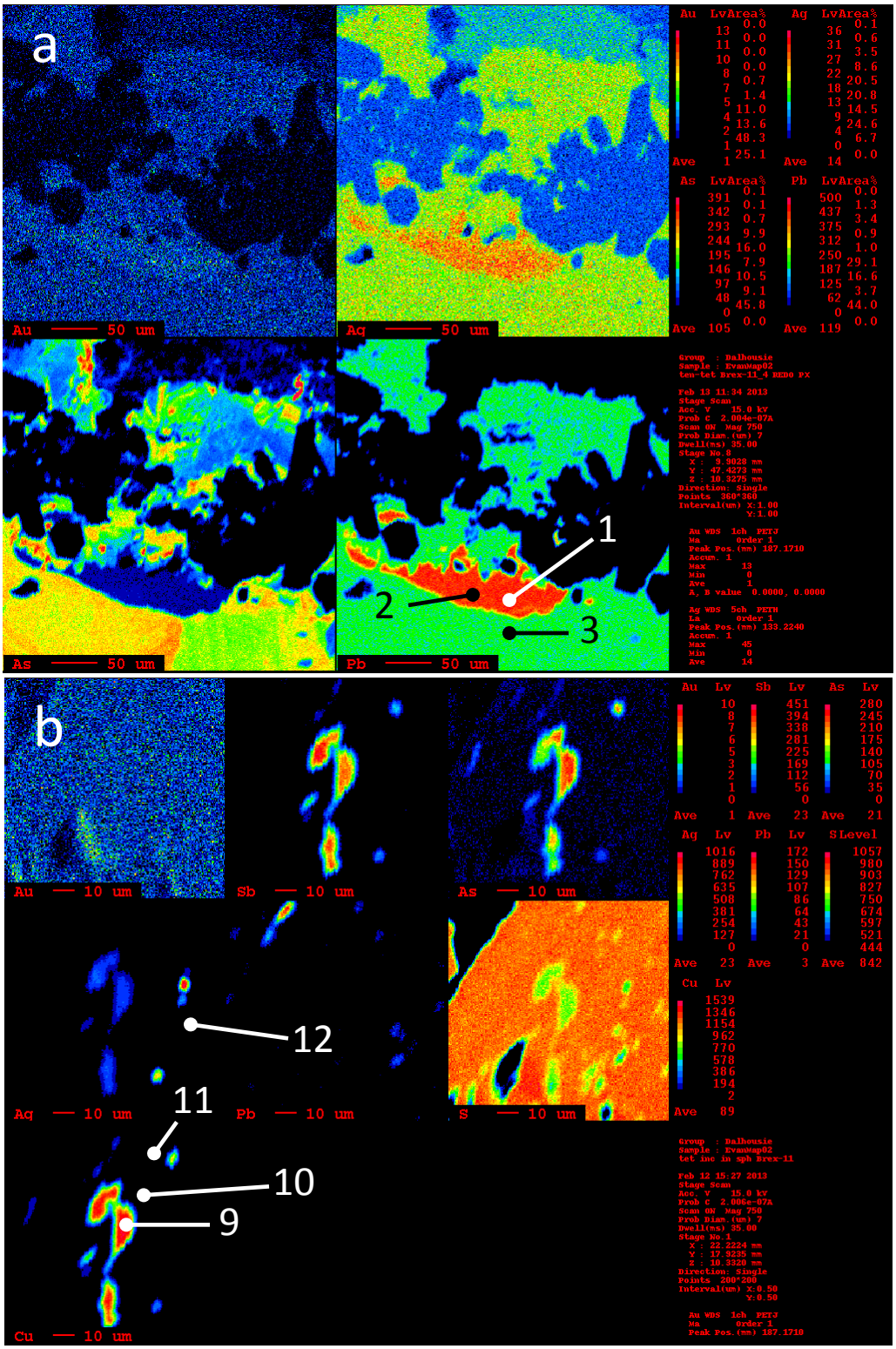

Figure 5.4-3: Element maps showing relative concentrations; (a) Bournonite-seligmannite, pyrite, and galena in Bre-X10. Galena is enriched in silver and hosts a very weak gold anomaly; (b) Tennantite-tetrahedrite inclusion in sphalerite in Bre-X11. Silver is enriched in the sulfosalt over the sphalerite. The highest silver anomaly is associated with a sulfur-poor 5 µm inclusion in the sphalerite and is of unknown composition.

Chalcopyrite in sample Bre-X9 has inclusions of arsenic- or copper-bearing phases which have sulfur-rich rims. These are the "star-clusters" noted in chapter 4. Here chalcopyrite or its inclusions are not associated with gold and are thus likely not the mineral hosting the gold anomaly in this sample.

5.4.2 Element point data

SEM point analysis was carried out on Bre-X samples in order to complement microscopy and to quantify gold and silver concentrations at specific points on element maps. Table 5.4-1 shows the point analysis number, the inferred mineral identity from atomic ratio data and Au and Ag concentrations in mass percent. Raw data is included in Appendix 2. The locations of these points are show in Figures 5.4-1,2,3.

Table 5.4-1: SEM point analyses

Point No.	Au	Ag	Mineral
1	0	0	Galena
2	0	0	Galena
3	0	0	Bournonite-seligmannite
4	0	0	Bournonite
5	0.063	0	Bournonite
6	0	0	Galena
7	0	0	Galena
8	0	0	Galena
9	0.016	2.594	Tennantite - tetrahedrite
10	0.058	0.013	Sphalerite
11	0.058	0.155	Sphalerite
12	0.059	0.249	Sphalerite
13	0	0.019	Galena
14	0	0	Bournonite
15	0	0	Bournonite
21	0.085	0.018	Unknown

These analyses show that the most abundant sulfosalt in the samples is a solid solution between bournonite (Sb end-member) and seligmannite (As end-member). Bournonite-seligmannite is thought to form a solid solution similar to that of tennantite-tetrahedrite (Wu & Birnie, 1977). The compositional zoning indicates seligmannite was more common early in the growth of the sulfosalts and that bournonite became predominate later. Only a very minor portion of the sulfosalts in the sample are tennantite-tetrahedrite which do not show the same compositional banding but show the only promising silver anomaly.

5.5 Summary of geochemistry results

The Bre-X samples are andesite to basaltic andesite based on geochemical classification using immobile elements, consistent with the Kalimantan Tertiary volcanic belt. Sodium and potassium appear to have mobility in the system and were likely redistributed by alteration, sodium more than potassium. Calcium does not appear to have been introduced to the system suggesting that calcite, which is abundant in these samples, formed largely from the destruction of Ca-rich feldspars. The relative enrichment of elements associated with epithermal mineralization is partially suggestive of a LS-epithermal style of mineralization as outlined by Hedenquist and White, (1995). Gold in these samples is associated with both copper and arsenic. In general vein samples are more enriched in gold and silver than wall-rock samples with the exception of sample Bre-X9. Bre-X9 has the highest gold, copper, and molybdenum anomalies suggestive of porphyry or HS-epithermal styles of mineralization.

SEM map and point analyses show that gold and silver are present only in trace amounts, silver showing a stronger anomaly with respect to the background X-rays as gold is barely visible above background. Silver is homogenously distributed in tennantite-tetrahedrite, galena, and sphalerite which likely accounts for the silver anomalies in these samples. It is possible that silver is associated with tellurides or selenides which were not mapped. A silver-rich 5 μm inclusion was present in sphalerite which was significantly elevated in silver over tennantite-tetrahedrite. There are rhythmic zonations in bournonite-seligmannite with respect to the relative proportions of As and Sb however, the general trend is that they have more arsenic in their cores.

Chapter 6: Fluid inclusion analysis

Fluid inclusion analysis is the study of the fluids from which minerals have precipitated, and can provide practical insight into the nature of hydrothermal systems. When a crystal forms in a hydrothermal system it often traps an aqueous fluid as small inclusions. These inclusions ideally preserve a record of the original fluid composition (have remained isoplethic), and density (have remained isochoric) from which the host mineral crystallized. Fluid inclusion analysis is very useful in exploration for epithermal gold systems as it can be used to distinguish between magmatic and meteoric fluids and identify processes associated with deposition of precious metals such as boiling and fluid mixing.

Three types of inclusion may be present: primary, secondary, and pseudo-secondary inclusions. Primary inclusions form along primary growth zones in the crystal and are interpreted to be representative of the fluids which formed the host crystals. Secondary inclusions form along secondary features such as fractures which annealed, trapping the fluids. Pseudo-secondary inclusions form along secondary features which are then truncated by additional growth zones.

In this study primary inclusions provide information on the fluids which formed the host mineral (quartz). Pseudo-secondary inclusions may provide information comparable to primary inclusions as they likely were trapped while quartz was still forming. Secondary inclusions formed after original quartz deposition and thus provide information about fluids present later in the system. It is possible that secondary

inclusions trapped the later fluids from which base metals and carbonates were precipitated in Bre-X samples.

Fluid inclusion data are most significant when inclusions are analysed in terms of belonging to a fluid inclusion assemblage (FIA). A FIA is a group of inclusions, or single inclusion in some cases, which have formed along a temporally constrained feature such as a growth zone or annealed fracture. If fluid inclusions belong to an assemblage, then they should all have similar fluid properties and morphology. If post-entrapment modification (PEM) has occurred then the T_h will likely not be the true minimum trapping temperature. The melting temperature of ice, and resultant calculated salinity, in dilute fluids are not usually affected by PEM and are likely a result of a fluid that has heterogeneous salinity possibly due to fluid mixing (Bodnar, 2003).

6.1 Significance of hydrothermal fluids to mineralization

As mentioned in Chapter 2, epithermal precious metal deposits form from hydrothermal fluids. HS deposits form from fluids exsolved from magmas which are acidic, hot, and saline whereas LS deposits form from predominantly meteoric fluids which are near-neutral, relatively cool, and dilute. It is postulated that heat from intrusions can drive the convection of meteoric water and that episodic input of magmatic fluids causes fluid mixing and contributes to precipitation of precious metals (Leach & Corbett, 1997).

The mobilization of gold is affected greatly by the properties of the fluid. In HS environments gold is often transported as a sulfide or bisulfide complex and is relatively

mobile at low temperatures. Here a rise in pH of the fluid is the main factor which contributes to ore precipitation. In LS environments iron is typically in excess over sulfur and thus gold is mobile at only high temperatures. Here ore is precipitated mainly from drops in temperature which could result from fluid mixing or reduction in pressure which is often accompanied by boiling (Heinrich et al., 2004). In LS type deposits the episodic reduction in the solubility of elements is accompanied by textures such as banded veins and lattice-textured quartz or calcite (Hedenquist & white, 1995).

Fluid inclusion analysis of Bre-X samples was carried out to determine if suitable conditions were present in the Busang Southeast Zone to effectively transport and precipitate metals. The nature of the fluid was determined and evidence for boiling or fluid mixing was interpreted.

6.2 Methods

Double-polished thin sections (DPTs) were made for fluid inclusion analysis of quartz in veins. Suitable inclusions were found in only two of the samples: Bre-X1, and Bre-X11. One DPT was made for Bre-X1 and three were made for Bre-X11. Inclusions were identified by microscopy and their locations indicated on thin section maps. Chips were cut from sections containing several inclusions and used for microthermometry.

Microthermometric measurements were taken at Saint Mary's University, Halifax, Nova Scotia using a Linkam FTIR 600 heating-freezing stage on an Olympus BX51 microscope. The stage was calibrated using synthetic inclusion standards containing pure H_2O (melting at 0^oC and critical behaviour at 374.1^oC).

Inclusions were classified as primary, psuedo-secondary, secondary or unclassified based on criteria described by Bodnar (2003). Inclusions were photographed at high- and low-magnification to constrain their petrographic context and where appropriate, grouped into assemblages.

The eutectics (first melting temperatures) and last melting temperatures (T_m) were measured to calculate the NaCl component in the fluid. NaCl weight percent equivalent was determined based on freezing point depressions described by Bodnar and Vityk (1994). The homogenization temperatures (T_h) were measured to determine minimum trapping temperatures and pressures. Melting temperatures were obtained by cooling the sample to well below freezing temperatures (around -40^{o}C) and were then heated. The temperatures were recorded when ice was first seen melting and when ice was last seen melting. Homogenization temperatures were measured by heating the stage until the vapour bubble fully contracted. For some inclusions these measurements were difficult since the shape of the inclusion made distinguishing between ice and water difficult. Multiple trials were performed until melting temperatures were observed with confidence where possible.

Microthermometric data were interpreted following procedures outlined by Bondar and Vityk (1994) as inclusions were approximated by a pure H_2O-NaCl system. Where appropriate inclusions were grouped into assemblages and classified before interpretations were made.

6.2.1 Error in measurements

The precision of measurements is unique to each inclusion and is limited by the size and clarity of the inclusion. First melting temperatures were determined within ±0.2^{o}C. Homogenization temperatures were determined within ±2^{o}C except in very irregular inclusions. Inclusions which could not be analysed with appropriate precision were excluded from the interpretations. Inclusions which are isolated and whose origins or isochoric/isoplethic conditions are suspect were treated with caution when making interpretations.

6.3 Observations

Inclusions in vein-hosted quartz are small (<25 µm), rare and irregular to prismatic (negative crystal shape). Inclusions consistently have two phases (aqueous liquid and vapour) at room temperature with consistent liquid-to-vapour ratios. The rarity of fluid inclusions restricts analysis to two samples from which microthermometry was completed to satisfactory precision for 28 inclusions. Most inclusions are unclassified as they do not occur along temporally constrained features, but some are likely of primary origin as they follow euhedral growth zones and have consistent morphologies and V:L ratios. In FIAs there is no heterogeneous entrapment observed and thus there is no evidence that the fluid was boiling. This does not rule out the possibility that boiling occurred here in the system but it is compatible with the theory that these samples were below the boiling zone in the hydrothermal system.

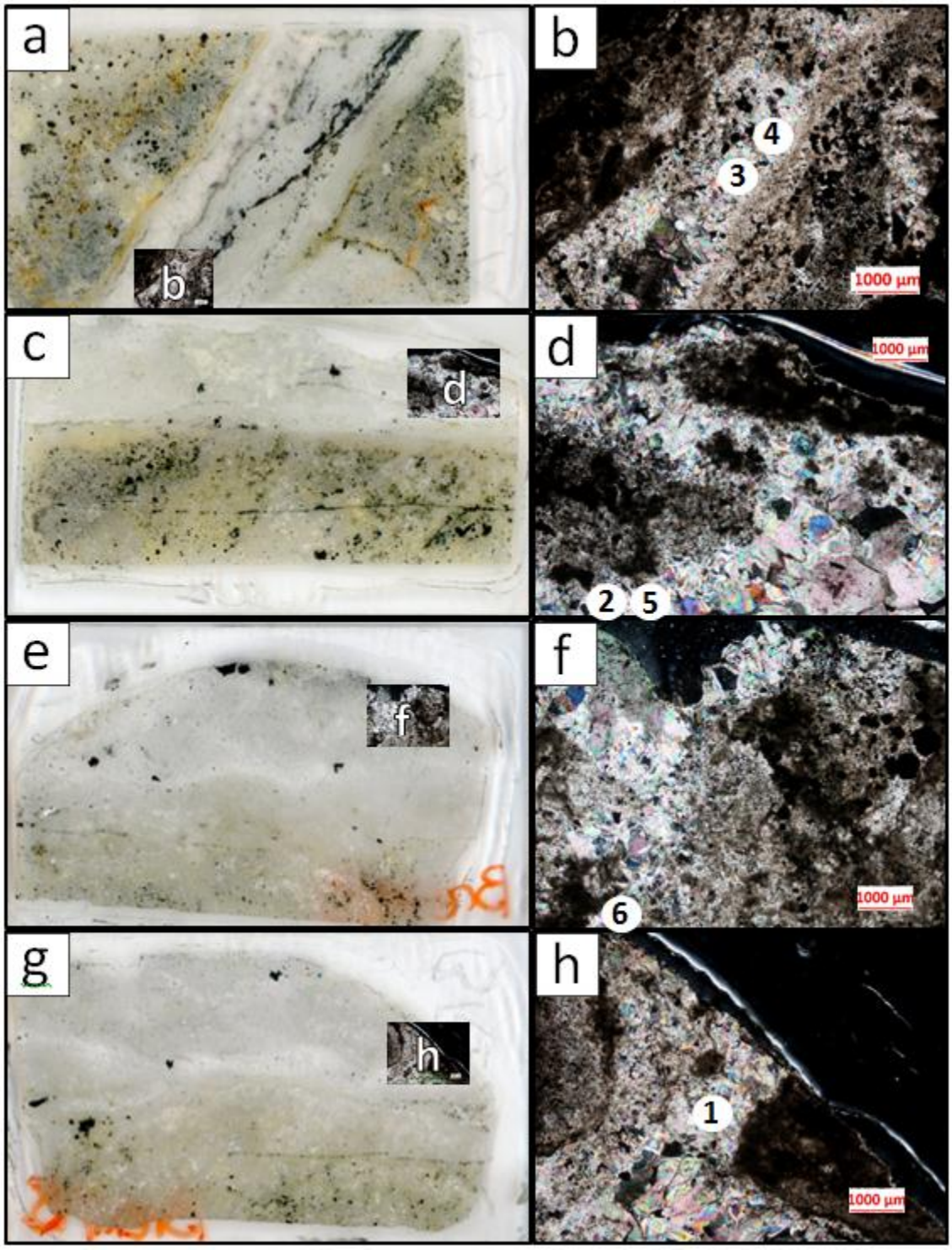

Figure 6.3-1: Scans of double-polished thinsections and transmitted light photographs containing FIAs. “a,b” are from sample Bre-X1 and “c-h” are from sample Bre-X11. Transmitted light photographs are superimposed on the thin sections to show their petrographic contect.

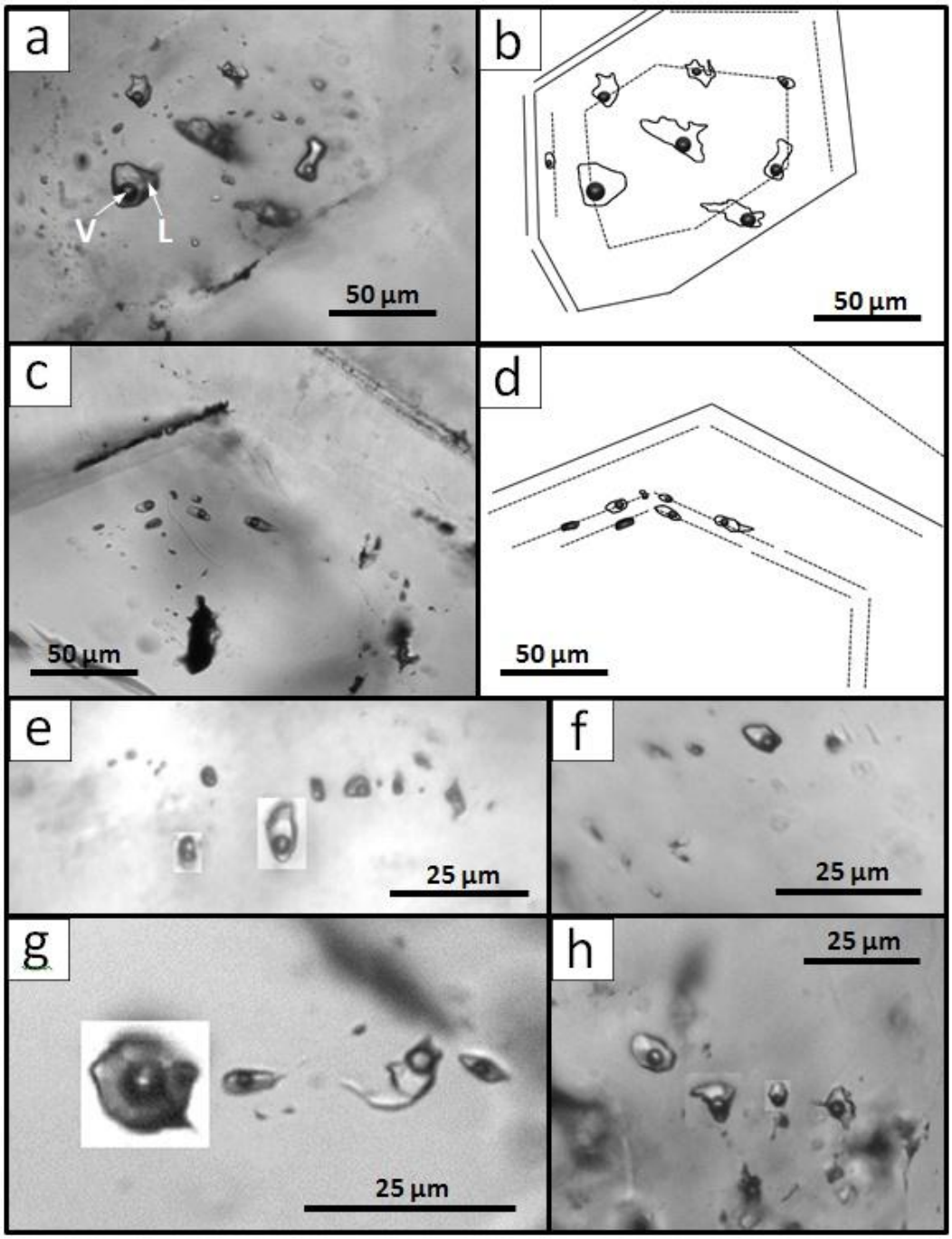

Figure 6.3-2: Microphotographs of FIAs; (a) Assemblage 1 - interpreted to be a primary FIA; (b) Schematic illustration of photograph "a" with quartz grain boundaries (solid lines) and infered growth zones (dashed lines); (c) Assemblage 2 - interpreted to be a primary FIA; (d) Schematic illustration of photograph "c" with quartz grain boundaries (solid lines) and infered growth zones (dashed lines). It is interpreted that the inclusions occur along primary growth zones; (e) Assemblage 3 - unclassified as no growth zones or annealed fractures were observed; (f) Assemblage 4 - unclassified; (5) Assemblage 5 - unclassified. Smaller inclusions appear to have necked so only the largest was measured; (h) Asseblage 6 – unclassified: Photographs "e,g, and f" have been compiled from several photographss to show all the inclusions in various planes.

Table 6.3-1: Fluid inclusion data by chip and assemblage

Sample	Chip	Inclusion No.	Assemblage	T_m^{ice} (°C)	NaCl (Wt % equivalent)	T_h (°C)	Origin	V:L ratio	Max. Size (µm)	Morphology
Bre-X11	1A5	Inc1	5	-1.6	2.7	280.7	Unclassified	0.20	15	Prismatic, equant
Bre-X11	1A5	Inc2	2	-0.8	1.4	330.4	Primary	0.15	7	Prismatic, elongate
Bre-X11	1A5	Inc3	2	-0.5	0.9	230.5	Primary	0.15	5	Rounded, elongate
Bre-X11	1A5	Inc4	2	-0.8	1.4	313.9	Primary	0.15	10	Rounded, elongate
Bre-X11	1A5	Inc5	2	-0.6	1.1	286.8	Primary	0.15	12	Rounded, elongate
Bre-X11	11C4	Inc6	1	-0.8	1.4	239.1	Primary	0.15	20	Rounded, elongate
Bre-X11	11C4	Inc7	1	-0.8	1.4	231.4	Primary	0.15	12	Irregular, equant
Bre-X11	11C4	Inc8	1	-0.3	0.5	240.5	Primary	0.15	25	Rounded, elongate
Bre-X11	11C4	Inc9		-0.8	1.4	197.5	Probably Primary	0.20	5	Rounded, elongate
Bre-X11	11C4	Inc10		-0.7	1.2	263.6	Probably Primary	0.15	4	Rounded, elongate
Bre-X1	1B1	Inc11	3	-1.6	2.7	251.4	Unclassified	0.15	10	Rounded, elongate
Bre-X1	1B1	Inc12	3	-1.6	2.7	258.8	Unclassified	0.15	4	Rounded, elongate
Bre-X1	1B1	Inc13	3	-1.5	2.6	245.9	Unclassified	0.15	4	Rounded, elongate
Bre-X1	1B1	Inc14	3	-1.5	2.6	245.9	Unclassified	0.15	4	Rounded, elongate
Bre-X1	1B1	Inc15	4	-1.2	2.1	295.3	Unclassified	0.15	10	Rounded, elongate
Bre-X1	1B1	Inc16	4	-1.1	1.9	289.7	Unclassified	0.15	6	Rounded, equant
Bre-X11	11A2	Inc17		-1.5	2.6	275.8	Unclassified	0.15	13	Prismatic, equant
Bre-X11	11A2	Inc18		-1.1	1.9	189.9	Unclassified	0.15	20	Prismatice, elongate
Bre-X11	11A2	Inc19		-1.1	1.9	244.1	Unclassified	0.15	12	Rounded, elongate
Bre-X11	11B6	Inc20	6	-1	1.7	276.6	Unclassified	0.15	10	Rounded, equant
Bre-X11	11B6	Inc21	6	-0.5	0.9	284.2	Unclassified	0.15	7	Irregular, equant
Bre-X11	11B6	Inc22	6	-0.4	0.7	280.2	Unclassified	0.15	5	Irregular, equant
Bre-X11	11B6	Inc23		-1.5	2.6	256.7	Unclassified	0.15	4	Rounded, elongate
Bre-X11	11B5	Inc24		-2.7	4.5	222.3	Unclassified	0.20	17	Iregular, equant
Bre-X11	11B5	Inc25		-1.7	2.9	214.3	Unclassified	0.15	20	Rounded, elongate
Bre-X11	11B5	Inc26		-0.8	1.4	269.7	Unclassified	0.10	20	very iregular, equant
Bre-X11	11A4	Inc27		-3.2	5.3	251.3	Unclassified	0.10	10	Irregular, elongate
Bre-X11	11A4	Inc28		-0.7	1.2	317.9	Unclassified	0.15	7	Rounded, elongate

*Only inclusions which had successful microthermometric measurements are included

Microthermometric data are summarized in Table 6.3-1. Inclusions which occurred along a planar feature with other inclusions were grouped into assemblages. Assemblages 1 and 2 occur along growth zones as seen in Figure 6.3-2a-d.

Assemblages 3-6 occur along planar features of unknown origin as seen in Figure 6.3-2e-h. Assemblage 5 has only one microthermometric measurement, but there are other smaller inclusions along the same plane which were too small to measure with appropriate precisions. Many inclusions in assemblages have a common orientation perpendicular to the plane which hosts the assemblage. This suggests that they have formed with their length oriented in the direction of crystal growth in the case that these are primary inclusions.

6.4 Results of fluid inclusion analysis

Fluid inclusion analysis indicates that quartz was precipitated from aqueous fluids which were dilute (0.5-5.7 wt% NaCl equivalent) and relatively hot (T_h: 198-330^{o}C). Isochores show that the fluids are compatible with a shallow depth of emplacement of aproximately 100-500 m (P_h: 1.2-12.8 MPa using a the lithostatic gradient) (Fig. 7.4-2,3). Primary FIA have tight ranges in temperature and salinity with the exception of several outliers which likely experienced post-entrapement modification (Fig. 7.4-3a).

FIAs show tight ranges in T_h and salinity. Some inclusions have anomalous values which in most cases are interpreted to be due to post-entrapment modification. FIAs which are likely primary (assemblages 1,2), unclassified assemblage 6, and several unclassified inclusions have low salinities (0.5-2 wt% NaCl equivalent) and a relatively tight range of T_h. Unclassified FIAs 3,4, and 5, and other isolated unclassified inclusions have slightly higher salinities (2-3 wt% NaCl equivalent) and also have a tight range of T_h. Inclusions Inc24 and Inc27 have salinities of 4.5 and 5.3 wt% NaCl equivalent, respectively, which are anomalously high. Both of these inclusions are very irregular and

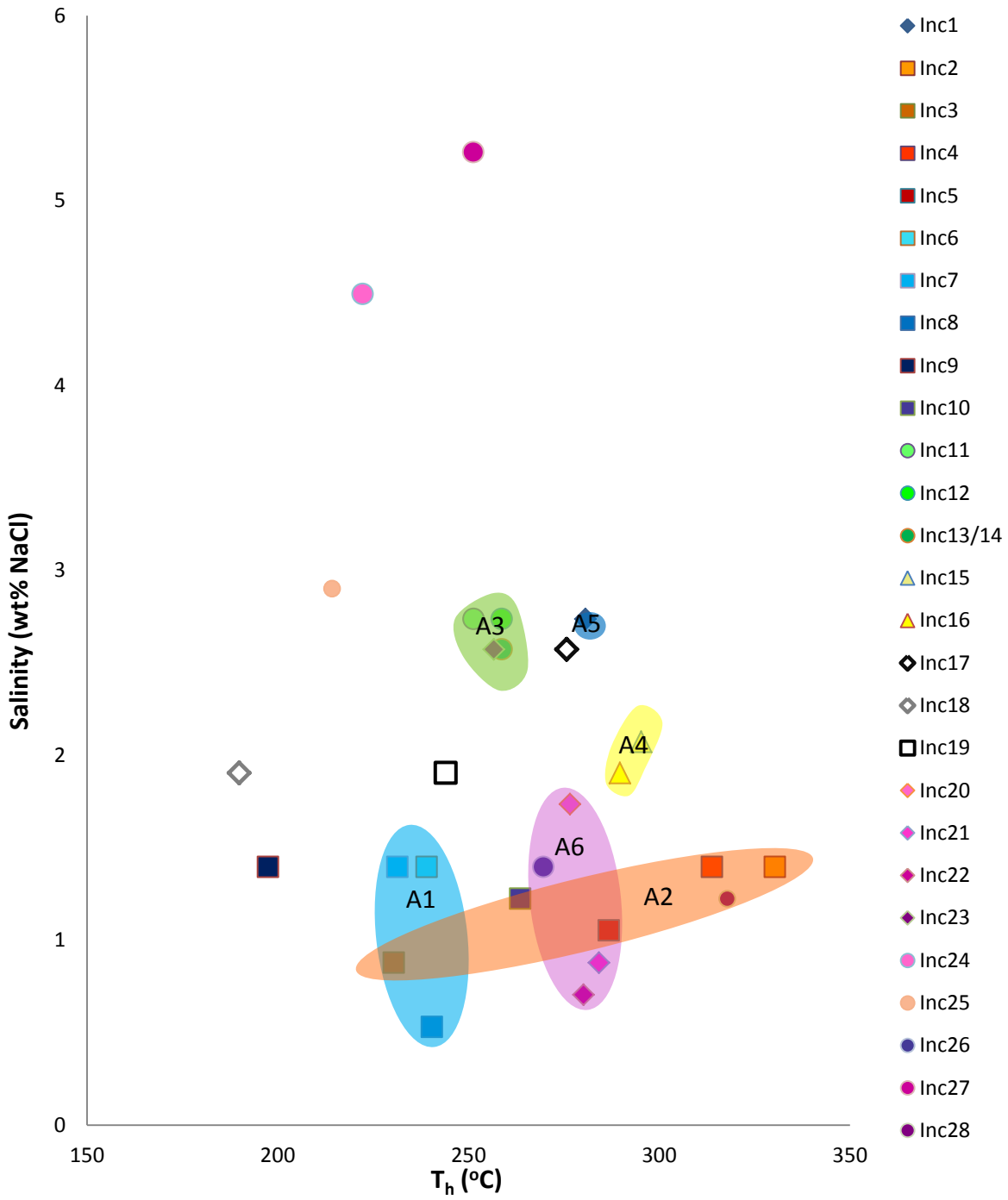

Figure 6.4-1: Plot of homogenisation temperature vs. salinity for all sucessfully measured inclusions. Approximate ranges for each FIA are shaded (A1-6): Blue – assemblage 1; Orange – assemblage 2; Green – assemblage 3; Yellow – assemblage 4; Blue – assemblage 5; Pink – assemblage 6. Symbol colour and shape were chosen to group inclusions together where appropriate.

thus it is possible that these inclusions did not yield accurate measurements. It is also possible that they are either late-forming secondary inclusions sampling a saline fluid, or that they have not maintained isoplethic conditions.

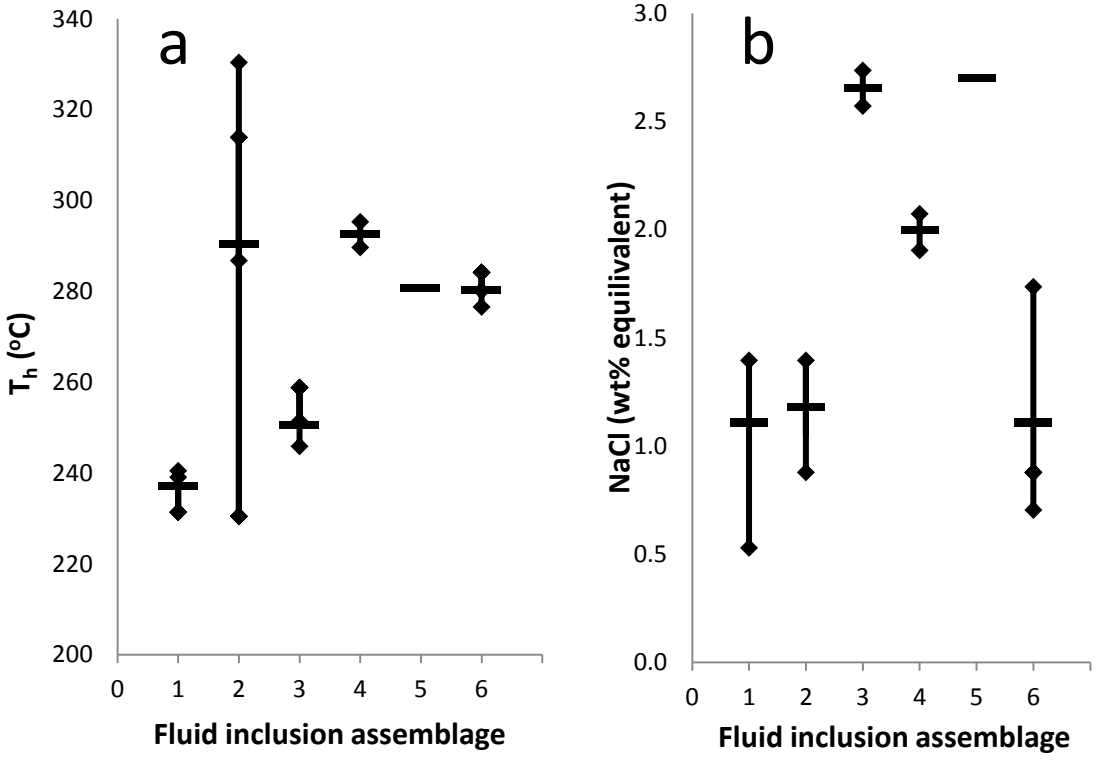

Figure 6.4-2: Whisker plots by FIA for T_h (a) and salinity (b) by FIA. Diamond shapes represent data points and the horizontal lines are the mean values for each FIA.

6.5 Interpretation of fluid inclusion data

Careful petrography of samples allows us to put fluid inclusion data into context. Conclusions drawn from unclassified inclusions are speculative and must be combined with other lines of evidence. Fluid inclusions from Bre-X1 and Bre-X11 are hosted in quartz crystals which are likely related to the same event at different locations in the

hydrothermal system based on petrography. Bre-X1 contains a crudely banded quartz-base metal-carbonate vein. Bre-X11 contains a quartz vein with base metal clots. Textural relationships indicate that quartz precipitated first followed by later base metals and carbonates, then lastly by carbonates alone.

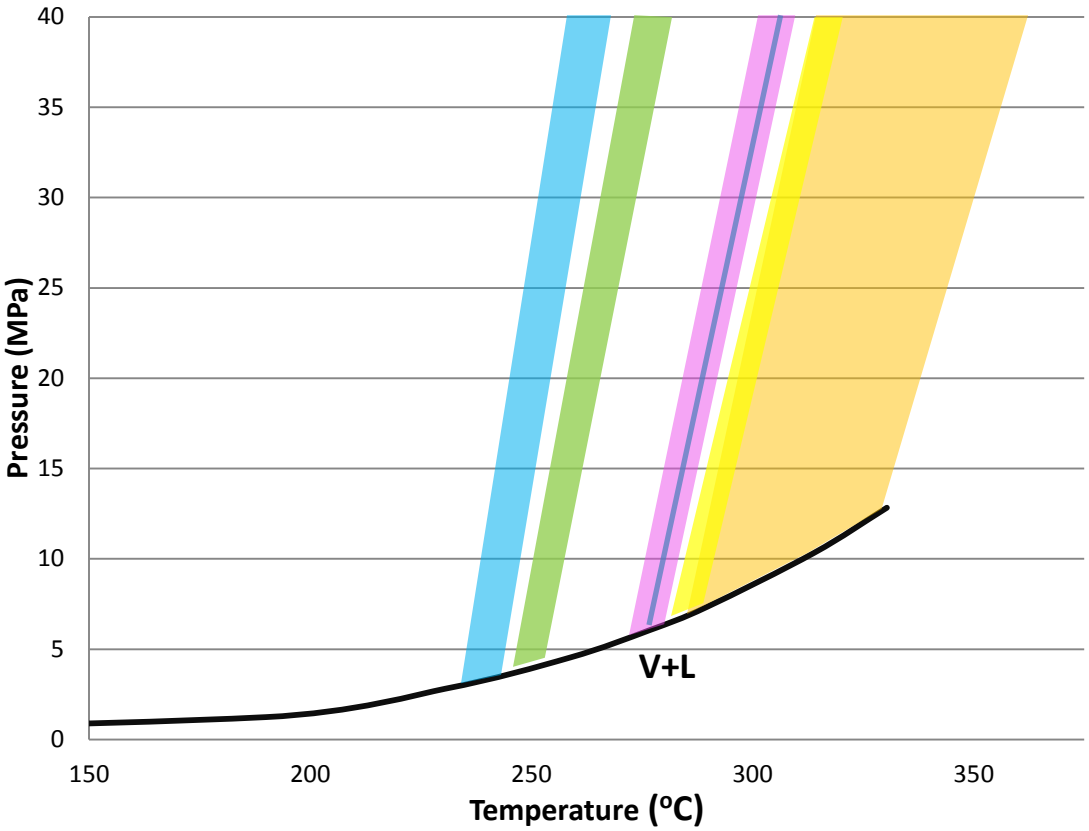

Figure 6.4-3: Approximate P-T ranges by FIA. Ranges were interpolated from isochores made using "Sowhatflinc" software. The boiling curve of pure H_2O is shown in black (V+L) which puts the lower constraint on P-T having trapped these fluids as a single phase. Blue – assemblage 1; Orange – assemblage 2; Green – assemblage 3; Yellow – assemblage 4; Blue – assemblage 5; Pink – assemblage 6.

Primary fluid inclusions provide insight into the hydrothermal fluids which precipitated quartz. Secondary inclusions provide insight into later fluids which may also

have precipitated quartz but may also have precipitated later base metals and carbonates.

Salinity ranges within FIAs are potentially indicators of fluid mixing as the eutectic of a pure H_2O-NaCl system is not significantly affected by changes in pressure from PEM. These ranges could be the result of mixing of two meteoric fluids which have dissolved different amounts of salts from wall-rocks or the mixing of a magmatic fluid with a meteoric fluid. Variations in salinity within a hydrothermal system could also be due to local disequilibrium within a single fluid.

Homogenization temperatures within FIAs fall within tight ranges with the exception of assemblage 2. Differences in T_h could be the result of PEM or variations in the temperature of fluids in time and space as hydrothermal systems are very dynamic. Fluid Inclusions within an FIA could have differences in closure times which are insignificant in geological terms but could be significant in the context of a dynamic hydrothermal system (Fig. 7.5-1).

It is possible that variations in salinity or T_h are the result of measurement error due to the limitations of optics and the clarity of inclusions. With a larger data set it would be easier to differentiate between real variations and analytical error. The sample size here is limited by the rarity of inclusions in the samples.

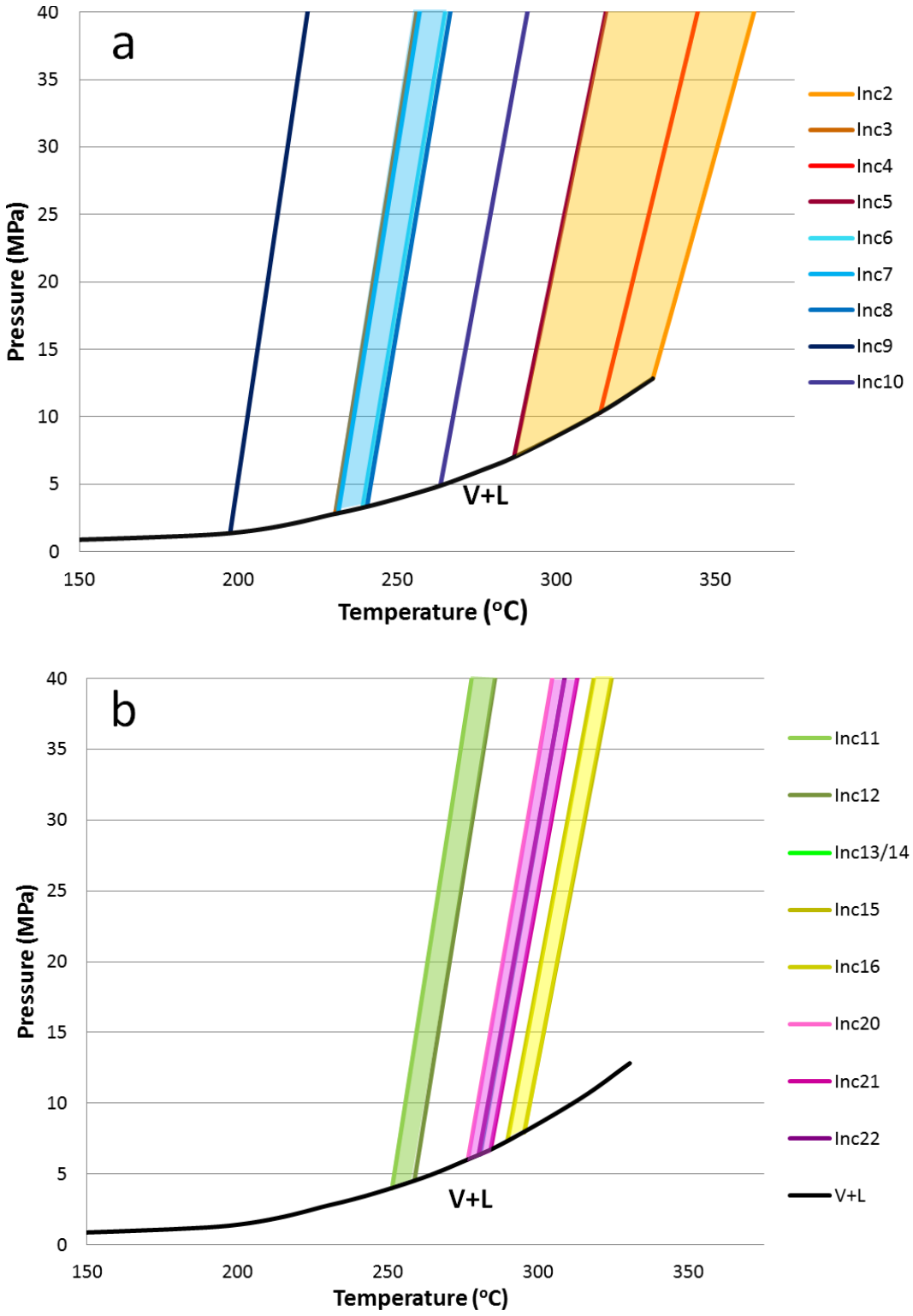

Figure 6.4-4: P-T ranges by FIA. Ranges were interpolated from isochores made using "Sowhatflinc" software. The boiling curve of pure H_2O is shown in black (V+L) which puts the lower constraint on P-T having trapped these fluids as a single phase. (a) Primary FIAs. Inclusions Inc9, and Inc10 may not belong to assemblage 1 as they occur closer to the edge of the quartz crystal likely in a later growth zone; (b) Unclassified FIAs.

Fluid inclusions indicate that quartz formed from a fluid that is compatible with deep-heated meteoric water. It is also compatible with a contracted vapour phase, but there is no evidence that these fluids have boiled. This fluid was relatively hot, suggesting that it was heated by a nearby intrusion. This is compatible with the LS epithermal deposit model in the Pacific Rim. However the absence of evidence for boiling or significant magmatic input is not promising when evaluating the potential of these samples to belong to a rich precious metal deposit.

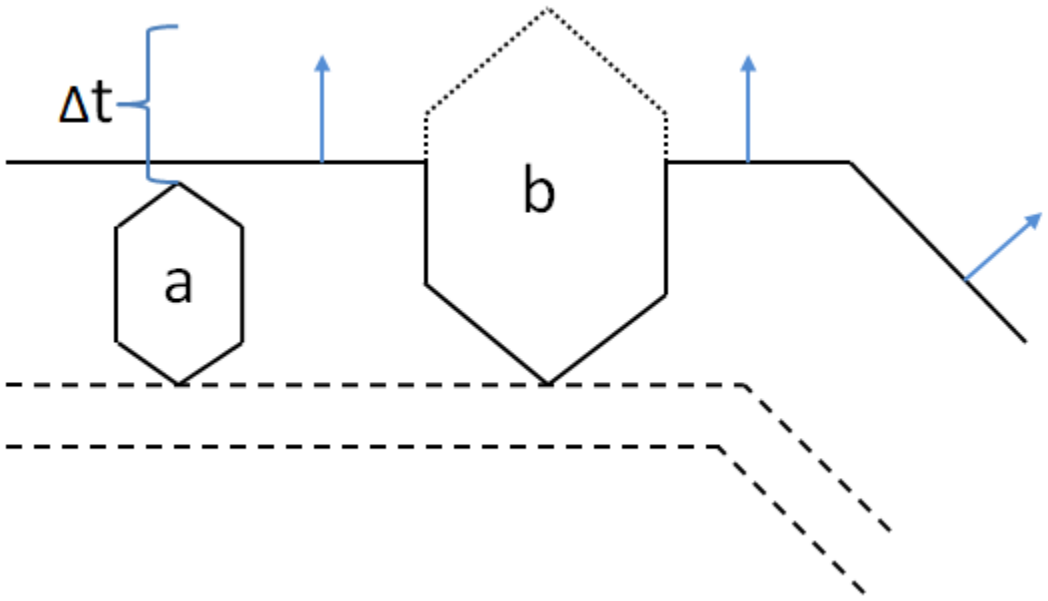

Figure 6.5-1: Schematic diagram explaining a possible reason for ranges in T_h and potentially salinity as well with in FIAs. Here two inclusions "a" and "b" have formed along the same growth zone in a quartz crystal. The solid black line indicates the present crystal boundary, the dashed line indicates previous crystal boundaries, and the dotted line indicates the future boundaries of the inclusion after closer. Although both inclusions occur along the same temporally constrained primary feature (in geological terms), they have slightly different closure times (Δt). In this amount of time it seems reasonable that temperatures, and maybe salinities, of a hydrothermal fluid could change in experimentally measureable amounts.

These fluids were also likely too hot to effectively precipitate gold at the stage of quartz deposition in veins. The absence of boiling suggests that these samples were too low in the system to host the richest ores; the richest ores are likely to have been associated with the zone of boiling and have likely been eroded away (if they were ever present).

Chapter 7: Summary of results

Bre-X samples were studied in terms of their geochemical associations, ore minerals, gangue minerals, hydrothermal textures, and fluid inclusion properties. Additional information from SEM analysis was obtained. These samples were studied and compared to criteria common to epithermal gold deposits as set out in Table 7-1a,b. A summary of observations from Bre-X samples is set out in Table 7-2 to compare them against the criteria previously defined.

Table 7-1a: Characteristics of epithermal gold deposits. Diagnostic minerals are shaded grey (e.g. White & Hedenquist, 1995)

	Low-sulfidation	**High-sulfidation**
Geochemical Associations		
Anonymously High	Au, Ag, As, Sb, Hg, Zn, Pb, Se, K, Ag/Au	Au, Ag, As, Cu, Sb, Bi, Hg, Te, Sn, Pb, Mo, Te/Se
Anonymously Low	Cu, Te/Se	K, Zn, Ag/Au
Ore Minerals		
Pyrite	ubiquitous (a)	ubiquitous (a)
Sphalerite	common (V)	common (vm)
Galena	common (V)	common (m)
Chalcopyrite	common (V)	common (m)
Enargite -Luzonite	rare (vm)	ubiquitous (V)
Tennantite-Tetrahedrite	common (vm)	common (V)
Covellite	uncommon (vm)	common (m)
Stibnite	uncommon (vm)	rare (vm)
Orpiment	rare (vm)	rare (vm)
Realgar	rare (vm)	rare (vm)
Arsenopyrite	common (m)	rare (vm)
Cinnabar	uncommon (m)	rare (vm)
Electrum	uncommon (V)	common (m)
Native Gold	common (vm)	common (m)
Tellurides-Selenides	common (vm)	uncommon (V)

Table 7-1b: Characteristics of epithermal gold deposits Diagnostic minerals are shaded grey (e.g. White & Hedenquist, 1995)

	Low-sulfidation	**High-sulfidation**
	Gangue Minerals	
Quartz	ubiquitous (a)	ubiquitous (a)
Chalcedony	common (V)	uncommon (m)
Calcite	common (V)	absent (except overprint)
Adularia	common (V)	absent
Illite	common (V)	uncommon (m)
Kaolinite	rare (except overprint)	common (m)
Pyrophyllite-Diaspore	absent (except overprint)	common (m)
Alunite	absent (except overprint)	common (m)
Barite	common (vm)	common (m)
	Characteristic Hydrothermal Textures	
	Banded veins	Vuggy quartz
	Crustified quartz veins	Massive quartz
	Drusy cavities	Massive sulfide veins
	Crustification	Crudely banded veins
	Breccia veins	
	Lattice texture	
	Hydrothermal Alteration	
Associated with ores	Highest pH assemblage	Lowest pH assemblage
Mineral Assemblages	Clay alteration:	(Advanced) Argillic alteration:
	Smectite	*kaolinite, dickite,*
	Illite/smectite	*pyrophyllite,*
	Illite ± adularia	*diaspore, and alunite,*
		zunyite, topaz, and andalusite
	Propylitic Alteration:	
	albite, calcite, epidote, chlorite, and pyrite	
Zoning	Temperature decreases	pH decreases with depth
	increases with depth	and distance from source
	and distance from source	

Table 7-2: Characteristics of Bre-X samples

Geochemical Associations	
Anonymously High	Au, Ag, As, Sb, Pb, Zn, Se
Anonymously Low	Hg
Ore Minerals	
Pyrite	ubiquitous (a)
Marcasite	common (V)
Sphalerite	common (V)
Galena	common (V)
Chalcopyrite	common (V)
Bournonite-Seligmannite	common (V)
Tennantite-Tetrahedrite	rare (Vm)
Gangue Mineral	
Quartz	ubiquitous (a)
Chalcedony	rare (vm)
Calcite	common (V)
Gypsum/Anhydrite	rare (vm)
Textures	
Crudely banded veins	
Stockwork veins	
Drusy cavities	
Massive quartz	
Breccias (rare)	
Alteration	
Associated with ores	Highest pH assemblage
Mineral Assemblages	Phyllic alteration: *Quartz, sericite, pyrite* Propylitic Alteration: *Calcite, epidote, chlorite, and pyrite*
Zoning	Intensity of alterations increases with depth
Fluids	
Predominately meteoric water	0.5-2.7 wt% NaCl, T_h: 180-330^{o}C

Bre-X samples have weak geochemical anomalies indicative of epithermal mineralization, specifically a LS-style of mineralization. The ore mineralogy is consistent with LS-style deposition with the exception of late copper-lead-bearing sulfosalts which are more commonly associated with HS epithermal or porphyry related mineralization. These may reflect late stage hypogene overprinting as suggested by Leach and Corbett (1997). Gangue minerals present are indicative of propylitic and phyllic alteration styles. Veins contain quartz, carbonates (calcite with minor Fe, Mn, and Mg) and gypsum/anhydrite; this is consistent with a high-pH environment such as a LS epithermal system. Textures are predominantly regional alteration textures, stockwork veins at depth, and crudely banded veins; this is not promising when exploring for epithermal gold deposits. Fluid inclusions show that quartz in veins was deposited from a fluid that is compatible with meteoric water which has acquired minor salinity or a contracted vapour from a boiling fluid. The absence of evidence for boiling, from fluid inclusions or petrography, suggests the former over the latter.

7.1 Geochemical anomalies

Element data for Bre-X samples normalized to the average UCC show that Au, Ag, As, Sb, Pb, Se are relatively enriched and Hg is relatively depleted. The abundance of sphalerite suggests that significant amounts of Zn were missed in geochemical analyses, likely the result of the nugget effect. These elements are indicative of epithermal

mineralization as described by White and Hedenquist (1995). Vein samples are more enriched in these elements than altered wall rock samples suggesting that mineralization is vein controlled. Sample Bre-X9 has the highest gold (139 ppb), copper, and molybdenum anomalies, suggesting that these elements are associated with the same processes which is also noted in porphyry-style deposits.

7.2 Ore minerals

Ore-microscopy recognizes pyrite, sphalerite, galena, chalcopyrite, sulfosalts (bournonite-seligmannite and tetrahedrite-tennantite), marcasite, as well as a grey mineral As-, Fe-, Cu-bearing sulfide or sulfosalt as rare inclusions in chalcopyrite. Ore minerals occur in three main styles: (1) disseminated isolated grains and dendritic clots; (2) stockwork veins and stringers; and (3) clots and seams in quartz-carbonate-base metal veins. Style 1 is exclusively pyrite. Isolated grains are euhedral-subhedral whereas dendritic clots are irregular and inclusion-rich. Style 2 contains two generations of pyrite, marcasite (restructured from pyrite), and minor chalcopyrite with composite inclusions. Original pyrite is inclusion-free and fractured. The second pyrite occurs as dendritic inclusion-rich rims around original pyrite. Chalcopyrite occurs as blebs in veins and is usually isolated from pyrite but is sometimes overgrown by it. Composite “star cluster” inclusions contain a grey mineral (As-Fe-Cu-sulfide or sulfosalt) or gangue minerals and are lined with a light yellow mineral (likely pyrite or arsenic pyrite). Style 3 has pyrite, sphalerite, galena, bournonite-seligmannite, and minor tennantite-tetrahedrite in poly-metallic clots or seams in veins.

Tennantite-tetrahedrite occurs as rare inclusions in other sulfides and was likely deposited early in the mineralizing event. Bournonite-seligmannite occurs as a late overgrowth replacing galena and is interpreted to be late stage hypogene overprinting.

7.3 Gangue minerals and alteration

Refracted light microscopy recognizes two styles of alteration along with vein-hosted minerals. The matrix and relict phenocrysts in the samples are altered with silicification, sericitization, pyritization, carbonatization, and chloritization. Ubiquitous quartz, sericite, and pyrite alterations are indicative of phyllic alteration. Local calcite, chlorite, and minor epidote (and pyrite) alterations are indicative of propylitic alteration. In veins there is quartz, carbonate, base metals, and rare gypsum/anhydrite. The gypsum/anhydrite is interpreted to be from late supergene alteration (weathering of sulfides).

The erratic potassium-silica trends and depletion in sodium suggest that alkalis have been mobilized by hydrothermal fluids. Calcium trends are consistent with igneous trends in the region and suggest that calcite formed from the destruction of calcium-bearing phases such as plagioclase; it was not significantly added to the system.

The striking depletion in sodium could be explained by muscovite/sericite formation which is abundant in the samples. In acidic solutions muscovite forms at the expense of albite (in phenocrysts) releasing sodium ions into solution and precipitating quartz (Equ. 7.3-1). This confirms that acidic fluids were present during the formation of muscovite/sericite.

Equation 7.3-1: $3\ NaAlSi_3O_8 + 2\ H^+ + K^+ \longrightarrow KAl_3Si_3O_{10}(OH)_2 + 6\ SiO_2 + 3\ Na^+$

7.4 Hydrothermal Fluids

Fluid inclusions trapped a dilute and relatively hot fluid which is compatible with heated meteoric water. Slight variations in salinity within FIAs suggest local heterogeneity in the fluids, possibly from mixing with a more saline fluid. Primary FIAs show that fluids which precipitated quartz were likely hotter than the ideal temperatures to form these deposits. The absence of conclusive evidence heterogeneous entrapment is compatible with a single-phase fluid that was not boiling. This is confirmed by the lack of textures indicative of boiling such as banded veins, brecciation, and lattice-textured quartz or calcite. Later fluids, likely not captured as fluid inclusions in quartz, may have had different trapping conditions and chemistries. Secondary fluid inclusions may have trapped later-stage fluids however there is no conclusive evidence for this.

Chapter 8: Discussions and conclusions

From the observations summarized previously along with observed textural relationships a paragenetic sequence of the Busang Southeast Zone (BSSE Zone) is created (Fig. 8-1). In the absence of additional geological information a schematic model for the formation of the BSSE Zone is shown in Figure 8-1 which is inspired by (Leach, 2001). This diagram shows only one of many possible scenarios which could have produced the observed features. Here six stages of mineralization are described. Stages I-VI were divided into a "porphyry" event and an "epithermal" event based on the genetic model for hydrothermal precious metal deposits in the Pacific Rim. An attempt is made to explain the processes which could account for the observations in the context of a hydrothermal system in a volcanic (island) arc setting; it is important to note that the processes described are merely inferences; the following is the inferred genetic sequence.

Stage-I: Porphyry stockwork

Emplacement of an intrusion causing the formation of porphyry-style stockwork veins containing pyrite and minor chalcopyrite. Stockwork veins are responsible for copper, gold, and molybdenum anomalies. A sampling of this intrusion could be the porphyritic basaltic-andesite of Bre-X7. There may be a diorite porphyry at greater depth. Chalcopyrite appears to texturally pre-date the second generation of pyrite but not the first in sample Bre-X9.

Stage-II: Phyllic/propylitic alteration

The heat and exsolved fluids from the intrusion permeated the surrounding rock resulting in silicification, pyritization (disseminated pyrite), rare chloritization, calcitization, and sericitization. The destruction of feldspars causes the mobilization of constituent elements such as calcium, potassium, and sodium; calcium formed calcite, potassium formed sericite, and sodium was likely dissolved in the fluid and transported. Where fluids are acidic, abundant sericite formed along with muscovite porphyroblasts in highly altered zones. Pyrite formed as disseminated isolated grains which are coeval with silicification. Quartz inclusions are present in late-forming pyrite but not early-forming pyrite.

Stage-III: Quartz veins

Massive quartz is deposited in a crudely banded habit in veins. Drusy cavities formed as euhedral quartz grows in open spaces. This quartz was precipitated from heated meteoric water which was likely heated from an intrusion (likely the intrusion in stage-I or a related magmatic event). Minor changes in fluid chemistry or pressure caused quartz to slowly be deposited in a crudely banded habit. The euhedral nature of quartz suggests that it formed slowly and was not the result of rapid cooling. Silicification of the wall rock occurred locally as alteration bands around veins.

Stage-IV: Base metal-carbonate veins

Fluid chemistry changed and allowed base metals and carbonates to be deposited almost exclusively in veins. This could be evidence for the cooling of the hydrothermal system (waning) or the input of magmatic fluids. Pyrite forms first, then

tennantite-tetrahedrite, galena, sphalerite and minor chalcopyrite. Pyrite pre-dates calcite but other ore minerals are coeval with minor calcite. The formation of calcite indicates that these fluids had a high pH, and are of probable meteoric origin. Chalcopyrite and bournonite-seligmannite form in the later stages of the mineralizing event. Bournonite-seligmannite appear to be replacing galena and is clearly interstitial to gangue minerals (i.e. it post-dates gangue minerals). Silver is trapped in galena, sulfosalts, and sphalertite as minor impurities, being most abundant in tennantite-tetrahedrite.

It is likely that this pyrite is the second generation of pyrite seen growing on original stockwork veins and as clots. It is concentrated in regions with abundant calcite. Calcite likely reduced the fluids locally allowing pyrite to form. At depth calcite is deposited along the edges of stockworks.

Stage-V: Carbonate veins

A high-pH fluid precipitates late calcite into opens spaces and in veins. Calcite often forms euhedral rhombs in open spaces or is interstitial to quartz in veins. Minor components of Fe, Mn, and Mg are present in these carbonates but not in high enough quantities to form other carbonates (ankerite, rhodochrosite or dolomite).

Stage-VI: Supergene alteration

The waning of the hydrothermal system lowers the temperature gradients. This results in the alteration of pyrite to marcasite. Minor sulfates (gypsum/anhydrite) form from oxidizing of sulfides by cool meteoric water.

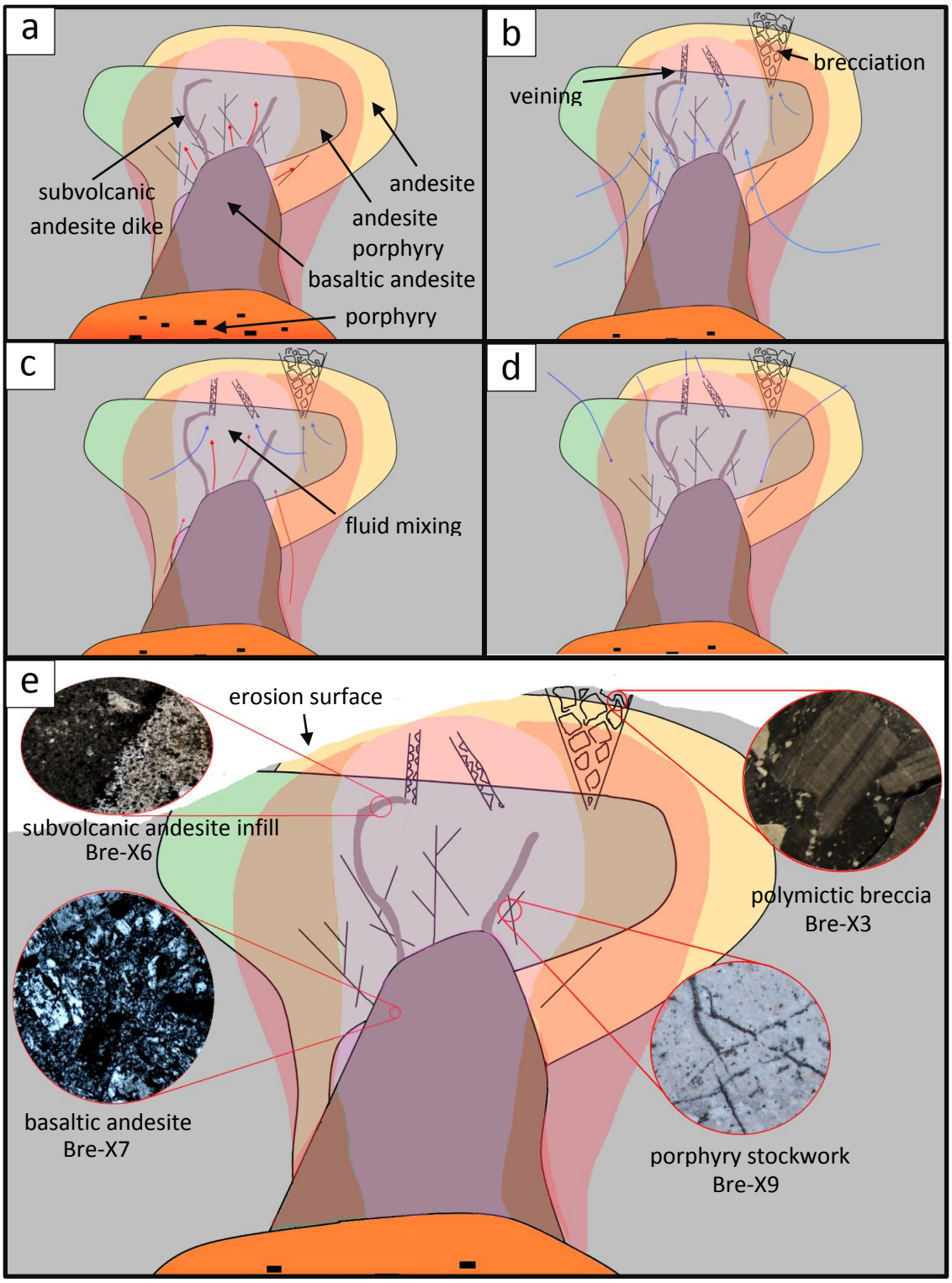

Figure 8-1: Schematic diagram of the genesis of the BSSE Zone (not to scale). Red arrows indicate magmatic fluids and blue arrows indicate meteoric fluids. (a) Stage I and II. Pyllic alteration – light pink, propylitic alteration – dark pink; (b) Stage III quartz veins and the formation of near surface breccias; (c) Stage IV base metal veins; (d) Stage V and VI. Calcite forms in veins and there is supergene alteration from descending meteoric water during waning; (e) Current geology of the BSSE Zone.

8.1 Evaluation of the Busang Southeast Zone as a hydrothermal mineral occurrence

Bre-X samples have many of the features that literature describes as being common to epithermal precious metal deposits in the Pacific Rim. Leach and Corbett (1997) described a genetic model for Pacific Rim epithermal carbonate-base metal deposits which is consistent with the paragenetic sequence of the Busang Southeast

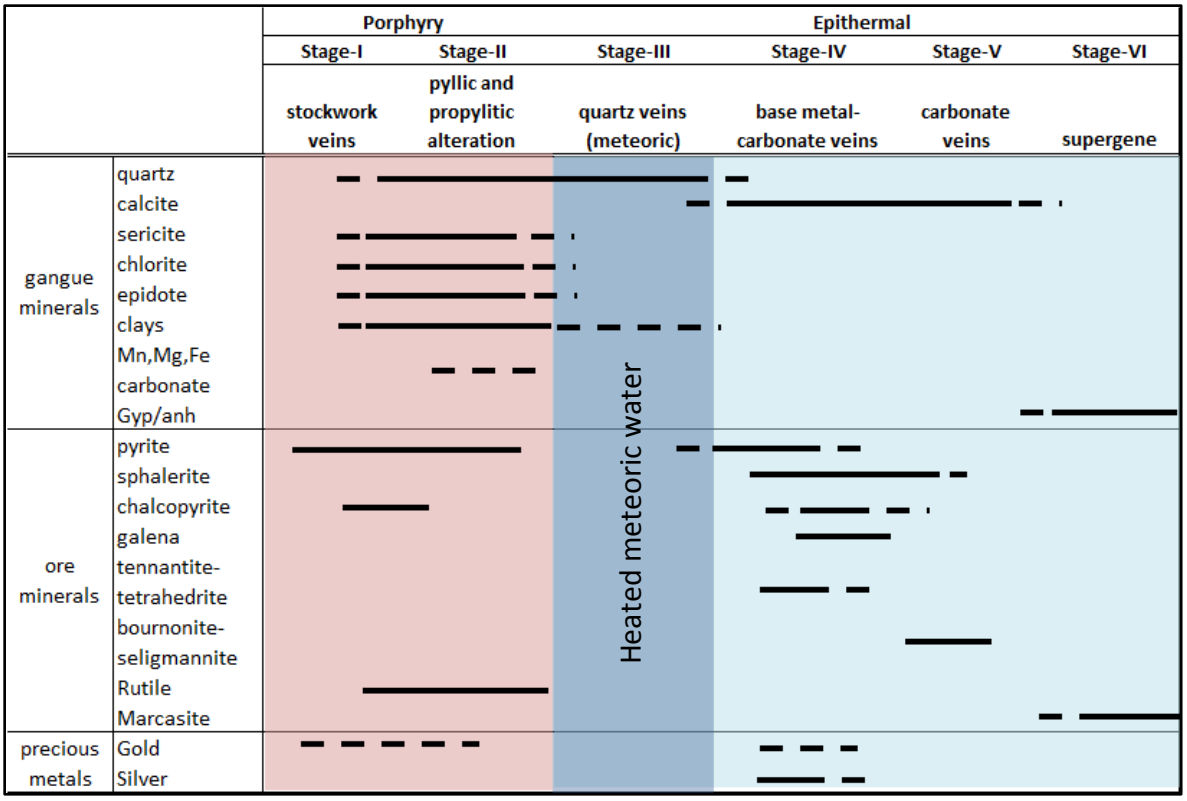

Figure 8-1: Inferred paragenetic sequence of the Busang Southeast Zone from Bre-X samples. The timing of the formation of primary FIAs is indicated with the dark blue. Secondary fluid inclusions could have formed in either the dark blue or the light blue. Dashed lines indicate probable timings of deposition which were not directly observed with textural evidence.

Zone (BSSE Zone) inferred from this study. Busang is located along the Kalimantan Gold Belt and hosted in porphyritic intermediate subvolcanic rocks. Geochemistry shows that the host rocks at BSSE Zone have igneous trends consistent with the Tertiary volcanic

rocks in the KGB. Geochemical anomalies show a general enrichment in elements, especially in veins, which are indicators of epithermal mineralization. Host rocks have been significantly altered by hydrothermal fluids, which is a requirement of a hydrothermal deposit. Ore minerals are consistent with those found in this style of deposit, although in relatively small quantities. Fluid inclusions show that the hydrothermal system here was hot, being likely heated by an intrusion, and was dominated by meteoric water.

This study concludes that the BSSE Zone is a gold- and silver-barren epithermal and porphyry system. The most important line of evidence is the conclusion that sample assays are very low in precious metals or any metals which could be economically viable. Although whole-rock geochemistry was limited by sample size, it shows that there is very little gold or silver present in this system. SEM analysis confirms this and demonstrates that precious metals, mainly silver, are only present in minor quantities as substitutions in galena, sphalerite, and sulfosalts (most abundant in tennantite-tetrahedrite). Textures, complemented by fluid inclusion analyses, are probably the best line of evidence in explaining why there are no significant concentrations of precious metals in these samples.

Recent research has found that specific textures can be linked to high-grades in epithermal deposits and that fluid inclusions can be used to hone in on mineralized veins (Moncada et al., 2011). Textures which are indicative of rapid reduction of solubility in fluids are associated with higher grades. These textures include banded

veins and lattice-textured quartz and calcite. Also, textures such as cockade breccias are indicators of a dynamic system which has experienced multiple episodes of brecciation and deposition, an important factor.

Solulity of gold in aqueous solution is low even in the best conditions and thus large volumes of fluids enriched in gold are needed to form high-grades. These fluids need to experience a change in conditions including pH, REDOX state, temperature, pressure, and salinity. Ideally these changes occur repeatedly over a long period of time which concentrates rare metals through multiple episodes of precipitation. The textures and fluid inclusions in Bre-X samples do not show evidence for episodic reduction in solubility (e.g. boiling), and they do not show the spectacular and varied textures associated with a dynamic hydrothermal system.

Boiling and fluid mixing are thought to be two significant mechanisms which contribute to gold deposition. Fluid inclusions and textures demonstrate that boiling was probably not occurring at the location of the Bre-X samples; inclusions only trapped a homogenous fluid phase. Fluids were also very hot, likely too hot to precipitate gold here. If gold were concentrated anywhere in this system it would likely be above where the samples came from; adiabatic rise of fluids into lower pressure regimes could cause them to boil. Since Bre-X samples were obtained from drill core at relatively shallow depths (<50-400 m) it is possible that a gold occurrence (likely a small one) occurred above the location of the samples but has been removed by erosion.

8.2 Conclusions

The study of the suite of samples belonging to Dr. Milligan leads to the conclusion that the Busang Southeast Zone is compatible with the fringe of a weakly mineralized low-sulfidation epithermal mineral occurrence. However, it is unlikely that these samples belong to or are associated with a rich gold or silver deposit. The geological setting at Busang is promising for epithermal mineralization, but evidence shows that conditions here were not ideal in this case. The pressure, temperature, and chemistry of the hydrothermal fluids were not ideal to effectively concentrate precious metals here in the system. These conclusions are based on observation of a small suite of samples with very little known about their provenance or their spatial context. With purposeful study, a great amount of information was acquired which is used to make inferences about the geological setting from which they came.

Chapter 9: Recommendations for further work

The scope of this study was limited by time, funding, and the small sample set. Several unanswered questions have arisen which could be investigated with further work. There are also several techniques which could have given further insight into the hydrothermal mineralization at Busang which were beyond the scope of an undergraduate thesis.

In situ stable isotope analysis (e.g. oxygen or carbon isotopes analysis) could be performed along traverses in euhedral quartz and calcite. Isotopic ratios could be used to estimate the origin of the fluid by comparison to isotope databases. One could distinguish between magmatic, metamorphic, and meteoric fluid by looking at stable isotope ratios. A traverse across a mineral grain could provide information on the relative input of meteoric versus magmatic fluid over time. This method was used by Hayashi et al. (2001) studying the mechanisms of gold precipitation in a low-sulfidation epithermal gold deposit.

Several observations during ore-microscopy could lead to further conclusions if studied with additional attention. The presence of inclusions of chalcopyrite in sphalerite is reminiscent of “chalcopyrite disease” and could provide information about the genetic history of these veins. These inclusions are interpreted here to be the result of co-precipitation of chalcopyrite and sphalerite. The solubility of copper in sphalerite is low at low temperatures expected in epithermal systems and cannot be the result of exsolution. They may however have formed by the reaction of copper ions in

hydrothermal solutions with the iron in sphalerite. Detailed SEM analysis might be able to determine the precise nature of the chalcopyrite inclusions and their implications of the genetic history of the veins (e.g Barton & Bethke, 1987 and Nagase & Kojima, 1997). An attempt was made to analyse the inclusions with the SEM, but the data was not of high enough quality to produce meaningful interpretations as the inclusions were too small.

Carbonate mineralogy is often used as a proxy to determine distance from intrusions in epithermal systems. Fe-, Mn-, and Mg-carbonates are more abundant than calcite in close proximity to an intrusion; calcite becomes more abundant with increasing distance from intrusions (Corbett & Leach, 1997). A detailed SEM analysis of carbonates in these samples could help us determine the location of the porphyry intrusion which likely exists at depth in this system.

The clay mineralogy of these samples is not well understood as they cannot be identified in thin section. X-ray diffraction (XRD) would be a useful method to determine the clays present in these samples. Clays are very temperature sensitive and could be used as a proxy for the temperature of alteration which would complement refracted light microscopy. The spatial zonation of clays could be mapped in cross-sections to determine paleo-isotherms in the hydrothermal system.

Fluid Inclusion analysis was limited to quartz in veins. From textural relationships the quartz was determined to predate the base metal mineralization in veins. Fluid

inclusions in vein-hosted calcite as well as sphalerite (using infrared light) could be used to directly study the ore forming fluid.

There are several examples in literature where the geochemistry of intrusions has been used to predict whether they are likely to have produced peripheral mineralization. Baldwin and Pearce (1982) noted that productive intrusions are typically depleted in Y, and Mn which they explained by the early crystallization of Y- and Mn-rich hydrous phases as well as the loss of Mn-rich fluids from the magma. This method would require directly sampling the intrusion in the Busang system and comparing it with other data from intrusions (productive and unproductive) in the same tectonic province with Y-MnO plots. This method was not used in this study as we cannot be sure that a mineralizing intrusion has been sampled in the suite of core collected by Dr. Milligan. Also, finding element data in literature for intrusions in this tectonic province is time consuming and was not deemed the most efficient use of time.

Very little is known about the spatial context from which these samples came. If more information were known then one could create a schematic model of the Busang Southeast Zone that is to scale. Data such as paleo-isotherms from fluid inclusions, and XRD analysis of clays could be plotted in cross-section to hone in on areas which most likely host mineralization.

Chapter 10: Closing remarks

The Bre-X affair is likely the most damaging mining hoax in all of history. Many of the details of this event to this day are shrouded in uncertainty. Why were many professionals so easily convinced of the legitimacy of Bre-X's assays? Also, John Felderhof invited his esteemed professor Dr. Milligan to visit Busang to collect samples for Dalhousie's Earth Science Department. Why would he have done this unless he genuinely believed Busang was a rich gold deposit?

The careful study of this set of samples was carried out to in an attempt to add unique insight to this affair. This study concludes, from examining these samples alone, that the Busang Southeast Zone is likely not a rich ore deposit. However, these samples were studied with great detail employing techniques which may not have been commonly used in mineral exploration at the time. Companies have a tendency to be more concerned with "what" is in the ground rather than "why", however this attitude is slowly changing. This study serves as a testament to the importance of academic study; with a relatively small budget an undergraduate student was able to learn a great deal about the geology from which the rocks came which could have proved valuable to industry.

The geological setting of these samples, along with the hydrothermal alteration and mineralization, could lead one to suspect they belong to a deposit if assay results were promising. However, it is the role of the geologist to not only interpret the data he or she is given but to ensure that the data is accurate and not falsified. In the after math

of the Bre-X affair the mining industry has learned many lessons and regulations have been put in place to ensure the accountability of companies and the professionals involved.

References

ACTLABS. (2013). Brochure Retrieved from Activision Laboratories Ltd., Ancaster, ON, Canada: http://www.actlabs.com/list.aspx?menu=64&app=226&cat1=549&tp=12&lk=no

Andrews, G. (2005). *Candian professional engineering and geoscience: Practice and ethics* (4 ed.). Toronto: Nelso Education Ltd.

Baldwin, J. A., & Pearce, J. A. (1982). Discrimination of productive and nonproductive porphyritic intrusions in the Chilean Andes. *Economic Geolgoy, 77*, 664-674.

Barton, P., & Bethke, P. (1987). Chalcopyrite disease in sphalerite: Pathology and epidemology. *American Mineralogist, 72*, 451-467.

Bodnar, R. (2003). *Fuid inclusions: analysis and interpretation* (Vol. 32). (I. Samson, A. Anderson, & D. Marshal, Eds.) Vancouver: Mineralogical Association of Canada.

Bodnar, R., & Vityk, M. (1994). Interpretation of microthermometric data for H2O-NaCl fluid inclusions. In B. De Vivo, & M. Frezzotti, *Fluid inclusions in minerals, methods and applications* (pp. 117-130). Blacksburg, VA: Virginia Tech.

Davies, A. G., Cooke, D. R., & Gemmell, B. J. (2008). Hydrothermal breccias and veins at the Kelian Gold Mine, Kalimantan, Indonesia: Genesis of a large epithermal gold deposit. *Economic Geology, 103*, 717-757.

Dostal, J., Zentilli, M., Caelles, J. C., & Clark, A. H. (1977). Geochemistry and origin of volcanic rocks of the Andes (26°-28°S). *Contributions to Mineralogy and Petrology, 63*(2), 113-129.

Francis, D. (1997). *Bre-X: The inside stroy.* Toronto: Key Porter Books. 240 p.

Goold, D., & Willis, A. (1997). *The Bre-X Fraud.* Toronto: McClelland & Stewart. 272 p.

Hamilton, W. (1979). *Tectonic of the Indonesia Region.* Washington: United States Government Printing Office. 345 p.

Hanley, J., & Kontak, D. (2013, February 1). Fluid Inclusions Workshop. *Atlantic Geoscience Colloquium*. Halifax, Nova Scotia.

Hayashi, K., Maruyama, T., & Satoh, H. (2001). Precipitation of gold in a low-sulfidation epithermal gold deposit: Insights from a submillimeter-scale oxygen isotope analysis of vein quartz. *Economic Geology, 96*(1), 211-216.

Hedenquist, J. W. (2000). Exploration for epithermal gold deposits. *SEG Reviews, 13*, 245-277.

Hedenquist, J. W., & Lowenstern, J. B. (1994). The role of magmas in the formation of hydrothermal ore deposists. *Nature, 370*, 519-527.

Hedenquist, J. W., Izawa, E., Arribas, A., & White, N. C. (1996). Epithermal gold deposits: styles, characteristics, and exploration. *Special Pulication Number 1(1)*. Tokyo, Japan.

Heinrich, C., Driesner, T., Stefansson, A., & Seward, T. (2004). Magmatic vapour contraction and the transportaion of gold from the porphyry environment to epithermal ore deposits. *Geology, 32*(9), 761-764.

Leach, T. M. (2001). Alteration and mineralization in drillcore from the Busang Prospect, East Kalimantan, Indonesia.

Leach, T. M., & Corbett, G. J. (1997). *Short course manual: Southwest Pacific rim gold-copper systems: Structure, alteration and mineralization* (5 ed.), 318 p.

Moncada, D., Mutchler, S., Nieto, A., Reynolds, T. J., Rimstidt, J. D., & Bodnar, R. J. (2011). Mineral textures and fluid inclusion petrography of the epithermal Ag–Au deposits at Guanajuato, Mexico: Application to exploration. *Journal of Geochemical Exploration*, 20-35.

Moss, S. J., & Finch, E. M. (1997). Geological implications of new biostratigraphic data from East and West Kalimantan, Indonesia. *Journal of Asian Earth Sciences, 15*(6), 489-506.

Nagase, T., & Kojima, S. (1997). An SEM examination of chalcopyrite disease texture and its genetic implications. *Mineralogical Magazine, 61*, 89-97.

Nagase, T., & Kojima, S. (1997). An SEM examination of the chalcopyrite disease texture and its genetic implications. *Mineralogical Magazine, 61*(404), 89-97.

Panteleyev, A. (1985). A Canadian Cordilleran model for epithermal gold-silver deposits. (R. G. Roberts, & P. A. Sheahan, Eds.) *Geoscience Canada Reprint Series 3, 13*(2).

Peccerillo, A., & Taylor, S. R. (1976). Geochemistry of Eocene calc-alkaline volcanic rocks from the Kastamonu area northen Turkey. *Contribs Mineral Petrol, 58*, 63-81.

Rudnik, R., & Gao, S. (2003). Composition of the continental crust. (R. Rudnik, Ed.) *The Crust, 3*, 1-64.

Soeria-Atmadja, R., Noeradi, D., & Priadi, B. (1999). Cenozoic magmatism in Kalimantan and its related geodynamic evolution. *Journal of Asian Earth Sciences, 17*, 25-45.

Sun, S., & McDonough, W. (1989). Chemical and isotope systematics of oceanic basalts: implications for mantle composition and processes. In A. Saunders, & M. Norry (Eds.), *Magmatism in the Ocean Basins* (42 ed., pp. 313-345). Geological Society Special Publication.

White, N. C. (2011, March 4 and 5). PDAC and SEG short course: Gold geology and deposit types. Toronto, Canada.

White, N. C., & Hedenquist, J. W. (1995). Epithermal gold deposits: Styles, characteristics and exploration. *Society of Economic Geology News Letter*(23), 1-9.

Winchester, J. A., & Floyd, P. A. (1977). Geochemical discrimination of different magma series and their differentiation products using immobile elements. *Chemical Geology, 20*(4), 325-343.

Wu, I., & Birnie, R. (1977). The bournonite-seligmannite solid solution. *American Mineralogist, 62*, 1097-1100.

Appendix 1: Actlabs report

Quality Analysis ... **Actlabs** *Innovative Technologies*

Date Submitted: 25-Oct-12
Invoice No.: A12-11865
Invoice Date: 23-Nov-12
Your Reference: Evan Slater Thesis

Dalhousie University
Dept of Earth Sciences
Life Sciences Centre
Halifax NS B3H 4J1
Canada

ATTN: Marcos Zentilli

CERTIFICATE OF ANALYSIS

8 Rock samples were submitted for analysis.

The following analytical packages were requested:

REPORT **A12-11865**

Code 4E-Res + ICPMS (FeO)(1-10) INAA(INAAGEO)/Major Elements Fusion ICP(WRA)/Total Digestion ICP(TOTAL)/Trace Element Fus ICP/MS
Code 4E-XRF XRF Pressed Pellet
Code 4F-C, S Infrared
Code 4F-Cl INAA(INAAGEO)
Code 4F-CO2 Infrared
Code 4F-FeO Titration
Code 4F-H2O+- Gravimetric

Notes:
The Fe2O3 for the standards is Total Fe2O3 and has not been adjusted for the FeO with the exception of SY-3, BIR-1 and GBW 07113. LOI2 is the LOI adjusted for the difference in oxygen between FeO and Fe2O3. TOTAL2 is the total including LOI2.
Total includes all elements in % oxide to the left of total. Values which exceed the upper limits should be assayed for most accurate values.

CERTIFIED BY :

Emmanuel Eseme , Ph.D.
Quality Control

ISO/IEC 17025
SCC Accredited
LAB 266
LAB 266
Accrédité CCN

ACTIVATION LABORATORIES LTD.
1336 Sandhill Drive, Ancaster, Ontario Canada L9G 4V5 TELEPHONE +1.905.648.9611 or +1.888.228.5227 FAX +1.905.648.9613
E-MAIL Ancaster@actlabs.com ACTLABS GROUP WEBSITE www.actlabs.com

Activation Laboratories Ltd. Report: A12-11865

Analyte Symbol	Ga	Pb	Sn	Nb	Rb	C-Total	Total S	Cl	Mass	CO2	FeO	H20+	H20-	SiO2	Al2O3	Fe2O3	MnO	MgO	CaO	Na2O	K2O	TiO2	P2O5	LOI
Unit Symbol	ppm	ppm	ppm	ppm	ppm	%	%	%	g	%	%	%	%	%	%	%	%	%	%	%	%	%	%	%
Detection Limit	5	5	5	1	2	0.01	0.01	0.01		0.01	0.1	0.1	0.1	0.01	0.01	0.01	0.001	0.01	0.01	0.01	0.01	0.001	0.01	
Analysis Method	PPXRF	PPXRF	PPXRF	PPXRF	PPXRF	IR	IR	INAA	INAA	IR	TITR	GRAV	GRAV	FUS-ICP	FUS-ICP	FUS-ICP	FUS-ICP	FUS-ICP	FUS-ICP	FUS-ICP	FUS-ICP	FUS-ICP	FUS-ICP	FUS-ICP
BREX-2	15	44	< 5	2	51	1.83	2.53	0.01	1.05	6.52	2.7	4.9	1.4	52.91	16.99	1.12	0.133	1.02	7.40	0.31	1.57	0.622	0.13	13.93
BREX-5	15	6	< 5	2	62	0.29	4.78	0.02	1.01	0.96	3.5	4.5	0.8	60.86	17.07	2.72	0.054	0.44	1.38	0.13	2.02	0.603	0.14	9.35
BREX-6	22	167	< 5	2	52	1.50	4.60	0.03	1.03	5.37	4.5	1.2	0.4	57.36	13.30	1.98	0.193	3.40	3.92	0.34	1.99	0.460	0.08	10.68
BREX-7	12	13	< 5	1	54	1.10	3.17	0.01	1.02	3.95	3.0	3.5	1.0	63.75	14.24	1.28	0.111	0.63	4.77	0.42	1.39	0.318	0.10	10.27
BREX-8	11	57	6	2	137	1.27	5.09	< 0.01	1.01	4.49	2.9	2.1	0.6	57.80	14.30	3.67	0.291	2.33	3.42	0.13	3.93	0.484	0.11	9.44
BREX-9	14	24	5	2	13	0.55	2.12	< 0.01	1.04	1.94	4.1	2.5	0.7	55.97	17.30	2.31	0.377	3.04	6.27	2.49	0.42	0.625	0.12	6.23
BREX-10	< 5	1300	< 5	< 1	43	0.27	1.53	< 0.01	1.02	0.97	0.4	1.3	0.5	80.87	8.21	2.10	0.393	0.52	0.84	0.11	2.15	0.185	0.04	3.71
BREX-11	11	263	< 5	2	111	0.20	3.03	0.01	1.02	0.71	3.5	2.0	0.6	68.61	14.41	0.90	0.163	0.86	0.68	0.17	3.86	0.343	0.09	5.47

Activation Laboratories Ltd. **Report: A12-11865**

Analyte Symbol	Ga	Pb	Sn	Nb	Rb	C-Total	Total S	Cl	Mass	CO2	FeO	H2O+	H2O-	SiO2	Al2O3	Fe2O3	MnO	MgO	CaO	Na2O	K2O	TiO2	P2O5	LOI
Unit Symbol	ppm	ppm	ppm	ppm	ppm	%	%	%	g	%	%	%	%	%	%	%	%	%	%	%	%	%	%	%
Detection Limit	5	5	5	1	2	0.01	0.01	0.01		0.01	0.1	0.1	0.1	0.01	0.01	0.01	0.001	0.01	0.01	0.01	0.01	0.001	0.01	
Analysis Method	PPXRF	PPXRF	PPXRF	PPXRF	PPXRF	IR	IR	INAA	INAA	IR	TITR	GRAV	GRAV	FUS-ICP	FUS-ICP	FUS-ICP	FUS-ICP	FUS-ICP	FUS-ICP	FUS-ICP	FUS-ICP	FUS-ICP	FUS-ICP	FUS-ICP
BREX-2	15	44	< 5	2	51	1.83	2.53	0.01	1.05	6.52	2.7	4.9	1.4	52.91	16.99	1.12	0.133	1.02	7.40	0.31	1.57	0.622	0.13	13.93
BREX-5	15	6	< 5	2	62	0.29	4.78	0.02	1.01	0.96	3.5	4.5	0.8	60.86	17.07	2.72	0.054	0.44	1.38	0.13	2.02	0.603	0.14	9.35
BREX-6	22	167	< 5	2	52	1.50	4.60	0.03	1.03	5.37	4.5	1.2	0.4	57.36	13.30	1.98	0.193	3.40	3.92	0.34	1.99	0.460	0.08	10.68
BREX-7	12	13	< 5	1	54	1.10	3.17	0.01	1.02	3.95	3.0	3.5	1.0	63.75	14.24	1.28	0.111	0.63	4.77	0.42	1.39	0.318	0.10	10.27
BREX-8	11	57	6	2	137	1.27	5.09	< 0.01	1.01	4.49	2.9	2.1	0.6	57.80	14.30	3.67	0.291	2.33	3.42	0.13	3.93	0.484	0.11	9.44
BREX-9	14	24	5	2	13	0.55	2.12	< 0.01	1.04	1.94	4.1	2.5	0.7	55.97	17.30	2.31	0.377	3.04	6.27	2.49	0.42	0.625	0.12	6.23
BREX-10	< 5	1300	< 5	< 1	43	0.27	1.53	< 0.01	1.02	0.97	0.4	1.3	0.5	80.87	8.21	2.10	0.393	0.52	0.84	0.11	2.15	0.185	0.04	3.71
BREX-11	11	263	< 5	2	111	0.20	3.03	0.01	1.02	0.71	3.5	2.0	0.6	68.61	14.41	0.90	0.163	0.86	0.68	0.17	3.86	0.343	0.09	5.47

Analyte Symbol	LOI2	Total 2	Total	Au	Ag	As	Ba	Be	Bi	Br	Cd	Co	Cr	Cs	Cu	Ga	Ge	Hf	Hg	In	Ir	Mo	Nb	Ni
Unit Symbol	%	%	%	ppb	ppm	ppm	ppm	ppm	ppm	ppm	ppm	ppm	ppm	ppm	ppm	ppm	ppm	ppm	ppm	ppm	ppb	ppm	ppm	ppm
Detection Limit		0.01	0.01	1	0.5	1	1	1	0.1	0.5	0.5	0.1	0.5	0.1	1	1	0.5	0.1	1	0.1	1	2	0.2	1
Analysis Method	FUS-ICP	FUS-ICP	FUS-ICP	INAA	MULT INAA / TD-ICP	INAA	FUS-ICP	FUS-ICP	FUS-MS	INAA	TD-ICP	INAA	INAA	FUS-MS	TD-ICP	FUS-MS	FUS-MS	FUS-MS	INAA	FUS-MS	INAA	FUS-MS	FUS-MS	TD-ICP
BREX-2	13.63	98.83	99.14	14	< 0.5	16	100	1	0.1	< 0.5	< 0.5	12.3	11.0	9.7	25	16	1.9	2.2	< 1	< 0.1	< 1	< 2	3.3	8
BREX-5	8.96	98.28	98.67	8	< 0.5	24	160	< 1	0.4	1.6	< 0.5	18.1	16.2	5.8	13	15	3.6	3.0	2	< 0.1	< 1	< 2	3.8	9
BREX-6	10.17	98.19	98.70	74	2.4	185	228	2	2.1	< 0.5	< 0.5	15.0	28.4	2.8	17	25	2.8	1.8	< 1	< 0.1	< 1	2	2.6	11
BREX-7	9.93	100.3	100.6	139	0.9	75	145	< 1	< 0.1	1.4	0.7	9.3	19.2	8.7	1140	13	0.9	2.0	< 1	< 0.1	< 1	19	2.6	10
BREX-8	9.11	98.80	99.12	20	< 0.5	33	380	< 1	0.4	1.1	1.5	16.2	10.7	9.4	15	13	< 0.5	2.2	< 1	< 0.1	< 1	2	3.1	4
BREX-9	5.77	99.26	99.71	14	< 0.5	24	182	< 1	0.1	< 0.5	< 0.5	14.8	9.9	6.8	69	15	0.8	2.4	< 1	< 0.1	< 1	< 2	2.7	6
BREX-10	3.67	99.54	99.58	32	1.6	70	185	< 1	0.5	1.1	< 0.5	5.7	12.6	4.6	122	7	1.3	1.5	< 1	< 0.1	< 1	6	6.8	13
BREX-11	5.08	99.05	99.45	47	6.8	77	467	< 1	1.6	< 0.5	< 0.5	8.3	28.9	6.7	211	14	< 0.5	2.1	< 1	< 0.1	< 1	< 2	2.3	8

Activation Laboratories Ltd. **Report: A12-11865**

Analyte Symbol	Pb	Rb	S	Sb	Sc	Se	Sn	Sr	Ta	Th	U	V	W	Y	Zn	Zr	La	Ce	Pr	Nd	Sm	Eu	Gd	Tb
Unit Symbol	ppm	ppm	%	ppm	ppm	ppm	ppm	ppm	ppm	ppm	ppm	ppm	ppm	ppm	ppm	ppm	ppm	ppm	ppm	ppm	ppm	ppm	ppm	ppm
Detection Limit	5	1	0.001	0.1	0.01	0.5	1	2	0.01	0.05	0.01	5	1	1	1	1	0.05	0.05	0.01	0.05	0.01	0.005	0.01	0.01
Analysis Method	TD-ICP	FUS-MS	TD-ICP	INAA	INAA	INAA	FUS-MS	FUS-ICP	FUS-MS	FUS-MS	FUS-MS	FUS-ICP	INAA	FUS-ICP	MULT INAA / TD-ICP	FUS-MS	FUS-MS	FUS-MS	FUS-MS	FUS-MS	FUS-MS	FUS-MS	FUS-MS	FUS-MS
BREX-2	39	51	2.67	4.1	14.7	< 0.5	3	94	0.20	3.47	0.85	160	< 1	16	29	87	9.24	19.9	2.41	10.3	2.41	0.685	2.69	0.44
BREX-5	< 5	61	5.21	2.9	13.3	< 0.5	3	37	0.24	4.54	1.07	123	3	15	8	114	9.29	19.5	2.28	8.91	2.18	0.704	2.43	0.44
BREX-6	157	56	4.93	9.0	12.6	5.4	2	63	0.14	2.73	1.04	124	< 1	15	35	65	4.41	10.4	1.27	5.44	1.32	0.251	1.73	0.35
BREX-7	9	52	3.38	1.3	7.90	14.6	1	101	0.15	2.63	0.65	67	< 1	9	98	80	7.47	14.7	1.55	5.93	1.29	0.550	1.31	0.22
BREX-8	55	144	5.13	6.0	11.7	10.2	2	51	0.19	4.17	0.94	119	< 1	12	215	85	10.2	20.1	2.25	8.68	1.82	0.588	2.02	0.33
BREX-9	27	10	2.05	4.2	14.1	< 0.5	< 1	262	0.20	3.07	0.73	145	< 1	13	112	83	8.22	18.1	2.21	9.36	2.11	0.725	2.13	0.38
BREX-10	1420	74	1.66	117	3.57	17.4	< 1	24	0.11	1.46	0.41	32	< 1	4	41	65	2.73	4.77	0.59	2.30	0.61	0.193	0.61	0.11
BREX-11	285	123	3.37	81.5	11.6	4.9	3	30	0.15	2.80	0.74	96	< 1	6	59	84	4.14	8.41	0.95	3.56	0.81	0.208	0.97	0.17

Analyte Symbol	Dy	Ho	Er	Tl	Tm	Yb	Lu	Mass
Unit Symbol	ppm	ppm	ppm	ppm	ppm	ppm	ppm	g
Detection Limit	0.01	0.01	0.01	0.05	0.005	0.01	0.002	
Analysis Method	FUS-MS	FUS-MS	FUS-MS	FUS-MS	FUS-MS	FUS-MS	FUS-MS	INAA
BREX-2	2.70	0.57	1.78	0.41	0.272	1.83	0.300	1.007
BREX-5	2.76	0.59	1.77	0.61	0.266	1.75	0.290	1.011
BREX-6	2.37	0.53	1.62	0.66	0.239	1.60	0.258	1.008
BREX-7	1.33	0.28	0.84	0.74	0.125	0.85	0.141	1.038
BREX-8	2.01	0.42	1.26	2.04	0.187	1.24	0.207	1.016
BREX-9	2.41	0.50	1.54	0.38	0.231	1.58	0.264	1.062
BREX-10	0.71	0.15	0.50	1.08	0.076	0.53	0.089	1.024
BREX-11	1.04	0.22	0.68	1.80	0.110	0.78	0.138	1.021

Quality Control

Analyte Symbol	Ga	Pb	Sn	Nb	Rb	C-Total	Total S	Cl	CO2	H2O+	H2O-	SiO2	Al2O3	Fe2O3	MnO	MgO	CaO	Na2O	K2O	TiO2	P2O5	LOI	LOI2	Total 2
Unit Symbol	ppm	ppm	ppm	ppm	ppm	%	%	%	%	%	%	%	%	%	%	%	%	%	%	%	%	%	%	%
Detection Limit	5	5	5	1	2	0.01	0.01	0.01	0.01	0.1	0.1	0.01	0.01	0.01	0.001	0.01	0.01	0.01	0.01	0.001	0.01			0.01
Analysis Method	PPXRF	PPXRF	PPXRF	PPXRF	PPXRF	IR	IR	INAA	IR	GRAV	GRAV	FUS-ICP	FUS-ICP	FUS-ICP	FUS-ICP	FUS-ICP	FUS-ICP	FUS-ICP	FUS-ICP	FUS-ICP	FUS-ICP	FUS-ICP	FUS-ICP	FUS-ICP
GXR-1 Meas																								
GXR-1 Cert																								
GXR-1 Meas																								
GXR-1 Cert																								
NIST 694 Meas												11.27	1.89	0.73	0.013	0.33	42.78	0.86	0.55	0.116	30.20			
NIST 694 Cert												11.2	1.80	0.790	0.0116	0.330	43.6	0.860	0.510	0.110	30.2			
DNC-1 Meas												46.69	18.21	9.85	0.146	9.90	11.41	1.90	0.22	0.474	0.05			
DNC-1 Cert												47.15	18.34	1.79	0.150	10.13	11.49	1.890	0.234	0.480	0.070			
GBW 07113 Meas												72.20	12.78	1.15	0.141	0.13	0.60	2.51	5.41	0.283	0.02			
GBW 07113 Cert												72.8	13.0	1.35	0.140	0.160	0.590	2.57	5.43	0.300	0.0500			
GXR-4 Meas																								
GXR-4 Cert																								
GXR-4 Meas																								
GXR-4 Cert																								
SDC-1 Meas																								
SDC-1 Cert																								
SDC-1 Meas																								
SDC-1 Cert																								
SCO-1 Meas																								
SCO-1 Cert																								
SCO-1 Meas																								
SCO-1 Cert																								
GXR-6 Meas																								
GXR-6 Cert																								
GXR-6 Meas																								
GXR-6 Cert																								
LKSD-3 Meas																								
LKSD-3 Cert																								
MAG-1 (Depleted) Meas								3.15																
MAG-1 (Depleted) Cert								3.10																
LKSD-4 Meas						17.9	1.04																	
LKSD-4 Cert						17.7	0.990																	
BE-N Meas	17	6	5	100	54																			
BE-N Cert	17.0	4.00	2.00	105	47.0																			
AC-E Meas	37	42	14	109	149																			
AC-E Cert	39.0	39.0	13.0	110	152																			
GA Meas																								
GA Cert																								
BaSO4 Meas							13.7																	
BaSO4 Cert							14.0																	
NIST 1632c Meas								0.11																
NIST 1632c Cert								0.110																
W-2a Meas												52.55	15.29	10.79	0.166	6.15	11.07	2.22	0.62	1.075	0.15			
W-2a Cert												52.4	15.4	1.53	0.163	6.37	10.9	2.14	0.626	1.06	0.130			
SY-4 Meas									3.29			49.82	20.56		0.108	0.48	8.14	6.97	1.66	0.285	0.13			
SY-4 Cert									3.5			49.9	20.69		0.108	0.54	8.05	7.10	1.66	0.287	0.131			
CTA-AC-1 Meas																								
CTA-AC-1 Cert																								
BIR-1a Meas												47.72	15.86	2.15	0.172	9.49	13.49	1.82	0.02	0.984	0.02			
BIR-1a Cert												47.96	15.50	2.06	0.175	9.700	13.30	1.82	0.030	0.96	0.021			
Calcium Carbonate Meas									45.1															
Calcium Carbonate Cert									44.05															
NCS DC86312 Meas																								
NCS DC86312 Cert																								
ZW-C Meas	98	85	1310	193	8530																			
ZW-C Cert	99	80	1300	198	8500																			

Quality Control

Analyte Symbol	Ga	Pb	Sn	Nb	Rb	C-Total	Total S	Cl	CO2	H2O+	H2O-	SiO2	Al2O3	Fe2O3	MnO	MgO	CaO	Na2O	K2O	TiO2	P2O5	LOI	LOI2	Total 2
Unit Symbol	ppm	ppm	ppm	ppm	ppm	%	%	%	%	%	%	%	%	%	%	%	%	%	%	%	%	%	%	%
Detection Limit	5	5	5	1	2	0.01	0.01	0.01	0.01	0.1	0.1	0.01	0.01	0.01	0.001	0.01	0.01	0.01	0.01	0.001	0.01			0.01
Analysis Method	PPXRF	PPXRF	PPXRF	PPXRF	PPXRF	IR	IR	INAA	IR	GRAV	GRAV	FUS-ICP	FUS-ICP	FUS-ICP	FUS-ICP	FUS-ICP	FUS-ICP	FUS-ICP	FUS-ICP	FUS-ICP	FUS-ICP	FUS-ICP	FUS-ICP	FUS-ICP
GL-O Meas										8.4														
GL-O Cert										5.58														
VS-N Meas	364	992	803	705	812																			
VS-N Cert	400	1000.0	803	700	800																			
JGb-2 Meas																								
JGb-2 Cert																								
JGb-2 Meas																								
JGb-2 Cert																								
NCS DC70014 Meas																								
NCS DC70014 Cert																								
NCS DC70009 (GBW07241) Meas																								
NCS DC70009 (GBW07241) Cert																								
OREAS 100a (Fusion) Meas																								
OREAS 100a (Fusion) Cert																								
OREAS 101a (Fusion) Meas																								
OREAS 101a (Fusion) Cert																								
JR-1 Meas																								
JR-1 Cert																								
SAR-M (U.S.G.S.) Meas																								
SAR-M (U.S.G.S.) Cert																								
SAR-M (U.S.G.S.) Meas																								
SAR-M (U.S.G.S.) Cert																								
DNC-1a Meas																								
DNC-1a Cert																								
DNC-1a Meas																								
DNC-1a Cert																								
BREX-10 Orig																								
BREX-10 Dup																								
BREX-11 Orig												69.61	14.52	0.96	0.165	0.86	0.67	0.17	3.90	0.345	0.07	5.47	5.08	100.2
BREX-11 Dup												67.62	14.30	0.83	0.160	0.86	0.69	0.17	3.82	0.341	0.11	5.47	5.08	97.86
Method Blank																								
Method Blank																								
Method Blank						< 0.01	< 0.01																	
Method Blank																								
Method Blank																								
Method Blank																								
Method Blank																								
Method Blank											< 0.1													
Method Blank											< 0.1													
Method Blank	< 5	< 5	< 5	< 1	< 2																			
Method Blank																								

Quality Control

Analyte Symbol	Total	Au	Ag	Ag	As	Ba	Be	Br	Cd	Co	Cr	Cu	Hg	Ir	Ni	Pb	S	Sb	Sc	Se	Sr	V	W	Y
Unit Symbol	%	ppb	ppm	ppm	ppm	ppm	ppm	ppm	ppm	ppm	ppm	ppm	ppm	ppb	ppm	ppm	%	ppm	ppm	ppm	ppm	ppm	ppm	ppm
Detection Limit	0.01	1	0.5	5	1	1	1	0.5	0.5	0.1	0.5	1	1	1	1	5	0.001	0.1	0.01	0.5	2	5	1	1
Analysis Method	FUS-ICP	INAA	TD-ICP	INAA	INAA	FUS-ICP	FUS-ICP	INAA	TD-ICP	INAA	INAA	TD-ICP	INAA	INAA	TD-ICP	TD-ICP	TD-ICP	INAA	INAA	INAA	FUS-ICP	FUS-ICP	INAA	FUS-ICP
GXR-1 Meas		3270	31.4	33	426			< 0.5	3.3	9.4	13.5	1200	< 1		42	748	0.254	121	1.65	17.1			177	
GXR-1 Cert		3300	31.0	31.0	427			0.500	3.30	8.20	12.0	1110	3.90		41.0	730	0.257	122	1.58	16.6			164	
GXR-1 Meas			31.4						3.3			1160			53	707	0.246							
GXR-1 Cert			31.0						3.30			1110			41.0	730	0.257							
NIST 694 Meas																						1658		
NIST 694 Cert																						1740		
DNC-1 Meas						103															143	157		15
DNC-1 Cert						118															144.0	148.0		18.0
GBW 07113 Meas						496	4														42	5		45
GBW 07113 Cert						506	4.00														43.0	5.00		43.0
GXR-4 Meas			3.5						0.6			6430			42	45	1.73							
GXR-4 Cert			4.00						0.860			6520			42.0	52.0	1.77							
GXR-4 Meas			3.6						< 0.5			6470			48	52	1.77							
GXR-4 Cert			4.00						0.860			6520			42.0	52.0	1.77							
SDC-1 Meas			< 0.5						< 0.5			33			38	21	0.070							
SDC-1 Cert			0.0410						0.0800			30.00			38.0	25.00	0.0650							
SDC-1 Meas			< 0.5						< 0.5			31			39	18	0.067							
SDC-1 Cert			0.0410						0.0800			30.00			38.0	25.00	0.0650							
SCO-1 Meas			< 0.5						< 0.5			31			30	28	0.065							
SCO-1 Cert			0.134						0.140			29			27	31.0	0.0630							
SCO-1 Meas			< 0.5						< 0.5			29			30	26	0.077							
SCO-1 Cert			0.134						0.140			29			27	31.0	0.0630							
GXR-6 Meas			< 0.5						< 0.5			75			29	98	0.017							
GXR-6 Cert			1.30						1.00			66.0			27.0	101	0.0160							
GXR-6 Meas			< 0.5						< 0.5			67			29	86	0.015							
GXR-6 Cert			1.30						1.00			66.0			27.0	101	0.0160							
LKSD-3 Meas																								
LKSD-3 Cert																								
MAG-1 (Depleted) Meas																								
MAG-1 (Depleted) Cert																								
LKSD-4 Meas																								
LKSD-4 Cert																								
BE-N Meas																								
BE-N Cert																								
AC-E Meas																								
AC-E Cert																								
GA Meas																								
GA Cert																								
BaSO4 Meas																								
BaSO4 Cert																								
NIST 1632c Meas																								
NIST 1632c Cert																								
W-2a Meas						170	< 1														192	278		18
W-2a Cert						182	1.30														190	262		24.0
SY-4 Meas						342	3														1198	8		115
SY-4 Cert						340	2.6														1191	8.0		119
CTA-AC-1 Meas																								
CTA-AC-1 Cert																								
BIR-1a Meas						8	< 1														109	340		14
BIR-1a Cert						6	0.58														110	310		16
Calcium Carbonate Meas																								
Calcium Carbonate Cert																								
NCS DC86312 Meas																								
NCS DC86312 Cert																								
ZW-C Meas																								
ZW-C Cert																								

Quality Control

Analyte Symbol	Total	Au	Ag	Ag	As	Ba	Be	Br	Cd	Co	Cr	Cu	Hg	Ir	Ni	Pb	S	Sb	Sc	Se	Sr	V	W	Y
Unit Symbol	%	ppb	ppm	ppm	ppm	ppm	ppm	ppm	ppm	ppm	ppm	ppm	ppm	ppb	ppm	ppm	%	ppm	ppm	ppm	ppm	ppm	ppm	ppm
Detection Limit	0.01	1	0.5	5	1	1	1	0.5	0.5	0.1	0.5	1	1	1	1	5	0.001	0.1	0.01	0.5	2	5	1	1
Analysis Method	FUS-ICP	INAA	TD-ICP	INAA	INAA	FUS-ICP	FUS-ICP	INAA	TD-ICP	INAA	INAA	TD-ICP	INAA	INAA	TD-ICP	TD-ICP	TD-ICP	INAA	INAA	INAA	FUS-ICP	FUS-ICP	INAA	FUS-ICP
GL-O Meas																								
GL-O Cert																								
VS-N Meas																								
VS-N Cert																								
JGb-2 Meas																								
JGb-2 Cert																								
JGb-2 Meas																								
JGb-2 Cert																								
NCS DC70014 Meas																								
NCS DC70014 Cert																								
NCS DC70009 (GBW07241) Meas																								
NCS DC70009 (GBW07241) Cert																								
OREAS 100a (Fusion) Meas																								
OREAS 100a (Fusion) Cert																								
OREAS 101a (Fusion) Meas																								
OREAS 101a (Fusion) Cert																								
JR-1 Meas																								
JR-1 Cert																								
SAR-M (U.S.G.S.) Meas			3.7						4.8			328			52	967								
SAR-M (U.S.G.S.) Cert			3.64						5.27			331			41.50	982								
SAR-M (U.S.G.S.) Meas			3.6						5.3			339			51	1020								
SAR-M (U.S.G.S.) Cert			3.64						5.27			331			41.50	982								
DNC-1a Meas												104			246									
DNC-1a Cert												100.0			247									
DNC-1a Meas												111			283									
DNC-1a Cert												100.0			247									
BREX-10 Orig																								
BREX-10 Dup																								
BREX-11 Orig	100.6					470	< 1														30	97		6
BREX-11 Dup	98.26					464	< 1														30	95		6
Method Blank		< 1		< 5	< 1			< 0.5		< 0.1	< 0.5		< 1	< 1				< 0.1	< 0.01	< 0.5			< 1	
Method Blank																								
Method Blank																								
Method Blank			< 0.5						< 0.5			< 1			< 1	< 5	< 0.001							
Method Blank			< 0.5						< 0.5			< 1			< 1	< 5	< 0.001							
Method Blank			< 0.5						< 0.5			< 1			< 1	< 5	< 0.001							
Method Blank			< 0.5						< 0.5			< 1			< 1	< 5	< 0.001							
Method Blank																								
Method Blank																								
Method Blank																								
Method Blank																								

Quality Control

Analyte Symbol	Zn	Zn	Mass	Bi	Cs	Ga	Ge	Hf	In	Mo	Nb	Rb	Sn	Ta	Th	U	Zr	La	Ce	Pr	Nd	Sm	Eu	Gd
Unit Symbol	ppm	ppm	g	ppm	ppm	ppm	ppm	ppm	ppm	ppm	ppm	ppm	ppm	ppm	ppm	ppm	ppm	ppm	ppm	ppm	ppm	ppm	ppm	ppm
Detection Limit	1	50		0.1	0.1	1	0.5	0.1	0.1	2	0.2	1	1	0.01	0.05	0.01	1	0.05	0.05	0.01	0.05	0.01	0.005	0.01
Analysis Method	TD-ICP	INAA	INAA	FUS-MS	FUS-MS	FUS-MS	FUS-MS	FUS-MS	FUS-MS	FUS-MS	FUS-MS	FUS-MS	FUS-MS	FUS-MS	FUS-MS	FUS-MS	FUS-MS	FUS-MS	FUS-MS	FUS-MS	FUS-MS	FUS-MS	FUS-MS	FUS-MS
GXR-1 Meas	766	730																						
GXR-1 Cert	760	760																						
GXR-1 Meas	735																							
GXR-1 Cert	760																							
NIST 694 Meas																								
NIST 694 Cert																								
DNC-1 Meas																	35				4.75		0.581	
DNC-1 Cert																	38				5.20		0.59	
GBW 07113 Meas																								
GBW 07113 Cert																								
GXR-4 Meas	77																							
GXR-4 Cert	73.0																							
GXR-4 Meas	77																							
GXR-4 Cert	73.0																							
SDC-1 Meas	108																							
SDC-1 Cert	103.00																							
SDC-1 Meas	98																							
SDC-1 Cert	103.00																							
SCO-1 Meas	106																							
SCO-1 Cert	100																							
SCO-1 Meas	96																							
SCO-1 Cert	100																							
GXR-6 Meas	145																							
GXR-6 Cert	118																							
GXR-6 Meas	133																							
GXR-6 Cert	118																							
LKSD-3 Meas					2.3					< 2		75		0.75	10.8	4.53	162	47.8	91.0		42.9	7.70	1.44	
LKSD-3 Cert					2.30					2.00		78.0		0.700	11.4	4.60	178	52.0	90.0		44.0	8.00	1.50	
MAG-1 (Depleted) Meas																								
MAG-1 (Depleted) Cert																								
LKSD-4 Meas																								
LKSD-4 Cert																								
BE-N Meas																								
BE-N Cert																								
AC-E Meas																								
AC-E Cert																								
GA Meas																								
GA Cert																								
BaSO4 Meas																								
BaSO4 Cert																								
NIST 1632c Meas																								
NIST 1632c Cert																								
W-2a Meas																								
W-2a Cert																								
SY-4 Meas																								
SY-4 Cert																								
CTA-AC-1 Meas															23.9	4.26		2170	> 3000		1130	166	45.3	128
CTA-AC-1 Cert															21.8	4.4		2176	3326		1087	162	46.7	124
BIR-1a Meas						15		0.6			0.6							0.68	1.94		2.35	1.09	0.499	1.87
BIR-1a Cert						16		0.60			0.6							0.63	1.9		2.5	1.1	0.55	2.0
Calcium Carbonate Meas																								
Calcium Carbonate Cert																								
NCS DC86312 Meas																		2370	184		1570			225
NCS DC86312 Cert																		2360.000	190.000		1600.000			225.0
ZW-C Meas						95		9.7				> 1000												
ZW-C Cert						99		9.7				8500												

Quality Control

Analyte Symbol	Zn	Zn	Mass	Bi	Cs	Ga	Ge	Hf	In	Mo	Nb	Rb	Sn	Ta	Th	U	Zr	La	Ce	Pr	Nd	Sm	Eu	Gd
Unit Symbol	ppm	ppm	g	ppm	ppm	ppm	ppm	ppm	ppm	ppm	ppm	ppm	ppm	ppm	ppm	ppm	ppm	ppm	ppm	ppm	ppm	ppm	ppm	ppm
Detection Limit	1	50		0.1	0.1	1	0.5	0.1	0.1	2	0.2	1	1	0.01	0.05	0.01	1	0.05	0.05	0.01	0.05	0.01	0.005	0.01
Analysis Method	TD-ICP	INAA	INAA	FUS-MS	FUS-MS	FUS-MS	FUS-MS	FUS-MS	FUS-MS	FUS-MS	FUS-MS	FUS-MS	FUS-MS	FUS-MS	FUS-MS	FUS-MS	FUS-MS	FUS-MS	FUS-MS	FUS-MS	FUS-MS	FUS-MS	FUS-MS	FUS-MS
GL-O Meas																								
GL-O Cert																								
VS-N Meas																								
VS-N Cert																								
JGb-2 Meas																								
JGb-2 Cert																								
JGb-2 Meas																								
JGb-2 Cert																								
NCS DC70014 Meas				80.3		25				> 100								42.5	84.2		37.0	7.62	1.65	7.03
NCS DC70014 Cert				80.3		25.2				270								45.3	87.0		39.9	8.0	1.8	7.4
NCS DC70009 (GBW07241) Meas					42.6	16	11.1		1.3			501	> 1000		28.0			22.8	57.7	7.33	29.8	11.9		14.1
NCS DC70009 (GBW07241) Cert					41	16.5	11.2		1.3			500.00	1701.000		28.3			23.7	60.3	7.9	32.9	12.5		14.8
OREAS 100a (Fusion) Meas										22					50.1	132		248	451	42.5	138	22.3	3.43	
OREAS 100a (Fusion) Cert										24.1					51.6	135		260	463	47.1	152	23.6	3.71	
OREAS 101a (Fusion) Meas										20					35.7	423		805	1370	124	381	49.3	7.88	
OREAS 101a (Fusion) Cert										21.9					36.6	422		816	1396	134	403	48.8	8.06	
JR-1 Meas					20.8	17		4.5	< 0.1	3	15.5	251	3	1.83	26.8	8.97	108	19.5	46.7	5.61	22.3	5.57		5.37
JR-1 Cert					20.8	16.1		4.51	0.028	3.25	15.2	257	2.86	1.86	26.7	8.88	99.9	19.7	47.2	5.58	23.3	6.03		5.06
SAR-M (U.S.G.S.) Meas	892																							
SAR-M (U.S.G.S.) Cert	930.0																							
SAR-M (U.S.G.S.) Meas	945																							
SAR-M (U.S.G.S.) Cert	930.0																							
DNC-1a Meas	57																							
DNC-1a Cert	70.0																							
DNC-1a Meas	60																							
DNC-1a Cert	70.0																							
BREX-10 Orig																								
BREX-10 Dup																								
BREX-11 Orig				1.5	6.7	14	< 0.5	2.0	< 0.1	< 2	2.3	123	3	0.15	2.80	0.71	85	4.13	8.57	0.97	3.70	0.76	0.212	0.94
BREX-11 Dup				1.7	6.7	14	0.7	2.1	< 0.1	< 2	2.2	123	3	0.15	2.81	0.77	83	4.14	8.26	0.93	3.43	0.86	0.203	1.00
Method Blank		< 50	1.000																					
Method Blank				< 0.1	< 0.1	< 1	< 0.5	< 0.1	< 0.1	< 2	< 0.2	< 1	< 1	< 0.01	< 0.05	< 0.01	< 1	< 0.05	< 0.05	< 0.01	< 0.05	< 0.01	< 0.005	< 0.01
Method Blank																								
Method Blank	< 1																							
Method Blank	< 1																							
Method Blank	< 1																							
Method Blank	< 1																							
Method Blank																								
Method Blank																								
Method Blank																								
Method Blank				< 0.1	< 0.1	< 1	< 0.5	< 0.1	< 0.1	< 2	< 0.2	< 1	< 1	< 0.01	< 0.05	< 0.01	< 1	< 0.05	< 0.05	< 0.01	< 0.05	< 0.01	< 0.005	< 0.01

Quality Control

Analyte Symbol	Tb	Dy	Ho	Er	Tl	Tm	Yb	Lu	FeO
Unit Symbol	ppm	ppm	ppm	ppm	ppm	ppm	ppm	ppm	%
Detection Limit	0.01	0.01	0.01	0.01	0.05	0.005	0.01	0.002	0.1
Analysis Method	FUS-MS	FUS-MS	FUS-MS	FUS-MS	FUS-MS	FUS-MS	FUS-MS	FUS-MS	TITR
GXR-1 Meas									
GXR-1 Cert									
GXR-1 Meas									
GXR-1 Cert									
NIST 694 Meas									
NIST 694 Cert									
DNC-1 Meas							1.97		
DNC-1 Cert							2.0		
GBW 07113 Meas									1.9
GBW 07113 Cert									1.86
GXR-4 Meas									
GXR-4 Cert									
GXR-4 Meas									
GXR-4 Cert									
SDC-1 Meas									
SDC-1 Cert									
SDC-1 Meas									
SDC-1 Cert									
SCO-1 Meas									
SCO-1 Cert									
SCO-1 Meas									
SCO-1 Cert									
GXR-6 Meas									
GXR-6 Cert									
GXR-6 Meas									
GXR-6 Cert									
LKSD-3 Meas		4.84					2.70	0.413	
LKSD-3 Cert		4.90					2.70	0.400	
MAG-1 (Depleted) Meas									
MAG-1 (Depleted) Cert									
LKSD-4 Meas									
LKSD-4 Cert									
BE-N Meas									
BE-N Cert									
AC-E Meas									
AC-E Cert									
GA Meas									1.3
GA Cert									1.32
BaSO4 Meas									
BaSO4 Cert									
NIST 1632c Meas									
NIST 1632c Cert									
W-2a Meas									
W-2a Cert									
SY-4 Meas									3.0
SY-4 Cert									2.86
CTA-AC-1 Meas	14.8						10.6	1.09	
CTA-AC-1 Cert	13.9						11.4	1.08	
BIR-1a Meas							1.70		8.4
BIR-1a Cert							1.7		8.34
Calcium Carbonate Meas									
Calcium Carbonate Cert									
NCS DC86312 Meas	34.4	184	35.7	96.5		14.4	87.7	12.1	
NCS DC86312 Cert	34.6	183.00	35.70	96.2		15.1	87.79	11.96	
ZW-C Meas					34.6				
ZW-C Cert					34				

Quality Control

Analyte Symbol	Tb	Dy	Ho	Er	Tl	Tm	Yb	Lu	FeO
Unit Symbol	ppm	ppm	ppm	ppm	ppm	ppm	ppm	ppm	%
Detection Limit	0.01	0.01	0.01	0.01	0.05	0.005	0.01	0.002	0.1
Analysis Method	FUS-MS	FUS-MS	FUS-MS	FUS-MS	FUS-MS	FUS-MS	FUS-MS	FUS-MS	TITR
GL-O Meas									
GL-O Cert									
VS-N Meas									
VS-N Cert									
JGb-2 Meas									5.8
JGb-2 Cert									5.41
JGb-2 Meas									5.4
JGb-2 Cert									5.41
NCS DC70014 Meas	1.13	6.09	1.26	3.46		0.535	3.40	0.482	
NCS DC70014 Cert	1.1	6.7	1.3	3.5		0.57	3.3	0.50	
NCS DC70009 (GBW07241) Meas	3.16	20.1	4.18	12.3		2.26	15.6	2.19	
NCS DC70009 (GBW07241) Cert	3.3	20.7	4.5	13.4		2.2	14.9	2.4	
OREAS 100a (Fusion) Meas	3.48	21.4	4.54	13.6		2.26	14.5	2.05	
OREAS 100a (Fusion) Cert	3.80	23.2	4.81	14.9		2.31	14.9	2.26	
OREAS 101a (Fusion) Meas		30.1	6.37	18.6		2.90	18.0	2.48	
OREAS 101a (Fusion) Cert		33.3	6.46	19.5		2.90	17.5	2.66	
JR-1 Meas	1.00	6.02	1.22	3.95	1.56	0.696	4.52	0.676	0.5
JR-1 Cert	1.01	5.69	1.11	3.61	1.56	0.67	4.55	0.71	0.49
SAR-M (U.S.G.S.) Meas									
SAR-M (U.S.G.S.) Cert									
SAR-M (U.S.G.S.) Meas									
SAR-M (U.S.G.S.) Cert									
DNC-1a Meas									
DNC-1a Cert									
DNC-1a Meas									
DNC-1a Cert									
BREX-10 Orig									0.4
BREX-10 Dup									0.4
BREX-11 Orig	0.17	1.03	0.22	0.68	1.70	0.110	0.78	0.138	3.4
BREX-11 Dup	0.17	1.05	0.22	0.69	1.89	0.111	0.78	0.139	3.6
Method Blank									
Method Blank	< 0.01	< 0.01	< 0.01	< 0.01	< 0.05	< 0.005	< 0.01	< 0.002	
Method Blank									
Method Blank									
Method Blank									
Method Blank									
Method Blank									
Method Blank									
Method Blank									
Method Blank									
Method Blank	< 0.01	< 0.01	< 0.01	< 0.01	< 0.05	< 0.005	< 0.01	< 0.002	

Appendix 2: SEM element point analyses

SEM element point analyses (atomic ratio)

Point No.	Au	Ag	As	Se	Fe	Pb	Sb	Cu	Bi	S	Zn	Hg	Cd	Te	Total
1	0	0	0	0	0.0185	50.3579	0.0536	0	0	49.2652	0.0498	0	0.1301	0.1248	100
2	0	0	0.0103	0.0457	0	49.8678	0.1434	0.1269	0	49.6618	0	0.0016	0.074	0.0684	99.9999
3	0	0	5.4314	0	0	17.0136	10.8138	16.5583	0	50.0915	0.017	0	0.0743	0	100
4	0	0	8.8028	0	0.0113	16.9325	7.7534	16.9206	0	49.5153	0	0	0.064	0	100
5	0.0254	0	5.1364	0	0	16.6537	11.3131	17.0863	0	49.7852	0	0	0	0	100
6	0	0	0	0.0833	0	50.653	0	0	0	48.6986	0.047	0.0697	0.4167	0.0317	100
7	0	0	0	0.0483	0.0084	50.8437	0.0095	0	0	48.8205	0.0169	0.0086	0.1975	0.0465	100
8	0	0	0	0.0765	0.0505	50.7522	0.0694	0.0676	0	48.5858	0	0.0422	0.3396	0.0163	100
9	0.0046	1.3607	4.6068	0	1.2512	0.0259	9.3042	31.4974	0	44.3901	7.5592	0	0	0	100
10	0.0149	0.0062	0	0	0.358	0.066	0.0384	0.1791	0	51.1693	47.9597	0	0.1951	0.0133	100
11	0.015	0.0729	0.2824	0	0.3645	0	0.4873	1.708	0.0076	50.5648	46.3527	0.0042	0.1405	0	100
12	0.015	0.1168	0	0	0.3236	0.0048	0	0.0156	0	50.9696	48.3514	0	0.1333	0.0699	100
13	0	0.0207	0	0.0734	0.0084	50.2534	0.0256	0.0541	0	49.125	0.1191	0	0.253	0.0673	100
14	0	0	5.1886	0	0	17.4305	11.473	17.0438	0	48.8641	0	0	0	0	100
15	0	0	3.8985	0	0	16.1672	14.7061	15.6496	0	49.5516	0	0.0271	0	0	100
21	0.0192	0.0076	4.7162	0	20.2822	0.045	0.0064	14.9595	0.0017	59.9291	0.03	0	0	0.0031	100
22	97.6808	0.8642	0	0	0.0167	0	0	0	0.2017	0	0	1.2089	0	0.0278	100
23	69.8975	28.84	0	0	0	0	0	0	0.0922	0	0	1.0702	0	0.1001	100
24	0.0336	99.3829	0	0	0	0.0402	0	0.0376	0.0289	0.4237	0.0063	0	0	0.0468	100

Appendix 2: SEM element point analyses

SEM element point analyses (atomic ratio)

Point No.	Au	Ag	As	Se	Fe	Pb	Sb	Cu	Bi	S	Zn	Hg	Cd	Te	Total
1	0	0	0	0	0.0185	50.3579	0.0536	0	0	49.2652	0.0498	0	0.1301	0.1248	100
2	0	0	0.0103	0.0457	0	49.8678	0.1434	0.1269	0	49.6618	0	0.0016	0.074	0.0684	99.9999
3	0	0	5.4314	0	0	17.0136	10.8138	16.5583	0	50.0915	0.017	0	0.0743	0	100
4	0	0	8.8028	0	0.0113	16.9325	7.7534	16.9206	0	49.5153	0	0	0.064	0	100
5	0.0254	0	5.1364	0	0	16.6537	11.3131	17.0863	0	49.7852	0	0	0	0	100
6	0	0	0	0.0833	0	50.653	0	0	0	48.6986	0.047	0.0697	0.4167	0.0317	100
7	0	0	0	0.0483	0.0084	50.8437	0.0095	0	0	48.8205	0.0169	0.0086	0.1975	0.0465	100
8	0	0	0	0.0765	0.0505	50.7522	0.0694	0.0676	0	48.5858	0	0.0422	0.3396	0.0163	100
9	0.0046	1.3607	4.6068	0	1.2512	0.0259	9.3042	31.4974	0	44.3901	7.5592	0	0	0	100
10	0.0149	0.0062	0	0	0.358	0.066	0.0384	0.1791	0	51.1693	47.9597	0	0.1951	0.0133	100
11	0.015	0.0729	0.2824	0	0.3645	0	0.4873	1.708	0.0076	50.5648	46.3527	0.0042	0.1405	0	100
12	0.015	0.1168	0	0	0.3236	0.0048	0	0.0156	0	50.9696	48.3514	0	0.1333	0.0699	100
13	0	0.0207	0	0.0734	0.0084	50.2534	0.0256	0.0541	0	49.125	0.1191	0	0.253	0.0673	100
14	0	0	5.1886	0	0	17.4305	11.473	17.0438	0	48.8641	0	0	0	0	100
15	0	0	3.8985	0	0	16.1672	14.7061	15.6496	0	49.5516	0	0.0271	0	0	100
21	0.0192	0.0076	4.7162	0	20.2822	0.045	0.0064	14.9595	0.0017	59.9291	0.03	0	0	0.0031	100
22	97.6808	0.8642	0	0	0.0167	0	0	0	0.2017	0	0	1.2089	0	0.0278	100
23	69.8975	28.84	0	0	0	0	0	0	0.0922	0	0	1.0702	0	0.1001	100
24	0.0336	99.3829	0	0	0	0.0402	0	0.0376	0.0289	0.4237	0.0063	0	0	0.0468	100